National and Technical University of Athens

School of Applied Mathematical and Physical Sciences

Nanoparticle Sensor Arrays on Flexible Substrates

PhD thesis

Evangelos Aslanidis

April 2021

Supervisor

Professor Dimitris Tsoukalas

National and Technical University of Athens
School of Applied Mathematical and Physical Sciences

Nanoparticle Sensor Arrays on Flexible Substrates

PhD thesis

Evangelos Aslanidis

Three-member committee

Prof. D. Tsoukalas (NTUA)

Prof. I. Raptis (NTUA)

Prof. C. Papavassiliou (Imperial College)

Seven-member committee

Prof. I. Zergioti (NTUA)

Prof. A. Kiritsis (NTUA)

Prof. E. Christoforou (NTUA)

Prof. T. Prodromakis (SOTON)

ABSTRACT

The main subject of the current thesis is the development and study of operation of metallic nanoparticle-based flexible strain sensors. In addition, it is presented how Al_2O_3 (alumina) thin films were developed by Atomic Layer Deposition (ALD) for sensors protection against humidity. A study concerning the strain sensor's characteristics before and after the deposition of alumina was carried out. Additionally, the already existing theory that describes the behavior of nanoparticles-based strain sensors was enriched in order to include the sputtering made nanoparticles. Throughout our study was successfully determined the critical thickness of the alumina film for the isolation and sufficient protection of nanoparticles from humidity. Apart from that, a Monte Carlo simulation tool that was written in Matlab, is developed to predict the sensitivities of various nanoparticle film under strain. This tool is capable of predicting the strain-sensitivity for different nanoparticle diameters as well as surface coverages, emerging as a powerful computational tool for design and optimization of nanoparticle based devices, while it could be extended to other nanocomposite materials used in flexible or stretchable electronic applications. Moreover, highly sensitive flexible strain sensors formed by a network of metallic nanoparticles on top of a cracked thin alumina film were fabricated and discussed. Sensors' sensitivity depends on the nanoparticles' surface density as well as on the thickness of alumina thin films. Both can be well controlled via the deposition techniques. A record strain sensitivity value of 2.6×10^8 was achieved by the sensors at 7.2% strain, while exhibiting high sensitivity in a large strain range from 0.1% to 7.2%. The demonstration is followed by a discussion enlightening the physical understanding of sensor operation, which enables the tuning of its performance according to the above process parameters. Finally, a strain sensor array was develop on a glove and measured by a custom made circuit. The measurements of the circuit were compared with measurements from a Keithley 2400 and found to be very precise in the operational range of the circuit.

ΠΕΡΙΛΗΨΗ

Η παρούσα διδακτορική διατριβή αφορά τη μελέτη συστοιχιών αισθητήρων νανοσωματιδίων σε εύκαμπτα υποστρώματα. Πιο συγκεκριμένα, μελετήθηκαν αισθητήρες παραμόρφωσης κατασκευασμένοι πάνω σε εύκαμπτο υπόστρωμα πολυιμιδίου (kapton), οι οποίοι είχαν ως υλικό αίσθησης μεταλλικά νανοσωματίδια πλατίνας ανάμεσα σε ηλεκτρόδια χρυσού. Παρακάτω θα γίνει μία εκτενής περιληπτική παρουσίαση του υλικού της έρευνας. Προς χάριν αναφοράς, η οργάνωση υλικού της παρουσίασης γίνεται βάσει των κεφαλαίων της διδακτορικής διατριβής.

Αρχικά (Chapter 1: Introduction, pp. 3-16) η μελέτη κάνει μία ιστορική αναδρομή στην μικροηλεκτρονική και την νανοτεχνολογία. Στο παρόν κεφάλαιο γίνεται αναφορά στα πρώτα τεχνολογικά επιτεύγματα της μικροηλεκτρονικής, όπως το πρώτο τρανζίστορ από τα Bell Laboratories το 1948, η πρώτη διάταξη n-p-n το 1955, η ανάπτυξη της οπτικής λιθογραφίας το 1957 κ.α. Σημασία της ιστορικής αυτής αναδρομής είναι οι επιπτώσεις της, καθώς η αλματώδης αυτή ανάπτυξη στον τομέα της μικροηλεκτρονικής οδήγησε στην μείωση του μεγέθους και του βάρους των ηλεκτρονικών συσκευών καθιστώντας τες ταυτόχρονα και αποδοτικότερες. Τα τρανζίστορ αντικατέστησαν της λυχνίες κενού που χρησιμοποιούσαν όλες οι συσκευές έως τότε (από ραδιόφωνα μέχρι πολύπλοκες υπολογιστές μηχανές) βελτιώνοντας την απόδοσή τους σε κατανάλωση ισχύος. Η τεχνολογική ανάπτυξη εκφράστηκε συνοπτικά από τον νόμο του Moore ο οποίος περιφραστικά ανέφερε ότι ο αριθμός των τρανζίστορ σε μία ολοκληρωμένη διάταξη επεξεργαστή θα διπλασιάζεται ανά δύο χρόνια. Ο νόμος του Moore επαληθεύτηκε με την σμίκρυνση των διατάξεων έως και στην τάξη των μερικών νανόμετρων, γεννώντας τις τεχνολογικές επιστήμες της μικροηλεκτρονικής και της νανοτεχνολογίας.

Η νανοτεχνολογία αφορά διατάξεις των οποίων η μία διάσταση είναι από 1 έως 100 νανόμετρα. Είναι ένας κλάδος με ραγδαία ανάπτυξη και συνεισφορά σε πάρα πολλά επιστημονικά πεδία όπως η επιστήμη των ημιαγωγών, η οργανική χημεία, η μοριακή βιολογία κ.α. Κατά την μετάβαση από ένα μακροσκοπικό υλικό σε ένα νανοϋλικό, οι ιδιότητες του υλικού μεταβάλλονται. Αυτές οι μεταβολές καθιστούν τα νανοϋλικά εξαιρετικά χρήσιμα και ενδιαφέροντα προς μελέτη.

Συνεχίζοντας στο ίδιο κεφάλαιο, περιγράφονται μερικές από τις βασικές τεχνικές εναπόθεσης υλικών κάποιες από τις οποίες χρησιμοποιήθηκαν και για την δημιουργία των διατάξεων που κατασκευάστηκαν για τις ανάγκες των πειραμάτων που περιγράφονται στην παρούσα διατριβή. Μία από αυτές είναι η εναπόθεση ατομικών στρώσεων (Atomic Layer Deposition). Αυτή η τεχνική είναι ικανή να εναποθέτει πολύ ομοιογενή –σε πάχος- μονοατομικά υμένια στο υπόστρωμα αλλά και να επικαλύπτει την τραχύτητα του υποστρώματος. Το σύστημα εναπόθεσης αποτελείται από έναν θάλαμο κενού, όπου λαμβάνουν χώρο οι αντιδράσεις, και δοχεία με τις πρόδρομες ενώσεις (ή αντιδρώντα), τα οποία βρίσκονται σε αέρια ή υγρή κατάσταση. Κατά την εναπόθεση ο θάλαμος βρίσκεται υπό κενό και διαδοχικά εισέρχονται τα αντιδρώντα με την βοήθεια αερίου Αζώτου πολύ υψηλής καθαρότητας. Κάθε κύκλος

εναπόθεσης ορίζεται ως την εισαγωγή όλων των αντιδρώντων. Το σύστημα χρησιμοποιήθηκε για την παρασκευή λεπτών υμενίων οξειδίου του αλουμινίου (ή αλουμίνα). Για την παρασκευή αλουμίνας οι πρόδρομες ενώσεις που χρησιμοποιηθήκαν ήταν το νερό και το τετραμεθυλαργίλιο (TMA) τα οποία βρίσκονταν σε υγρή κατάσταση. Κατά τον πρώτο κύκλο έγινε εισαγωγή του TMA στον θάλαμο με την βοήθεια του αζώτου το οποίο διέρχεται από το δοχείο του TMA και στην συνέχεια το συμπαρασέρνει προς τον θάλαμο. Η αντίδραση του TMA με τα υδροξύλια που βρίσκονται στην επιφάνεια του υποστρώματος και θα προκαλέσει τελικά ένωση με το υπόστρωμα απελευθερώνοντας Μεθάνιο. Στην συνέχεια, ο θάλαμος καθαρίζεται από τα ελεύθερα μεθάνια με την συνεχόμενη εισαγωγή Αζώτου. Έπειτα, στον θάλαμο εισάγεται νερό, με τον ίδιο τρόπο όπως και με το TMA, το οποίο αντιδράει με τα μεθύλια του TMA έχοντας ως αποτέλεσμα δημιουργία αλουμίνας στο υπόστρωμα και ελευθέρων Μεθανίων τα οποία αποβάλλονται από τον θάλαμο μέσω καθαρισμού του με Άζωτο. Το αποτέλεσμα αυτής της διαδικασίας είναι ένα μονατομικό υμένιο αλουμίνας πάνω στο υπόστρωμα. Επαναλαμβάνοντας την προηγούμενη διαδικασία είναι δυνατή η εναπόθεση παχύτερων στρωμάτων.

Μια άλλη ευρέως διαδεδομένη οικογένεια τεχνικών είναι η φυσική εναπόθεση ατμών κατά την οποία δημιουργούνται ατμοί από το υλικό προς εναπόθεση με κάποιον φυσικό τρόπο. Στην συγκεκριμένα διατριβή χρησιμοποιήθηκε η ιοντοβολή, η οποία μπορεί να εναποθέσει μέταλλα και κεραμικά υλικά καθώς και η θερμική εξάχνωση που κατά κύριο λόγο εναποθέτει μέταλλα. Στην ιοντοβολή το προς εναπόθεση υλικό (στόχος) βρίσκεται σε στερεά μορφή και τοποθετείται μέσα σε έναν θάλαμο κενού. Κατά την εναπόθεση εισάγεται εντός του θαλάμου αέριο (Αργό στην συγκεκριμένη περίπτωση) και εφαρμόζεται πάνω στον στόχο μια τάση είτε συνεχής είτε εναλλασσόμενη. Η διαφορά δυναμικού που εφαρμόζεται ιονίζει το Αργό δημιουργώντας πλάσμα του αερίου ακριβώς πάνω από τον στόχο.

Ανάλογα του είδους της τάσης που έχει εφαρμοστεί στον στόχο μπορούμε να διακρίνουμε δυο περιπτώσεις. Στην πρώτη περίπτωση, εφαρμόζεται συνεχής αρνητική τάση ώστε να επιταχυνθούν τα ιόντα του αερίου πάνω στον στόχο και να συγκρουστούν μαζί του. Κατά την σύγκρουση δημιουργούνται ατμοί από τον στόχο οι οποίοι στην συνέχεια εναποτίθενται στο υπόστρωμα που έχει εισαχθεί εντός του θαλάμου. Αυτή η τεχνική μπορεί να εφαρμοστεί μόνο σε μέταλλα καθώς -σε αντίθετη περίπτωση- η έλξη των ιόντων προς τον στόχο συσσωρεύει φορτίο πάνω του, δημιουργώντας ένα αντίθετο πεδίο που θα εμποδίσει τα ιόντα να προσκρούσουν πάνω του[1]. Για την εναπόθεση μη μεταλλικών στόχων χρησιμοποιείται η εφαρμογή εναλλασσόμενου πεδίου στον στόχο ώστε μετά την έλξη των ιόντων που δημιουργούνται από τους ατμούς και στη συνέχεια συσσωρεύονται πάνω στον στόχο, έλκονται και τα ελευθέρα ηλεκτρόνια τα οποία επανασυνδέονται με τα ιόντα του αργού και θα τα ουδετεροποιήσουν. Μια εφαρμογή της ιοντοβολής με συνεχή τάση είναι η δημιουργία μεταλλικών νανοσωματιδίων. Η διαδικασία είναι η ίδια, απλώς η δημιουργία των ατμών γίνεται εντός ενός μικρού θαλάμου ο οποίος επικοινωνεί με τον κύριο θάλαμο κενού μέσω μιας μικρής οπής. Καθώς η εισαγωγή του Αργού και η δημιουργία πλάσματος γίνεται εντός του μικρού

[1] Ένας μεταλλικός στόχος είναι μόνιμα γειωμένος και δεν αποθηκεύει φορτία.

θαλάμου, η πίεσή του σε σχέση με την πίεση που υπάρχει στον κυρίως θάλαμο κενού είναι αυξημένη. Το αποτέλεσμα είναι οι ατμοί να έλκονται προς την οπή, λόγω βαθμίδας στην πίεση, και να αναγκάζονται να δημιουργούν συσσωματώματα (νανοσωματίδια). Μετά την έξοδό τους από την οπή τα νανοσωματίδια εναποτίθενται στο υπόστρωμα που υπάρχει στον θάλαμο. Με αυτήν την τεχνική μπορούμε να ελέγξουμε το μέγεθος των νανοσωματιδίων μεταβάλλοντας την απόσταση του στόχου από την οπή αλλά και την επιφανειακή κάλυψη των νανοσωματιδίων με τον χρόνο. Με την παραπάνω τεχνική δημιουργήθηκαν τα νανοσωματίδια πλατίνας που είναι το κύριο υλικό με το οποίο δημιουργήθηκαν οι αισθητήρες μας.

Μια άλλη κατηγορία εναπόθεσης μετάλλων είναι η θερμική εξάχνωση και συγκεκριμένα η εξάχνωση με δέσμη ηλεκτρονίων. Σε αυτήν την τεχνική το προς εξάχνωση υλικό τοποθετείται εντός ενός μεταλλικού δοχείου μέσα σε έναν θάλαμο κενού. Πολύ κοντά στο δοχείο υπάρχει ένα νήμα Βολφραμίου το οποίο είναι ηλεκτρικά ανεξάρτητο ως από το δοχείο. Στο δοχείο εφαρμόζεται τάση 2000 V και στο νήμα μια μικρή ισχύς έτσι ώστε να αρχίσει να εκπέμπει θερμιονικά ηλεκτρόνια. Τα ηλεκτρόνια έλκονται από την πολύ υψηλή τάση του δοχείου έχοντας ως αποτέλεσμα την θέρμανσή του και την εξάχνωση του μετάλλου στο εσωτερικό του. Αυτή η τεχνική εναποθέτει μέταλλα πολύ καλής ποιότητας και χρησιμοποιήθηκε για την δημιουργία των ηλεκτροδίων χρυσού στους αισθητήρες μας.

Συνεχίζοντας (Chapter 2: Nanoparticle based strain sensors and nanoparticles' layer conductivity, pp. 17-35) γίνεται μια εκτενής αναφορά στους αισθητήρες, τους διαφορετικούς τύπους των αισθητήρων και τα χαρακτηριστικά τους. Πέραν αυτών, περιγράφεται η ηλεκτρική αγωγιμότητα των μεταλλικών νανοσωματιδίων και η εφαρμογή τους σε αισθητήρες παραμόρφωσης. Αναφορικά με το πρώτο θέμα, κάποια από τα κύρια χαρακτηριστικά των αισθητήρων είναι η ακρίβεια, η ευαισθησία, η επαναληψημότητα, το εύρος, η γραμμικότητα κ.α. Η βέλτιστη λειτουργία ενός αισθητήρα επιτυγχάνεται όταν τα χαρακτηριστικά του λαμβάνουν ιδανικές τιμές, όπως άμεση απόκριση, άπειρο εύρος κ.λπ. Στην πράξη, ωστόσο, δεν μπορεί να κατασκευαστεί ένας ιδανικός αισθητήρας, καθώς υπάρχουν παράμετροι - όπως τα ελαττώματα κατασκευής, το περιβάλλον λειτουργίας, τα διάφορα μέρη του κυκλώματος κ.λπ. - που καθιστούν τον «ιδανικό αισθητήρα» ουτοπικό. Επομένως, αυτό που επιδιώκεται είναι η καλύτερη δυνατή προσέγγιση μέσω της βελτίωσης ορισμένων χαρακτηριστικών που επηρεάζουν το σήμα εξόδου. Μερικά από αυτά είναι η έλλειψη γραμμικότητας, το μικρό εύρος λειτουργίας (επομένως και περιορισμένο εύρος μέτρησης και χαμηλή ευαισθησία) ο θόρυβος (ο οποίος μεταφέρει λανθασμένες πληροφορίες και περιλαμβάνεται στο σήμα εξόδου) και πολλά άλλα.

Οι αισθητήρες εμπίπτουν σε δύο ευρείες κατηγορίες: παθητικούς και ενεργητικούς. Παθητικοί χαρακτηρίζονται οι αισθητήρες που δεν χρειάζονται πρόσθετη πηγή ισχύος για να λειτουργήσουν, καθώς έχουν τη δυνατότητα να μετατρέψουν την ενέργεια εισόδου που προκαλείται από ένα εξωτερικό ερέθισμα σε ένα σήμα εξόδου. Τυπικά παραδείγματα παθητικών αισθητήρων είναι τα θερμοζεύγη, οι φωτοδίοδοι και οι πιεζοηλεκτρικοί αισθητήρες. Σε αντίθεση με τους παθητικούς αισθητήρες, οι ενεργητικοί αισθητήρες απαιτούν παροχή

ρεύματος για τη λειτουργία τους, Η απαιτουμενη αυτή παροχή ενέργειας ονομάζεται σήμα διέγερσης και μετατρέπεται από τον αισθητήρα σε σήμα εξόδου. Τυπικό παράδειγμα ενεργητικού αισθητήρα είναι ένα θερμίστορ, το οποίο αποτελεί μια ευαίσθητη στη θερμότητα αντίσταση, που από μόνη της δεν παράγει σήμα εξόδου, αλλά, αν ένα ηλεκτρικό ρεύμα διέλθει από αυτό, η τιμή της αντίστασης γίνεται μετρήσιμη καθιστώντας έτσι την αλλαγή στο ρεύμα και την τάση υπολογίσιμη. Οι αισθητήρες ταξινομούνται περαιτέρω, συνηθέστερα βάσει της μορφής ενέργειας που μεταδίδεται από το σήμα τους ως: μηχανικοί, θερμικοί, μαγνητικοί, αισθητήρες μέτρησης ακτινοβολίας, οπτικοί, χημικοί και βιολογικοί. Η παρούσα διατριβή αφορά μηχανικούς αισθητήρες παραμόρφωσης.

Η παραμόρφωση και κατά συνέπεια η αλλαγή στις διαστάσεις ενός αντικειμένου μετριέται από αισθητήρες αντίστασης, οι οποίοι κατασκευάζονται πάνω σε υποστρώματα πυριτίου ή σε πολυμερή εύκαμπτα υποστρώματα. Το πυρίτιο προτάθηκε από πολύ νωρίς ως υλικό στην ευρύτερη οικογένεια μηχανικών αισθητήρων για τη μέτρηση διαφόρων ποσοτήτων, όπως η πίεση, η δύναμη και η επιτάχυνση, λόγω των καλών μηχανικών ιδιοτήτων του. Μια κοινή αρχή λειτουργίας όλων των μηχανικών αισθητήρων είναι η αλλαγή της ηλεκτρικής αντίστασης του υλικού κατά την εφαρμογή μηχανικής παραμόρφωσης. Στους συμβατικούς αισθητήρες παραμόρφωσης , οι οποίοι αποτελούνται από ένα συνεχές μεταλλικό υμένιο, η συνολική αντίσταση του υμενίου είναι ανάλογη του μήκους του. Συνεπώς όταν εφαρμόζεται παραμόρφωση το μήκος αυξάνεται και η αντίστασή του αυξάνεται ως επακόλουθο. Από την μεταβολή της αντίστασης μπορούμε να ορίσουμε την ευαισθησία του αισθητήρα, η οποία ορίζεται ως ο λόγος της σχετικής μεταβολής της αντίστασης ως προς την εφαρμοζόμενη παραμόρφωση.

Οι αισθητήρες που έχουν σαν ευαίσθητο υλικό ένα υμένιο μεταλλικών νανοσωματιδίων έχουν ως αρχή λειτουργίας τους το κβαντικό φαινόμενο σήραγγας. Τα μεταλλικά νανοσωματίδια είναι εναποτεθειμένα, ανάμεσα σε δυο ηλεκτρόδια, ώστε να μην δημιουργούν έναν συνεχή δρόμο, από το ένα ηλεκτρόδιο στο άλλο και ταυτόχρονα να μην απέχουν μεταξύ τους απόσταση μεγαλύτερη των λίγων νανομέτρων. Όταν αυτές οι συνθήκες ικανοποιούνται, εφαρμόζοντας μια ηλεκτρική τάση στα ηλεκτρόδια τα ηλεκτρόνια ταξιδεύουν προς την θετική τάση μέσω των νανοσωματιδίων και καθώς δεν υπάρχει συνεχής δρόμος μεταβαίνουν από το ένα νανοσωματίδιο στο άλλο μέσω του φαινομένου σήραγγας. Κατά το φαινόμενο σήραγγας υπάρχει μια μη μηδενική πιθανότητα για ένα ηλεκτρόνιο να διεισδύσει ένα φράγμα δυναμικού μεγαλύτερο από την ενέργεια του. Υπολογίζοντας την πυκνότητα ρεύματος του φαινομένου καθίσταται υπολογίσιμη η αντίσταση του υμενίου. Η αντίσταση εξαρτάται εκθετικά από την μέση απόσταση των νανοσωματιδίων, γεγονός που υποδηλώνει την αυξημένη απόκρισή τους σε σχέση με τους συμβατικούς αισθητήρες παραμόρφωσης. Η ευαισθησία έχει εκθετική εξάρτηση προς την παραμόρφωση. Για μικρές όμως τιμές παραμόρφωσης και αναπτύσσοντας κατά Taylor η εξάρτηση αυτή γίνεται γραμμική.

Στην συνέχεια (Chapter 3: Platinum nanoparticles based strain sensors, pp. 36-65) εστιάζουμε στις ιδιότητες ανίχνευσης των αισθητήρων νανοσωματιδίων πλατίνας οι οποίες

κατασκευάζονται σε εύκαμπτα υποστρώματα πολυϊμιδίου. Αρχικά, διερευνάται η απόκριση στην παραμόρφωση του αισθητήρα για τιμές παραμόρφωσης έως και 1,2 % . Για τον σκοπό αυτόν, παρουσιάζεται ένα φυσικό μοντέλο ώστε να εξηγηθεί η παρατηρούμενη αύξηση της ευαισθησίας με την αυξανόμενη παραμόρφωση. Το μοντέλο συγκρίνεται με τα δεδομένα της έρευνάς μας, καθώς και με βιβλιογραφικά αποτελέσματα. Έως σήμερα, η πλειονότητα των προσπαθειών μοντελοποίησης της συμπεριφοράς των αισθητήρων παραμόρφωσης -είτε από γυμνά είτε από κολλοειδή νανοσωματίδια- βασίζονται στο μοντέλο που προτάθηκε από τους Herrmann et al[2]. Ωστόσο, αυτή η προσέγγιση δεν λαμβάνει υπόψη βασικές πτυχές της παραμόρφωσης ευκάμπτων συσκευών που χρησιμοποιούν γυμνά νανοσωματίδια χωρίς διαλύτες. Σε αντίθεση με την ομοιόμορφη επιμήκυνση των διακένων μεταξύ των νανοσωματιδίων, τα οποία υπήρχαν πριν από οποιαδήποτε παραμόρφωση (στην περίπτωση των διασυνδεδεμένων νανοσωματιδίων), η παραμόρφωση διατάξεων που βασίζονται σε νανοσωματίδια χωρίς διαλύτες έχει ως αποτέλεσμα τον σχηματισμό και την αύξηση πολλών νέων διάκενων που συμβάλλουν στην αύξηση της αντίστασης της διάταξης. Το μοντέλο που προτείνεται σε αυτήν τη μελέτη είναι σε θέση να εξηγήσει πειραματικές διαφορές, αναφορικά με την ευαισθησία που διαθέτουν οι αισθητήρες νανοσωματιδίων χωρίς διαλύτες και οι αισθητήρες με διασυνδεδεμένα νανοσωματίδια. Στην συνέχεια, ακολουθεί μελέτη απόκρισης του αισθητήρα σε περιβάλλον με υγρασία. Η υγρασία είναι ένας γνωστός παράγοντας επιρροής της μακροπρόθεσμη συμπεριφοράς των αισθητήρων που βασίζονται σε νανοσωματίδια. Έτσι, κρίθηκε σκόπιμη η διερεύνηση της σχέσης και της αλληλεπίδρασης μεταξύ των δύο, με απώτερο σκοπό να πειραματιστούμε πάνω στον αποτελεσματικό τρόπο προστασίας των εύκαμπτων αισθητήρων παραμόρφωσης από την υγρασία, καθιστώντας έτσι τους αισθητήρες μας αποτελεσματικότερους ως προς τους εξωτερικούς παράγοντες.

Όλα τα πειράματα κατασκευής διεξήχθησαν σε θερμοκρασία δωματίου. Τα χημικά αντιδραστήρια που χρησιμοποιήθηκαν στην παρούσα μελέτη αγοράστηκαν από τη Sigma Aldrich. Ως υποστρώματα εναπόθεσης χρησιμοποιήθηκαν φύλλα πολυϊμιδίου με μέσο πάχος 120 μm και τραχύτητα επιφάνειας 0,7 - 0,8 nm, . Πριν από οποιαδήποτε επεξεργασία, τα υποστρώματα πολυϊμιδίου καθαρίστηκαν χρησιμοποιώντας απιονισμένο νερό και υπέρηχους. Ο σχηματισμός των χρυσών αλληλοδιαπλεκόμενων ηλεκτρόδιων πάνω στα υποστρώματα πολυϊμιδίου έγινε με την τεχνική της οπτικής λιθογραφίας και της τεχνικής θερμικής εξάχνωσής δέσμης ηλεκτρονίων: αρχικά, ένα λεπτό στρώμα τιτανίου (περίπου 4 nm) εναποτίθεται με ρυθμό απόθεσης 0,2 Å/s. Το στρώμα τιτανίου δρα ως στρώμα πρόσφυσης μεταξύ του χρυσού και του υποστρώματος πολυϊμιδίου. Ως δεύτερο βήμα εναποτίθεται στρώμα χρυσού 30 nm με ρυθμό εναπόθεσης 0,5 Å/s. Ως τελικό βήμα, χρησιμοποιήθηκε η τεχνική ανύψωσης (lift-off) για την παραγωγή της τελικής δομής των αλληλοδιαπλεκόμεμων ηλεκτροδίων. Το συνολικό ύψος των ηλεκτροδίων είναι κρίσιμο στην παραγωγή των αισθητήρων, δεδομένου ότι είναι ικανό να «σκιάσει» το υπόστρωμα πολυϊμιδίου κατά τη διάρκεια του σταδίου εναπόθεσης των νανοσωματιδίων, εμποδίζοντας έτσι την καλή επαφή μεταξύ νανοσωματιδίων και ηλεκτροδίων.

[2] Herrmann J, Müller KH, Reda T, Baxter GR, Raguse BD, De Groot GJ, Chai R, Roberts M, Wieczorek L, Nanoparticle films as sensitive strain gauges, Applied Physics Letters, 2007 Oct 29;91(18):183105.

Η απόσταση μεταξύ των δακτύλων των ηλεκτροδίων (ή το διάκενο των ηλεκτροδίων) ήταν –στην περίπτωσή μας- 10 μm. Τα νανοσωματίδια, με μέση διάμετρο 4 nm και τυπική απόκλιση 1,5 nm, εναποτέθηκαν πάνω από όλη την διάταξη χρησιμοποιώντας ένα τροποποιημένο σύστημα ιοντοβολής συνεχούς τάσης. Οι εναποθέσεις των ηλεκτροδίων και των νανοσωματιδίων πλατίνας πραγματοποιήθηκαν σε πίεση 10^{-5} mbar.

Για τη διερεύνηση της προστασίας των αισθητήρων από την υγρασία, εναποτέθηκε ένα προστατευτικό επίστρωμα αλουμίνας πάνω από τις διατάξεις χρησιμοποιώντας ένα σύστημα εναπόθεσης ατομικής στρώσης (Picosun ALD R-200). Ως πρόδρομες ενώσεις της αλουμίνας χρησιμοποιήθηκαν TMA και απιονισμένο νερό. Κατά τη διάρκεια της εναπόθεσης, ο αντιδραστήρας ALD ήταν υπό πίεση 10 mbar και υπήρχε σταθερή ροή αζώτου, καθαρότητας 99,999%, 300 sccm. Ο χρόνος έκθεσης του νερού και του TMA ήταν 0,1 s, ενώ ο χρόνος καθαρισμού ήταν 10 s όσον αφορά το TMA και 15 s το νερό για κάθε κύκλο. Η θερμοκρασία εναπόθεσης ήταν στους 150°C, για 50 και 100 κύκλους, με αποτέλεσμα το πάχος της αλουμίνας να είναι 5,5 nm και 11 nm αντίστοιχα. Αυτή η θερμοκρασία εναπόθεσης είναι συμβατή με την θερμοκρασία επεξεργασίας του υποστρώματος πολυϊμιδίου, ενώ, παράλληλα, οδηγεί σε χαμηλή συγκέντρωση μορίων OH στο υμένιο, τα οποία βοηθούν στην απορρόφηση μορίων νερού από το περιβάλλον, Πραγματοποιήθηκαν αρκετές δοκιμές κόπωσης πριν και μετά την εναπόθεση της αλουμίνας και μελετήθηκαν οι προστατευτικές ικανότητες της επικάλυψης αλουμίνας από την σχετική υγρασία. Οι αισθητήρες πίεσης έχουν χαρακτηριστεί από ηλεκτρικές μετρήσεις, μετρήσεις με Ηλεκτρονικό Μικροσκόπιο Διέλευσης (TEM), καθώς και από μετρήσεις οπτικής μικροσκοπίας.

Η ευαισθησία των αισθητήρων προσδιορίστηκε από μετρήσεις αντίστασης χρησιμοποιώντας έναν μετρητή Keithley 2400 κατά την εφαρμογή των βημάτων παραμόρφωσής από μια πειραματική διάταξη. Η παραμόρφωση εφαρμόστηκε με ακρίβεια 0,007%, χρησιμοποιώντας ένα μικρομετρικό έμβολο που ελέγχεται από έναν βηματικό κινητήρα. Ο βηματικός κινητήρας τροφοδοτείται και ελέγχεται από έναν μικροελεγκτή (Arduino Uno), ο οποίος επιτρέπει την εκτέλεση αξιόπιστων δοκιμών παραμόρφωσής. Οι αισθητήρες κολλήθηκαν σε μια PCB πλακέτα για να διασφαλιστεί η ομοιόμορφη παραμόρφωση του υποστρώματος κατά τη διάρκεια της εφαρμογής παραμόρφωσης. Το σύστημα περιβλήθηκε σε θάλαμο στον οποίο ήταν δυνατός ο έλεγχος της σχετικής υγρασίας και της θερμοκρασίας. Η σχετική υγρασία ελέγχεται είτε μέσω της εφαρμογής αζώτου, καθαρότητας 99,999%, είτε μέσω ατμών απιονισμένου νερού που μεταφέρονται στον θάλαμο του αισθητήρα παραμόρφωσής, μέσω μιας δεξαμενής που χρησιμοποιεί μια μηχανική αντλία. Με αυτήν τη διάταξη, επιτεύχθηκαν τιμές σχετικής υγρασίας μεταξύ 10% και 70%. Τόσο η θερμοκρασία όσο και η σχετική υγρασία παρακολουθήθηκαν από τους αντίστοιχους εμπορικούς αισθητήρες. Κατά τη διάρκεια των μετρήσεων, η θερμοκρασία διατηρήθηκε σταθερή στους 23°C, ενώ η αντίσταση παρακολουθήθηκε εφαρμόζοντας σταθερή τάση 1 Volt.

Η αντίσταση του φιλμ των νανοσωματιδίων πλατίνας που σχηματίζονται σε κενό με ιοντοβολή εξαρτάται σε μεγάλο βαθμό από την επιφανειακή κάλυψη των νανοσωματιδίων. Οι

διατάξεις με την καλύτερη απόδοση επιτεύχθηκαν όταν η επιφανειακή κάλυψη είναι ακριβώς κάτω από το όριο διήθησης (συσκευές με κάλυψη επιφάνειας 50%). Το υπάρχον γραμμικό μοντέλο περιγραφής της ευαισθησίας[3] δεν είναι ικανό να περιγράψει την σχετική μεταβολή της αντίστασης των νανοσωματιδίων. Η σχετική αλλαγή αντίστασης εμφανίζει ορισμένα εύρη παραμορφώσεων τα οποία μπορούν να περιγράφουν με μια μοναδική γραμμική εξίσωση και ορισμένα άλλα τα οποία παραμένουν γραμμικά αλλά με πολλαπλές κλίσεις και, ως εκ τούτου, διαφορετική ευαισθησία. Αυτό έχει ως επακόλουθο την ανάγκη περιγραφής τους με επιπλέον γραμμικές εξισώσεις, ανάλογα με την κλίση. Το ήδη υπάρχον μοντέλο που βασίζεται στο φαινόμενο σήραγγας των ηλεκτρονίων μεταξύ νανοσωματιδίων [παράγραφος 3.4] είναι απολύτως επαρκές για να περιγράψει την ευαισθησία των διασυνδεδεμένων νανοσωματιδίων, αλλά δεν προβλέπει αλλαγή της τιμής της ευαισθησίας. Στην περίπτωσή μας, τα νανοσωματίδια πλατίνας δεν είναι διασυνδεδεμένα αλλά εναποτίθενται στο υπόστρωμα με τυχαία κατανομή, έχοντας ως αποτέλεσμα να υπάρχουν περιοχές όπου όλα τα νανοσωματίδια να βρίσκονται σε επαφή (δημιουργώντας έτσι νησιά νανοσωματιδίων) και άλλες περιοχές όπου υπάρχει απόσταση μεταξύ νησιών-νανοσωματιδίων ή μεμονωμένων νανοσωματιδίων. Επομένως, κατά την εφαρμογή παραμόρφωσης, τα προϋπάρχοντα κενά μεταξύ των νανοσωματιδίων αυξάνονται, ενώ τα μεγαλύτερα νησιά νανοσωματιδίων θραύονται σε μικρότερες συστάδες νανοσωματιδίων δημιουργώντας νέα κενά. Αυτό υπογραμμίζει σαφώς την ανάγκη επανεξέτασης του προϋπάρχοντος μοντέλου και την δημιουργία ενός νέου, κατάλληλου μοντέλου, όπως αναλύεται εκτενώς στην παρούσα διατριβή.

Στα πλαίσια της πειραματικής διαδικασίας πραγματοποιήθηκε τεχνική μελέτη των αισθητήρων παραμόρφωσης με στόχο την ευρύτερη διερεύνηση της επικάλυψής τους σκοπεύοντας τελικά στην προστασία τους έναντι στην σχετική υγρασία. Έτσι, μελετήθηκε η περιβαλλοντική σταθερότητα των αισθητήρων νανοσωματιδίων με την έκθεσή τους σε αντίξοες συνθήκες, καθώς και η αποτελεσματικότητα του προτεινόμενου μοντέλου για προσαρμογή των πειραματικών δεδομένων. Το φιλμ αλουμίνας αξιολογήθηκε ως προς τις προστατευτικές του ιδιότητες έναντι της επίδρασης της κόπωσης, υπό ποικίλες συνθήκες σχετικής υγρασίας τόσο για αισθητήρες χωρίς εφαρμογή παραμόρφωσής όσο και για αισθητήρες που βρίσκονται υπό κάμψη. Η διακύμανση της αντίστασης των αισθητήρων χωρίς αλουμίνα αλλά και με επικάλυψη αλουμίνας, συγκρίθηκε με τη διακύμανση της αντίστασης μετά από πειράματα κόπωσης, σε ποικίλες συνθήκες σχετικής υγρασίας. Τα αποτελέσματα συνδέουν το πάχος της αλουμίνας με την αντοχή της συσκευής για διάφορες συγκεντρώσεις υγρασίας και την σταθερότητά τους για μεγάλα χρονικά διαστήματα. Επίσης, αποδεικνύουν ότι αλουμίνα πάχους 11 nm κατασκευασμένη στους 150 °C μπορεί να προστατεύσει αποτελεσματικά τους αισθητήρες παραμόρφωσης με βάση τα νανοσωματίδια πλατίνας από την υγρασία, ακόμη και μετά από

[3] Herrmann J, Müller KH, Reda T, Baxter GR, Raguse BD, De Groot GJ, Chai R, Roberts M, Wieczorek L, Nanoparticle films as sensitive strain gauges, Applied Physics Letters, 2007 Oct 29;91(18):183105.

επαναλαμβανόμενη κάμψη της διάταξης. Τα συμπεράσματα της εργασίας που παρουσιάσθηκε στο κεφ. 3 δημοσιεύθηκαν στο επιστημονικό περιοδικό Sensors[4].

Συνεχίζοντας (Chapter 4: Monte Carlo simulations, pp. 66-86) παρουσιάζεται ένα εργαλείο προσομοίωσης Monte Carlo, που υλοποιήθηκε στο Matlab, το οποίο αναπτύχθηκε με σκοπό τον υπολογισμό της ευαισθησίας των αισθητήρων παραμόρφωσης βασισμένων σε νανοσωματίδια. Το πλεονέκτημα που παρέχει η προσομοίωση είναι ότι -συγκρινόμενη με πειραματικά δεδομένα- καθιστά δυνατή την εκτέλεση μεγάλου αριθμού προσομοιώσεων, δίνοντας έτσι μια θετική ανατροφοδότηση για σχεδιασμό νέων πειραμάτων. Η μέθοδος Monte Carlo είναι μια απλή, ντετερμινιστική μέθοδος, η οποία έχει χρησιμοποιηθεί για την προσομοίωση ποικίλων φαινομένων και έχει υιοθετηθεί εδώ για να περιγράψει την τυχαία φύση της διαδικασίας εναπόθεσης των νανοσωματιδίων πλατίνας.

Οι είσοδοι της προσομοίωσης περιλαμβάνουν την διάμετρο των νανοσωματιδίων και την επιφανειακή κάλυψή τους καθώς και την τιμή της παραμόρφωσης που θα υποστεί το υπόστρωμα, ενώ η έξοδος του εργαλείου επιστρέφει την τιμή αντίστασης και την ευαισθησία του φιλμ. Μπορούμε να αναφέρουμε εν συντομία ότι η ακολουθούμενη μεθοδολογία για την επίτευξη του υπολογισμού επιτυγχάνεται μέσω του υπολογισμού όλων των αγώγιμων δρόμων και της τιμής αντίστασής τους.

Η προσομοίωση βασίζεται στον ορισμό ενός δισδιάστατου πίνακα (n x n) που αντιπροσωπεύει την περιοχή προσομοίωσης. Ο πίνακας αποτελείται από n x n κελιά προσομοίωσης, με κάθε κελί να έχει επιφάνεια 1 x 1 nm. Υποτίθεται ότι η περιοχή προσομοίωσης είναι μόνο ένα κλάσμα της ευαίσθητης περιοχής των αισθητήρων και έτσι αντιπροσωπεύει μόνο ένα μέρος της συνολικής αντίστασης, υποθέτοντας ότι τα νανοσωματίδια έχουν εναποτεθεί τυχαία αλλά ομοιόμορφα. Έτσι, προσομοιώνεται ένα μικρό μέρος της ευαίσθητης περιοχής και όχι ολόκληρη η περιοχή του αισθητήρα, μειώνοντας τον απαιτούμενο χρόνο προσομοίωσης καθώς και την επεξεργαστική ισχύ. Η συνολική αντίσταση της συσκευής μπορεί στη συνέχεια να υπολογιστεί επεκτείνοντας την n x n περιοχή του αισθητήρα, σε ολόκληρη την επιφάνεια του. Αυτό έχει ως αποτέλεσμα ένα δίκτυο αντιστάσεων συνδεδεμένων τόσο κατά σειρά όσο και παράλληλα, η συνολική αντίσταση των οποίων μπορεί εύκολα να υπολογιστεί. Το πρώτο βήμα της προσομοίωσης είναι η τυχαία τοποθέτηση νανοσωματιδίων πλατίνας με μέση διάμετρο 4 nm και τυπική απόκλιση 0,8 nm, πάνω στην την περιοχή προσομοίωσης. Η τοποθέτηση των νανοσωματιδίων επιτυγχάνεται με τη μέθοδο Monte Carlo, βάσει της οποίας σε κάθε κελί προσομοίωσης υπάρχει μια προκαθορισμένη πιθανότητα. Αν η πιθανότητα είναι μεγαλύτερη από έναν τυχαίο αριθμό που δημιουργείται από τον κώδικα, τότε αυτό το κελί θα είναι το κέντρο ενός νανοσωματιδίου. Το επόμενο βήμα είναι να ξεκινήσει μια διαδικασία αναζήτησης των αγώγιμων διαδρομών μεταξύ των άκρων της προκαθορισμένης περιοχής. Οι αγώγιμες διαδρομές ορίζονται είτε από συνεχή μονοπάτια νανοσωματιδίων είτε από διαδρομές που επιτρέπουν ένα μόνο κενό κελί. Μετά τον υπολογισμό των αγώγιμων

[4] Aslanidis E, Skotadis E, Moutoulas E, Tsoukalas D, Thin Film Protected Flexible Nanoparticle Strain Sensors: Experiments and Modeling, Sensors, 2020 Jan;20(9):2584.

διαδρομών, ο κώδικας υπολογίζει την αντίσταση. Η διαδρομή μετασχηματίζεται σε ένα ισοδύναμο κύκλωμα θεωρώντας ότι τα νανοσωματίδια αντιστοιχούν σε κόμβους και οι αποστάσεις μεταξύ των νανοσωματιδίων σε αντιστάσεις. Ακολουθεί ο υπολογισμός της αντίστασης ολόκληρου του κυκλώματος. Λόγω της πολυπλοκότητας των κυκλωμάτων, η αντίσταση υπολογίζεται με τη χρήση του πίνακα Laplace. Για τον υπολογισμό της αντίστασης σε σύνθετα κυκλώματα, η συνηθέστερη μέθοδος είναι να υπολογιστεί το ρεύμα που ρέει στο κύκλωμα μέσω των εξισώσεων Kirchhoff. Σε αυτήν την περίπτωση πρέπει να επιλυθεί ένας μεγάλος αριθμός εξισώσεων και έτσι ο υπολογιστικός χρόνος γίνεται εξαιρετικά μεγάλος. Με την χρήση του πίνακα Laplace, ο υπολογισμός της αντίστασης οποιουδήποτε κυκλώματος (όσο ικανοποιείται η συνθήκη ότι το κύκλωμα αποτελείται μόνο από αντιστάσεις) γίνεται πολύ απλός. Αρκεί να υπολογιστεί ο ψευδοαντίστροφος κατά Moore- Penrose πίνακας Laplace και να γίνει μια απλή πράξη ανάμεσα στα στοιχεία του. Τέλος, αφού έχει υπολογιστεί η συνολική αντίσταση, εφαρμόζεται παραμόρφωση η οποία μεταβάλλει τις εκάστοτε τιμές των αντιστάσεων του κυκλώματος και ως εκ τούτου και την συνολική αντίσταση. Γνωρίζοντας τις αντιστάσεις του φιλμ για κάθε εφαρμοζόμενη παραμόρφωση καθίσταται τελικά δυνατός και ο υπολογισμός της ευαισθησίας του φιλμ.

Οι αισθητήρες που βασίζονται σε μεταλλικά νανοσωματίδια παρουσιάζουν τη βέλτιστη απόδοση για ένα συγκεκριμένο εύρος τιμών επιφανειακής κάλυψης το οποίο αποτελεί το παράθυρο εργασίας . Σε αυτό το παράθυρο εργασίας τα νανοσωματίδια θα πρέπει να είναι αρκετά πυκνά για να δημιουργήσουν μια αγώγιμη διαδρομή από το ένα ηλεκτρόδιο στο άλλο, αλλά ταυτόχρονα όχι υπερβολικά πυκνά ώστε να δημιουργηθεί βραχυκύκλωμα μεταξύ των ηλεκτροδίων. Ο υπολογισμός αυτού του παραθύρου εργασίας πραγματοποιήθηκε υπολογίζοντας την πιθανότητα σχηματισμού της αγώγιμης διαδρομής η οποία δεν δημιουργεί βραχυκύκλωμα μεταξύ των ηλεκτροδίων, μετά από την εκτέλεση 100 προσομοιώσεων για νανοσωματίδια με μέγεθος 2, 4, 6, 8 και 10 nm και με διαφορετική επιφανειακή κάλυψη. Για τον ακριβή υπολογισμό του παραθύρου εργασίας, πρέπει να επιλεχθεί ένα αποδεκτό ποσοστό αισθητήρων με αγώγιμη διαδρομή και χωρίς βραχυκύκλωμα. Σε αυτήν την μελέτη, το ποσοστό επιλέγεται να είναι πάνω από 50 % για κάθε επιφανειακή κάλυψη και μέγεθος νανοσωματιδίων. Στη συνέχεια, μπορούμε να υπολογίσουμε το παράθυρο της επιφανειακής κάλυψης του οποίου η προκύπτουσα τιμή κατανομής Gauss θα πρέπει να είναι μεγαλύτερη ή ίση του 0,5 (50 %).

Μία από τις κύριες χρήσεις μιας προσομοίωσης είναι να διερευνήσει τον αντίκτυπο ενός μεγάλου αριθμού παραμέτρων της απόδοσης της συσκευής, μια διαδικασία που μπορεί να είναι αργή ή και αδύνατη σε περίπτωση πειραματικής εκτέλεσης. Η προσομοίωση που παρουσιάζεται εδώ έχει την ικανότητα να προβλέπει τις ευαισθησίες αισθητήρων με βάση τα νανοσωματίδια με ποικίλο μέγεθος και κάλυψη επιφάνειας. Μετά τον υπολογισμό του παραθύρου εργασίας για διαφορετικά μεγέθη, υπολογίστηκαν επίσης οι αντίστοιχες ευαισθησίες για κάθε αισθητήρα. Οι ευαισθησίες κυμάνθηκαν από 26 έως 36 για παραμορφώσεις έως 0,41%, γεγονός που υποδηλώνει ότι τέτοιου είδους αισθητήρες έχουν ένα φυσικό άνω όριο της τάξης των μερικών δεκάδων το οποίο δεν είναι δυνατό να ξεπεραστεί. Η μέγιστη εκατοστιαία μεταβολή της αντίστασης μπορεί να επιτευχθεί εάν τοποθετηθεί ένα μόνο νανοσωματίδιο μεταξύ δύο

ηλεκτροδίων με για μια μικρή απόσταση (0,5 nm), ώστε να γίνεται δυνατό το φαινόμενα σήραγγας. Τα αποτελέσματα προσομοίωσης συγκρίνουν την ευαισθησία του αισθητήρα ενός νανοσωματιδίου και των αισθητήρων με φιλμ νανοσωματιδίων για ποικίλο μέγεθος νανοσωματιδίων. Και οι δύο ευαισθησίες ξεκινούν με μεγάλες τιμές, λόγω του πολύ μικρού μεγέθους των νανοσωματιδίων, οι οποίες, στη συνέχεια, μειώνονται σταδιακά. Η ευαισθησία του αισθητήρα ενός νανοσωματιδίου πλησιάζει την τιμή των 30 ενώ των αισθητήρων με φιλμ νανοσωματιδίων πρώτα μειώνεται σαν συνάρτηση του μεγέθους νανοσωματιδίων και μετά αυξάνεται ελαφρώς πλησιάζοντας την ίδια τιμή με τον αισθητήρα ενός νανοσωματιδίου. Η αρχική μείωση της ευαισθησίας του αισθητήρα φιλμ νανοσωματιδίων οφείλεται στην προσθήκη παράλληλων (ως προς τα ηλεκτρόδια) αποστάσεων μεταξύ των σωματιδίων, οι οποίες μειώνουν την τιμή μεταβολής της σχετικής αντίστασης. Αφού το μέγεθος των νανοσωματιδίων γίνει μεγαλύτερο από 6 nm, η αύξηση της ευαισθησίας πλησιάζει την ίδια τιμή με τον αισθητήρα ενός νανοσωματιδίου. Καθώς το μέγεθος των νανοσωματιδίων αυξάνεται, τα περισσότερα κενά μεταξύ των σωματιδίων εξαφανίζονται και οι δύο ευαισθησίες πλησιάζουν την ίδια τιμή.

Η προσομοίωση Monte Carlo μπορεί να χρησιμοποιηθεί για την πρόβλεψη της βέλτιστης επιφανειακή κάλυψης, ώστε να επιτυγχάνεται η υψηλότερη ευαισθησία όταν είναι γνωστό το μέγεθος των νανοσωματιδίων. Εκτός αυτού είναι ένα ικανό μέσο πρόβλεψης της ευαισθησίας του αισθητήρα για διάφορα μεγέθη νανοσωματιδίων, και καθορισμού της βέλτιστης επιφανειακής κάλυψης για καθένα από αυτά. Όλα τα παραπάνω είναι χρήσιμα για τη βελτιστοποίηση της κατασκευής αισθητήρων παραμόρφωσης, δεδομένης της ποικιλίας των περιοχών εφαρμογής και της συνεχούς αυξανόμενης ανάγκης εξοικονόμησης ενέργειας, μείωσης κόστους και αυξημένων αναγκών στην καθημερινή ζωή. Τα συμπεράσματα της εργασίας που παρουσιάσθηκε στο κεφ. 4 δημοσιεύθηκαν στο επιστημονικό περιοδικό Nanotechnology[5] .

Εν συνεχεία, (Chapter 5: Crack-based strain sensors, pp. 87-109) περιγράφεται η ανάπτυξη ενός εύκαμπτου αισθητήρα παραμόρφωσης με βάση τη χρήση των νανοσωματιδίων αλλά και των ρωγμών. Για επίτευξη του σκοπού αυτού, εναποτέθηκαν λεπτά φιλμ αλουμίνας, διαφόρων παχών (μεταξύ 6 και 20 nm), σε ένα εύκαμπτο υπόστρωμα πολυϊμιδίου και εφαρμόζοντας παραμόρφωση δημιουργήθηκαν σκόπιμα ρωγμές στην αλουμίνα. Τα νανοσωματίδια πλατίνας εναποτέθηκαν στο πάνω μέρος των σπασμένων φιλμ αλουμίνας ώστε να δράσουν ως ευαίσθητο / αγώγιμο υλικό. Εναποτέθηκαν δύο διαφορετικά φιλμ νανοσωματιδίων πλατίνας με διαφορετικές επιφανειακές επικαλύψεις: ένα αραιό και ένα πυκνό. Το αραιό αντιστοιχεί σε επιφανειακή κάλυψη περίπου 49 % που είναι ακριβώς κάτω από το όριο διήθησης του συστήματος. Το πυκνό αντιστοιχεί σε επιφανειακή κάλυψη 73 % που υπερβαίνει το κατώφλι διήθησης. Η αντίσταση των αραιών φιλμ νανοσωματιδίων καθορίζεται από την απόσταση μεταξύ των νανοσωματιδίων και μετρήθηκε περίπου στα 600 kΩ. Μετά την εφαρμογή της παραμόρφωσης οι ρωγμές αρχίζουν να διευρύνονται και επομένως η απόσταση μεταξύ των

[5] Aslanidis E, Skotadis E, Tsoukalas D, Simulation tool for predicting and optimizing the performance of nanoparticle based strain sensors, Nanotechnology, 2021 Mar 24.

νανοσωματιδίων αυξάνεται περαιτέρω, έχοντας ως αποτέλεσμα την αύξηση της αντίστασης του αισθητήρα. Όσον αφορά τα πυκνά φιλμ νανοσωματιδίων, τα νανοσωματίδια βρίσκονται σε πραγματική επαφή και η ευαισθησία τους καθορίζεται κυρίως από το άνοιγμα ρωγμών και την παραμόρφωση που εφαρμόζεται στον αισθητήρα. Η αρχική τους αντίσταση ήταν περίπου 20 Ω και με την εφαρμογή παραμόρφωσης 7,2 % η τελική αντίστασή τους έφτασε σε τιμές έως και 700 ΜΩ. Αυτό έδωσε μία κολοσσιαία ευαισθησία τιμής 2,6 x 10^8, η οποία είναι η υψηλότερη που έχει καταγραφεί έως την στιγμή της συγγραφής. Αυτή η ευαισθησία οφείλεται στη μικρή αρχική αντίσταση του αισθητήρα και στο γεγονός ότι οι ρωγμές έχουν διαταράξει τη συνέχεια του φιλμ των νανοσωματιδίων, έχοντας ως αποτέλεσμα μια τεράστια αύξηση της αντίστασης του αισθητήρα. Στην περίπτωση των αραιών φιλμ, η μέγιστη ευαισθησία που επιτευχθεί ήταν 2795 για τιμή παραμόρφωσης 7,2 %, ενώ τιμές μεγαλύτερες από 100 επιτεύχθηκαν για μικρές τιμές παραμόρφωσης έως 0,1 %. Και στις δυο περιπτώσεις, αραιών και πυκνών φιλμ νανοσωματιδίων, η ευαισθησία μπορεί να ελεγχθεί από το πάχος του φιλμ της αλουμίνας. Τα παχύτερα φιλμ αλουμίνας (20 nm) έχουν ως αποτέλεσμα ευρύτερα ανοίγματα ρωγμών, τα οποία αυξάνουν σταδιακά τις τιμές αντίστασης του αισθητήρα και κατά συνέπεια την ευαισθησία του.

Όλοι οι αισθητήρες κατασκευάστηκαν πάνω σε εύκαμπτα υποστρώματα πολυϊμιδίου, πάχους 125 μm. Λεπτά φιλμ αλουμίνας με διαφορετικά πάχη (6 nm, 10 nm και 20 nm), εναποτέθηκαν χρησιμοποιώντας το σύστημα ALD RS-200 της Picosun. Κατά τη διάρκεια της εναπόθεσης, ο αντιδραστήρας ALD ήταν υπό πίεση 10 mbar και υπό σταθερή ροή 300 sccm αζώτου καθαρότητας 99,999 %. Κάθε κύκλος είχε χρόνο έκθεσης 0,1 δευτερόλεπτα (τόσο για το TMA όσο και για το απιονισμένο νερό), ενώ ο χρόνος καθαρισμού ήταν 10 s για TMA και 15 s για το απιονισμένο νερό. Η θερμοκρασία εναπόθεσης ήταν 80°C, για 60, 100 και 200 κύκλους. Ο αριθμός των κύκλων καθώς και η θερμοκρασία, καθόρισαν το συνολικό πάχος του εναποτιθέμενου φιλμ, με αποτέλεσμα πάχη των 6 nm, 10 nm και 20 nm για 60, 100 και 200 κύκλους αντίστοιχα. Στην συνέχεια, νανοσωματίδια πλατίνας με μέση διάμετρο 4 nm εναποτέθηκαν πάνω από τα φιλμ της αλουμίνας. Δέκα αισθητήρες κατασκευάστηκαν για κάθε πάχος αλουμίνας και κάθε επιφανειακή κάλυψη των νανοσωματιδίων πλατίνας. Ως επόμενο βήμα, δύο χρυσά ηλεκτρόδια εναποτέθηκαν στο πάνω μέρος του φιλμ των νανοσωματιδίων, χρησιμοποιώντας τον εξαχνωτή δέσμης ηλεκτρονίων και μια μάσκα σκίασης. Πριν από την εναπόθεση το χρυσού, 4 nm τιτανίου εναποτέθηκαν ως στρώμα προσκόλλησης. Τα ηλεκτρόδια είχαν πάχος 40 nm, πλάτος 4 mm και διάκενο μεταξύ ηλεκτροδίων 150 μm. Πριν από οποιαδήποτε πειράματα ανίχνευσης παραμόρφωσης, οι αισθητήρες υποβλήθηκαν σε 200 κύκλους καταπόνησης (για τιμές παραμόρφωσης μεταξύ 0 και 10 %) προκειμένου να δημιουργηθούν ρωγμές στο φιλμ αλουμίνας. Όταν οι ρωγμές τελικά σχηματιστήκαν, η αρχική αντίσταση αυξήθηκε ελαφρώς αφού ακόμη και για μηδενική παραμόρφωση οι ρωγμές παραμένουν ελαφρώς ανοιχτές. Να παρατηρηθεί ότι κατά την πρώτη εφαρμογή της παραμόρφωσης οι ρωγμές δεν σχηματίζονται στο σύνολο του φιλμ της αλουμίνας. Αυτό μπορεί να γίνει αντιληπτό από την αυξανόμενη ευαισθησία του αισθητήρα κατά τους πρώτους κύκλους καταπόνησης. Όταν η ευαισθησία, η οποία σε αυτήν την περίπτωση είναι περίπου στους 200

κύκλους καταπόνησης έως 7,2 %, σταματήσει να αυξάνεται οι ρωγμές έχουν σχηματιστεί σε όλο το φιλμ της αλουμίνας και οι αισθητήρες είναι έτοιμοι για μέτρηση. Εκτός από τους παραπάνω αισθητήρες, κατασκευάστηκαν επίσης δείγματα αναφοράς - χωρίς στρώμα αλουμίνας για την σύγκριση τους με τους αισθητήρες με φιλμ αλουμίνας. Η ευαισθησία των αισθητήρων υπολογίστηκε παρακολουθώντας την αντίστασή τους υπό εφαρμογή σταδιακής παραμόρφωσης. Η αντίσταση των συσκευών μετρήθηκε με ένα πολύμετρο Keithley 2400, υπό σταθερή τάση 1 Volt.

Κάθε χαρακτηριστικό γράφημα αισθητήρων που βασίζεται σε ρωγμές χωρίζεται σε τρεις περιοχές. Κάθε περιοχή αντιστοιχεί σε διαφορετική ευαισθησία αισθητήρα. Στην περίπτωση του αισθητήρα αναφοράς, οι δύο μετρηθείσες ευαισθησίες αποδίδονται στα νέα κενά μεταξύ των σωματιδίων που έχουν δημιουργηθεί λόγω της παραμόρφωσης. Οι τρεις περιοχές που παρατηρούνται στους αισθητήρες που έχουν ρωγμές είναι αποτέλεσμα του σχηματισμού των ρωγμών. Οι ρωγμές δεν σχηματίζουν ευθεία γραμμή αλλά έχουν μια τραχύτητα. Ωστόσο, οι ρωγμές σχηματίζονται παράλληλα μεταξύ τους και κάθετα προς την εφαρμοζόμενη παραμόρφωση. Όταν δεν εφαρμόζεται παραμόρφωση, υπάρχει ένας μέγιστος αριθμός αγώγιμων διαδρομών. Καθώς η παραμόρφωση εφαρμόζεται σταδιακά, αρχίζουν να εμφανίζονται ρωγμές στο φιλμ της αλουμίνας, με αποτέλεσμα τον τερματισμό ορισμένων από τα αγώγιμα μονοπάτια. Εφ 'όσον το άνοιγμα της ρωγμής είναι μικρότερο από το ύψος της τραχύτητάς της ρωγμής, ένας πεπερασμένος αριθμός αγώγιμων διαδρομών θα παραμείνει ενεργός. Ως εκ τούτου η αντίσταση -άρα και η ευαισθησία- θα είναι αρκετά αυξημένη. Οποιαδήποτε περαιτέρω εφαρμογή παραμόρφωσης θα έχει ως αποτέλεσμα τη διακοπή της πλειονότητας των αγώγιμων διαδρομών, καθώς πλέον το άνοιγμα της ρωγμής να γίνει μεγαλύτερο από την τραχύτητάς της. Ωστόσο, ορισμένες αγώγιμες διαδρομές θα παραμείνουν, μέσω του φαινομένου σήραγγας με αποτέλεσμα την ραγδαία αύξηση της αντίστασης και της ευαισθησίας. Η παραπάνω διαδικασία περιγράφει τις τρεις παρατηρούμενες περιοχές στην ευαισθησία των αισθητήρων.

Η συνολική απόδοση των αισθητήρων με πυκνά νανοσωματίδια για μικρές τιμές παραμόρφωσης είναι κατώτερη από εκείνη των αραιών νανοσωματιδίων. Αυτό οφείλεται στους διαφορετικούς μηχανισμούς αγωγιμότητας για κάθε πυκνότητα. Για αραιά νανοσωματίδια, η αγωγιμότητα διέπεται από τον αριθμό των αγώγιμων διαδρομών καθώς και από το φαινόμενο σήραγγας μεταξύ των σωματιδίων. Έτσι είναι πολύ ευαίσθητοι ακόμη και στις μικρότερες παραμορφώσεις. Στην περίπτωση πυκνών νανοσωματιδίων δεν υπάρχει φαινόμενο σήραγγας και είναι διαθέσιμος ένας εξαιρετικά μεγάλος αριθμός «συνεχών» αγώγιμων διαδρομών για την μεταφορά ηλεκτρικού φορτίου. Σε αυτήν την περίπτωση υπάρχει περιορισμένη ευαισθησία για μικρές τιμές παραμόρφωσης. Ο ρόλος του διαρραγέντος στρώματος της αλουμίνας είναι να περιορίσει τον αριθμό των αγώγιμων διαδρομών. Το πάχος του στρώματος είναι καθοριστικής σημασίας αφού επηρεάζει το άνοιγμα της ρωγμής. Τα λεπτά φιλμ αλουμίνας διαθέτουν πολύ μικρά ανοίγματα ρωγμών για μικρές τιμές παραμόρφωσης. Αυτό αφήνει την αντίσταση είτε εντελώς ανεπηρέαστη είτε με πολύ μικρή αλλαγή. Τα παχύτερα φιλμ έχουν μεγάλα ανοίγματα ρωγμών, ακόμη και για πολύ μικρές τιμές παραμόρφωσης επομένως αυξάνεται η ευαισθησία

των αισθητήρων. Για τιμές παραμόρφωσης άνω του 0,6 %, όλα τα πάχη αλουμίνας φαίνεται να επηρεάζουν την απόδοση των αισθητήρων, δείχνοντας αυξημένη ευαισθησία, περιορίζοντας τον αριθμό των αγώγιμων διαδρομών. Για μεγαλύτερες τιμές παραμόρφωσης (1,12 % < ε <7,2 %) οι αισθητήρες εμφανίζουν εξαιρετικά υψηλές ευαισθησίες. Συγκεκριμένα αισθητήρες με φιλμ αλουμίνας πάχους 20 nm έχουν ευαισθησίες GF 7998 για παραμορφώσεις έως 4,17 % και μια κολοσσιαία ευαισθησία 2,6 x 10^8 για παραμορφώσεις έως 7,2 %.

Συμπερασματικά, οι αισθητήρες με βάση της ρωγμές και τα νανοσωματίδια πλατίνας έχουν δείξει υψηλές ευαισθησίες για παραμορφώσεις σε εύρος από 0,1 % έως 7,2 %. Το πάχος του φιλμ της αλουμίνας επιτρέπει την ρύθμιση της μέγιστης ευαισθησίας για μια συγκεκριμένη τιμή παραμόρφωσης και δημιουργεί εξαιρετικά ευαίσθητους αισθητήρες για τιμές παραμόρφωσης άνω του 4,17 %. Τα αραιά φιλμ νανοσωματιδίων δείχνουν υψηλές ευαισθησίες για μικρές τιμές παραμόρφωσης, ενώ τα πυκνά φιλμ νανοσωματιδίων καταγράφουν μια εξαιρετικά υψηλή ευαισθησία για μεγάλες τιμές παραμόρφωσης. Αυτή η ευελιξία ανοίγει το δρόμο σε ένα ευρύ φάσμα εφαρμογών που εκτείνονται από αναδυόμενα νέα πεδία όπως η κατασκευή ηλεκτρονικού δέρματος (e-skin) και βιοϊατρικών εφαρμογών σε πιο παραδοσιακά, όπως η δομική παρακολούθηση της υγείας και οι αισθητήρες πίεσης. Τα συμπεράσματα της εργασίας που περιγράφθηκε στο κεφ. 5 δημοσιεύθηκαν στο επιστημονικό περιοδικό Nanoscale[6].

Οι αισθητήρες που αναπτύχθηκαν και μελετήθηκαν κατά την έρευνα χρησιμοποιήθηκαν πειραματικά για τη δημιουργία μιας σειράς αισθητήρων παραμόρφωσης (Chapter 6: Strain sensor array on flexible substrates, pp. 111-125). Οι αισθητήρες κατασκευάστηκαν πάνω σε εύκαμπτο υπόστρωμα kapton και τοποθετήθηκαν σε ένα λαστιχένιο γάντι ακριβώς πάνω στις μετακαρποφαλαγγικές αρθρώσεις του χεριού Οι μετρήσεις των αισθητήρων πραγματοποιήθηκαν χρησιμοποιώντας ένα ηλεκτρονικό κύκλωμα σχεδιασμένο για την ταυτόχρονη μέτρηση μιας συστοιχίας αισθητήρων καθώς και μιας μονάδας Keithley 2400. Χρησιμοποιήσαμε δύο τύπους αισθητήρων παραμόρφωσης για αυτές τις μετρήσεις. Ο πρώτος ήταν αισθητήρες με βάση τα νανοσωματίδια πλατίνας με κάλυψη επιφάνειας 49% που εναποτέθηκαν απευθείας στο υπόστρωμα χωρίς τη χρήση αλουμίνας. Αυτοί οι αισθητήρες έχουν τιμή ευαισθησίας περίπου 67. Ο δεύτερος τρόπος ήταν αισθητήρες με ραγισμένη αλουμίνα πάχους 20 nm. Η κάλυψη επιφανείας των νανοσωματιδίων ήταν 79%, με αποτέλεσμα την πολύ υψηλή ευαισθησία της τάξης του 8000 για τιμές παραμορφώσεων από 1,2% έως 4,2%. Όλοι οι αισθητήρες κολλήθηκαν σε ένα λαστιχένιο γάντι και τα ηλεκτρόδια τους συνδέθηκαν με ένα αγώγιμο νήμα χρησιμοποιώντας αγώγιμη κόλλα. Στη συνέχεια, το αγώγιμο νήμα συνδέθηκε με εμπορικά καλώδια που ενώθηκαν με τη μονάδα μέτρησης.

Το κύκλωμα είναι μια τροποποίηση ενός κυκλώματος που είχε αρχικά σχεδιαστεί στο ΕΚΕΦΕ Δημόκριτος. Έγιναν τροποποιήσεις και επιλέχτηκαν εξαρτήματα και τελεστικοί ενισχυτές έτσι ώστε το σύστημα να ανταποκρίνεται βέλτιστα. Το πλεονέκτημα του κυκλώματος και ο λόγος που επικράτησε έναντι άλλων επιλογών, είναι ότι παράγει ως έξοδο μια τετραγωνική κυματομορφή,

[6] Aslanidis E, Skotadis E, Tsoukalas D, Resistive crack-based nanoparticle strain sensors with extreme sensitivity and adjustable gauge factor, made on flexible substrates, Nanoscale, 2021;13(5):3263-74.

με μια περίοδο ανάλογη της αντίστασης των αισθητήρων. Επιλέγοντας σωστά την τροφοδοσία του κυκλώματος, δημιουργείται τελικά μια σειρά ψηφιακών παλμών που τροφοδοτούνται απευθείας στο ψηφιακό κύκλωμα (Arduino Mega), χωρίς τη χρήση μετατροπής από αναλογικό σήμα σε ψηφιακό.

Για τη λειτουργία του συστήματος ο τελεστικός ενισχυτής T1 καθορίζει το όριο σύγκρισης βάσει -του οποίου θα πραγματοποιηθεί η έξοδος του τελεστικού ενισχυτή T4 (σειρές ψηφιακού παλμού μεταξύ 0 και 5 V). Ο τελεστικός ενισχυτής T2 ρυθμίζει κατάλληλα το πλάτος του τετραγωνικού παλμού που τροφοδοτεί τον αισθητήρα. Τέλος, ο τελεστικός ενισχυτής T3 παράγει έναν τριγωνικό παλμό ο οποίος συγκρίνεται με την τάση κατωφλίου προκειμένου να παραχθεί ο παλμός εξόδου και καθορίζει - ανάλογα με την επιλογή παθητικών στοιχείων - την περίοδο κυματομορφής εξόδου. Για να μετρηθεί την περίοδο της σειράς των παλμών, αρκεί να βρεθεί το διάστημα μεταξύ δύο θετικών άκρων. Όταν φτάσει ο πρώτος θετικός παλμός, ενεργοποιείται ένας από τους μετρητές του μικροελεγκτή, η τιμή του οποίου αυξάνεται με μια συχνότητα που καθορίζεται από εμάς. Η τιμή που επιλέχθηκε είναι 16 Mhz, η οποία είναι η μέγιστη δυνατή συχνότητα. Μόλις φτάσει ο δεύτερος θετικός παλμός, σταματά ο μετρητής. Εάν η τιμή του μετρητή και η περίοδος αύξησής του είναι γνωστές, μπορεί να υπολογιστεί το χρονικό διάστημα από τον πρώτο έως τον δεύτερο παλμό. Για την ορθή μέτρηση της τιμής του μετρητή πρέπει να λάβουμε υπόψη την υπερχείλιση που μπορεί να συμβεί κατά τη διαδικασία. Ο μετρητής είναι 16 bit που σημαίνει ότι μετράει από 0 έως 216 - 1. Κάθε φορά που συμβαίνει υπερχείλιση καλείται μια ρουτίνα που οδηγεί στην αύξηση ενός άλλου μετρητή που διατηρεί τον αριθμό των υπερχειλίσεων.

Βασική απαίτηση του συστήματος είναι η ικανότητα μέτρησης πολλαπλών αντιστάσεων από μία μήτρα αισθητήρων. Για λόγους απλότητας κατά την ανάπτυξη του συστήματος, εφαρμόστηκε ένας πίνακας 1 x 8. Χρησιμοποιήθηκαν δύο πολυπλέκτες 8 σε 1 με τη δυνατότητα αμφίδρομης ροής ρεύματος. Κάθε αντίσταση / αισθητήρας της μήτρας συνδέθηκε με τις εισόδους των δύο πολυπλεκτών. Οι έξοδοι των πολυπλεκτών συνδέθηκαν με το κύκλωμα στη θέση της αντίστασης του αισθητήρα. Ο μικροεπεξεργαστής ελέγχει τους πολυπλέκτες έτσι ώστε η επιθυμητή αντίσταση να επιλέγεται κάθε φορά και τα υπόλοιπα να απομονώνονται.

Οι μετρήσεις πραγματοποιήθηκαν ενώ το γάντι είχε φορεθεί. Οι αισθητήρες αντιδρούσαν όταν υπάρχει κίνηση στο αντίστοιχο δάκτυλο. Για παράδειγμα, η κίνηση του δείκτη προκαλεί στον αντίστοιχο αισθητήρα να αντιδράσει και να αυξήσει την αντίστασή του. Με τον ίδιο τρόπο, όταν οποιοδήποτε δάχτυλο κινείται, οι αισθητήρες ανιχνεύουν την κίνηση και αυξάνουν την αντίστασή τους. Οι μετρήσεις έγιναν και με το Keithley 2400 για σύγκριση των δύο συστημάτων. Τα αποτελέσματα δείχνουν ότι ο θόρυβος είναι εξαιρετικά χαμηλός στο Keithley σε σύγκριση με το δικό μας σύστημα. Ωστόσο, οι τιμές για τις αντιστάσεις καθώς και οι τιμές για τη σχετική αλλαγή στην αντίσταση παραμένουν οι ίδιες και για τα δύο συστήματα. Αυτό αποδεικνύει ότι - στο παράθυρο όπου το σύστημα έχει ρυθμιστεί για να μέτρα σωστά- το κάνει σε πολύ ικανοποιητικό βαθμό.

Τέλος (Chapter 7: Conclusions and Perspectives, pp. 126-128), θα ακολουθήσει μία συνολική θεώρηση των δεδομένων που παρουσιάστηκαν στα προηγούμενα κεφάλαια, στην οποία θα αναφερθούν τα συμπεράσματα του θέματος μελέτης και θα προταθούν ιδέες για μελλοντική μελέτη. Όσον αφορά τους αισθητήρες του τρίτου κεφαλαίου προτείνεται η περαιτέρω μελέτη διαφορετικών επικαλύψεων για την προστασία από την υγρασία. Ενώ το φιλμ της αλουμίνας κατάφερε να προστατεύσει επαρκώς από την υγρασία, έχει την τάση να δημιουργεί ρωγμές όταν του εφαρμόζεται μια μεγάλη τιμή παραμόρφωσης. Οι ρωγμές μπορεί να επιτρέπουν στην υγρασία να εισέλθει στο φιλμ των νανοσωματιδίων και να δημιουργήσει ένα μεγάλο σφάλμα κατά την μέτρηση της παραμόρφωσης. Πρέπει να μελετηθούν επικαλύψεις όχι τόσο δύσκαμπτες, όπως η αλουμίνα, που να μην είναι εύκολο να δημιουργούν ρωγμές με άσκηση μηχανικής παραμόρφωσης και συνάμα να εμποδίζουν τα μόρια του νερού. Ως εναλλακτικές επιστρώσεις προτείνονται τα πολυμερικά φιλμ, τα οποία είναι εξαιρετικά εύκαμπτα, όπως το DPMS ή ακόμα και ένας συνδυασμός πολυμερικών φιλμ με αλουμίνα. Έτσι, η αλουμίνα (που γνωρίζουμε ότι δεν επιτρέπει την διέλευση των μορίων του νερού) θα εναποτίθεται πάνω σε ένα εύκαμπτο πολυμερές (ή και ανάμεσα από διάφορα πολυμερή) και συνδυαστικά θα προστατεύουν τα νανοσωματίδια. Μια άλλη μελέτη με πολύ μεγάλο ενδιαφέρον θα ήταν ο χαρακτηρισμός των διατάξεων νανοσωματιδίων σε εναλλασσόμενη τάση και η μέτρηση της εμπέδησής τους. Με μια τέτοια μελέτη θα μπορούσαμε να εμβαθύνουμε την κατανόηση της ηλεκτρική συμπεριφορά των αισθητήρων. Επίσης σημαντικός κρίνεται και ο χαρακτηρισμός των αισθητήρων σε διάφορες τιμές θερμοκρασίας καθώς και ο τρόπος που θα μπορούσε να εξαλειφθεί η συσχέτισή τους με την θερμοκρασία -καθώς οι αισθητήρες νανοσωματιδίων είναι ευαίσθητοι στις μεταβολές της. Βέβαια θα μπορούσαν επίσης να μελετηθούν και άλλα υλικά τόσο για το υπόστρωμα, όπως το PDMS το οποίο είναι ελαστικό (σε αντίθεση με το kapton), αλλά και για τα νανοσωματίδια, όπως άλλα μη ευγενή μέταλλα και συνεπώς φθηνότερα.

Όσον αφορά την προσομοίωση, της οποίας ο κώδικας παρατίθεται στο παράρτημα Α, θα μπορούσε εύκολα να εμπλουτιστεί και να είναι ικανή να προσομοιώσει και άλλες δομές πέραν από σφαιρικά νανοσωματίδια. Για παράδειγμα θα μπορούσε να προσομοιώσει φιλμ από νανοσωλήνες αλλά και πιο σύνθετες δομές. Επιπλέον, θα ήταν χρήσιμο να τροποποιηθεί ώστε να μπορεί να προβλέπει και την εμπέδηση ενός συστήματος για διάφορες συχνότητες. Βέβαια το παραπάνω πιθανόν να είναι αρκετά δύσκολο καθώς έτσι όπως έχει γραφτεί μπορεί να λύνει μόνο συστήματα γραμμικών εξισώσεων και η μετάβαση στις διαφορικές (που ενδεχομένως να χρειαστεί για την εύρεση της εμπέδηση) να είναι πολύ περίπλοκη.

Στη συνέχεια η τεχνική με τους αισθητήρες με τις ρωγμές πιθανόν να μπορεί να εισαχθεί και σε άλλους τομείς. Θα μπορούσαν, για παράδειγμα, να χρησιμοποιηθούν σαν χημικοί αισθητήρες για την ανίχνευση υγρασίας, φυτοφαρμάκων ή και άλλων ουσιών. Αυτό θα μπορούσε να γίνει εναποθέτοντας πάνω τους κάποια πολυμερή, τα οποία διογκώνονται όταν βρεθούν σε υγρό περιβάλλον. Ουσιαστικά απορροφούν την υγρασία και αυξάνουν το μέγεθός τους συμπαρασέρνοντας ταυτόχρονα και τα νανοσωματίδια που βρίσκονται από κάτω τους. Εάν συνδυαστεί αυτή η τεχνική μαζί με έναν αισθητήρα με ρωγμές θα μπορούσε να καταλήξει σε έναν χημικό αισθητήρα με εξαιρετικά αυξημένη ευαισθησία. Και στη συγκεκριμένη περίπτωση

είναι πολύ σημαντικός ο χαρακτηρισμός των αισθητήρων στην θερμοκρασία αλλά και η μελέτη της εμπέδησής τους.

Πέραν αυτού, θα μπορούσαν να μελετηθούν και άλλα υλικά για τον ρόλου του ραγισμένου υποστρώματος. Πιθανόν και άλλες τεχνικές εναπόθεσης όπως η ιοντοβολή. Ταυτόχρονα θα ήταν πολύ ενδιαφέρον να μελετηθεί σε βάθος ο φυσικός μηχανισμός που δημιουργεί τις ρωγμές και ο τρόπος με τον οποίο θα μπορούσε κανείς να ελέγξει την πυκνότητά τους την διεύθυνσή τους την περιοδικότητά τους (αν υπάρχει) και άλλα μεγέθη. Ελέγχοντας, για παράδειγμα, την περιοδικότητα και την κατεύθυνση, ένα ραγισμένο φιλμ θα μπορούσε να χρησιμοποιηθεί σαν μάσκα για λιθογραφία.

Τέλος, όσον αφορά το σύστημα καταμέτρησης της συστοιχίας των αισθητήρων, θα μπορούσε να εξελιχθεί σαν μια φορητή συσκευή για μέτρηση συστοιχίας αισθητήρων χωρίς την ανάγκη να συνδέεται σε έναν υπολογιστή. Έτσι θα μπορούσαν να γίνουν μετρήσεις για παράδειγμα ενός φυτοφαρμάκου απευθείας στο πεδίο (χωράφι, θερμοκήπιο κτλ.) για μεγάλα χρονικά διαστήματα χωρίς την παρουσία ανθρώπου εκεί. Αρχικά, θα πρέπει να σχεδιαστεί και να κατασκευαστεί κατάλληλη θήκη η οποία θα μπορούσε να εκτυπωθεί με έναν 3D printer. Έπειτα, θα πρέπει να σχεδιαστεί κατάλληλα το κύκλωμα για να τροφοδοτείται μέσω μιας μπαταρίας. επίσης, μπορεί να σχεδιαστεί και κατάλληλο λογισμικό, το οποίο ενδεχομένως να ελέγχεται και από ένα κινητό τηλέφωνο, με το οποίο θα μπορούν να ληφθούν οι μετρήσεις αλλά και να ελέγχεται η λειτουργία του συστήματος εξ αποστάσεως. Τέλος, θα πρέπει να μελετηθεί η δυνατότητα μέτρησης των αισθητήρων ως στοιχεία μια μήτρας και το πως θα απομονωθούν ηλεκτρικά τα εκάστοτε μετρούμενα στοιχεία.

ACKNOWLEDGEMENTS

The present study was carried out in the framework of a doctoral dissertation in the Physics Department of the School of Applied Mathematics and Natural Sciences in National Technical University of Athens. Upon completion of this work I would like to thank a number of people whose contribution has been crucial for the completion of this dissertation. Firstly and most importantly, I would like to thank my supervisor, Professor Dimitris Tsoukalas for the opportunity he gave me and the introduction to this very cut- edge field of research and for our very good cooperation to the end of our ad joint research. His guidance, ideas and advice have been valuable for the completion of the work. I would also like to thank the other six members of the committee: Professors Yannis Raptis, Christos Papavassiliou, Ioanna Zergioti, Apostolos Kiritsis, Evangelos Christoforou and Themis Prodromakis. For their cooperation and advices, I would like to thank the researchers Dr. Konstantinos Giannakopoulos and Christina Skoulikidou from NCSR Demokritos for the SEM and TEM images.

I would especially like to thank Dr. Evangelos Skotadis and Dr. Lampros Patsiouras for their contribution and ongoing oversight of my research work. I must also thank the other members of the laboratory Dr. Panagiotis Bousoulas, Dr. Charalampos - Menelaos Tsigkourakos, Dr. Marianthi Panagopoulou and the PhD students Dionisis Sakelaropoulos, Charalampos Papakontsantinopoulos, Stauros Kitsios and Maria Kainourgiaki for our cooperation during these years. I would also like to thank Dr. Spyros Stathopoulos for his continued help in the laboratory despite the kilometers that separate us. I must thank Fotini Vasilopoulou, Thanasis Markou, Christos Mistilidis and Agelos Ferikoglou for their contribution in the fabrication of the measuring system. Finally, I would like to thank Dr. Leonidas Madianos, Evangelos Moutoulas and Oleg Talajevic for their contribution to the lab, as well as their friendship and of course all the members of Prof. Zergioti's team.

I would like to extend a huge thank you to my parents for their support during all these years. Last but not least, to my partner Eleni for her patience, proofreading and editing of the manuscript, thank you.

I would like also to acknowledge support from the International Consortium of Nanotechnologies (ICON) coordinated by the University of Southampton and funded by Lloyd's Register Foundation, a charitable foundation which helps to protect life and property by supporting engineering-related education, public engagement and the application of research.

Contents

Prologue

The object of the present dissertation is the study of strain sensors based on platinum nanoparticles. Specifically, the sensors were built on flexible substrates to allow high strain values. Initially simple sensor structures are studied and characterized under different conditions such as different humidity values. Then, in order to explain their sensitivity, a Monte Carlo simulation was written in Matlab which predicted the sensitivities that such devices might have. Strain sensors with a different structure but always based on platinum nanoparticles were then fabricated and studied, which showed extremely high sensitivities. Finally, the sensors were applied to a glove to monitor hand movements. The measurements were made with a system that was built to measure multiple sensors simultaneously. The structure of the doctoral dissertation is as follows:

The first chapter introduce the nanotechnology and nanoparticles. Describes the deposition techniques used extensively for the preparation of thin films which were also used for the preparation of the thesis devices.

In the second chapter, an extensive reference is made to all the categories of deformation sensors and mainly to the sensors based on nanoparticles, since to this category belong the sensors that were made in the present work. It also describes in detail the mechanism of conductivity in nanoparticle films and the resulting quantum phenomena such as the tunnel effect and the corresponding resistance that we use to detect deformation.

Chapter 3 presents the strain sensor device on a flexible substrate. A detailed description is given for the manufacturing process but also for the characterization of the devices. The existing model for the characterization of nanoparticle-based sensors is then extended to cover all nanoparticle fabrication techniques (chemical and physical methods). The response of the sensors to different relative humidity conditions is then studied and the use of a thin Al_2O_3 (alumina) film to protect it is proposed. Two thicknesses of alumina were used and it was proved that the thickest adequately protects the platinum nanoparticle film from moisture.

Chapter 4 describes the Monte Carlo code written in Matlab, which simulates nanoparticle-based strain sensors. During the simulation process the code calculates the conductive paths formed in the nanoparticle films and from them finds the total resistance of the film using the Laplace matrix. It was initially compared with the results of the third chapter to examine its validity. He then predicted the sensitivities for different nanoparticle films (different average diameter and surface coverages).

Chapter 5 describes a new strain sensor based on platinum nanoparticles and cracks. The sensors were created on an alumina film which creates cracks when subjected to large deformation. The cracks were exploited to increase the sensitivity of the sensors as when they are under strain they further increase the distance of the nanoparticles resulting in a very large increase in their resistance and hence the sensitivity. The effect of alumina thickness on the

sensitivity and the effect of the surface coverage of the nanoparticles were studied in detail. Sensitivities of the order of 10^8 have been achieved which are the largest that have been published so far.

Chapter 6 describes an application for strain sensors and describes a system for measuring sensor arrays. Specifically, strain sensors were attached to a flexible glove to detect hand movements. A system mounted on an oscillator was built to measure the sensors, the oscillation period of which depends on the value of the sensor resistance, controlled by an Arduino. The system measurements were compared with measurements from a Keithley 2400 which is one of the most reliable resistance measuring tools, and it was shown that for a given resistance window the system measures the resistances satisfactorily. In addition, the sensors proved capable of detecting hand movements.

Finally, the dissertation concludes with a review of the research issues resolved and also evaluates the scientific contribution of the present work. Future work and experimental procedures are proposed to assist in further understanding of conductivity mechanisms, as well as new sensor applications.

Chapter 1: Introduction

1.1. Nanoscience and Nanotechnology

During the last five decades the fastest advancing field was -by far- that of microelectronics. Within less than seventy years from the invention of transistor from J. Bardeen, W. Shockley and W. Brattain in Bell Telephone laboratories in 1948 [1], the electronic computers were transformed from enormous, complex, noisy and very difficult to maintain machines, into today's personal computers. The invention of the transistor obsoletes the vacuum tubes, which was the main processing component at the time. Vacuum tubes consume a lot of power, are extremely inefficient, with the majority of the consumable energy turning into heat and needing big and heavy transformers in order to operate. The replacement of vacuum tube with semiconductor transistors made the electronic devices lightweight and more efficient. The enormous technological rise of semiconductors has been used as an advantage from the heavy industry as well as car and aircraft manufactures and medicine, soft robotics etc. Nowadays, all electronic devices are based on semiconductors, which are by far more powerful, faster, more compact, and consume less power than their predecessors did. Laptops, smartphones, tablets, smartwatches -and so on- have become essential in everyday life thanks to microelectronics.

Some of the remarkable steps that microelectronics achieved and led to the development of microelectronic devices and the integrated circuits are:

i. The investigation and development of silicon as the first n-p-n device in 1955 [2]
ii. The development of silicon oxide as passivation layer for devices on silicon in 1956 [3]
iii. The development of photolithography technic in 1957 [4]
iv. The first massively production silicon transistor in 1958 [5]
v. The production of the first intergraded circuit in 1959 [6]

Many more technological accomplishments followed, such us the planar integration process [7] which led to the development of the first BJT (Bipolar Junction Transistor) and the MOSFET (Metal Oxide Semiconductor Field Effect Transistor) [8, 9]. All the above-mentioned led to the shrining of dimensions and gradually the devices became much smaller and faster. All that can be summed up in Moore's most famous notion (Moore's law) that the number of transistors in a dense integrated circuit doubles about every two years. Eventually the smallest dimension of the devices became smaller than 1 μm (10^{-6}m). By shrinking the dimensions and entering the world of nanoscale, exotic material properties came to surface. The science field that explores these phenomena is called nanoscience.

Nanotechnology is the next technological step of microelectronics. By definition, nanotechnology is the manipulation of matter with at least one dimension sized from 1 to 100 nanometers (10^{-9}m). Many different science fields are associate with nanotechnology as surface science [10], organic chemistry, molecular biology, semiconductor physics, energy storage [11],

engineering [12], microfabrication [13] and molecular engineering [14]. Nanotechnology has now entered many fields of scientific research and can only be considered inextricably linked in the way that human technology will continue to evolve and the ever-increasing impact it will have on our lives. It is noteworthy that most universities have at least one research team related to nanoscience or nanotechnology and that several countries have established national research centers based on nanotechnology, thus the importance that the scientific community and the market attach to it in terms of promoting research and economic development. Nanotechnology is applied in many areas of everyday life related to medicine, materials for environmental applications and in the field of energy production and storage, information technology and microsystems such as sensors and everyday products (cleaners, protective paints).

In particular, nano-medicine and nano-biotechnology have attached great interest in recent years due to drug delivery to the human body using nanoparticles appropriately modified to target harmful cells. Apart from that nano-medicine and nano-biotechnology focus on the development of sensory devices for detection biomolecules, such as DNA and its mutations and proteins. Especially at the time of writing this dissertation (January 2021) the world is suffering from the Covid-19 pandemic and one of the first vaccines against the Covid-19 is based on nanoparticles [15, 16].

Apart from that, flexible electronics and electronic skin for energy production devices as well as sensors (wearable electronics) [17], intend to make it possible to monitor human physiology indicators (blood pressure, body temperature, heart rate). Furthermore, monitoring external parameters in the human environment (room temperature and humidity, pollutant concentration) and evaluating these data will help in the course of treatment and prevention of chronic diseases. However, like in any technological field, nanotechnology poses risks and challenges to the scientific community. There is a great deal of research on the effects of nanomaterials on human health, such as the exposure to nanoparticles, as their extremely small size makes them difficult to manage and their toxicity is still being investigated.

Also, the development of biochemical sensors for the detection of pathogens and toxins could be used in the food industry and agricultural production as well as the detection of hazardous substances, such as heavy metals, etc. The size reduction of the devices and the use of nanomaterials leads to energy savings, cost reduction, increased speed and sensitivity. Finally, nanotechnology has contributed to the integration of new devices, such as organic transistors and flexible electronics and as far as the reduction of power consumption and larger storage space is concerned non-volatile memories and hard drives are invented.

1.2. The impact of the nanoscale transition.

During the transition from a macroscopic (bulk) material to the nanoscale many of the critical parameters that determine the properties of the material are changing. These changes in the macroscopic properties of the material has aroused great interest around nanostructured materials. When the size of the crystalline material decreases and eventually reaches nanometric dimensions, the wavelength of the valence electrons is comparable to the size of the crystal. This

results in the available energy states for electrons becoming distinct due to phenomenon of quantum localization and the energy difference between the different energy levels depends on its size nanocrystallite. The average energy difference between successive energy levels (δ) is known as the Kubo gap [18],

$$\delta = \frac{4E_F}{3N} \tag{1.1}$$

where E_F the Fermi Energy of the nanocrystal and N the number of the atoms in the nanocrystal. It is obvious that as the size of the crystal decreases the separation between energy levels increases. In fact, when the Kubo gap becomes larger than the thermal energy of the electrons, the nanocrystal switches from conductive to insulating (Metal to Insulator Transition, MIT).

The proportions between atoms and nanoparticles extend beyond the discrete energy levels. As atoms are the building blocks of any material, nanoparticles can be used as artificial building blocks in order to synthesize new macroscopic materials with distinct properties. In conventional materials these properties generally arise from the interaction between atoms as well as their arrangement in space. The properties of nanostructured materials depend respectively on the size, composition, shape, bonding material and arrangement of the nanoparticles.

1.3. Applications of nanomaterials

In addition, nanoparticles and nanomaterials, in general, are already used in various sectors of the economy and medical research, while many of their future applications are still being researched. The following figure briefly shows their application areas.

Automotive industry • lightweight construction • painting (fillers, base coat, clear coat) • catalysts • tires (fillers) • sensors • Coatings for wind-screen and car bodies	**Chemical industry** • fillers for paint systems • coating systems based on nanocomposites • impregnation of papers • switchable adhesives • magnetic fluids	**Engineering** • wear protection for tools and machines (anti blocking coatings, scratch resistant coatings on plastic parts, etc.) • lubricant-free bearings
Electronic industry • data memory (MRAM, GMR-HD) • displays (OLED, FED) • laser diodes • glass fibres • optical switches • filters (IR-blocking) • conductive, antistatic coatings	**Construction** • construction materials • thermal insulation • flame retardants • surface-functionalised building materials for wood, floors, stone, facades, tiles, roof tiles, etc. • facade coatings • groove mortar	**Medicine** • drug delivery systems • active agents • contrast medium • medical rapid tests • prostheses and implants • antimicrobial agents and coatings • agents in cancer therapy
Textile/fabrics/non-wovens • surface-processed textiles • smart clothes	**Energy** • fuel cells • solar cells • batteries • capacitors	**Cosmetics** • sun protection • lipsticks • skin creams • tooth paste
Food and drinks • package materials • storage life sensors • additives • clarification of fruit juices	**Household** • ceramic coatings for irons • odors catalyst • cleaner for glass, ceramic, floor, windows	**Sports /outdoor** • ski wax • antifogging of glasses/goggles • antifouling coatings for ships/boats • reinforced tennis rackets and balls

Figure 1.1: Application areas of nanomaterials [19]

In biomedicine, many nanomaterials, such as metal nanoparticles, are being investigated for cancer treatment and targeted drug delivery, as they can receive biomolecules and drug chemicals on their surface, with proper functionalization. In addition, Nanocomposites, such as Nano clays, are used in packaging materials due to their good barrier properties to moisture and gases.

Utilization of nanomaterial scale phenomena, which can be made comparable in size to some of the substances we want to detect (e.g. DNA strand binding), has led scientists to use nanomaterials as sensing materials. For example nanoparticle thin films, such as piezoelectric ZnO and metal nanoparticles (mainly Au and Pt), are systematically researched in the development of distortion and touch sensors, as well as in transducers with many potential applications. One challenging application is the integration of sensors in flexible substrates that will be worn in the human body (wearable electronics) with the simultaneous measurement of various parameters of the environment and the human body.

1.4. Nanomaterial manufacturing techniques

A classification of manufacturing methods distinguishes them into "top-down" and "bottom-up" manufacturing techniques. Below are some of the most common manufacturing techniques.

1.4.1. Chemical Vapor Deposition (CVD)

CVD is a bottom-up thin film deposition technique (Fig. 1.2), widely used in microelectronic technology. During deposition, gases are introduced into a deposition chamber and react over a substrate, on the surface of which the desired material is formed. These gases carry the chemical compounds from the reactions (precursors) of which the new material will be formed. The precursors are in liquid, gaseous or solid form stored in containers outside the chamber and are entrained by the flow of a carrier gas which may be hydrogen or argon or high purity nitrogen. Usually the chamber and the substrate are under high temperature, which can be as high as 1000 °C.

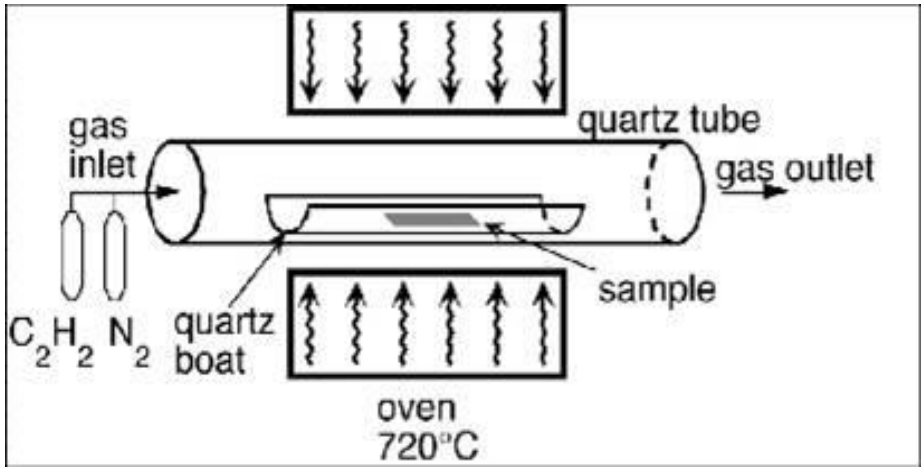

Figure 1.2: Schematic representation of a CVD system [20]

Variations of the technique also include Low-pressure CVD (LPCVD), Plasma-enhanced (PCVD) and High Density Plasma (HDPCVD). In the case of LPCVD, the reactions are carried out at pressures between 0.25 to 2 Torr and at temperatures between 300-900 °C. The lower the pressure, the lower the gas consumption and the faster the diffusion of the reactants to the substrate. Also, the advantage of this technique is that it entails the possibility of denser arrangement of the substrates (silicon wafers) and therefore the larger wafer treatment per deposition. In the case of PECVD, plasma gas is used to provide some of the energy required by the high kinetic energy of the electrons and ions of the plasma, leading to thermal energy savings from the heating elements of the chamber. This technique is applicable in cases where the substrates do not withstand high temperatures. Therefore, the operating temperature range is up to 200-350 °C, although this technique allows deposits to be made even at room temperature.

More specifically, inside the deposition chamber there is an anode electrode and the substrate is grounded at the cathode. The temperature of the substrate can be controlled by heating elements. Applying high voltage to the anode, usually at a frequency of 13.56 MHz, the gas that enters the chamber at pressures of 50 mTorr - 5 Torr and transports the reactants becomes ionized, creating free electrons and ions. High kinetic energy electrons collide with the molecules of the reactants ionizing them or breaking them down into other compounds. This way the products of these reactions reacts on the surface of the substrate and forms the desired material. Finally, in HDPCVD, the plasma application is accompanied by alternating field ion deposition on the substrate, which is bombarded by plasma ions resulting in denser materials with fewer voids inside. CVD is used, among others, in the manufacture of epitaxial silicon, silicon dioxide, silicon nitride, but, also, in two-dimensional inorganic and organic materials (graphene, MoS_2). The advantages of this technique include the construction of films with good uniformity and low porosity.

1.4.2. Atomic Layer Deposition (ALD)

The ALD technique is a chemical method of synthesizing thin films on the substrate surface with very good thickness control and the possibility of making a monoatomic layer or a layer of a few nm even on surfaces with a high geometric ratio of dimensions in different directions (high aspect ratio). The films synthesized by this technique have a high degree of homogeneity and uniformity of thickness, low concentration of impurities and are usually amorphous. Inorganic and organic materials and elemental materials (e.g. pure metals or semiconductors) can be made with this technique. Typical examples are metal oxides, nitrides, copper ions (e.g. sulfides, selenides, etc.), metals, semiconductor compounds [21], but also polymers such as polyamide and polyimide [22].

The method consists in the individual reaction of precursors or reactants, which are isolated from each other and are led to the chamber in which the substrate is located, reacting with it. That is, the reactants (at least two, A and B) react individually with the substrate, without simultaneously being in the reaction chamber and a successive number of alternating cycles of A and B result in the development of the film with an almost monoatomic layer at a time. Unlike the CVD technique, the reactants are present at the same time and react with each other on the

surface of the substrate thus creating continuous layers of material. More specifically, the steps of forming a film in the simplest case of two precursors are the following:

1. The first precursor A enters the chamber and reacts with some surface chemical groups of the substrate.
2. An inert gas is introduced to remove the unreacted molecules of substance and the by-products of the first reaction. This process is referred to as purge.
3. The second precursor B enters the chamber and reacts with the modified surface due to the first reaction, while preparing the substrate to repeat the reaction with substance A.
4. Repeat the purging with the inert gas.

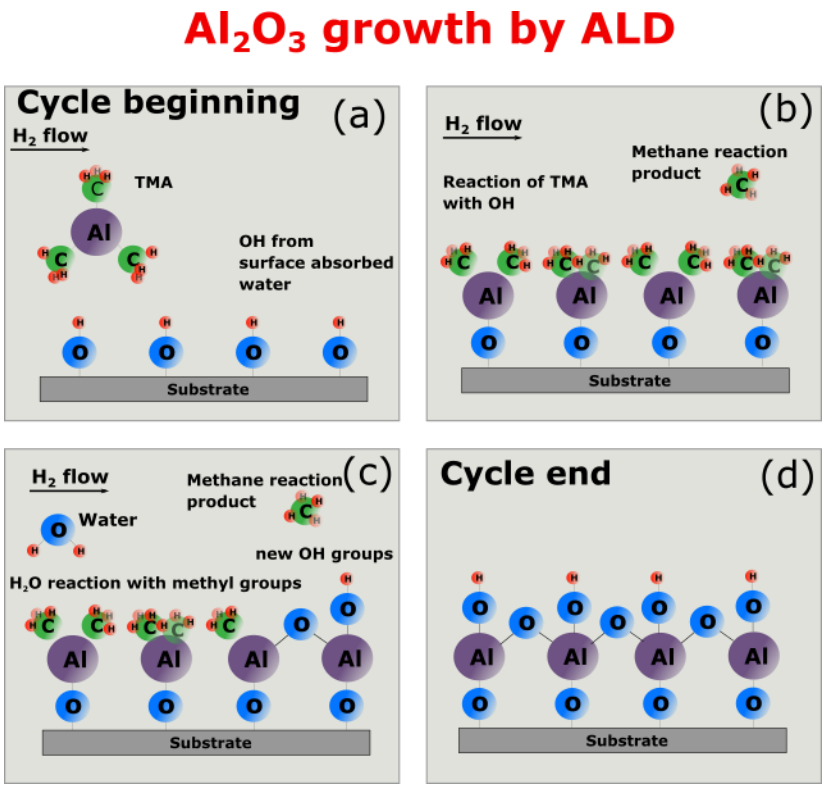

Figure 1.3: Schematic representation of the Al_2O_3 growth by ALD cycles.

This four-step routine is called “the deposition cycle” and at the end an individual layer of the material is formed. A cycle is divided into two half cycles involving the corresponding reactions of substance A and B with the substrate. The precursors are usually transported to the chamber via a carrier gas which is also used in the intermediate purifications between the precursors. Due to the existence of self-terminating reactions, the thickness of the film is controlled by the number of cycles, thus leading to precise thickness control. The pressure that must prevail in the deposition chamber must be at the level of 1 Torr, in order that the flow of inert gas is smooth and efficiently transfer the precursors from it [23].

The precursors used are gaseous, liquid, or solid. They must meet certain conditions, such as being volatile at temperature equal to or higher than room temperature, not decomposing at the operating temperatures of the deposit, and gas-solid phase reactions meeting the self-

termination criterion. In a self-terminating reaction all surface groups of the substrate react with the reactant molecules (saturation) and the excess molecules that are left over do not contribute to the reactions.

Surface reactions in ALD consist of the adsorption of molecules of the gaseous precursors on the substrate and the reaction (or decomposition on the surface) with surface groups. Adsorption is divided into physical adsorption (physisorption) and chemical adsorption (chemisorption). During natural adsorption, the molecule interacts with the surface group weakly and can be easily removed, while the structure of the molecule can be slightly altered. During chemical adsorption, chemical bonds are formed or dissolved between the molecule and the surface group. This process results in the creation of a monolayer. In contrast to natural adsorption, multiple layers can be developed on the surface due to the indistinguishable attachment of the molecules to the surface atoms or groups.

There are certain factors that affect the growth rate of the film (growth per cycle, GPC), i.e. the thickness per deposition cycle. One factor is the number of cycles. During the first cycle, the reacting molecules sees a free surface, where all the active points are available for adsorption. As the layer develops, more and more spots are covered and a smaller percentage of the initial surface is exposed to the precursor molecules, while in the remaining percentage of the surface the reactants interact with the deposited material that has been created. Eventually, when a continuous layer of material is formed, the reacting molecules no longer interact only with the surface of the desired material.

A second important parameter that affects the GPC during deposition is temperature. Phenomena due to temperature fluctuations are related to the effect on the number and type of reactive sites and the energy-appropriate reactions that take place [24]. At low temperatures either the precursors will condense on the surface (increasing GPC), or the desired reactions due to low thermal energy will not be completed (decreasing GPC). At high temperatures, decomposition of surface species can occur, either resulting in adsorption of more molecules on the surface, resulting in increased GPC, or, on the contrary, surface groups may be desorbed, leading to fewer reactions and thus a reduction in GPC [25, 26].

1.4.3. Physical Vapor Deposition (PVD)

1.4.3.1. Sputtering

Sputtering deposition is a bottom-up method of fabrication metal and dielectric thin films as well as nanoparticles and is widely used in microelectronics. Sputtering is defined as the bombardment of a surface with high energy ions resulting in the subsequent detachment of atoms of the surface material (target). The multiple elastic scattering of ions in the target, produce secondary electrons and the emission of X-rays and photons of other frequencies due to the excitation and de-excitation of the target atoms.

1.4.3.2. RF sputtering

To avoid the above problem the insulating the target is polarized with an alternating voltage with radio frequency (hence the term RF). During a frequency period, there is a constant bombardment of the target surface with ions as they are more cumbersome in their response to the alternating electric field, while the electrons follow the alternations of the electric field. In this case, the accumulation of positive charge on the target surface is neutralized by the collision of electrons in the second half of the period of alternating voltage. This allows the positive ions to hit the surface of the insulator unhindered and the plasma to be stable in the chamber.

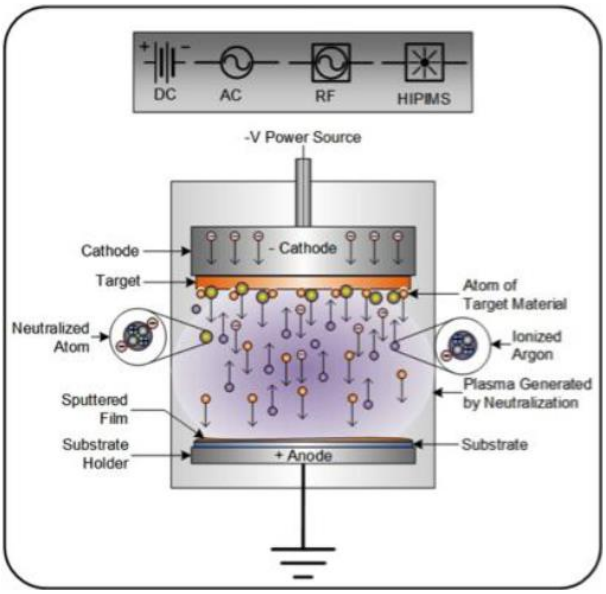

Figure 1.4: Schematic representation of a sputtering device [27]

The target electrode and the anode -due to the oscillation of the electron charge- develop a continuous potential more negative than the plasma potential, so that the slower gas ions during field oscillation "feel" an average continuous field and bomb the target. At the same time, the anode electrode is bombarded, but the ratio of the anode and cathode dynamics depends on the ratio of the surface areas of the electrodes. As the area of the anode is much larger than that of the target (the anode is grounded together with the walls of the chamber), the voltage dropping across the target will be much larger, so the ionization will be much more intense on the target surface. With RF sputtering, the ionization of the gas atoms, due to the energy of the alternating field, becomes more efficient allowing operation at lower pressures. With this technique, thin films of metals, semiconductors and insulating materials, such as oxides and metal nitrides, are deposited.

In conventional DC and RF sputtering systems, the free electrons, due to inelastic collisions with the gas atoms, escape to the anode, participate to a small extent in the ionization of the inert gas. This results in a low ionization rate and therefore an increase in deposition time. For this purpose is developed a technique of applying a magnetic field around the target for keeping

the electrons at a short distance from it and the increasing the percentage of the ions involved in the process. This technique is called magnetron sputtering and is implemented by placing strong magnets behind the target, which create a magnetic field with dynamic lines perpendicular to the electric field. The magnetic field in combination with the electric field apply a Lorentz force on the electrons, forcing them to a spiral orbit around the target and to remain in the plasma for a longer period of time, thus achieving a better ionization rate.

This results in an increase in the deposition rate compared to the conventional technique and the use of lower inert gas pressure. In addition to the sputtering technique, it is possible to simultaneously deposit more materials (co-sputtering) in order to create alloys. As a technique it is also flexible, as a wide variety of materials can be deposited. However, the presence of gas at the deposition site results in the possible formation of impurities as the film develops and the substrate is stressed due to the impact of the charged particles.

1.4.3.3. DC sputtering

This technique, which can be attributed to direct current sputtering, takes place in a very low pressure chamber, where the target is polarized under a constant negative voltage of a few hundred to a few thousand volts and the substrate is grounded to the anode electrode along with the chamber walls (Fig. 1.4). Inside the chamber there is an inert gas, which, with the application of the negative voltage, is transformed into a plasma, with a part of its atoms being positive ions and free electrons in theoretically equal populations, while the rest are neutral atoms of the gas. The ions are directed towards the negatively polarized target, collide with its surface and the energy they carry breaks the bonds of the target atoms and detaches them from the surface. Then the vapors of the target atoms travel to the substrate and is being deposited on its surface forming a thin film.

During DC sputtering the target must be conductive, so only metals can be deposited. The application of DC voltage in the case of insulating materials, such as metal oxides, would result in the accumulation of charge on the surface of the insulator due to the collision of gas ions that would prevent subsequent ions from reaching the surface, reducing the applied voltage to the target and eventually the quenching of the plasma.

1.4.3.3.1. Production of nanoparticles by DC magnetron sputtering

The nanoparticles are produced by the DC magnetron sputtering method, followed by gas phase condensation. Eventually the nanoparticles produced tend to hold an extra electron and that excess electron allows their electrostatic handling. The nanoparticles can be accelerated to the substrate producing a wide variety of morphologies, such as its individual islands up to very thin layers of coating films. The shape of the nanoparticles is affected by several different parameters. The magnetron sputtering head can be moved inside condensation zone. By reducing the distance from the head to the expansion opening, the distance and the condensation time are being reduced - resulting to the consequent reduction of the average size of the nanoparticles. The source allows the introduction of gas (argon) that will act as a carrier

of produced nanoparticles. By increasing the gas flow rate there is a decrease in the average size of the nanoparticles produced, due to the reduction of their residence time in the agglomeration zone. The pressure in the pumping (or agglomeration) zone of the nanoparticles is about $1x10^{-3}$ mbar, while the pressure in the storage chamber is about $5x10^{-5}$ mbar. Due to this gradient in the pressure, the nanoparticles are entrained in deposition chamber and deposited on the sample.

In a DC magnetron sputtering system (Fig. 1.5) the plasma dc state caused by the inert gas being close to the target thanks to the magnetic field of DC magnetron sputtering. The result is creating supersaturated vapors of the target containing its atoms. Typically, entering in the agglomeration zone where the gas exist, the process of condensation and nucleation, resulting in the creation of a distribution of nanoparticles with a variety of sizes. Target atoms with very high kinetic energies are cooled by the gas (equivalently led to lower kinetic energy states) causing the target particles (clusters of particles) to nucleate. The nucleation of these small particles (granules) is followed by the growth of granules into larger particles (clusters). The development of swarms is strongly dependent on cross-sectional collisions (here the presence of inert gas becomes apparent). Since the inert gas is primarily responsible for the cluster formation process (condensation), its pressure is used to control the cluster size distribution.

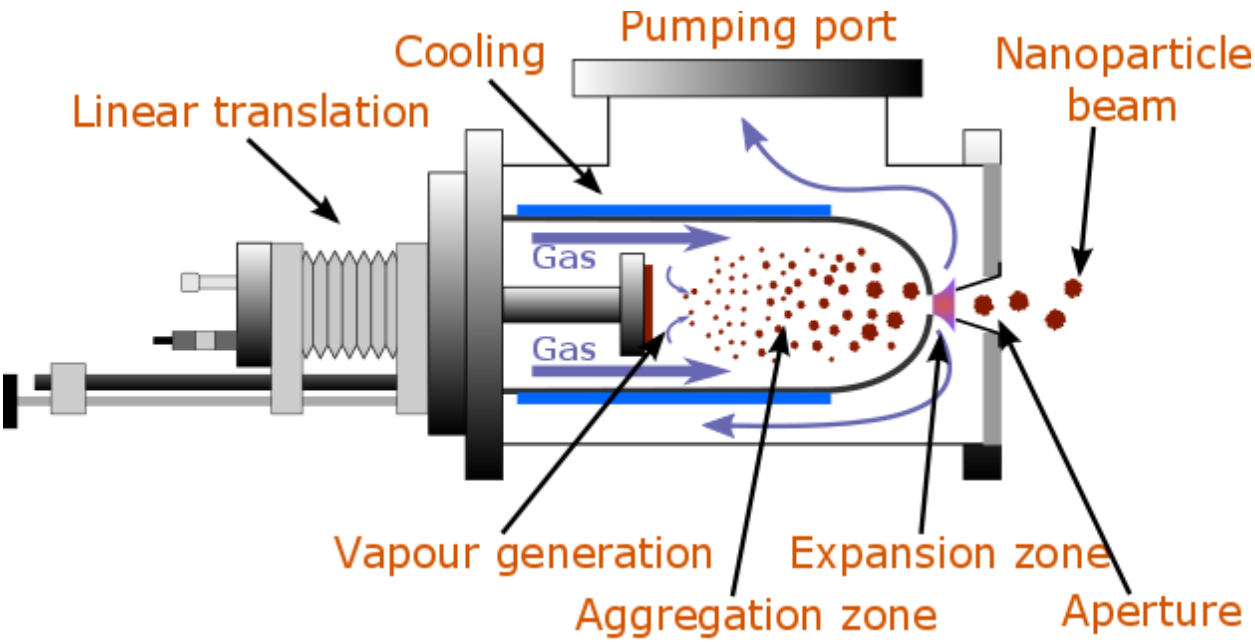

Figure 1.5: Schematic representation of the DC magnetron sputtering nanoparticle generator.

The growth and nucleation of the cluster is being stopped as the cluster enters through a small hole in the filtration zone, where significantly lower pressure prevails. In this phase the nanoparticles that will be deposited on the substrate are formed. The deposition conditions affecting surface density of nanoparticles and their size distribution, is the temperature of the substrate, the deposition time, the strength of the deposition and inert gas flow rate.

1.4.3.4. Electron gun evaporation (e-gun)

E-gun evaporation is another common technique of physical vapor deposition (bottom-up also), to create thin films on substrates. The deposited material is being placed in a vessel (crucible) of high thermal resistance in a vacuum chamber (<10^{-5} mbar) and heated, either by means of a heating element (thermal sublimation) or by impact of an electron beam in the vessel (sublimation by electron beam). The high temperature that develops sublimates the material, and the vapors of its atoms travel forming a cone of material, condensing on the surface of the substrate forming a film. As the deposition takes place at low pressure and in the absence of any other gas, the orbits of the atoms are less random and the angles of incidence are less dispersed.

In the case of thermal evaporation, first developed and used to make aluminum, the container consists of a refractory ceramic (e.g. Al_2O_3 alumina, ZrO_2 zirconia) or a refractory metal (e.g. molybdenum Mo) heated either by means of a resistor (in the case of the ceramic one), or by applying high voltage (5-100V) to the container (in the case of metallic one). Materials with high thermal conductivity, such as silver and gold, are easier to be deposited with e-gun evaporation.

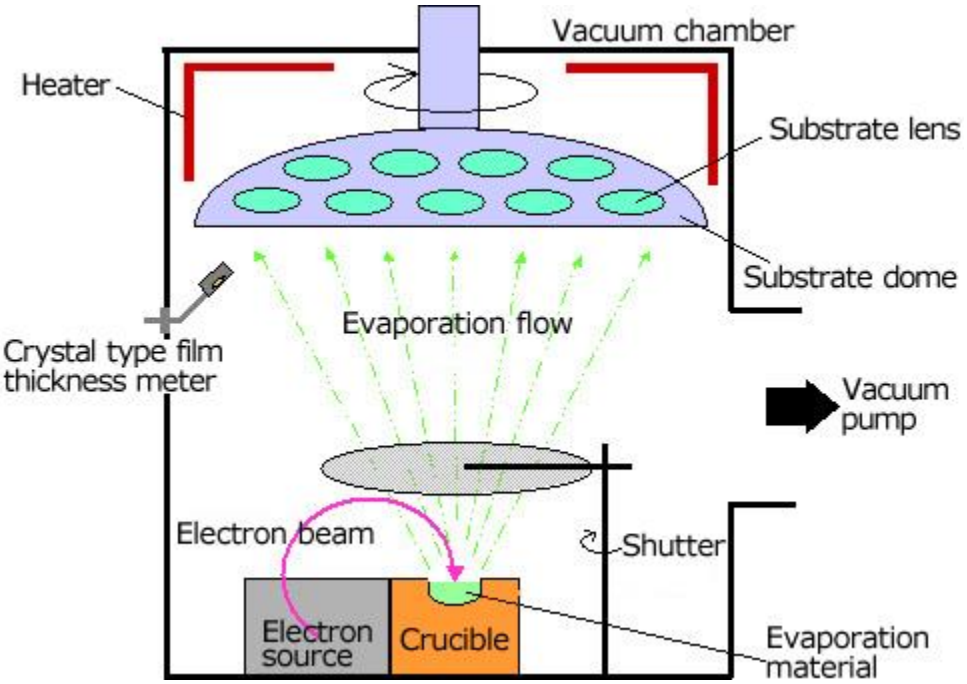

Figure 1.6: Schematic representation of an electron gun evaporator [28]

In the case of e-gun evaporation, electrons produced thermally by a tungsten filament (W) leaking from a small current form a beam that directs and strikes the target vessel when it is polarized at high potential (2 kV) (Fig. 1.6). The kinetic energy carried by the electrons upon impact on the surface of the vessel heats the target material. During deposition, the target container is being cooled. The power of the W filament and the high potential applied are what

control the deposition rate. Targeted heating of the electron beam allows the development of higher temperatures and therefore the deposition of metals. In addition, the continuous cooling of the target in combination with the local heating reduces the vapors from other peripheral materials, such as the metal resistors. This ensures the formation of films with fewer impurities. Disadvantages of the technique include the smaller material emission cone.

The required temperatures for evaporation vary from material to material, but the maximum temperatures that develop locally are in the order of a few thousand °C. Therefore, the deposition rates are strongly dependent on the material and in particular on their vapor pressure, in contrast to the sputtering. The small angle of incidence and the small area of the target result in less uniformity in the film than sputtering. Also, with this technique, a smaller range of materials is being produced. Its advantage is, among others, the high purity of the materials, as they are made under low pressure and the deposited material comes from a small part at the top of the target and is not contaminated by the material of the container (as the case of electron evaporation). E-gun evaporation is being used especially in microelectronics for the construction of metal contacts in circuits, as the nature of the technique allows the selective deposition of material in structures imprinted on the substrate by lithography.

1.5. References

[1] Bardeen J, Brattain WH, The transistor, a semi-conductor triode, Physical Review, 1948 Jul 15;74(2):230.

[2] Tanenbaum M, Valdes LB, Buehler E, Hannay NB, Silicon n-p-n Grown Junction Transistors, Journal of Applied Physics, 1955 Jun;26(6):686-92.

[3] Frosch CJ, Derick L, Surface protection and selective masking during diffusion in silicon, Journal of the Electrochemical Society, 1957 Sep 1;104(9):547.

[4] Nall JR, Lathrop JW, Photolithographic fabrication techniques for transistors which are an integral part of a printed circuit, In1957 International Electron Devices Meeting 1958 Apr (pp. 117-117), IEEE.

[5] G.E. Moore και R.N. Noyce, "Method for fabricating transistors"

[6] Kilby JS, Semiconductor Solid Circuits, presented at American Rocket Society 14th Annual Meeting.

[7] J.A. Hoerni, "Method of manufacturing semiconductor devices"

[8] J.E. Lilienfeld, "Method and apparatus for controlling electric currents"

[9] Kahng D, Silicon-silicon dioxide field induced surface devices, Inthe Solid State Device Research Conf., Pittsburgh, PA. June 1960.

[10] Fischer-Wolfarth JH, Farmer JA, Flores-Camacho JM, Genest A, Yudanov IV, Rösch N, Campbell CT, Schauermann S, Freund HJ, Particle-size dependent heats of adsorption of CO on supported Pd nanoparticles as measured with a single-crystal microcalorimeter, Physical Review B, 2010 Jun 30;81(24):241416.

[11] Shinn E, Hübler A, Lyon D, Perdekamp MG, Bezryadin A, Belkin A, Nuclear energy conversion with stacks of graphene nanocapacitors, Complexity, 2013 Jan;18(3):24-7.

[12] Elishakoff I, Dujat K, Muscolino G, Bucas S, Natsuki T, Wang CM, Pentaras D, Versaci C, Storch J, Challamel N, Zhang Y, Carbon Nanotubes and Nanosensors: Vibration, Buckling and Balistic Impact, John Wiley & Sons; 2013 Mar 4.

[13] Lyon D, Hubler A, Gap size dependence of the dielectric strength in nano vacuum gaps, IEEE Transactions on Dielectrics and Electrical Insulation, 2013 Aug 2;20(4):1467-71.

[14] Saini R, Saini S, Sharma S, Nanotechnology: the future medicine, Journal of cutaneous and aesthetic surgery, 2010 Jan;3(1):32.

[15] Shin MD, Shukla S, Chung YH, Beiss V, Chan SK, Ortega-Rivera OA, Wirth DM, Chen A, Sack M, Pokorski JK, Steinmetz NF, COVID-19 vaccine development and a potential nanomaterial path forward, Nature nanotechnology, 2020 Aug;15(8):646-55.

[16] Medhi R, Srinoi P, Ngo N, Tran HV, Lee TR, Nanoparticle-based strategies to combat COVID-19, ACS Applied Nano Materials, 2020 Aug 26;3(9):8557-80.

[17] Yao S, Swetha P, Zhu Y, Nanomaterial-enabled wearable sensors for healthcare, Advanced healthcare materials, 2018 Jan;7(1):1700889.

[18] Rao CR, Kulkarni GU, Thomas PJ, Edwards PP, Metal nanoparticles and their assemblies, Chemical Society Reviews, 2000;29(1):27-35.

[19] W. Luther (ed.), Industrial application of nanomaterials-chances and risks, Future Technologies Division-VDI Technologiezentrum, Dusseldorf, 2004.

[20] https://sites.google.com/site/nanomodern/Home/CNT/syncnt/cvd

[21] Puurunen RL, Surface chemistry of atomic layer deposition: A case study for the trimethylaluminum/water process, Journal of applied physics, 2005 Jun 15;97(12):9.

[22] George SM, Yoon B, Dameron AA, Surface chemistry for molecular layer deposition of organic and hybrid organic− inorganic polymers, Accounts of Chemical Research, 2009 Apr 21;42(4):498-508.

[23] George SM, Atomic layer deposition: an overview, Chemical reviews, 2010 Jan 13;110(1):111-31.

[24] Puurunen RL, Vandervorst W, Island growth as a growth mode in atomic layer deposition: A phenomenological model, Journal of Applied Physics, 2004 Dec 15;96(12):7686-95.

[25] Ritala M, Leskelä M, Rauhala E, Haussalo P, Atomic layer epitaxy growth of TiN thin films, Journal of the Electrochemical Society, 1995 Aug 1;142(8):2731.

[26] Ritala M, Leskelä M, Rauhala E, Jokinen J, Atomic layer epitaxy growth of TiN thin films from Til4 and NH 3, Journal of the Electrochemical Society, 1998 Aug 1;145(8):2914.

[27] http://www.semicore.com/what-is-sputtering.

[28] https://www.jeol.co.jp/en/science/eb.html.

Chapter 2: Nanoparticle based Strain Sensors and Nanoparticles' Layer Conductivity

2.1. Sensors

As a sensor, we define the device that has the ability to detect a signal and convert it into a measured quantity. Each sensor consists of two main parts; the converter, which converts the received signal into an electrically measurable signal, and the drive circuit that converts the converter signal into a fixed electrical signal, amplifies and modifies it according to the sensor applications. An important role in choosing the right sensor are its features, environment and the application in which it will be used.

These characteristics are determined by the size that is being measured and the output signal of the sensor. There are two main categories of static and dynamic characteristics. Each application requires the selection of the sensor with the best response to the desired characteristics. The static characteristics of the sensor apply when the system of the size being measured and the sensor are in equilibrium, i.e. the sensor does not detect any measurable change. These features are:

- **Accuracy:** Accuracy is the deviation of the actual value of the measured quantity from the value given by the sensor. Accuracy can be expressed as absolute value of the measurement error either as a percentage of the input scale or as a percentage of the output scale.
- **Sensitivity:** Sensitivity indicates the response of the sensor to a given change in magnitude. It is equal to the ratio of the sensor response to the amount of substance being measured. Similarly, cross-sensitivity refers to the contribution of other, undesirable parameters that affect the sensor response.

  Reliability: Reliability of a sensor is the sensor's ability to meet technical specifications when used in applications under specified conditions. It expresses the stability and validity of the sensor output signals. In addition, it is how the operating time of the device is referred as.

- **Repeatability:** Repeatability of a sensor determines the sensor's ability to give the same value for each measurement when the quantity being measured does not change.
- **Range:** Range of a sensor shows us the minimum and maximum value the sensor can measure.
- **Hysteresis:** Hysteresis expresses the deviation of the output value for a specific value of the input signal when the direction of change in the input is reversed. The error generated this way affects the accuracy of the device. Factors that cause hysteresis

are usually friction, mechanical stress and change the structure of the materials under use.

- **Dead zone:** Dead zone is the maximum range of input values for which the output value does not change.
- **Threshold:** Threshold is the minimum value of the input signal for which the output signal of the sensor is non-zero.
- **Resolution:** Resolution is defined as the required minimum change of the input signal in order to change the output signal of a sensor.
- **Reversibility:** Reversibility in the dependence of the sensor response on its previous exposure to analyzers.
- **Selectivity:** Selectivity is defined as the ability of a sensor to respond primarily to a single stimulus in the presence of different stimuli.
- **Limit of Detection (LOD):** The LOD associated with the lowest concentration of an analyzer that can be detected.
- **Response:** Response time usually refers to the time it takes for a sensor to reach 70% of its constant value.

In addition to the static characteristics of the sensor that only make sense when the sensor does not detect any change, i.e. when the system is in equilibrium, there are also dynamic characteristics that play important role when the input signal varies**.** In that case, we take into account the dynamic characteristics, which are determined by the response of the sensor depending on the input signal.

According to the above mentioned the optimal operation of a sensor is achieved when its characteristics receive ideal values, like instant response, infinite range etc. In practice, however, an ideal sensor cannot be constructed since there are parameters -such as construction defects, the operating environment, various parts of the circuit etc. - that make it impossible. Therefore, what is sought is the best possible approach to ideal values by improving some features that causing the alteration of the output signal. Some of them are the lack of linearity, the small operating range, therefore limited measurement range and low sensitivity, the noise, which conveys incorrect information and is included in the output signal and many others.

The rapid development of nanotechnology during the last decade combined with the extremely interesting properties of nanomaterials have resulted in the improvement of the values of the features mentioned above as well as in their wide range of applications. Nanotechnology has become a top priority in the field of research in most developed countries of the world and finds applications not only in the established and traditional fields of microelectronics but penetrates to new ones such as nanomedicine. This is due to the extremely small size of the structures but also due to the continuously development of research in the field of materials, which allows the creation of structures with better resistance and less probability to quickly wear out due to the operating environment and time. More specifically, nanotechnology products are used in microelectronics, composite tires, photographic materials,

dyes, cosmetics, dental materials, detergents, scientific instruments and dozens of other applications [1].

2.2. Sensors types

All sensors can fall into two broad categories: passive and active. Passive are the sensors that do not need any additional power source to operate, as they have the ability to convert the input energy caused by an external stimulus into an output signal. Typical examples of passive sensors are thermocouples, photodiodes and piezoelectric sensors. In contrast to passive sensors, active sensors require a power supply for their operation, which is called an excitation signal. This signal is converted by the sensor to an output signal. For example, a thermistor is a heat-sensitive resistor, which does not in itself, generate an output signal, but, if an electric current passes through it, we can measure the value of the resistance by calculating the change in current and voltage.

The most common classification of sensors used is based on the form of energy transmitted by the signal, so the main categories of sensors are:

i. Mechanical
ii. Thermal
iii. Magnetic
iv. Radiation sensors
v. Optical
vi. Chemical
vii. Biological

i. Mechanical sensors consist of a mechanical structure, which is being deformed and allows us to measure a physical size. The main quantities we can measure are strain, speed, acceleration, elasticity, deformation, torque, etc., while the most common structures used are diaphragms, membranes and floating discs. The deformation of the structure is usually caused due to mechanical voltage, static electricity, temperature, pressure, etc. [2].
ii. Thermal sensors convert thermal energy into a corresponding amount of electricity that can be processed and measured. They are classified into two categories depending on their output signal: electrical and non-electrical. The first category includes thermocouples, thermistors, circuit breakers, etc. whereas the second category, the non-electric ones include thermometers, fiber optic thermal sensors, surface acoustic wave sensors, etc. [3].
iii. Magnetic sensors convert the change in magnetic field into an electrically measurable signal. They are classified according to their principle of operation into quantum cells capable of detecting extremely weak fields, acoustics based on the modification of the acoustic characteristics of a magneto-elastic material in the presence of an external magnetic field, exploiting the Hall Effect [4].

iv. Radiation sensors detect radiation that is not perceived by the naked eye. This is being achieved by converting the radiation incident into electricity. They are classified into two categories: nuclear energy sensors and nuclear particle sensors. The former detect electromagnetic radiation such as X and γ rays and the latter have the ability to detect particles emitted by a radioactive material such as particles α and β, neutrons and protons [3].

v. Optical sensors use fiber optics or integrated optics and offer high sensitivity and short response times. The bio/ chemical- optical conversion level (converter) provides selectivity since the measurable quantity is chemically selective. The desired physical properties of the inverter are speed, small size and cost, safety, portability or remote control (depending on the application).

vi. Chemical sensors are devices that have the ability to convert a chemical change into an electrically measurable signal. The structure of a typical chemical sensor consists of a selective detection medium, which has the ability to detect the substance under detection, a transducer that will detect the change caused by the analyzer and convert it into an electrical signal. The analyzer is usually in a liquid or gaseous phase and is usually surrounded by other substances. The possible applications of chemical sensors cover a huge range.

vii. Biological or biosensors are chemical detectors that take advantage of the high selectivity and sensitivity of biologically active materials. More specifically, a biosensor is an analytical tool consisting of biologically active material, in combination with a biochemical signal converter into an electrical signal. The high market demand for such sensors has fueled the development of related sensor technologies. In other words, biosensors are small-sized devices that use bio-recognition to detect analytes. To simplify, a biosensor is an analytical device that can convert a biological response into an electrical signal. It consists of three parts: the receptor, which is usually a biological molecule, the transducer, which is in contact with the receptor and the electronic part.

2.3. Conventional strain sensors

The deformation and consequently the change in the dimensions of an object are measured by resistance sensors, which are based on a silicon substrate or a polymeric flexible substrate. Silicon, due to its good mechanical properties, was proposed from a very early [5] as a material in the wider family of mechanical sensors for measuring various quantities, such as pressure, force and acceleration. A common principle of operation of all mechanical sensors is the change of the electrical resistance of the material during the application of mechanical voltage (e.g. during the bending of the substrate).

In a metal conductor of length *l*, square cross section *S* and resistivity *ρ* the resistance is given by the equation:

$$R = \rho \frac{l}{s} \tag{2.1}$$

Assuming that the initial length of the conductor l_o changes by an elementary difference *∂l*, its initial resistance R_o will change by:

$$\partial R = \rho \frac{\partial l}{s} - \rho \frac{l \partial s}{s^2} + \partial \rho \frac{l}{s} \tag{2.2}$$

The differential elementary change, ignoring the change of *p*, with respect to the initial resistance will be:

$$\frac{\partial R}{R} = \frac{\partial l}{l} - \frac{\partial s}{s} \rightarrow \frac{\Delta R}{R_0} = \frac{\Delta l}{l_0} - \frac{\Delta s}{s_0} \tag{2.3}$$

If we consider that the cross section decreases with the simultaneous increase of length *l* due to Poisson effect, the final cross-sectional area will be:

$$S = (1 - \nu\varepsilon)^2 S_0 \tag{2.4}$$

Where ν is the Poisson ratio and ε the strain, which defined as $\varepsilon = \frac{l - l_0}{l_0}$. The equation (2.3) becomes:

$$\frac{\Delta R_0}{R_0} = \varepsilon - (1 - \nu\varepsilon)^2 + 1 \tag{2.5}$$

$$\frac{\Delta R}{R_0} \sim (1 + 2\nu)\varepsilon \rightarrow \frac{\Delta R}{R_0} \sim g\varepsilon \tag{2.6}$$

Where *g* is a constant which expresses sensitivity and is called a gauge factor. In this simplified example the change in resistance, which represents the output signal, is directly proportional to the strain *ε* of the sensor, which represents the input signal. This is the principle of operation of the first commercial metal sensors. To this day, usually, a thin layer of metal alloy (e.g. copper-nickel, nickel-chromium) in the form of a meander, built on a flexible substrate (Fig. 2.1) is the

sensor device, the change in resistance of which translates into a deformation value. The sensitivity factor g of such a sensor is about 2 to 4 and its resistance ranges to a few hundred Ω. Strain is measured in micro-strains (10^{-6}). Flexible substrates are used to detect deformations from 0.001% to 4% (40000 $\mu\varepsilon$).

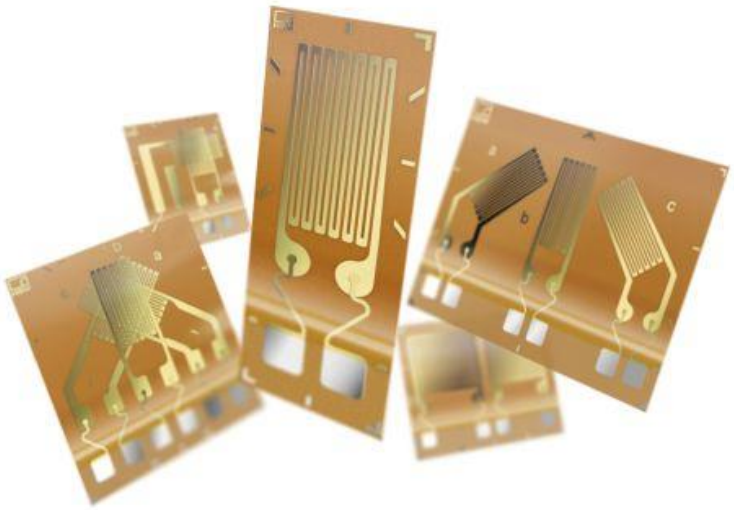

Figure 2.1: Flexible resistive strain sensors (Durham Instruments)

Another category of commercial deformation sensors are the semiconductors sensors. In a semiconductor with a specific impurity density of *N*, the imposition of deformation results in a change in the current of the conductivity carriers. In micromechanical sensor devices is being used silicon and germanium, due to the existing conventional silicon technology and their good mechanical properties. In particular, monocrystalline silicon does not lag in deformation up to 3000 $\mu\varepsilon$ and has a linear stress-strain relationship. The change in the resistivity of the semiconductor is given by the equation:

$$\frac{\Delta\rho}{\rho} = \Pi_{ij}\varepsilon_{ij}E \tag{2.7}$$

Where Π_{ij} is the tensile strength of the piezoelectric resistance coefficient, ε_{ij} is the tensile strength of the deformation and *E* is the Young elastic measure of the material. The piezoelectric resistance coefficient depends on the crystal structure. In the case of crystalline silicon, if only the carrier current in the direction parallel to the axis of the deformation is taken into account, then from equations (2.2), (2.3) and (2.7) it follows that:

$$\frac{\Delta R}{R_0} = (1 + 2\nu + \Pi_L E)\varepsilon_L \tag{2.8}$$

Where Π_L is the piezoelectric resistance coefficient in the direction parallel to the strain ε_L. Monocrystalline and polycrystalline silicon with donor (n-type) or recipient (p-type) implant is used as a deformation sensor. The sensitivity factor of such a sensor is around 150 and therefore semiconductor sensors are able to detect much smaller strains, of the order of 0.001 $\mu\varepsilon$, when compared to metal sensors. The maximum deformations that can be detected are of the order of 3000 $\mu\varepsilon$ (0.3%) due to their fragility, a value that depends on the thickness, the quality of the crystal and the measure of elasticity. The resistances of such sensors range from about 100 Ω to 10 kΩ. As the impurity concentration and temperature increases, the sensitivity of the sensor decreases to an impurity density of 10^{19} cm^{-3}. For silicon with N> 10^{20} cm^{-3} the sensitivity is constant, independent of strain and temperature. On the other hand, at increased impurity concentrations the sensitivity is lower and the contribution of the thermal resistance coefficient increases.

Semiconductor strain sensors are suitable for measuring very small strains as they produce a lower signal-to-noise ratio, thus leading to better resolution than metallic sensors. One of their disadvantages, however, is that they are more sensitive to temperature. The output signal of the strain sensors is usually measured by means of a Wheatstone bridge, based on which one or more of the bridge resistors are the sheet metal or the semiconductor plate and thus the contribution of the temperature change to the measured signal is corrected. Micromechanical structures with silicon in the form of cantilever, bridge, etc. are used in acceleration, pressure and force sensors [6, 7]. An example of a force sensor is a silicon cantilever that deforms according to the roughness of a surface and is applicable to atomic force microscopy [8].

2.4. Nanoparticles based strain sensors

2.4.1. Nanoparticles' layer electrical conductivity

Nanoparticles are units of matter consisting of a few thousand atoms, depending on their size, which are either naturally created or artificially made. Examples of natural formation of nanoparticles are the particles contained in volcanic ash and particles produced during chemical reactions of water or the wider environment (chemical weathering) with mineral rocks and the consequent formation of clays and other compounds. Elsewhere, nanoparticles are also produced by human activity, such as oil burning and ore mining. Engineered nanoparticles are widely used nanomaterials that due to their unique properties, have a variety of applications in various fields of science, but also in everyday life, where they are found in commercial industrial products.

Nanoparticles, due to their large surface to volume ratio, exhibit different optical, electronic, chemical and mechanical properties from macroscopic materials. One of their features, for example, is their large contact surface, which results in the use of noble metal nanoparticles as

reinforced catalysts and the chemical modification of their surface to detect molecules in sensor devices. Conductivity in a metal nanoparticle structure, such as a two-dimensional lattice or a nanowire, is of great interest, as critical quantum conductivity phenomena occur that do not occur in a continuous material. The following are various approaches of classical and quantum theory based on the experimental study of the literature of transfer of charge in such structures.

In the classical conductivity model, electrons travel through the material as particles that are scattered by the lattice oscillations of the metal. In case of the nanoparticles coming into contact, forming a continuous conductive path, the electrons are scattered due to different crystalline levels of the nanoparticles. When the nanoparticle size decreases considerably, the elastic scattering strongly contributes to the conductivity, as the mean free path between two successive scatterings is larger than the nanoparticle size, causing the electrons to travel a shorter path before scattering at the edge of the nanoparticle or the thin film.

Two charge scattering models have been proposed for the scattering of electrons in thin polycrystalline metal films or nanowires [9, 10]. According to the model of Fuchs and Sondheimer [11, 12] who experimentally calculated the resistivity of thin films Al and Sn, when the thickness of a metal film is comparable to the mean free path *l* of the macroscopic material, then a percentage of the electrons are subject to diffusive scattering at the film border. Therefore, the passage of the load becomes more difficult and the resistivity increases. Later, the Mayadas and Shatzkes [13, 14] proposed the model of "specular scattering" of electrons at grain boundaries in a polycrystalline film[7]. Therefore, as the film thickness or width of a nanowire or nanoparticle agglomerate decreases, the discrete grains that make up the material increase and their average size decreases, making it comparable to or less than *l* and therefore its resistivity hardware is growing. According to the model of the Mayadas and Shatzkes, the resistivity of the material will be given by the following equation:

$$\rho = \frac{\rho_0}{3(\frac{1}{3} - \frac{a}{2} + a^2 + a^3 \ln(\frac{1}{a} + 1))} \tag{2.9}$$

Where:

$$a = \frac{lR}{D_{50}(1-R)} \tag{2.10}$$

[7] The two terms for scattering are borrowed from Optics.

R is the reflection coefficient of the electrons at the grain boundaries and D_{50} is the mean grain diameter.

The above two approaches seem to satisfactorily explain the electrical properties of Au and Cu nanowires depending on their thickness and width. In addition, in the work of Durkan *et al*. [9] and Huang *et al.* [10], is suggested that the specific resistance to thin films depends on the mean free path, thickness and width of the film, the percentage of electrons scattered at the grain interface and the average grain size. As a result, the conductivity at absolute zero is lower (and therefore the resistivity is higher) in the case of nanoparticles, as temperature-independent elastic scattering due to scale effects strongly contribute. It is reported that the specific conductivity values of nanoparticle films have been measured lower than the values of continuous materials for various metals, such as gold and silver [15 - 17]. For example the specific conductivity of Au nanoparticle films has been found to range from 10^{-1} Ω^{-1}cm to $2.5 \cdot 10^{-4}$ Ω^{-1}cm, in relation to the specific conductivity of bulk Au which is so = $4.5 \cdot 10^{-4}$ Ω^{-1}cm .

2.4.2. Tunneling effect

When the arrangement of nanoparticles in space is such that their inter-particle distances are large (e.g. several nm) then the resistance of the nanoparticle film is very high, as the charge cannot be propagated in the vacuum between two nanoparticles. However, when the nanoparticles are very close, at a distance of 1-2 nm, then there is a chance that an electron will be transferred from one nanoparticle to another through a tunneling effect. If we approach two adjacent metal nanoparticles, as electrodes with distance *s*, between which a dielectric means with dielectric constant ε_r is inserted and there is a potential barrier *U*, then the energy diagram of the two nanoparticles will be given as in Fig. 2.2.

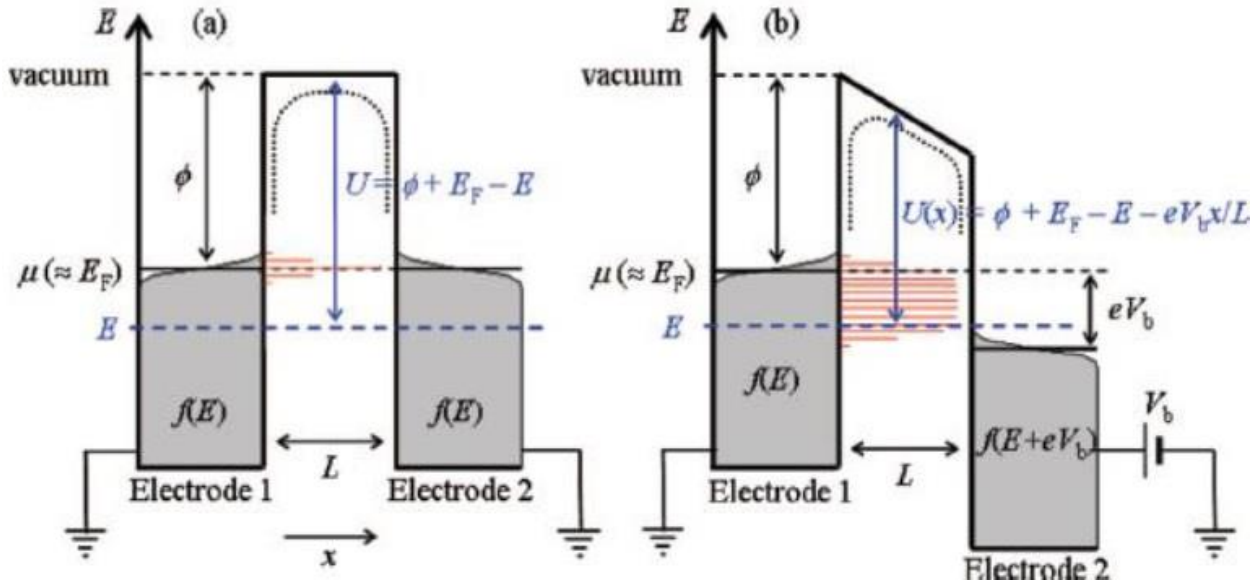

Figure 2.2: Energy diagram of metal electrodes (a) without and (b) with the application of external potential difference [18].

The barrier potential is given by the equation:

$$U = \varphi_m + E_F - E \tag{2.11}$$

Where φ_m is the metal extraction energy, E_F is the Fermi level energy and E is the electron energy. Every dielectric medium gives an electron affinity x term of the medium, which lowers this potential barrier but is ignored at first glance (e.g. for absolute vacuum x = 0). The probability distribution of an energy level E to be occupied by the electron at one electrode and empty at the other, so that tunneling will occur is *f (E)(1-f (E)),* where *f (E)* the Fermi-Dirac distribution of the probability of occupying an energy level E.

$$f(E) = \frac{1}{1 - e^{(E-\mu)/kT}} \tag{2.12}$$

The application of an external potential difference V_b to the two electrodes will result in the displacement of the electrode energy stations and the modification of the potential barrier [Fig. 2.2 (b)], which in a first approach is given as follows:

$$U(x) = \varphi_m + E_F - E - \frac{eV_b x}{s} + \varphi_{image} \tag{2.13}$$

The image charge potential φ_{image} is a contribution taken into account by the Simmons' model [19], according to which, when the electron leaves the electrode, it charges it, inducing a virtual opposite charge that exerts a force on the electron. The total potential is approximated by an average value given by the following equation.

$$\overline{U} = \frac{1}{s}\int_0^s U(x)dx \tag{2.14}$$

Due to the finite probability of an electron from the Fermi level will penetrate the potential barrier and be at the Fermi level of the neighboring electrode, there is a current of electrons from the electrode at the lowest potential to the electrode at the highest potential, as well as a current in the opposite direction. The tunnel current results from the subtraction of the two currents and is given by the equation:

$$I_t = \frac{4\pi e}{\hbar}\int_0^{+\infty} \rho(E)\rho(E + eV_b)|T(E)|^2[f(E) - f(E + eV_b)]dE \quad (2.15)$$

Where *ρ(E)* and *ρ(E + eV$_b$)* are the state densities at the energy level E in a nanoparticle and at the energy level *E + V$_b$* in the adjacent nanoparticle with the highest potential respectively.

$$|T(E)|^2 \sim e^{-2\kappa s} \quad (2.16)$$

Where T(E) is the probability of passing through a tunnel, which depends exponentially on the distance s and the damping constant κ given by the equation:

$$\kappa = \sqrt{\frac{2m_e\bar{U}}{\hbar^2}} \quad (2.17)$$

For energy values *E* very close to the Fermi level and low *eV$_b$* ≪*E$_F$* values, equation (2.15) is simplified to the following equation:

$$I_t = \frac{4\pi e}{\hbar}\rho(E_F)^2|T(E_F)|^2\int_0^{+\infty}[f(E) - f(E + eV_b)]dE = GV_D \quad (2.18)$$

Where:

$$G = \frac{4\pi e^2}{\hbar}\rho(E_F)^2|T(E_F)|^2 \quad (2.19)$$

Where G is the conductivity of the tunnel effect for very low values *V$_b$*. From the above it ensures that the specific conductivity of a tunnel between two nanoparticles follows the dependence

$$\sigma \propto \exp(-\beta s) \quad (2.20)$$

Where $\beta=2\kappa$ is the electron coupling term. Tunnel conductivity is independent of temperature.

The surfaces of chemically prepared nanoparticle films have molecular chains that bridge the nanoparticles together, keeping them at a distance. In this case, the constant β depends on the type of molecule and the size of the nanoparticle, as usually the potential barrier is lower than in the "naked" nanoparticles, due to the energy gap of each molecule that forms the barrier. This results in β being smaller and therefore the tunnel current through these intermediate molecules being larger. Additional contributions to the potential barrier come from the potential corresponding to the electron space charge and the electron exchange-correlation potential. The latter relates to the electron-to-electron interaction that occur based on the theory of the existence of a particle in an electron cloud [20]. According to Zheng[21], the contribution of these last two terms to the tunnel current calculation results in a different tunnel current calculation than that predicted by the Simmons' model, and thus a new self-consistent model is introduced (Self Consistency Model, SCM). It should be noted here that the Simmons' model applies to parallel electrode plates, while to spherical electrodes it applies when $s << r$, with r being the radius of the electrodes. For applied potential $V_b < 1$ and range s 1 nm, the Simmons' model satisfactorily calculates the tunnel current, but in the range of the highest values V_b, $1 < V_b < 10$ V, the estimation of the contribution of the two potentials predicts a larger tunnel current (approximately 1 class larger), although the Simmons' model [19] is still accurate. Conversely, in the range $V_b > 10$ V, the Simmons' model cannot be applied and the SCM must be taken into account. It is also reported that for s < 1 nm (sub-nanometer junctions) the SCM model gives more accurate results.

2.4.3. Electron charge phenomena-conductivity with Arrhenius dependence

The transfer of an electron to a metal nanoparticle requires the supply of a quantity of energy to charge the neutral nanoparticle and consequently create a hole in the original nanoparticle. This charge is equivalent to a potential barrier that the electron must overcome, the so called the Coulomb blockade. At temperatures above absolute zero, the electron has a finite amount of thermal energy, which allows it to jump the Coulomb barrier as the thermal energy exceeds the potential value. This required energy is also called activation energy. As stated in the work of Abeles et al. [22], which is based on the work of Neugebauer and Webb [23], the phenomenon of charging between adjacent nanoparticles with random sizes and interparticle distances can be approached with a simplified model. According to the model, adjacent nanoparticles are a continuous metal electrode which surrounds a "central" nanoparticle of radius r, while they are separated by a distance s and an insulating means with dielectric constant εr (Fig. 2.5).

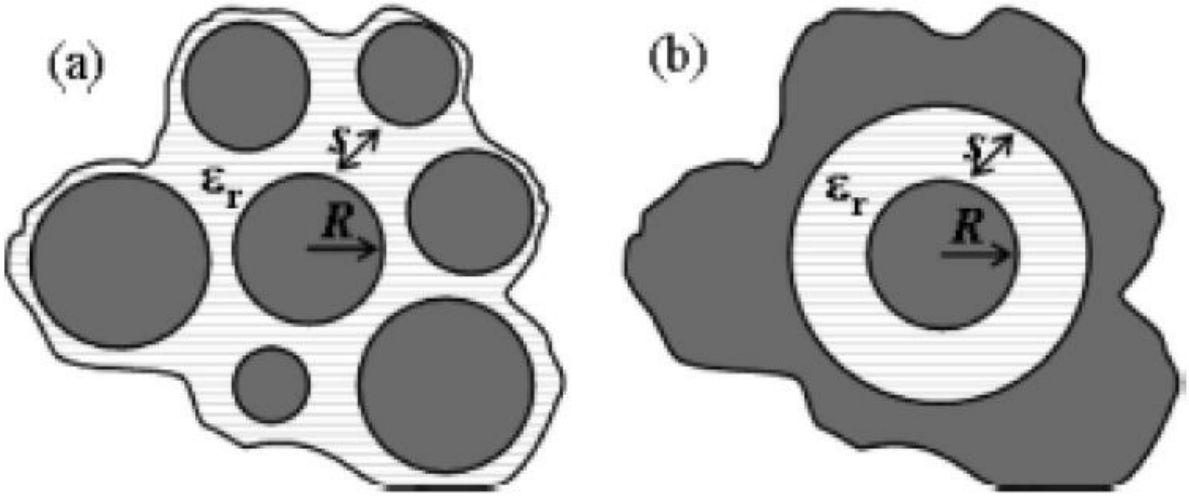

Figure 2.3: a) Distribution of nanoparticles at random distances from each other, (b) Simplified charge model in which the nanoparticle is surrounded by a continuous electrode representing its adjacent nanoparticles. In the shapes R is the radius r of the nanoparticle [22].

The charge energy of the nanoparticle is given by the equation:

$$E_C = \frac{e^2}{2C} \tag{2.21}$$

Where *C* is the capacitance of the nanoparticle given by the equation:

$$C = 4\pi\varepsilon_0\varepsilon_r\left(\frac{1}{r} - \frac{1}{r+s}\right)^{-1} \tag{2.22}$$

Therefore, the equation (2.21) is completed through:

$$E_C = \frac{e^2}{8\pi\varepsilon_0\varepsilon_r}\left(\frac{1}{r} - \frac{1}{r+s}\right) \tag{2.23}$$

From equation (2.23) it occurs that the activation energy is inversely proportional to the radius and the interparticle distance, as well as to the relative dielectric constant of the medium. Therefore, the smaller the particle size of the charge energy, the less energy is required to charge the particle electrostatically. Based on this result, the model of the thermally activated tunnel effect was proposed, according to which the specific conductivity of a set of nanoparticles depends on the probability of the electrons passing through a tunneling effect and the probability of the Coulomb barrier jumping in relation to the thermal state of the system. The model can be summarized in the following equation:

$$\sigma = \sigma_0 e^{-\beta s} e^{-\frac{E_C}{kT}} \tag{2.24}$$

Where σ_0 is an exponential constant. The energy diagram of the thermally activated tunneling is demonstrated in Fig. 2.6 (a).

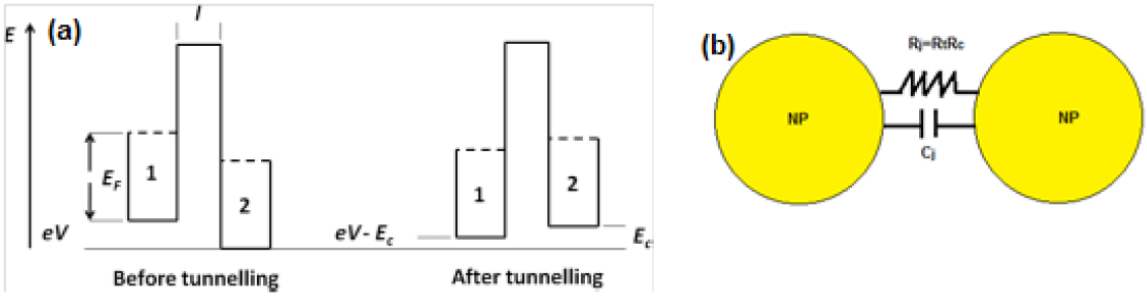

Figure 2.4: (a) Energy diagrams in a tunneling contact between particles 1 and 2 before and after tunneling. (b) Equivalent circuit in tunneling contact [24].

The dependence of conductivity on temperature follows an Arrhenius equation:

$$ln\sigma \propto -\frac{1}{r} \tag{2.25}$$

Where the conductivity, due to Coulomb barrier effect, increases because of temperature. This results by the fact that electrons, with increased temperature, are statistically more likely to jump the Coulomb barrier between nanoparticles, due to their thermal energy. In this case, the temperature behavior of the conductivity differs from the classical theory of metals, in which the conductivity decreases when the temperature (and the resistance) increases as a result of the scattering with the phonons of the grid of the material. Thus the equivalent circuit between two nanoparticles consists of a resistor and a capacitance connected in parallel [Fig. 2.4 (b)].

This model is temperature dependent and as mentioned below (pp.), there are different temperature ranges. Moreover, it can presented various conductivity mechanisms, depending on the structure of the nanoparticle film. As can be deduced from equation (2.24), when the

thermal energy of the electrons $\sim kT$ becomes comparable to the charge energy, the term $exp(-(E_C)/kT)$ contributes significantly as the electrons have sufficient energy to overcome the Coulomb barrier and the current rises. This is also manifested by the current-voltage relationship $I(V)$(2.26). From experimental studies of nanoparticle structures [25 - 28] a law of power law in the current-voltage relationship has emerged empirically, which is summarized into the following equation:

$$I \propto (V - V_t)^{\zeta} \tag{2.26}$$

Where $V_t = \alpha N E_c$ is the value of the threshold voltage [29] with α a parameter that depends on the dimensionality and geometry of a system and N the number of particles that create a conductive path from one electrode to the other. The parameter ζ usually takes values from 2 to 3.5 and depends on the dimension of the system. The above relationship can be explained by the fact that due to the Coulomb barrier there is a critical threshold voltage above which the electron has a sufficient amount of energy to jump over the barrier. Theoretically, below this voltage the current is zero for $T = 0$, as the electrons have no available thermal energy, while a threshold voltage value is required that will provide them with this energy. At a temperature $T > 0$ there will always be a current due to tunneling effect and Coulomb effect, as some electrons will be able to statistically overcome the barrier. As the temperature increases the contribution of the second mechanism will become more significant. In addition, the value of V_t depends on the temperature, as with the temperature increase, the electrons require a lower threshold voltage because of the increased thermal energy.

2.4.4. Conductivity phenomena with deviation from Arrhenius dependence

Experimental demonstration of conductivity mechanisms that deviate from Arrhenius dependence on nanoparticle films has led to the formulation of other conductivity models to explain these deviations. These discrepancies seem to have their origin in the deviation of the shape, size and inter-particle distances of the metal nanoparticles that the films actually present. Consequently, the dispersion of the charge energy values and its modification over different temperatures. Conductivity-temperature dependence can be described by the following equation [18]:

$$\sigma \approx \exp(-(\frac{T_0}{T})^{v}) \tag{2.27}$$

Where T_0 is a constant and v is a parameter that takes values from 0 to 1. In the case where $v = 1$, the relation (2.27) expresses the Arrhenius dependence, while in several cases the dependence with $v = 1/2$, [30 - 32]. The latter usually has been observed - in lower ambient

temperatures. In the latter case, it has been proposed the model of electron jumping (hopping) based on Mott's model [33] for energy charge transitions in impurity semiconductors. According to Mott's model, there is a probability that a charge in the E_i energy state with the appropriate thermal energy will jump to another point on the grid at a higher E_j energy state.

2.4.5. Random resistor nanoparticle networks.

A different approach to explain conductivity models with ν = ½ is to consider nanoparticle sets as random networks resistors. Based on this approach any pair of nanoparticles can be considered to be a resistance:

$$R_{ij} = R_0 e^{2ks_{ij}} e^{E_{ij}/k_B T} \tag{2.28}$$

Where s_{ij} is the distance between them and E_{ij} is the activation energy. Variations and changes in the distance between particles and activation energy results in subsequent large changes in resistance. The resistance of the nanoparticle network in this case can be estimated considering that a path of minimal resistance develops in the nanoparticle film. Such a path can be found if for a random resistance R, we consider that two nanoparticles are connected only if the $R_{ij} < R$ and also suppose that the portion of the bound nanoparticles is ρ. If R is too small then a very small portion of nanoparticles are bonded and therefore when $R \rightarrow 0$ and $\rho \rightarrow 0$. As R increases so does ρ. When R tends to infinity all the nanoparticles are connected and $\rho \rightarrow 1$. Hence, there is a critical value of the R_C resistor, for which the connected particles form a conductive chain or path of least resistance through the film. The amount of bonded nanoparticles when R is made R_C, corresponds to the limit of percolation, ρ_C. The ρ_C is a characteristic of nanoparticles' network and depends only on geometric characteristics. To estimate R_C one must know the distribution of R_{ij} resistors. If the distribution is declared as $f(R_{ij})$ then R_C is given by:

$$\int_0^{R_C} f(R_{ij}) dR_{ij} = \rho_C \tag{2.29}$$

2.5. References

[1] Donaldson K, Stone V, Tran CL, Kreyling W, Borm PJ, Nanotoxicology, 2004, 727-8.

[2] Elwenspoek M, Wiegerink R, Wiegerink RJ, Mechanical microsensors, Springer Science & Business Media, 2001 Jan 12.

[3] Sinclair I R, Sensors and Transducers, 2001.

[4] Hara T, IEEE Trans. On Electron Devices, 2000, Vol. 87.

[5] Petersen KE, Silicon as a mechanical material, Proceedings of the IEEE, 1982 May;70(5):420-57.

[6] Brugger J, Buser RA, De Rooij NF, Silicon cantilevers and tips for scanning force microscopy, Sensors and Actuators A: Physical, 1992 Sep 1;34(3):193-200.

[7] Tai YC, Muller RS, Integrated stylus-force gauge, Sensors and Actuators A: Physical, 1990 Jun 1;22(1-3):410-3.

[8] Borky JM, Wise KD, Integrated signal conditioning for silicon pressure sensors, IEEE Transactions on Electron Devices, 1979 Dec;26(12):1906-10.

[9] Durkan C, Welland ME, Size effects in the electrical resistivity of polycrystalline nanowires, Physical review B, 2000 May 15;61(20):14215.

[10] Huang Q, Lilley CM, Bode M, Divan R, Surface and size effects on the electrical properties of Cu nanowires, Journal of Applied Physics, 2008 Jul 15;104(2):023709.

[11] Fuchs K, The conductivity of thin metallic films according to the electron theory of metals, InMathematical Proceedings of the Cambridge Philosophical Society, Cambridge University Press, 1938 Jan (Vol. 34, No. 1, pp. 100-108).

[12] Sondheimer EH, The mean free path of electrons in metals, Advances in physics, 2001 Sep 1;50(6):499-537.

[13] Mayadas AF, Shatzkes M, Janak JF, Electrical resistivity model for polycrystalline films: the case of specular reflection at external surfaces, Applied Physics Letters, 1969 Jun 1;14(11):345-7.

[14] Mayadas AF, Shatzkes M, Electrical-resistivity model for polycrystalline films: the case of arbitrary reflection at external surfaces, Physical review B, 1970 Feb 15;1(4):1382.

[15] Liu Y, Wang Y, Claus RO, Layer-by-layer ionic self-assembly of Au colloids into multilayer thin-films with bulk metal conductivity, Chemical Physics Letters, 1998 Dec 18;298(4-6):315-9.

[16] Musick MD, Keating CD, Lyon LA, Botsko SL, Pena DJ, Holliway WD, McEvoy TM, Richardson JN, Natan MJ, Metal films prepared by stepwise assembly, construction and characterization of colloidal Au and Ag multilayers, Chemistry of materials, 2000 Oct 16;12(10):2869-81.

[17] Wessels JM, Nothofer HG, Ford WE, von Wrochem F, Scholz F, Vossmeyer T, Schroedter A, Weller H, Yasuda A, Optical and electrical properties of three-dimensional interlinked gold nanoparticle assemblies, Journal of the American Chemical Society, 2004 Mar 17;126(10):3349-56.

[18] Zabet-Khosousi A, Dhirani AA, Charge transport in nanoparticle assemblies, Chemical reviews, 2008 Oct 8;108(10):4072-124.

[19] Simmons JG, Potential barriers and emission-limited current flow between closely spaced parallel metal electrodes, Journal of Applied Physics, 1964 Aug;35(8):2472-81.

[20] Kohn W, Sham LJ, Self-consistent equations including exchange and correlation effects, Physical review, 1965 Nov 15;140(4A):A1133.

[21] Zhang P, Scaling for quantum tunneling current in nano-and subnano-scale plasmonic junctions, Scientific Reports, 2015 May 19;5(1):1-1.

[22] Abeles B, Sheng P, Coutts MD, Arie Y, Structural and electrical properties of granular metal films, Advances in Physics, 1975 May 1;24(3):407-61.

[23] Neugebauer CA, Webb MB, Electrical conduction mechanism in ultrathin, evaporated metal films, Journal of Applied Physics, 1962 Jan;33(1):74-82.

[24] Aghili Yajadda MM, Calculating electronic tunnel currents in networks of disordered irregularly shaped nanoparticles by mapping networks to arrays of parallel nonlinear resistors, Journal of Applied Physics, 2014 Oct 21;116(15):153707.

[25] Parthasarathy R, Lin XM, Jaeger HM, Electronic transport in metal nanocrystal arrays: The effect of structural disorder on scaling behavior, Physical Review Letters, 2001 Oct 16;87(18):186807.

[26] Clarke L, Wybourne MN, Brown LO, Hutchison JE, Yan M, Cai SX, Keana JF, Room-temperature Coulomb-blockade-dominated transport in gold nanocluster structures, Semiconductor science and technology, 1998 Aug 1;13(8A):A111.

[27] Romero HE, Drndic M, Coulomb blockade and hopping conduction in PbSe quantum dots, Physical review letters, 2005 Oct 3;95(15):156801.

[28] Tran TB, Beloborodov IS, Hu J, Lin XM, Rosenbaum TF, Jaeger HM, Sequential tunneling and inelastic cotunneling in nanoparticle arrays, Physical Review B, 2008 Aug 26;78(7):075437.

[29] Middleton AA, Wingreen NS, Collective transport in arrays of small metallic dots, Physical review letters, 1993 Nov 8;71(19):3198.

[30] Sheng P, Abeles B, Arie Y, Hopping conductivity in granular metals, Physical Review Letters, 1973 Jul 2;31(1):44.

[31] Terrill RH, Postlethwaite TA, Chen CH, Poon CD, Terzis A, Chen A, Hutchison JE, Clark MR, Wignall G, Monolayers in three dimensions: NMR, SAXS, thermal, and electron hopping studies of alkanethiol stabilized gold clusters, Journal of the American Chemical Society, 1995 Dec;117(50):12537-48.

[32] Zabet-Khosousi A, Trudeau PE, Suganuma Y, Dhirani AA, Statt B. Metal to insulator transition in films of molecularly linked gold nanoparticles, Physical review letters, 2006 Apr 21;96(15):156403.

[33] Mott NF. Conduction in glasses containing transition metal ions, Journal of Non-Crystalline Solids, 1968 Dec 1;1(1):1-7.

[34] Éfros AL, Shklovskii BI, Coulomb gap and low temperature conductivity of disordered systems, Journal of Physics C: Solid State Physics, 1975 Feb 21;8(4):L49.

Chapter 3: Platinum Nanoparticle Based Flexible Strain Sensors

3.1. Introduction

As mentioned before, the vast areas of applications of flexible electronics [1, 2, 3-6, 7-10] caused a lot of interest during the last decades. The ever-growing research over the last decade focused especially on many novel nanomaterials, such as carbon nanotubes [11-13], nanowires [5, 14, 15], MoS2 [16], graphene [17] and nanoparticles (NPs) [6, 18-22]. In this study we will be mainly be focusing on nanoparticles and nanoparticle based sensors.

The main reason is the increased sensitivity of strain sensors based on NP films [19-21, 28], when compared to existing metal strain sensors that incorporate thin film technology [23]. In addition, the low processing temperatures required in the case of NP-based strain sensing devices, render them fully compatible with flexible substrate technology [24]. These qualities allows them to find new applications in healthcare [1, 4] and the development of electronic skin areas [4, 15, 25-27]. For this reason many research groups focus their interest on increasing the NP-based sensors' sensitivity. To achieve this they usually incorporate NP films with varying conductivities, so as to manipulate the charge transport mechanisms of the device [19, 20, 22, 29]. Lee et al [19], for example, studied the combination of metallic and insulated NPs as sensitive materials; by combining Au NPs, CdSe NPs and nanocracks. As a result a gauge factor of up to 5045 has been achieved. In the field of bio-inspired sensing devices, cracks have often been employed, so as to radically increase the sensor's sensitivity [19, 30-32]. In the study of Han et al [31], they created a crack-based strain-sensor by depositing Au NPs on top of a cracked PDMS substrate obtaining so a sensitivity of 5888. However, high sensitivities are also possible without cracks on the substrate. In the case of Shengbo et al [5] they combined Ag NPs and nanowires, achieving a sensitivity of up to 3766.

The above-mentioned studies focused on increasing the strain sensors' sensitivity by utilizing various NPs. This study is concentrated on strain sensors utilizing Pt NPs, which are fabricated on oxidized silicon substrates via the DC sputtering technique. While Pt NP sensors demonstrate an increased sensitivity [33], more recently, we have also investigated the means to protect them against humidity [34]. Zheng et al [35] have also manufactured nanoparticle-based flexible strain sensors using DC sputtering technique, highlighting their superior performance against the semiconductor gauges.

In this chapter we focus on the sensing properties of Pt NP sensors made on flexible polyimide substrates. Firstly, we discuss the sensor strain response up to 1.2% strain. To do so, we present a physical model to explain the observed increase of the g-factor with increasing strain. The model is compared with our data as well as with other results reported in the literature, such as the one of Xie et al [36]. In their study they manufactured Pd NPs-based strain sensors, using the sputtering technique and found that the g-factor is not a constant, but changes over the applied

strain range. The report of Lee et al [37] also reports non-linear behavior of their sensor based on silver NPs.

To this day, the majority of the attempts to model the behavior of strain sensors made by either naked or colloidal NPs are based on the physical model proposed by Herman et al. [28], which suggest directly applying it to the experimental data set or by applying minor modifications [36]. However, this approach does not take into account key aspects of straining flexible devices that employ solvent-free NPs. Contrary to a uniform elongation of solely inter-particle gaps, which existed prior to any strain (the case of cross-linked NPs), straining solvent-free NP-based devices results in the formation and rise of multiple new gaps that contribute in the exponential rise of device Resistance. The model we propose in this study is able to explain experimental differences, in terms of sensing performance observed between solvent-free (naked) NP strain sensors and cross-linked NP strain sensors [28] and therefore constitutes a better fit as far as solvent-free NP strain sensing data is concerned.

Secondly, the analysis is followed by a study of how the sensor responses in a humid environment. Humidity is known to influence the long-term behavior of NP strain sensors [38] and for that it was deemed crucial to investigate the relation and interaction between the two of them. The endurance characteristics of strain gauges on flexible substrates, based on cross-linked gold NPs after performing a large number of strain/relaxation cycles has also been reported by Ketelsen et al [39] in their 2018 study. However, during their tests there is no modification of the humidity environment taking place. As it has been proposed by Digianantonio et al. [40] using SAXS measurements, water molecules incorporated between nanoparticles result in a swelling of the NP film which increases the resistance of the nanoparticle network in a competitive way to the measured strain. As a result, it is crucial to investigate the effective way of protecting flexible strain sensors against humidity, as well as the effectiveness of the protection itself in increased strain (offered by the increased flexibility of the polyimide substrate).

Having that in mind, we evaluated the sensor's endurance in repeated mechanical stress under varying environmental conditions, i.e. R.H.; naked (with no ALD coating) as well as alumina-coated strain sensors (alumina coatings of 5.5 and 11 nm in thickness) were submitted to "fatigue experiments" (undergone multiple strain cycles: 1000 cycles of 0 to 1.2% strain), so that we could evaluate possible alumina degradation. The ability of such coatings to retain their protective properties against humidity and strain/fatigue was determined by monitoring device resistance in various case scenarios, while R.H. has been modified between two extreme values (10%-70%).

Our model is equally applied to alumina-coated and uncoated NP networks (both before and after the endurance experiments), which indicates the universal appliance to solvent-free NP-based strain sensors as well as its validity of it, even after operating the sensors in extreme conditions. An optimized device, suitable for a wide range of demanding applications (e.g. e-skin etc.), was eventually produced while, at the same time, a novel physical model brought new insight to the physical properties of solvent-free NP-based strain sensors.

3.2. Sensors Fabrication

To explain the method used during our experiment it is necessary to describe the materials used as well as the environmental conditions under which the experiment took place. First of all, every fabrication experiments was conducted at room temperature. Sigma Aldrich supplied all chemical reagents used during the study.

Throughout our experiments we used polyimide sheets with a mean thickness of 120 μm and a surface roughness of 0.7-0.8 nm as deposition substrates. Prior to any processing, the abovementioned polyimide substrates were cleaned using IPA, DI water and ultra-sonication. On top of the polyimide substrates were patterned gold interdigitated electrodes (IDEs) via optical lithography and the e-gun technique: firstly a thin titanium layer (approximately 4 nm) was deposited using a deposition rate of 0.2 Å/sec. The titanium layer acts as an adhesion layer between the gold and the polyimide substrate; as a second step a 30 nm gold layer has been deposited using a deposition rate of 0.5 Å/sec. Finally, we used the lift-off technique to produce the finalized IDEs structure. The overall height of the IDEs is of critical role in the sensors' production since it is able to "shadow" the polyimide substrate during the process of NP deposition, thus preventing a good contact between NPs and IDEs. The IDEs inter-finger spacing (alternatively: electrode gap) was 10 μm, while the width was 2 μm (Fig. 3.1a). With the use of a modified dc magnetron sputtering system we deposited Pt NPs, of a mean diameter of 4 nm and standard deviation of 1.5 nm (Fig. 3.5b) on top of the IDEs. Sputtering is a well-known room temperature technique for the production of both thin films and NPs. It allows control over particle size, as it can adjust the target material to the deposition substrate distance, over nanoparticle flux, by modifying the argon flux, and nanoparticle density concentration on the substrate surface, by adjusting the deposition time. Both electrode and Pt NPs depositions were performed at 10^{-5} mbar pressure.

In order to investigate the effective protection of sensors against humidity, we deposited an alumina protective coating on top of the devices (Fig. 3.1b) using an Atomic Layer Deposition system (Picosun ALD R-200). The ALD deposited films are fabricated by consecutive cycles using specific precursors. The alumina precursors used were tetramethylaluminum (TMA) and deionized water (DI water). During the deposition, the ALD reactor was placed under 10 mbar pressure and a constant flow of 300 sccm of 99.999% purity N2. For both TMA and DI water the exposure time was 0.1s, while the purge time was 10 s for TMA and 15 s for DI water for each cycle. The temperature of the deposition was at 150 °C, for 50 and 100 cycles, resulting in 5.5 nm and 11 nm of alumina respectively. These deposition temperatures result in a low concentration of OH molecules in the film [34] which can facilitate the absorption of water molecules from the environment, while it is compatible with polyimide substrate temperature processing. Our team performed several fatigue tests before and after the alumina deposition and studied the protective capabilities of the alumina coating from relative humidity. The finalized strain-sensing devices were characterized by electrical, Transmission Electron Microscopy (TEM), as well as optical microscopy measurements.

The sensor sensitivity was determined by resistance measurements, using a Keithley 2400 source meter, with the application of strain steps by a home-made experimental setup. With the use of a micrometric piston controlled by a stepper motor we applied strain of 0.007% precision. The stepper motor was powered and controlled by a microcontroller (Arduino Uno) that allows the performance of reliable fatigue tests (small variations in the applied strain, for each strain cycle). During the whole process the sensors were glued on a PCB board (in order to ensure uniform deformation of the substrate during stress application, as depictured in Fig. 3.1d), whereas the system was encased in a climate chamber in which R.H. and temperature were under control (Fig. 3.1c). The relative humidity was controlled by either applying through Nitrogen of 99.999% purity, in, or transporting DI water vapors to the strain sensor's chamber from a tank using a mechanical vacuum pump. This configuration lead to the achievement of R.H. values between 10% and 70%. Both temperature and relative humidity were monitored by respective commercial sensors. Prior any measurement, preceded a calibration of the stage using a commercial flexible strain sensor with a gauge factor of 2.13. During the measurements, the temperature was kept constant at 23°C, while the resistance was monitored through the application of a constant voltage of 1 Volt.

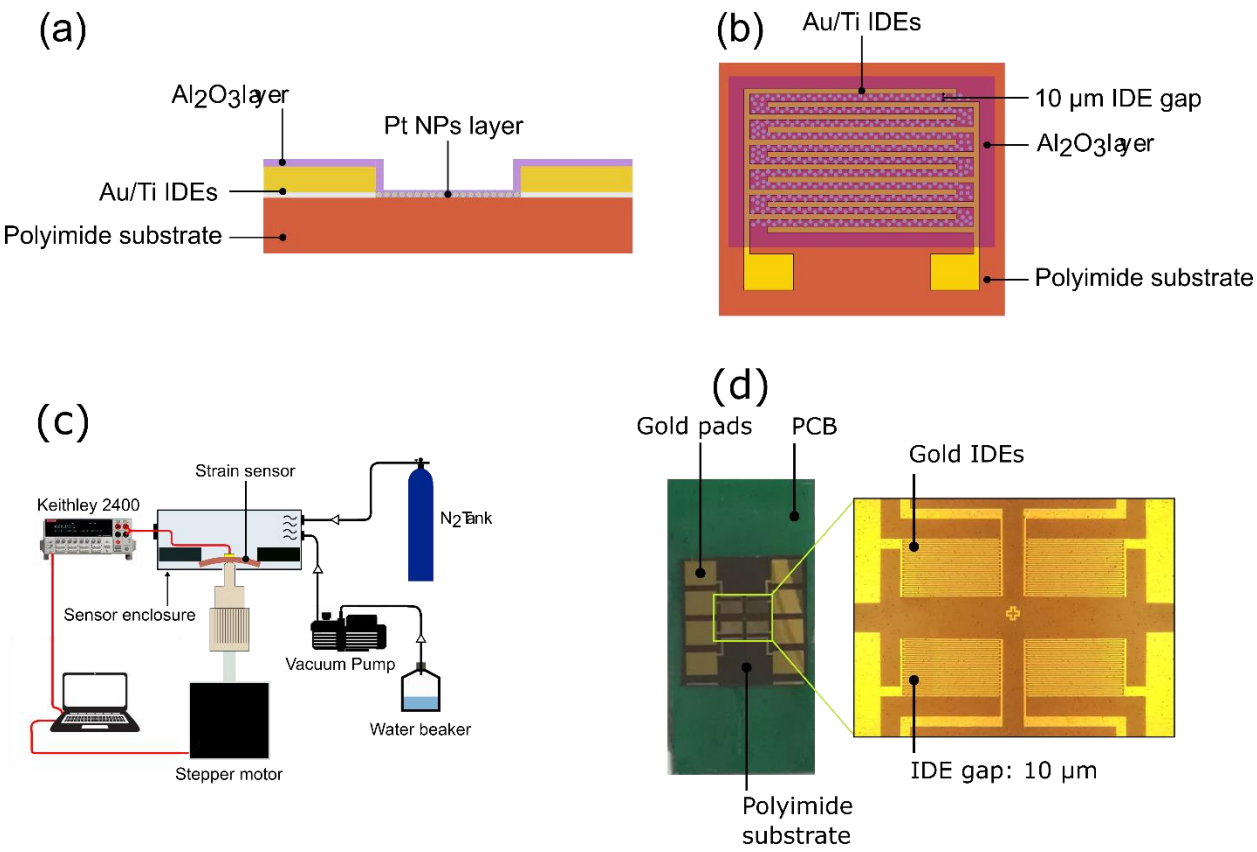

Figure 3.1: a) Schematic cross section of the sensor b) top down view of the sensor c) Schematic of the experimental setup. d) Image of the strain sensors on a PCB. There are 4 identical strain sensors in each device [41]

3.3. Strain calculation

The characterization of the strain sensors was done during the home-made stage of application of tensile strain. The sensor was attached to an aluminum metal sampler as to be supported at both ends of the underside of the sampler with carbon tape. The sampler was screwed to a wooden base, at the bottom of which was placed a micrometer Vernier. The Vernier has a bronze metal cantilever attached to its end, having a perpendicular movement to the direction of the sample. The sample was subjected to a three-point bend while the cantilever pushed the back of the sample upwards. The movement of the Vernier could be controlled by a motor (stepper motor) for automated measurements. The whole device was mounted on an iron optical table in order to prevent any vibration. The rotation of the Vernier by 1 mm corresponds to a horizontal displacement of 10 μm of the cantilever.

For the theoretical calculation of the applied strain we consider necessary the determination of the radius of curvature of the substrate for a specific displacement value of the cantilever. If we consider a uniform deformation of the substrate, the substrate will follow an arc, part of which can be approached from the linear portion of the hypotenuse of the triangle formed between the vertical displacement of the cantilever and half the length of the substrate (Fig. 3.2).

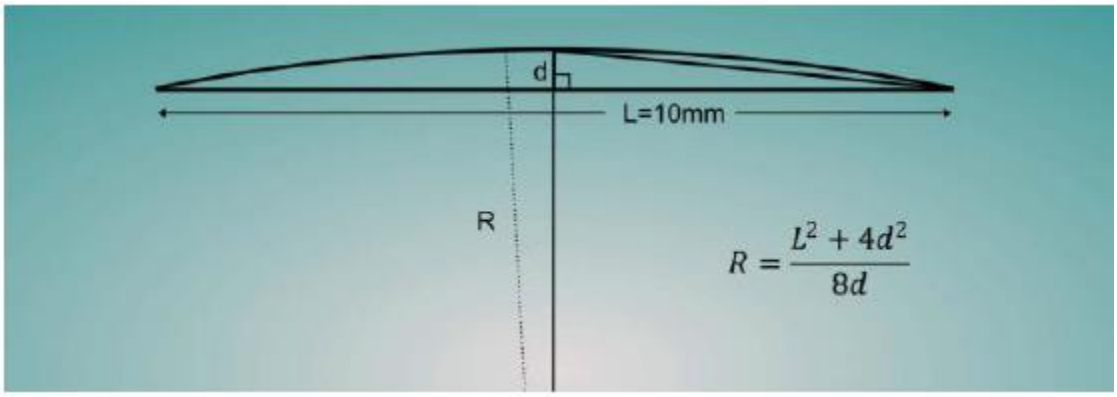

Figure 3.2: Geometry for calculation of the curvature radius.

Afterwards, the radius of curvature R_b that is perpendicular to the straight section of the arc forming a right triangle, is given by the Pythagorean Theorem:

$$R_b^2 = (R_b - d)^2 + (\frac{l}{2})^2 \quad (3.1)$$

$$R_b = \frac{l^2 + 4d^2}{8d} \quad (3.2).$$

If the substrate is bent, its front side lengthens, while, at the same time, its back side compresses. In the middle of the cross section of the substrate there is an imaginary line, the neutral axis, where the length *l* remains unchanged (Fig. 3.3). To calculate the length's change in *l'* on the substrate surface of thickness *d*, we consider that it corresponds to an arc portion with an angle ϑ and a radius of curvature R_{b2}.

$$l' = (R_{b2} + \frac{d}{2})d\theta \tag{3.3}$$

For $l = R_{b2}d\vartheta$

$$\gamma = \frac{l' - l}{l} = \frac{(R_{b2} + \frac{d}{2} - R_{b2})d\theta}{R_{b2}d\theta} = \frac{d}{2R_{b2}} \tag{3.4}$$

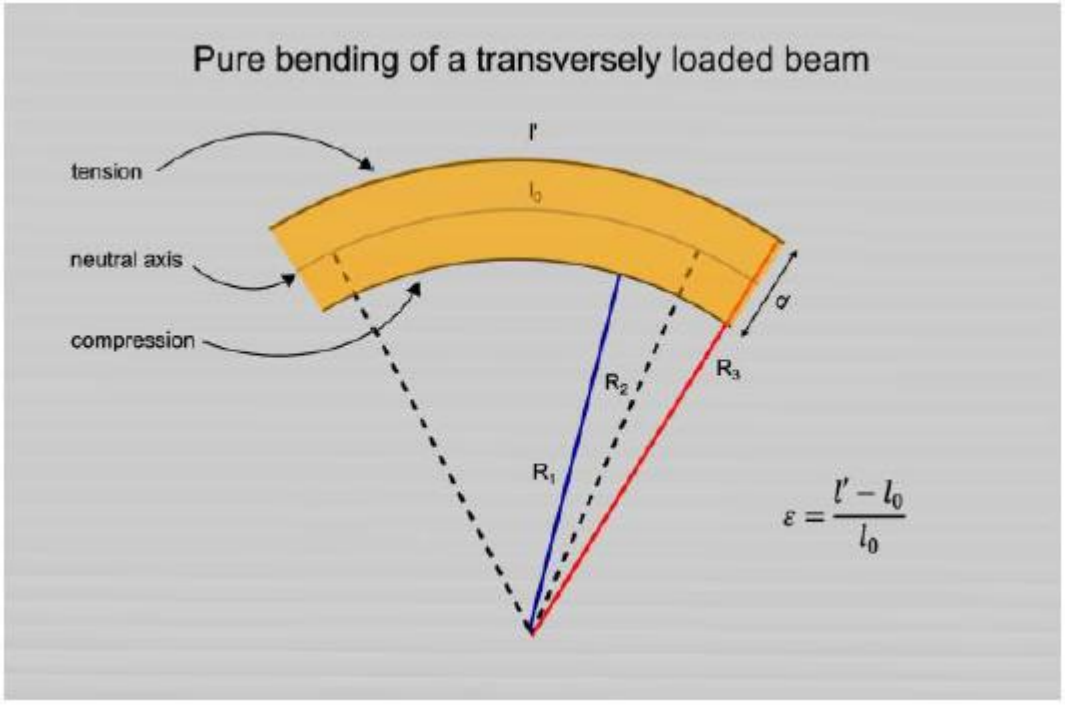

Figure 3.3: Geometry of strain calculation γ (ε).

Calculation of strain in polyimide on PCB substrate

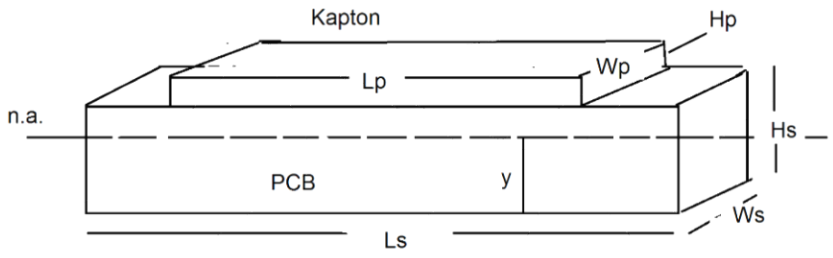

Figure 3.4: Schematic representation of polyimide (kapton) substrate on a PCB substrate

In case of having two substrates, the distance y from the neutral region (axis n.a) is calculated as follows:

$$y = \frac{Ls \cdot Ws \cdot \frac{Hs}{2} + Lp \cdot Wp \cdot (Hp + \frac{Hs}{2})}{Ls \cdot Ws + Lp \cdot Wp} \quad (3.5).$$

Therefore, the radius of curvature will be *R '= R + y*, where in the initial radius of curvature *R* we consider as length the *Ls*. Taking into account that *Hs + Hp = d*, the total thickness of the two substrates, the strain will be determined from the relation *ε = (d-y) / R '*.

In case we have PCB length *Ls = 13 mm*, width *Ws = 60mm* and thickness *Hs = 450um.* For sensor dimensions *Lp = 12mm*, *Wp = 6mm* and *Hp = 125um, y = 296.8um* so *d-y = 278.2um.*

3.4. Results

The operational principle of NPs based strain sensors is based upon the fact that NPs have an inter-particle distance and the charge transport happens due to the tunneling effect. If we assume that the inter-particle distance is l, the conductivity is given by the following equation:

$$R = r_0 \exp(\beta l) \exp(\frac{E_C}{K_b T}) \quad (3.6),$$

where β is the tunneling constant, r_0 a pre-exponential constant, K_b is the Boltzmann constant, T the temperature and E_C the activation energy which is given by:

$$E_C = \frac{e^2}{8\pi\varepsilon\varepsilon_0}\left(\frac{1}{r} - \frac{1}{r+l}\right) \quad (3.7),$$

where, r is the nanoparticles' size and ε the electric permittivity of the dielectric medium. The theory proposed by Herrmann et al [28] suggests that the differential resistance change, at room temperature, is given by the following equation:

$$\frac{\Delta R}{R} = \exp(g\gamma) - 1 \quad (3.8),$$

where, *g* is the strain sensitivity or the strain gauge factor (g-factor). For small deformations *γ*, the equation (3.8) becomes:

$$\frac{\Delta R}{R} = g\gamma \quad (3.9).$$

This model precedes that the NPs are cross-linked and they all have an initial inter-particle gap *l*. With the application of strain, all the inter-particle gaps change from *l* to *l+dl*. In Fig. 3.5 we use the equation (3.9) to compare with experimental results of strain NP sensors made on flexibles by using cross linked nanoparticles, as reported in the literature. The comparison showed that the above model describes sufficiently the sensors response.

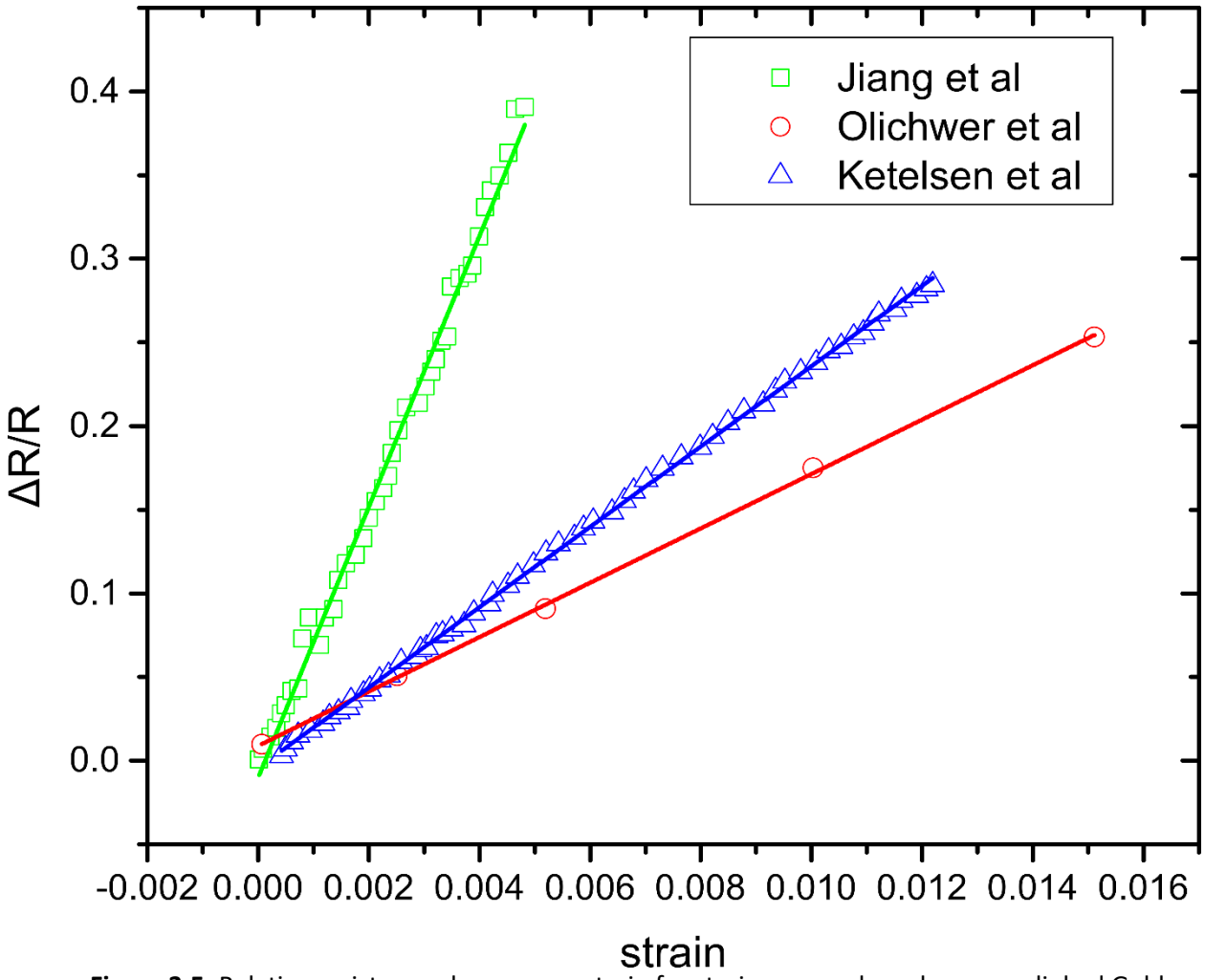

Figure 3.5: Relative resistance change over strain for strain sensors based on cross-linked Gold nanoparticles Jiang et al [42] Ketelsen et al [39] and Olichwer et al [43]. Equation (3.9) is used for the fitting lines. [41]

3.4.1. Sensor response using solvent-free nanoparticles and modeling

The resistivity of the Pt NPs film formed in vacuum by sputtering and gas condensation technics strongly depends on the NP surface coverage. The relation between NP surface coverage and sensor sensitivity has been already investigated [33], leading to the conclution that the best-performing devices were achieved when the surface coverage are just below the percolation threshold (NPs surface coverage of 50%) (Fig. 3.6a). A typical response of Pt NPs sensors made on flexible substrates is depicted in Fig. 3.7.

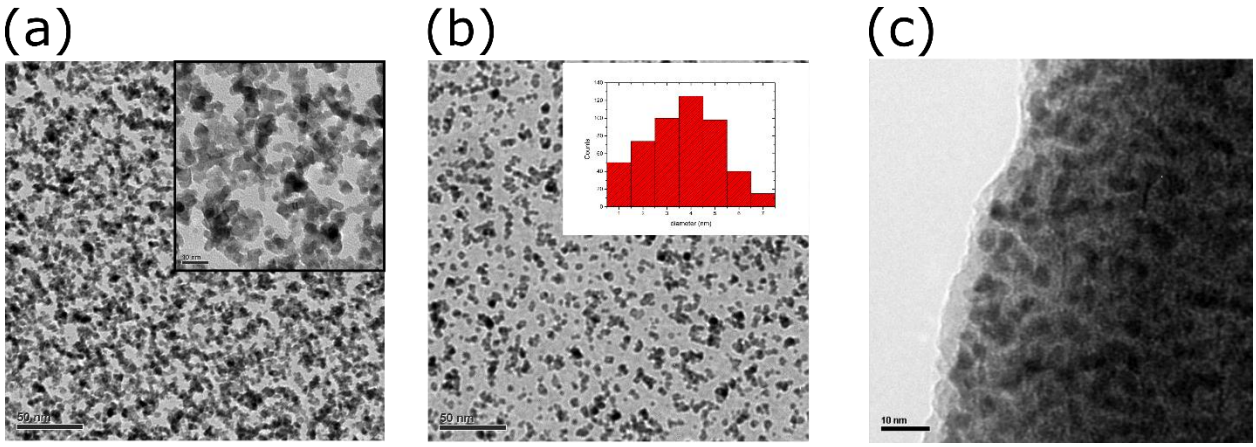

Figure 3.6: a) TEM images of naked Pt NPs with 50% surface coverage. Inset: higher magnification b) TEM image of naked Pt NPs with 28% surface coverage. Inset: NPs size distribution c) TEM image of Pt NPs covered with 5.5 nm thick alumina [41]

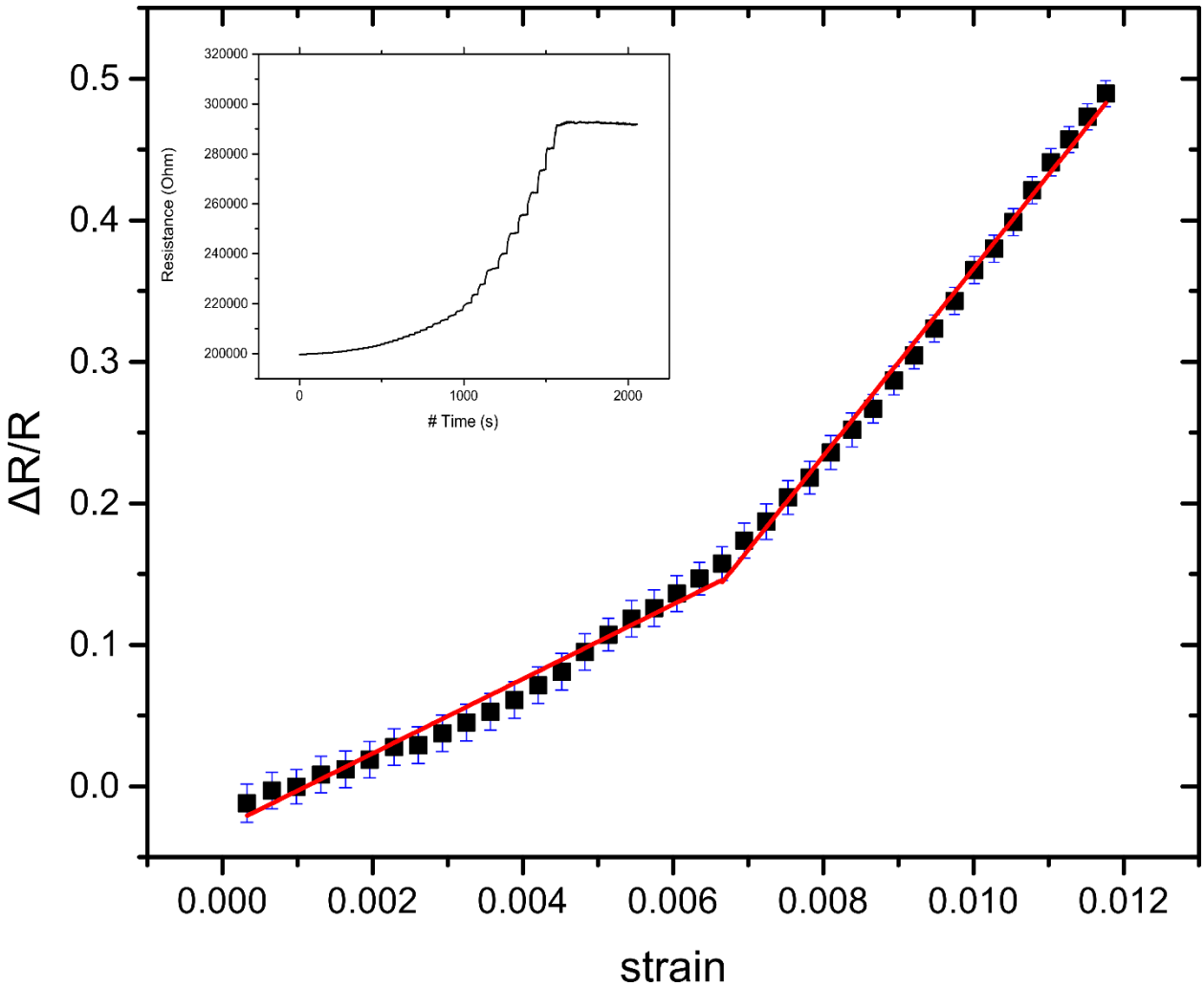

Figure 3.7: Relative resistance change over strain graph. The GF is calculated by the slopes of the fitting lines. Error bars represent the standard deviation of the measurements. The sensitivities of the sensor were GF1~ 26 for lower strains and GF2~ 66 for higher strains. [41]

In Fig. 3.8 can be seen the relative resistance change of sputtered (naked) NPs on as reported by different groups [35, 36], underlying that equation (3.8) is not describe their behavior sufficiently. The relative resistance change displays different linear areas having different slops. Strain ranges that can be described with the equation (3.9) and others which are also linear but with a different slope (Fig. 3.10) and, hence, different sensitivity. Even if higher orders of Taylor approximation are used to fit the data of naked NPs the fitting remains linear due to the very small strain value (Fig. 3.9). The already existing model [paragraph 3.4] is perfectly adequate to describe the sensitivity of cross-linked NPs, but does not predict a change of the GF value within the reported measurement range.

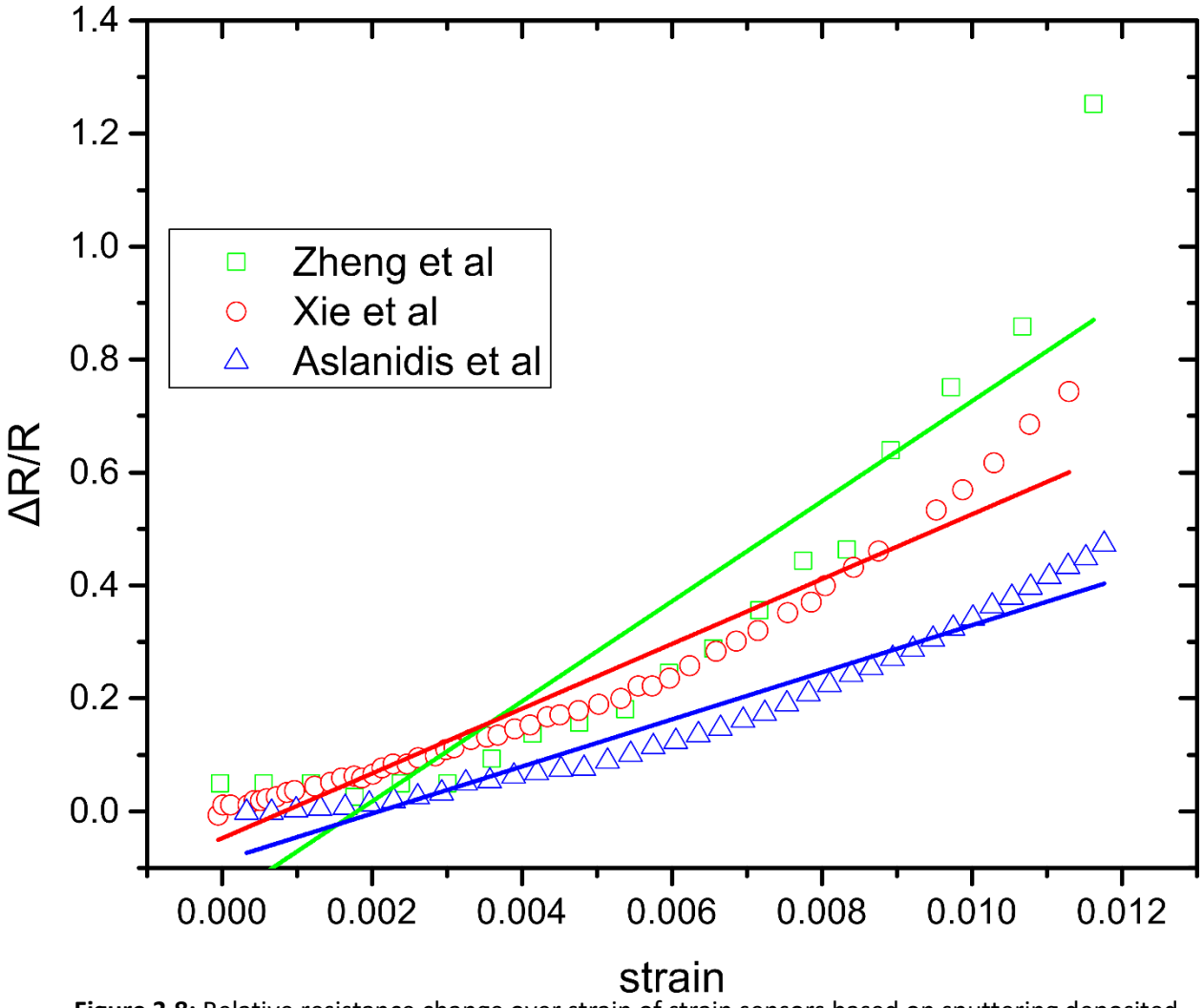

Figure 3.8: Relative resistance change over strain of strain sensors based on sputtering deposited NPs (naked). Zheng et al [35] Cr NPs -based sensor, Xie et al [36] Pd NPs -based sensor and this work [41] strain sensors with Pt NPs. Equation (3.9) is used for the fitting lines.

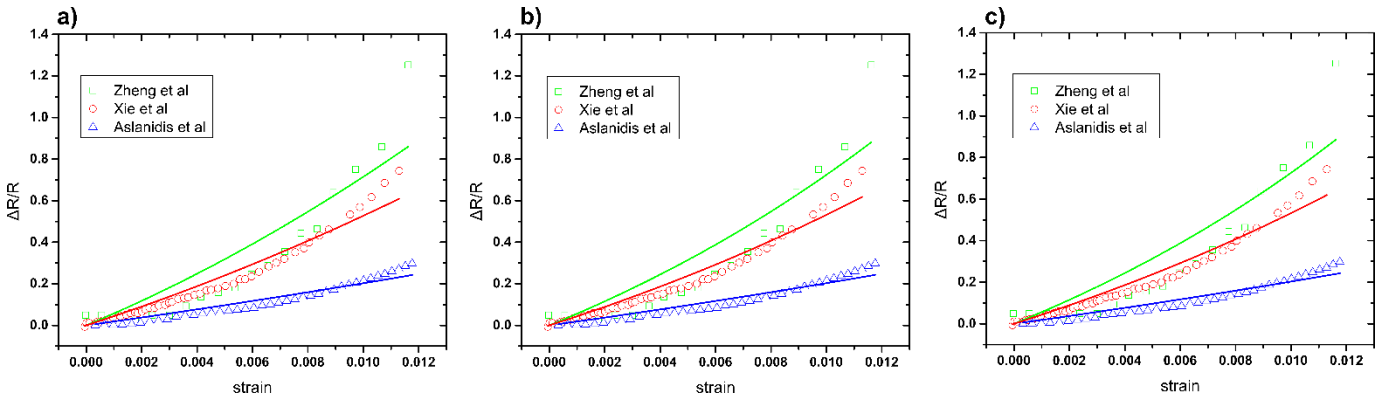

Figure 3.9: Relative resistance change over strain of strain sensors based on sputtering deposited NPs. Zheng et al [35] Cr NPs-based sensor, Xie et al [36] Pd NPs -based sensor and this work [41] strain sensor with Pt NPs. The fiting lines are created by a) the second order Taylor approximation, b) the third order Taylor approximation and c) the equation 3.8

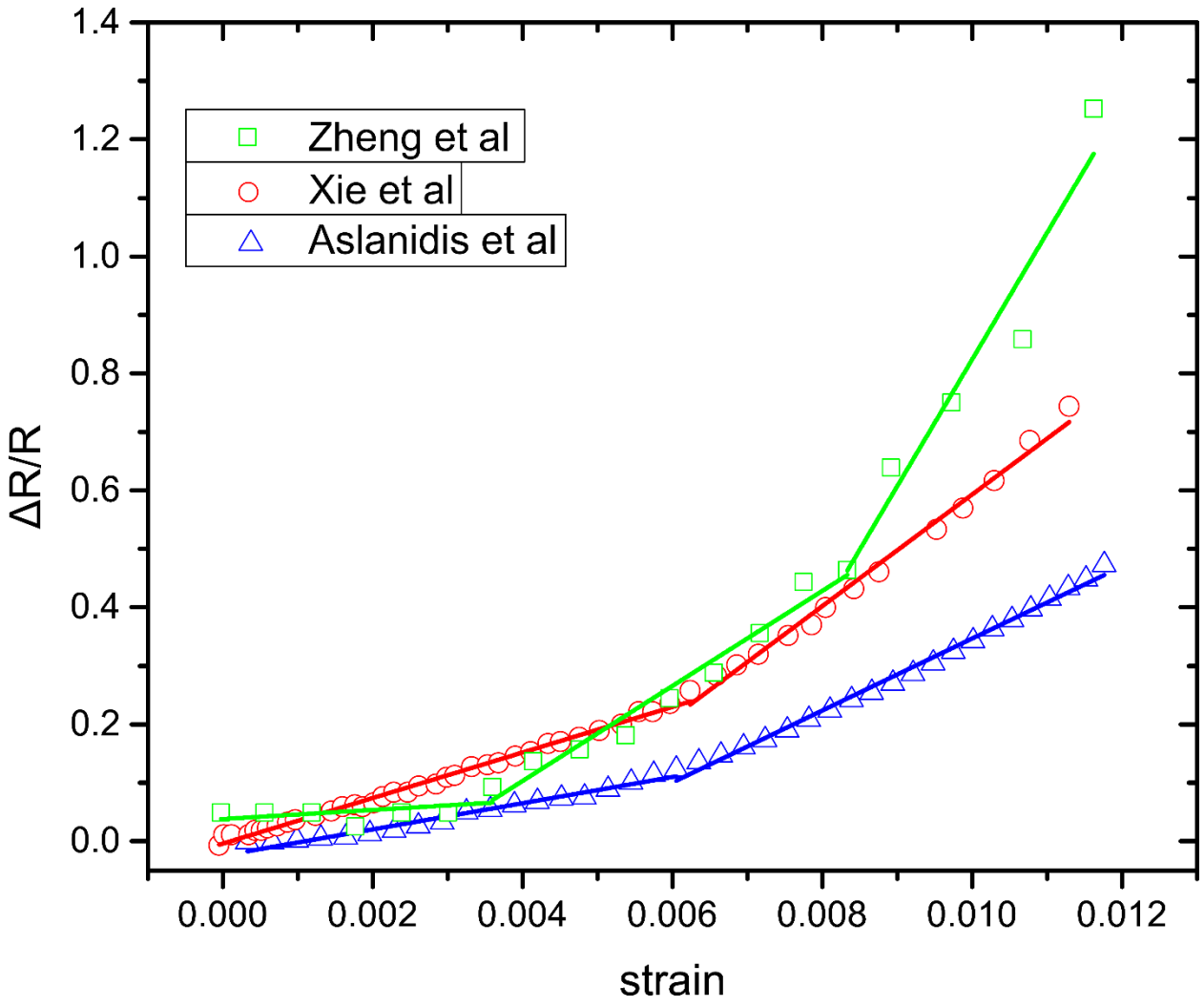

Figure 3.10: Relative resistance change over strain of strain sensors based on sputtering deposited NPs. Zheng et al [35] Cr NPs-based sensor, Xie et al [36] Pd NPs -based sensor and this work [41] strain

sensor with Pt NPs. Equations (3.9) and (3.14) are used for the fitting lines in the case of strain sensors, exhibiting two distinctive linear regions and the fitting of equations (3.9), (3.14) and (3.17) for strain sensors with 3 different linear regions.

In the case this particular study, the Pt NPs are naked; they soft-land on the substrate randomly, having as a result the creation of areas where all the NPs are in contact (therefore creating NP islands) and of other areas where an inter-particle distance exists between either NP islands or individual NPs. Subsequently, after the application of strain, the already existing inter-particle gaps increase, while larger NP islands fragment to form smaller NP clusters (Fig. 3.11); this highlights the need for revisiting the model proposed in paragraph 3.4 and ultimately producing a new, appropriate model, as discussed below.

At room temperature, if the mean value of the initial inter-particle distance is *l*, the resistivity is given by:

$$R_0 = r_0 \exp(\beta l) \tag{3.10}.$$

By applying strain, new inter-particle distances are created, therefore the resistivity will be given by:

$$R_s = r_0 \exp(\beta (l + dl)) + N r_0 \exp(\beta dl) \tag{3.11},$$

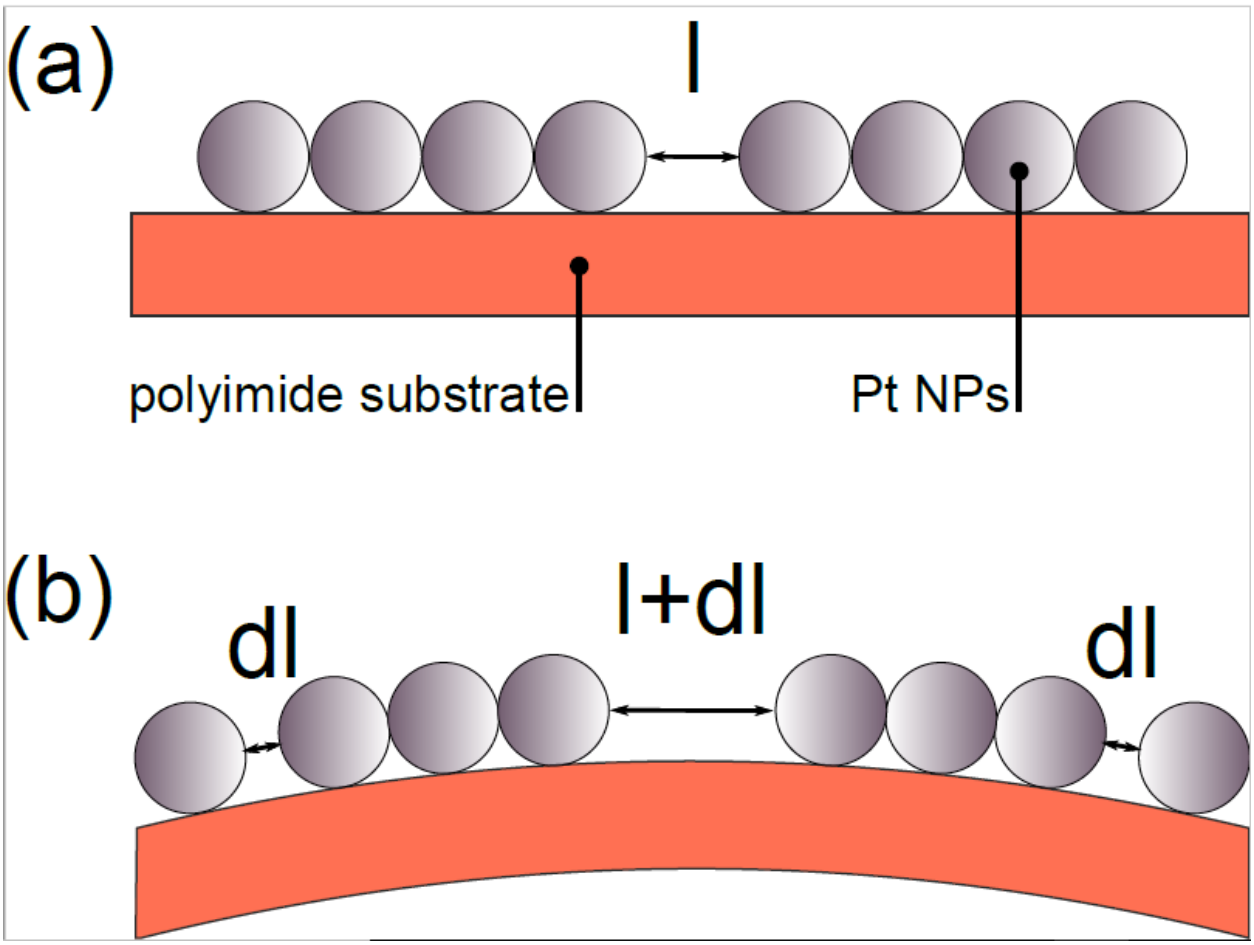

Figure 3.11: Graphic representation of inter-particle gaps between NP islands. Firstly, there is an inter-particle distance *l* (Fig. 3.11a) which after the appliance of strain is increased by *dl*. The application of strain creates two additional gaps (Fig. 3.11b). [41]

where the first term results from the already existing inter-particle distances and the second term results from the new ones. *N* is a dimensionless number depending on several parameters such as the number of the new inter-particle distances, as well as on the strength of their contribution to the overall resistivity. For instance, in case that all the NPs are assembled in a straight line, all the inter-particle distances will contribute equally. In our case however, in which the NPs create complex paths with several possible conductive paths that are parallel to each other, each inter-particle distance contributes differently to the final resistance. Additionally, N depends on the strain value that creates the new inter-particle distances. If $N = k\gamma$, with *k* defined as the number of gaps/strain unit (this being valid above a threshold strain value) the differential resistance change is now given by:

$$\frac{\Delta R}{R_0} = \frac{r_0 \exp(\beta(l + dl)) + k\gamma r_0 \exp(\beta dl) - R_0}{R_0} \quad (3.12),$$

from which we obtain equation (3.13):

$$\frac{\Delta R}{R_0} = \exp(\beta dl) - 1 + \frac{k\gamma r_0 \exp(\beta dl)}{R_0} \quad (3.13).$$

Since strain *γ* is defined by *γ = dl/l*, we can obtain that *dl = γl*. Introducing it to equation (3.13) and considering that *g = βl*, we obtain:

$$\frac{\Delta R}{R_0} = \exp(g\gamma) - 1 + \frac{k\gamma r_0}{R_0}\exp(g\gamma) \quad (3.14).$$

For small strain values, the equation becomes:

$$\frac{\Delta R}{R_0} = g\gamma + \frac{kr_0}{R_0}\gamma \quad (3.15),$$

from which we obtain equation (3.16):

$$\frac{\Delta R}{R_0} = \gamma(g + \frac{kr_0}{R_0}) \quad (3.16).$$

Within the parenthesis of the above ginen equation (3.16) is the modified GF that is valid above a threshold strain value, where new gaps start to form, while g is the GF below this strain threshold.

Assuming that, after the application of *nγ* strain, new inter-particle distances are created and the resistance will be given by:

$$R_s = r_0 \exp\big(\beta(l + ndl)\big) + k\gamma r_0 \exp(\beta ndl) + k'\gamma r_0 \exp(\beta dl) \quad (3.17),$$

where *k'* is the equivalent of *k* for the newest distances, *n* the number of strain applied steps. The differential resistance change is given by:

$$\frac{\Delta R}{R_0} = \exp(g\gamma) - 1 + \gamma \frac{k\gamma r_0}{R_0} \exp(g\gamma) + \frac{k'\gamma r_0}{R_0} \exp(g\frac{\gamma}{n}) \quad (3.18).$$

For small strain values, equation (3.18) becomes:

$$\frac{\Delta R}{R_0} = \gamma(g + \frac{kr_0}{R_0} + \frac{k'r_0}{R_0}) \quad (3.19).$$

Inside the parenthesis of the (3.19) equation is the new sensitivity that depends on the strain value and creates the new inter-particle distances. Equations (3.9), (3.16) and (3.19), which are linear with different slopes and -as depicted- in Fig. 3.10, express more accurately the behavior of the sensor than the one proposed in Herrmann's model. Because of the random deposition of the NPs, it is impossible to know exactly the strain values for which new inter-particle distances are formed, thus influencing the sensor sensitivity. For example, in Fig. 3.10 (green lines) it is observed that three lines are required to fit the graph accurately. This suggests that a critical threshold of new inter-particle distances has been reached twice, due to strain application. Each group of new inter particle distances, was created at a different strain value, having as a result the gradual increase of the sensor's sensitivity. In the case that the NPs' allocation was different, the change in the sensor's sensitivity would be observed at a different strain value. During our experiments the strain value that this occurred was around 0.64%. In addition, equations (3.16) and (3.19) indicate why randomly deposited naked NPs should have different behavior from cross-linked NPs. Finally, the Pearson's Correlation Coefficient (Pearson's r) was calculated after fitting Herrmann's model (Fig. 3.8 and 3.9) and the model proposed herein (Fig. 3.10). The Pearson Correlation Coefficient is a measure of the linear correlation between strain and Resistance; the coefficient has a value between +1 and −1, where 1 stands for total positive linear correlation. The results are given in table 3.1 and indicate that the fitting lines that where generated from our model show better linear correlation than the ones deriving from Herrmann's model.

TABLE 3.1

	materials	substrate	fabrication method	Herrmann's model Pearson's r	this paper's model Pearson's r		
					first line	second line	third line

Zheng et al [35]	Cr NPs	PET	Sputtering	0.91238	0.99059	0.96269	0.92329
Xie et al [36]	Pd NPs	PET	Sputtering	0.9711	0.99548	0.99491	-
Aslanidis et al [41]	Pt NPs	polyimide	Sputtering	0.97147	0.98129	0.99651	-

Table 3.1: Comparison between this work and two strain-sensing devices based on naked NPs.

3.4.2. Model effectiveness and exposure in adverse conditions

3.4.2.1. Fatigue experiments

The sensors' performance were investigated under close to real-word operational conditions and the model was afterwards compared to the experimental results, as to test its validity. The NP surface coverage of all the results presented herein was close to 50% [established after Transmission Electron Microscopy measurements with the use of carbon grids (Fig. 3.6a)] corresponding so to a resistance value of hundreds kOhms and optimum device sensitivity. For the needs of the strain sensing experiments were employed 10 distinctive sensors. The above mentioned sensors were subjected to a number of fatigue tests during which the GF was measured after the application of 1000 cycles of applied strain up to 1.2%. The value of the sensors' G-factor was determined from the slope of ΔR/R-strain graphs (Fig. 3.5), from which two G-factors were extracted: one for small strain values (GF1 for $\gamma < 0.64\%$) and one for large strain values (GF2 for $\gamma > 0.64\%$); this behavior is aggregable to our model that predicts different GF for different strain. For every measurement both the temperature and R.H. were kept constant and the mean value of the GFs remained practically unchanged, regardless of the number of strain cycles. Changes in the GF after 1000 cycles of fatigue tests are being presented in Fig. 3.13 (Mean GF1 of 19, and GF2 of 49 for the reference sensors and GF1 of 22 and GF2 of 45 for the sensors after fatigue tests). The effectiveness of the model in predicting the strain sensing response of the solvent-free NP-based sensors is observed in Fig. 3.12, where even after 1000 strain cycles the response of the sensors can be adequately fitted.

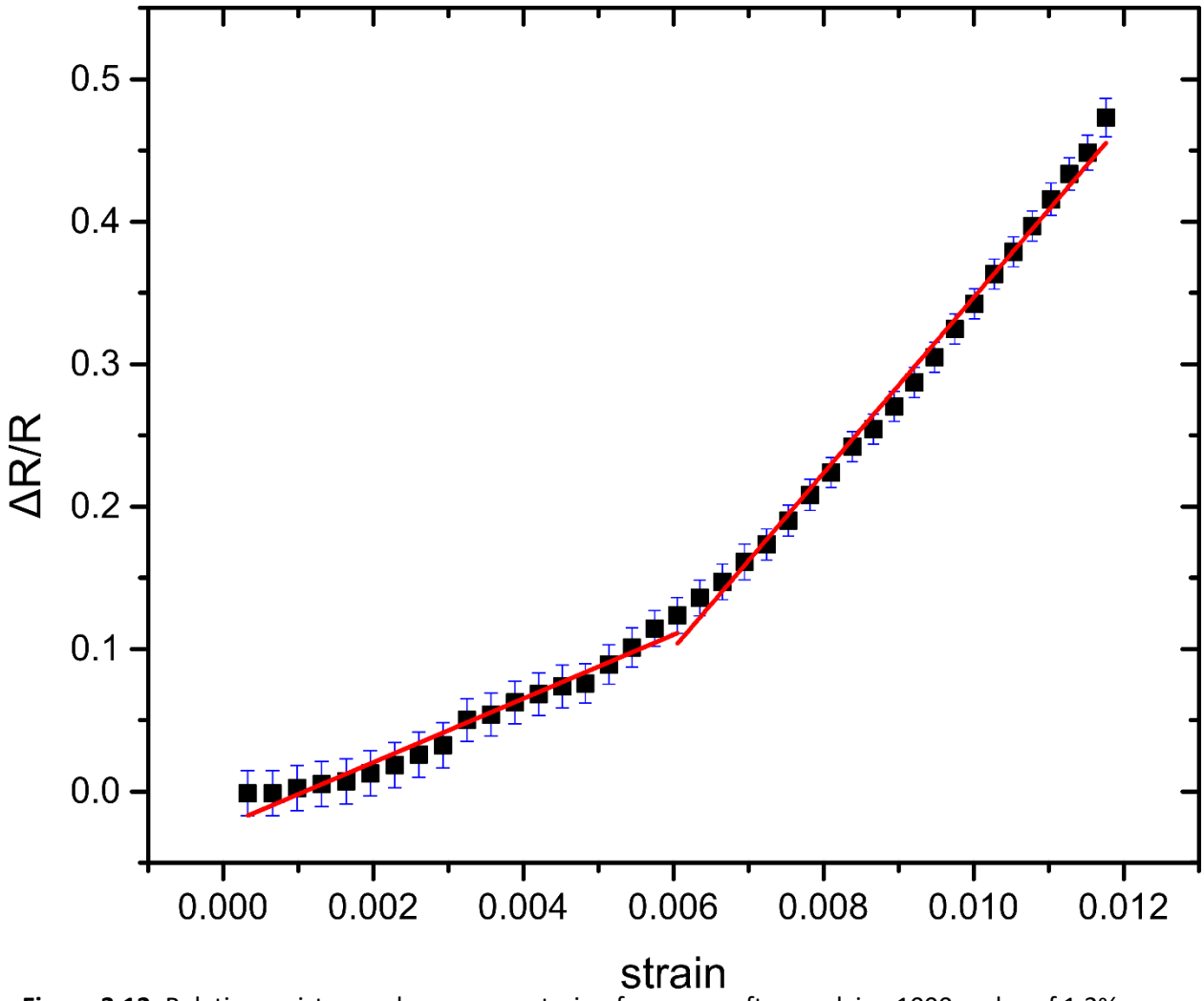

Figure 3.12: Relative resistance change over strain of a sensor after applying 1000 cycles of 1.2% strain. Error bars represent the standard deviation of the measurements. Our model predicts the sensor behavior, using two linear slopes in order to fit the experiment results. The sensor has GF1~ 22 for lower strains and GF2~ 61 for higher strains. [41]

3.4.2.2. Protection of the sensor against humidity and model effectiveness

As presented, the GF of the devices remains unchanged after 1000 cycles of fatigue experiments, and for constant R.H. Nevertheless, unprotected Pt NP films continue to be sensitive to environmental changes, such as changes in humidity. Variations of R.H. influence the resistance of the device, resulting, as so, in affecting its strain sensitivity. An unprotected device has the tendency to be more sensitive and, apart from that, as discussed by Kano et al. [44], has linear response to humidity and could be therefore also used as a humidity sensor. This effect leads to uncertainty of the value of the applied external stimulus as well as an increase of the sensor's strain detection limit. That being said, the preservation of high sensitivity of the NP strain sensors -without although being correlated to any R.H. variations- is crucial for their use. Having

that in mind, we deposited a protective Al_2O_3 coating using ALD system as we considered it critical to study the validity of the proposed model in various humidity conditions.

Initially, and as to evaluate the degradation, if any, of the alumina coatings after intensive fatigue tests, and for varying humidity environments, a total of 20 sensors were employed for the results that will be discussed below. More specifically the sensors were protected with two different alumina coatings of5.5 or 11 nm, using the ALD technique. In Fig. 3.6c is depicted a TEM image of Pt NPs covered with a 5.5 nm thick alumina. It is noteworthy that alumina films thicker than 5.5 nm resulted in images of poor quality. This is attributed to the insulating properties of the alumina layer. Patsiouras et al [34] have studied the alumina coatings as protective agent against relative humidity for strain sensors and concluded that the minimum alumina thickness required for adequate R.H. protection is 5.5 nm (deposited under 150°C). This study, however, was performed with NP strain sensors made on silicon substrates and, as a result, the strain values applied were low. As far as the flexible substrates studied herein is concerned, a 5.5 nm thick alumina coating was unable to protect the sensor from humidity. We determined that a probable explanation for that is the formation of cracks in the alumina layer at high strain values, a fact that creates free paths for water molecules to penetrate the film. Consequently, alumina films of 11 nm in thickness were employed in all of the following results.

Before the process of examining the protective properties of alumina films against variations in R.H, the effect of the alumina layer itself on sensor performance was evaluated in parallel with the efficacy of the model proposed in par. 3.4.1. In Fig. 3.13a is pictured the performance of an alumina-protected strain sensor right after the alumina is deposed. It is obvious that the GF of the device was reduced by 33% (Fig. 3.15); this happens probably due to the alumina's built-in stress, which hinders, to some extent, NP dislocation [34]. The need of a two straight-line model as to accurately match the experimental results is also evident. We can also observe that the second line starts from a higher strain value than usual (~0.9% instead of 0.64% -which typically the start of strain value for the second line). For high strain values (0.9%), the film starts to relax (in terms of stress) and the NPs starts to move more freely. In Fig. 3.13b san be observed the performance of an alumina-coated sensor after 1000 stress cycles; the sensor is much more sensitive compared to sensors without coating, as well as to alumina-coated sensors that have not been subjected to fatigue tests. The fatigue experiments induce cracks in the alumina film which enhance NP dislocation in the vicinity of the cracks, having as a result a much higher GF - as already reported in the literature [39]. The foretold argument is also supported by the fact that the initial resistance of the alumina-coated sensors is slightly increased by 3.7% after 1000 stress cycles. Ketelsen et al. [39] performed similar fatigue tests on cross-linked gold NP sensors. They, also, reported that after 1000 stress cycles a 5% increase of the resistance was noticed, but afterwards the sensor performance remained unaltered for up to 10000 cycles. The team attributed this behavior to the formation of microcracks within the cross-linked NP film. In the case of our experiments we can attribute this change to the cracks formed in the alumina layer since NPs are fabricated using the sputtering technique, forming a two dimensional network of

non-cross-linked objects. Furthermore, our model fits accurately the experimental data emphasizing the need of a two-line model in order to achieve correct fitting.

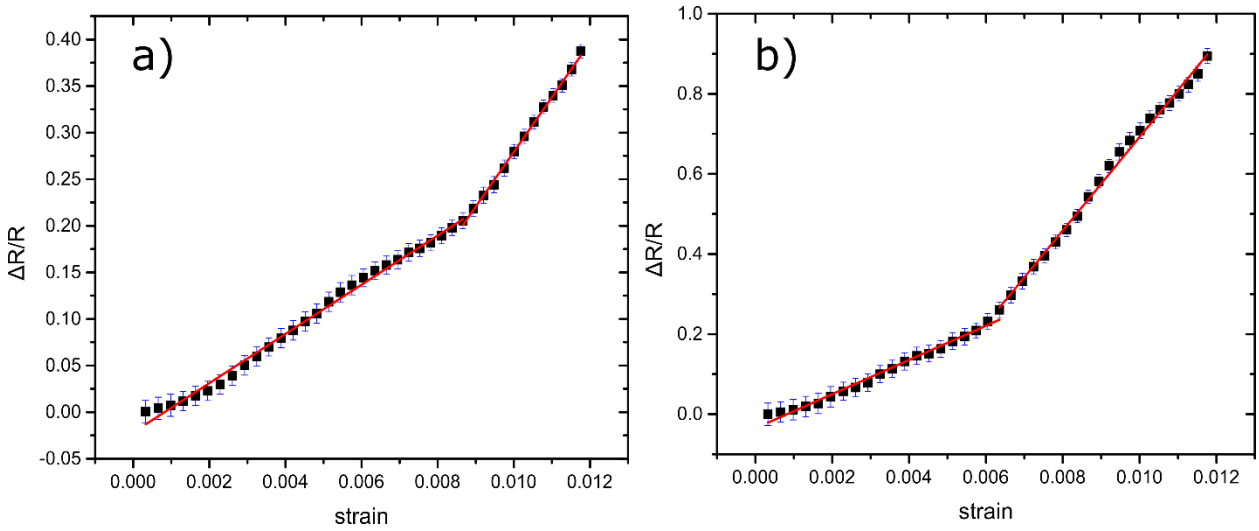

Figure 3.13: a) Relative resistance change over strain graph for a sensor right after the alumina deposition. Error bars represent the standard deviation of the measurements. Two straight lines were used to fit, accurately, the experimental results as our model has proposed. In this example, the sensor has GF1~ 20 for lower strains and GF2~ 50 for higher strains. b) Relative resistance change over strain graph for a sensor with alumina coating after 1000 stress cycles up to 1.2% strain. The sensor has GF1~ 60 for lower strains and GF2~ 85 for higher strains. [41]

As reported [45, 46], mechanical strain alters the sensor's sensitivity towards R.H.; for that purpose, the protective properties of the 11 nm thick alumina layer against humidity were investigated by measuring the $\Delta R/R_0$ of the sensors under a number of different R.H. conditions for unstrained sensors, as well as for strain values up to 1.2%. For every each applied strain condition (0, 0.3, 0.6, 0.9 and 1.2%), we have varied the humidity from 10-70% and measured relative changes in resistance (Fig. 3.14). It is worth mentioning that our model can be applied to every RH conditions (Fig. 3.12) given that two GFs are essential in order to fit the experimental data. Results in Fig. 3.14 (and Fig. 3.16) indicate that in the case of uncoated sensors, ΔR/R0 changes attributed to R.H variation are comparable to resistance changes due to strain, therefore limiting the sensor performance. The use of the alumina coating on top of the NPs causes the effect of humidity to reduce below 2% proving that the alumina coating is, indeed an effective protective barrier against humidity [43]. This results in a much increased sensor's sensitivity; the NP sensors protected can detect strains down to 0.007% while the uncoated ones have a strain detection limit of 0.107%. Additional fatigue tests were performed for 1000 strain cycles and for strains up to 1.2% with ΔR/R0 measured under different R.H. conditions (10 – 70 %) for coated and uncoated sensors (Fig. 3.16). After 1000 strain cycles, the ΔR/R0 has been increased up to 3% and for high strain values up to 7.5%. In any case, it remained much lower than the values that the samples without the protective alumina coating performed. Finally, it is worth mentioning that an alumina coating of 11 nm contributes in enhanced sensor stability and performance over time; measurements conducted 1 and 3 months following the initial

experiments, revealed that sensors with an alumina coating of 11 nm featured minimal variance in device resistance and device sensitivity (compared to uncoated sensors and sensors with a 5nm coating, Fig. 3.17).

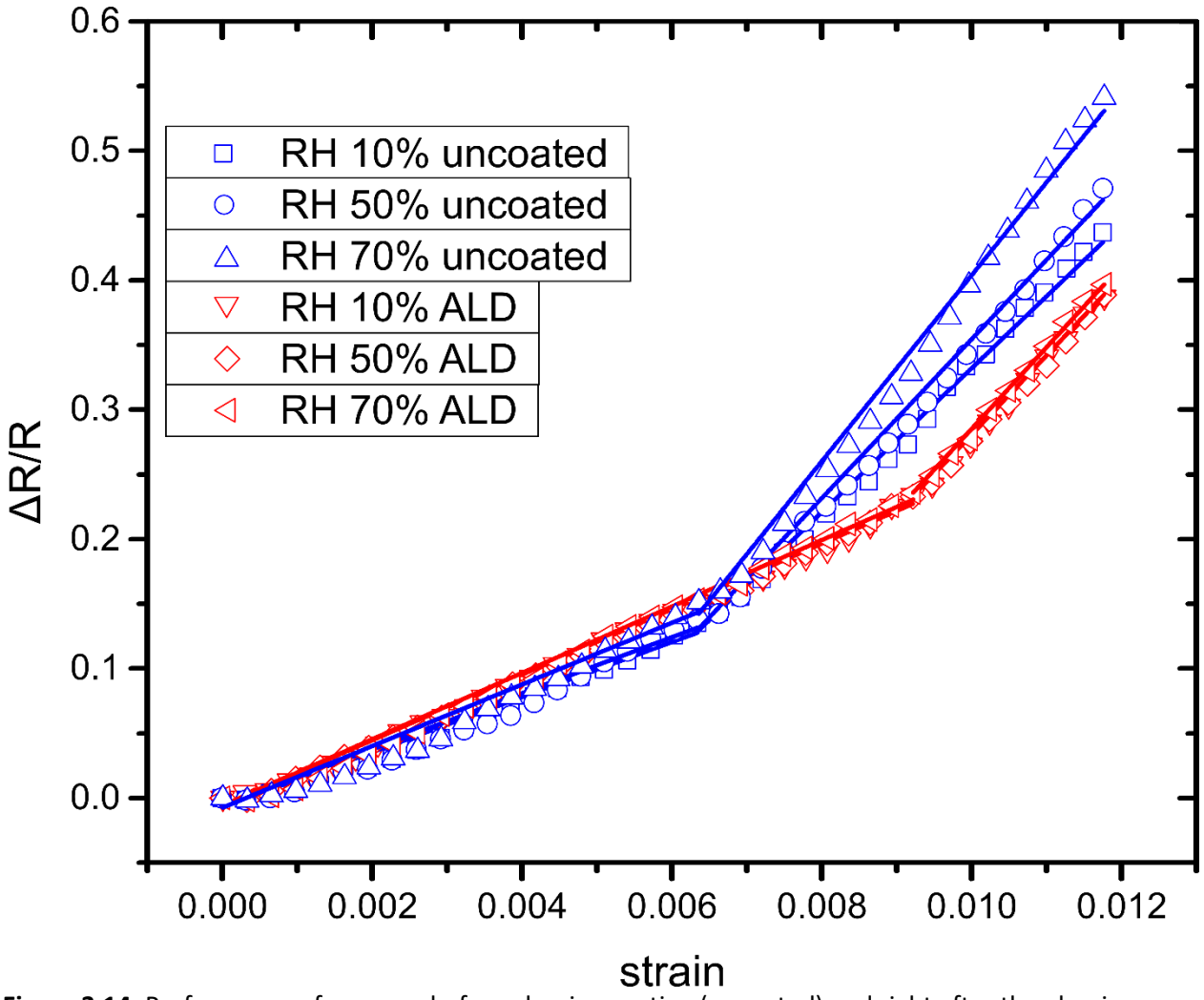

Figure 3.14: Performance of a sensor before alumina coating (uncoated) and right after the alumina coating (ALD) for RH conditions of 10%, 50% and 70%. The fitting lines for the uncoated sensor are the blue ones, while the red ones indicate the coated one. [41]

3.5. Sensors performance

The GF of all fabricated sensors has been measured both for small ($\varepsilon < 0.64\%$) and large ($\varepsilon > 0.64\%$) strain values by our team. The GFs of the uncoated sensors were measured twice; right after the fabrication (resulting in GF1=19 with standard deviation (SD) of 9 and GF2=49 with SD of 24) and, then, after 1000 cycles of stress up to 1.2% (resulting in GF1=22 with SD of 8 and GF2=45 with SD of 19). The GFs of the alumina coated sensors were also measured right after the alumina deposition (resulting in GF1=15 with SD of 6 and GF2 of 39 with SD of 12) and after 1000

cycles of stress up to 1.2 (resulting in GF1=61 with SD of 19 and GF2=82 with SD of 17) as shown in Fig. 3.15.

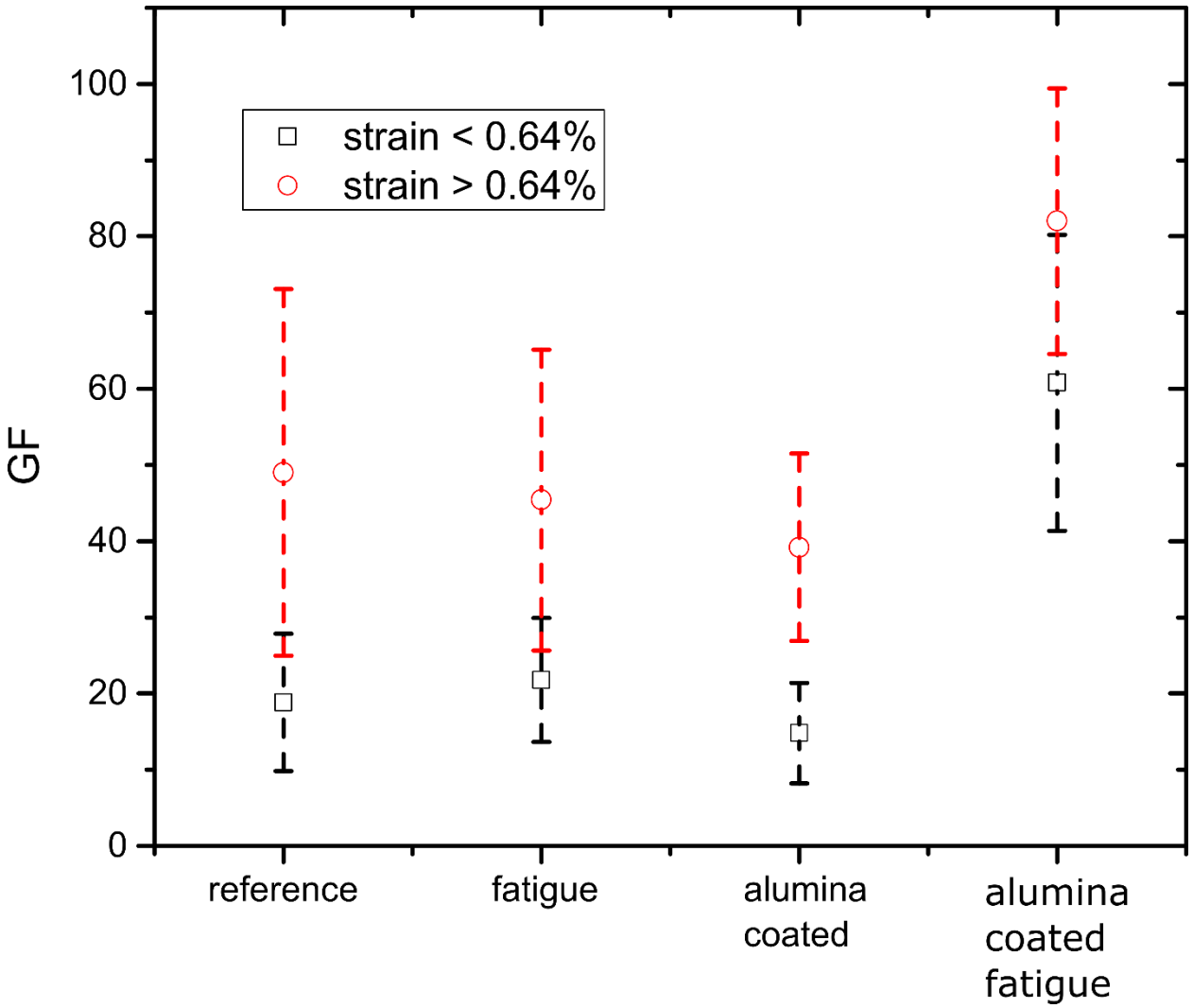

Figure 3.15: Variation in the Sensors' GFs for uncoated as well as alumina coated sensors, before and after Fatigue experiments. [41]

According to the above mentioned results the fatigue test did not significantly affect the GFs of the uncoated sensors.

After the alumina coating, the GF was reduced by 33% for $\varepsilon < 0.64\%$ and by 13% for $\varepsilon > 0.64\%$. This reduction is believed to be attributed to the built in stress of the alumina film. After 1000 strain cycles (with maximum strain up to 1.2%) for the sensors with alumina coating, the mean GF value was increased by 77% (for the small strain values) and by 110% (for the large strain values); this is probably due to the cracks' formation in the alumina film which consequently causes increased NP dislocation, as well as increased GFs.

In Fig. 3.16 are depicted resistance changes for R.H. concentrations in the range of 10% - 70%. The results correspond to the sensors measured right after the fabrication (reference), to the ones measured after 1000 stress cycles up to 1.2% (fatigue), as well as to the ones right after the alumina coating (alumina coated) and after 1000 stress cycles up to 1.2% (alumina coated fatigue). The measurements were performed by imposing a constant strain of 0, 0.3, 0.6, 0.9 or 1.2%. For each of the previous strain values (0%, 0.3%, 0.6%, 0.9% and 1.2%) R.H. varied between 10 and 70%, while the resistance response was measured- without taking into account the resistance response to strain. The results depicted in Fig. 3.16 show the protective properties of the alumina film against R.H. The deferential resistance change for the uncoated sensors (both reference and fatigue) was between 11 and 15%, while for the alumina coated sensors it was in the range of 0.5 to 2%. After the fatigue experiments the differential resistance change increased to values between 3 and 7.5%.

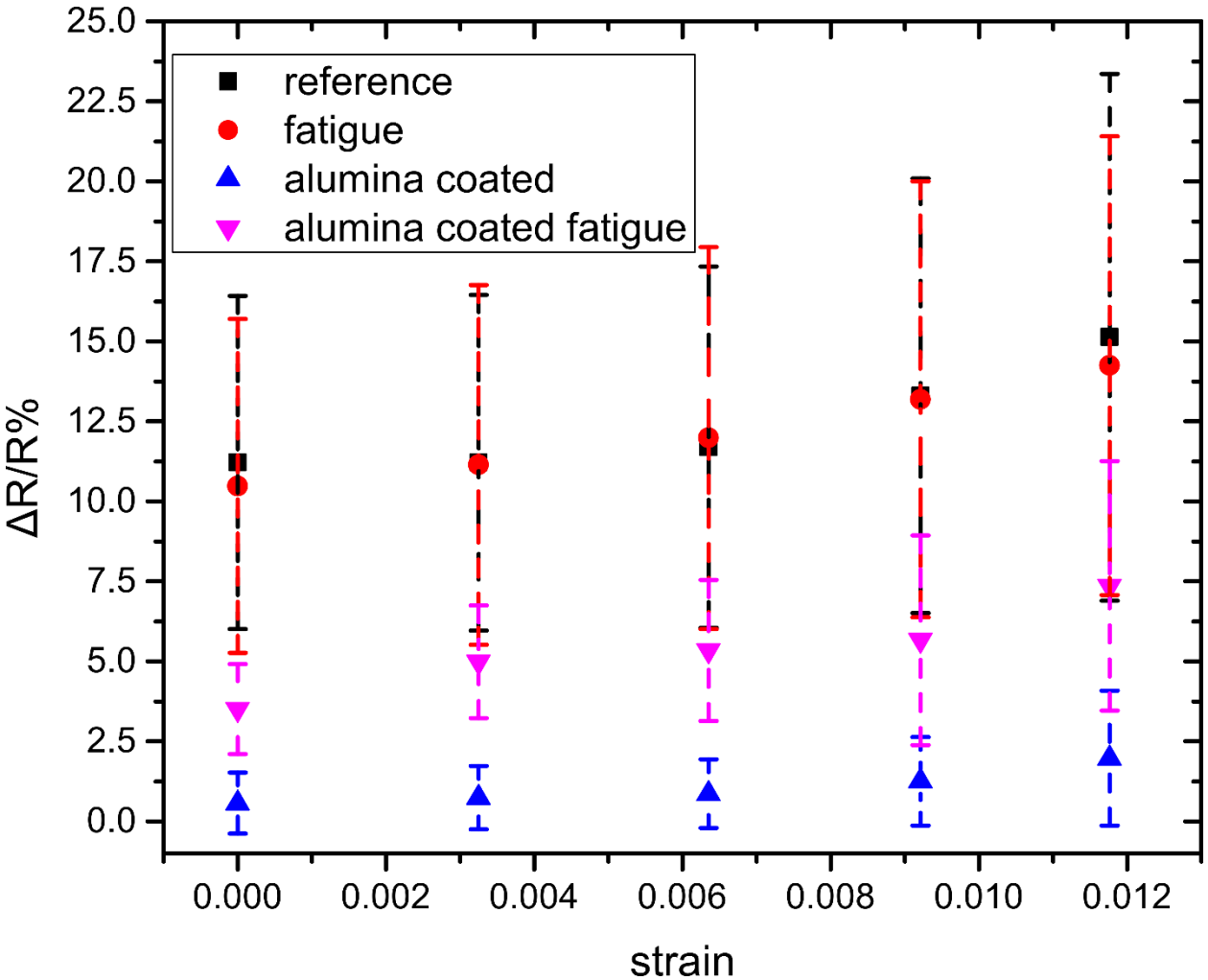

Figure 3.16: Resistance variance for sensors under fixed strain (strain values of 0%, 0.3%, 0.6%, 0.9% and 1.2%), in a varying humidity environment. R.H. varies between 10% and 70%. [41]

3.6. Sensors stability and repeatability

Following the fatigue experiments, each sensor was measured twice as to ensure the reliability of the measurement. The sensors showed excellent repeatability, with minimal change in their GF (in the order of 0.5% for uncoated sensors and 0.2% for the coated ones). Apart from that, sensors' resistance was measured during the period of one day, one month and three months subsequently, in order to determine their endurance over time. As above-mentioned, sensors GF is directly connected to the initial value of the resistance. All sensors were measured after 1000 cycles of strain up to 1.2%. In Fig. 3.17 is showed the mean values of 30 sensors in total; 10 uncoated, 10 with 5nm alumina coating and 10 with 11 nm alumina coating. The error bars represent the standard deviation. For all sensors, the relative resistance change after a day was almost negligible. Particularly, the uncoated sensors exhibited a mean value of 0.37 with SD 0.1, the sensors with a 5 nm alumina coating a mean value of 0.018 with SD 0.08 and the sensors with the 11 nm alumina coating a mean value of 0.015 with SD 0.03. After the period of one month uncoated sensors increased their resistance by 12% (SD of 2.1). After the passing of 3 months period 6 out of 10 sensors increased their resistance by 59% (SD of 5.6), while 4 sensors were not operational. The GF of the operational sensors changed by 10 and 40% after 1 month and 3 months respectively. For the 5 nm alumina coated sensors the GF increased by 6% (SD of 2.4) after one month. After 3 months 7 out of 10 sensors increased their resistance by 21% (SD of 4.3), while 3 sensors were rendered useless. The GF of the operational sensors changed by 5 and 15% after 1 month and 3 months period respectively. Finally, the 11 nm alumina coated sensors featured an increased resistance by 1% (SD of 0.8) after one month, with 9 out of 10 sensors still remaining operational. After three months their resistance increased by 4% (SD of 1.4) and the same sensors still remained operative; the GF of the operational sensors changed by 1 and 2% after 1 month and 3 months period respectively. This resistance change resulted in a change in GF, making many of the uncoated sensors useless, while the majority of the protected sensors remained functional. Sensors with a 5 nm alumina coating featured again a significant change in resistance (especially after the three months period), indicating insufficient protection against humidity. On the contrary, the alumina coating of 11 nm thickness prevented large resistance fluctuations, prolonging the operational lifespan of the fabricated sensors. The above results indeed confirmed the need for an alumina protective film, not only as a protection against humidity but also as a mean to extend the operational lifetime of the sensors'.

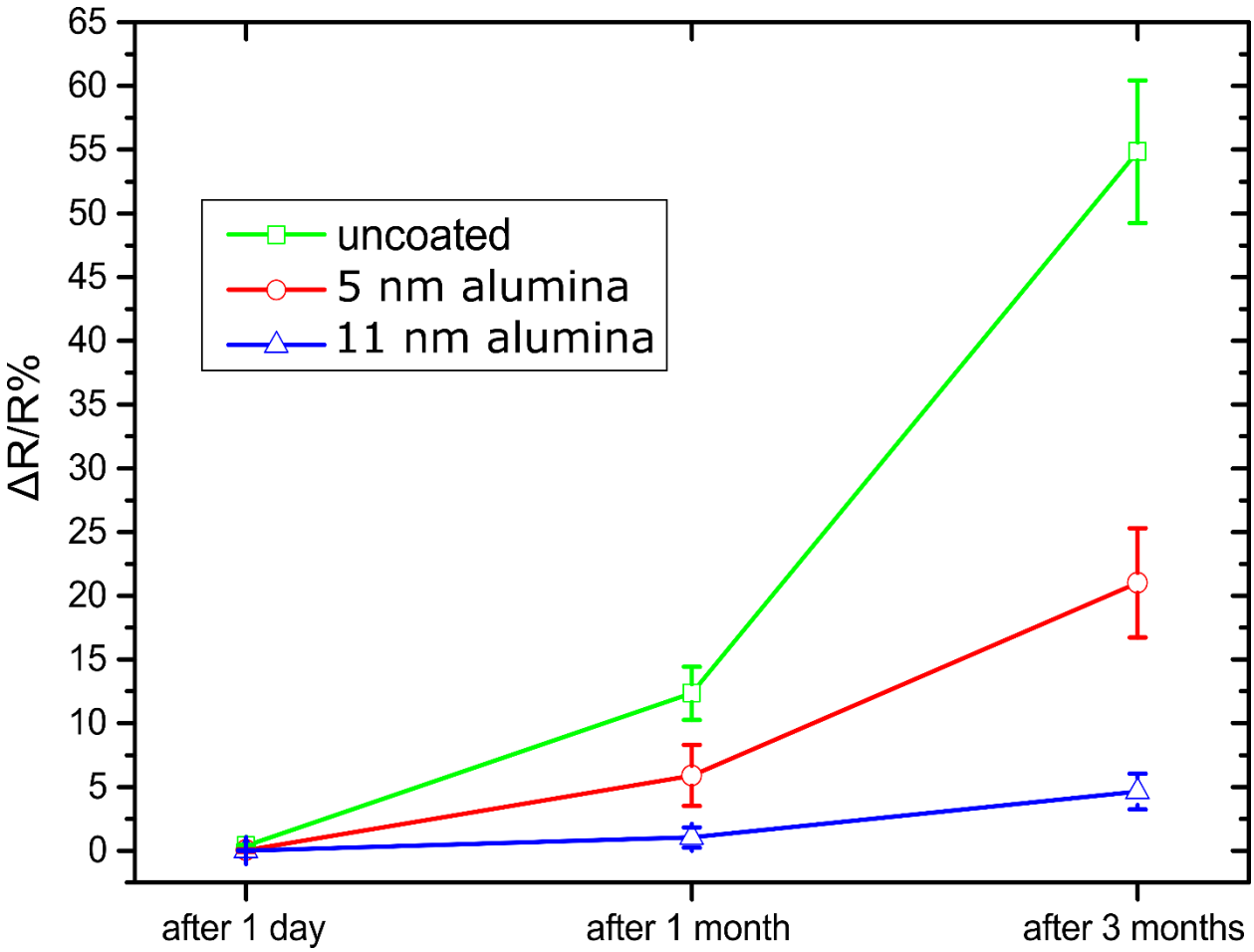

Figure 3.17: Relative resistance change over time. Sensors' resistance was measured after one day, one month and three months for sensors without alumina coating (uncoated) and with 5 nm and 11 nm alumina coating. [41]

3.7. Conclusions

As foresaid in the beginning of the chapter, the previously reported model for electronic conduction in these films, which is based on electron tunneling between NPs [28], is adequate to describe cross-linked NP strain sensors and has been in use so far. However, it needed to be revisited and modified in order to include and explain how naked NP devices behave. The striking difference arises from the uniformly 2-D interconnected network that is being formed just after cross-linked NPs being deposited, while naked NPs are randomly being deposited. As a result, for higher strains new gaps between NPs are created, increasing the sensitivity. Our model takes into account the properties of naked NPs, so creating an appropriate tool for the respective strain-sensing devices while, at the same time, offering significant insight into their physical properties.

Apart from that, we performed a technical study of solvent-free NPs based strain sensors by investigating protective coatings against R.H., the limitations they exhibited and the eventual

optimization of the devices. To that end, we investigated the environmental stability of solvent-free NP sensors as well as the effectiveness of the proposed model to fit experimental data, by exposing the sensors to adverse conditions. As the sole protective coating against humidity we used alumina deposited via the ALD technique. The alumina layer was evaluated as far as its protective qualities against the effect of fatigue, of under varying relative humidity conditions for both unstrained and under applied strain devices.

Resistance variance of alumina-free and alumina-coated devices, in varying relative humidity conditions and before any fatigue experiments, has been compared to their resistance variance after the fatigue experiments. These results associate alumina thickness with device endurance for varying humidity concentrations and stability over long periods of time. Such results prove that an alumina film thickness of 11 nm fabricated at 150 °C can effectively protect flexible NP-based strain sensors from humidity, even after repeated device-bending.

This work was published in the scientific journal Sensors [41].

3.8. References

[1] Kang MS, Joh H, Kim H, Yun HW, Kim D, Woo HK, Lee WS, Hong SH, Oh SJ, Synergetic effects of ligand exchange and reduction process enhancing both electrical and optical properties of Ag nanocrystals for multifunctional transparent electrodes, Nanoscale, 2018;10(38):18415-22.

[2] Russo S, Ranzani T, Liu H, Nefti-Meziani S, Althoefer K, Menciassi A, Soft and stretchable sensor using biocompatible electrodes and liquid for medical applications, Soft robotics, 2015 Dec 1;2(4):146-54.

[3] Ha M, Lim S, Ko H, Wearable and flexible sensors for user-interactive health-monitoring devices, Journal of Materials Chemistry B, 2018;6(24):4043-64.

[4] Lee WS, Jeon S, Oh SJ, Wearable sensors based on colloidal nanocrystals, Nano convergence, 2019 Dec 1;6(1):10.

[5] Shengbo S, Lihua L, Aoqun J, Qianqian D, Jianlong J, Qiang Z, Wendong Z, Highly sensitive wearable strain sensor based on silver nanowires and nanoparticles, Nanotechnology, 2018 Apr 25;29(25):255202.

[6] Joh H, Lee SW, Seong M, Lee WS, Oh SJ, Engineering the Charge Transport of Ag Nanocrystals for Highly Accurate, Wearable Temperature Sensors through All-Solution Processes, Small, 2017 Jun;13(24):1700247.

[7] Laflamme S, Kollosche M, Connor JJ, Kofod G, Robust flexible capacitive surface sensor for structural health monitoring applications, Journal of Engineering Mechanics, 2013 Jul 1;139(7):879-85.

[8] Yi Y, Wang B, Bermak A, A low-cost strain gauge displacement sensor fabricated via shadow mask printing, Sensors, 2019 Jan;19(21):4713.

[9] Zhang Y, Anderson N, Bland S, Nutt S, Jursich G, Joshi S, All-printed strain sensors: Building blocks of the aircraft structural health monitoring system, Sensors and Actuators A: Physical, 2017 Jan 1;253:165-72.

[10] Takei K, Yu Z, Zheng M, Ota H, Takahashi T, Javey A, Highly sensitive electronic whiskers based on patterned carbon nanotube and silver nanoparticle composite films, Proceedings of the National Academy of Sciences, 2014 Feb 4;111(5):1703-7.

[11] Fang X, Tan J, Gao Y, Lu Y, Xuan F, High-performance wearable strain sensors based on fragmented carbonized melamine sponges for human motion detection, Nanoscale, 2017;9(45):17948-56.

[12] Li Q, Li J, Tran D, Luo C, Gao Y, Yu C, Xuan F, Engineering of carbon nanotube/polydimethylsiloxane nanocomposites with enhanced sensitivity for wearable motion sensors, Journal of Materials Chemistry C, 2017;5(42):11092-9.

[13] Guo X, Huang Y, Zhao Y, Mao L, Gao L, Pan W, Zhang Y, Liu P, Highly stretchable strain sensor based on SWCNTs/CB synergistic conductive network for wearable human-activity monitoring and recognition, Smart Materials and Structures, 2017 Aug 9;26(9):095017.

[14] Sekitani T, Nakajima H, Maeda H, Fukushima T, Aida T, Hata K, Someya T, Stretchable active-matrix organic light-emitting diode display using printable elastic conductors, Nature materials, 2009 Jun;8(6):494-9.

[15] Lee CJ, Park KH, Han CJ, Oh MS, You B, Kim YS, Kim JW, Crack-induced Ag nanowire networks for transparent, stretchable, and highly sensitive strain sensors, Scientific reports, 2017 Aug 11;7(1):1-8.

[16] Park M, Park YJ, Chen X, Park YK, Kim MS, Ahn JH, MoS2-based tactile sensor for electronic skin applications, Advanced Materials, 2016 Apr;28(13):2556-62.

[17] Khalil I, Rahmati S, Julkapli NM, Yehye WA, Graphene metal nanocomposites—Recent progress in electrochemical biosensing applications, Journal of industrial and engineering chemistry, 2018 Mar 25;59:425-39.

[18] Hossain MA, Jeon S, Ahn J, Joh H, Bang J, Oh SJ, Control of tunneling gap between nanocrystals by introduction of solution processed interfacial layers for wearable sensor applications, Journal of Industrial and Engineering Chemistry, 2019 May 25;73:214-20.

[19] Lee WS, Lee SW, Joh H, Seong M, Kim H, Kang MS, Cho KH, Sung YM, Oh SJ, Designing metallic and insulating nanocrystal heterostructures to fabricate highly sensitive and solution processed strain gauges for wearable sensors, Small, 2017 Dec;13(47):1702534.

[20] Lee WS, Kim D, Park B, Joh H, Woo HK, Hong YK, Kim TI, Ha DH, Oh SJ, Multiaxial and Transparent Strain Sensors Based on Synergetically Reinforced and Orthogonally Cracked Hetero-Nanocrystal Solids, Advanced Functional Materials, 2019 Jan;29(4):1806714.

[21] Zhang S, Cai L, Li W, Miao J, Wang T, Yeom J, Sepúlveda N, Wang C, Fully Printed Silver-Nanoparticle-Based Strain Gauges with Record High Sensitivity, Advanced Electronic Materials, 2017 Jul;3(7):1700067.

[22] Zhao X, Guo J, Xiao T, Zhang Y, Yan Y, Grzybowski BA, Charged Metal Nanoparticles for Chemoelectronic Circuits, Advanced Materials, 2019 Nov;31(45):1804864.

[23] Wilson JS, Sensor technology handbook, Elsevier; 2004 Dec 21.

[24] Segev-Bar M, Haick H, Flexible sensors based on nanoparticles, ACS nano, 2013 Oct 22;7(10):8366-78.

[25] Wang S, Oh JY, Xu J, Tran H, Bao Z, Skin-inspired electronics: an emerging paradigm, Accounts of chemical research, 2018 Apr 25;51(5):1033-45.

[26] Yang K, Yin F, Xia D, Peng H, Yang J, Yuan W, A highly flexible and multifunctional strain sensor based on a network-structured MXene/polyurethane mat with ultra-high sensitivity and a broad sensing range, Nanoscale, 2019;11(20):9949-57.

[27] Zhang W, Liu Q, Chen P, Flexible strain sensor based on carbon black/silver nanoparticles composite for human motion detection, Materials, 2018 Oct;11(10):1836.

[28] Herrmann J, Müller KH, Reda T, Baxter GR, Raguse BD, De Groot GJ, Chai R, Roberts M, Wieczorek L, Nanoparticle films as sensitive strain gauges, Applied Physics Letters, 2007 Oct 29;91(18):183105.

[29] Zhang P, Bousack H, Dai Y, Offenhäusser A, Mayer D, Shell-binary nanoparticle materials with variable electrical and electro-mechanical properties, Nanoscale, 2018;10(3):992-1003.

[30] Kang D, Pikhitsa PV, Choi YW, Lee C, Shin SS, Piao L, Park B, Suh KY, Kim TI, Choi M, Ultrasensitive mechanical crack-based sensor inspired by the spider sensory system, Nature, 2014 Dec;516(7530):222-6.

[31] Han Z, Liu L, Zhang J, Han Q, Wang K, Song H, Wang Z, Jiao Z, Niu S, Ren L, High-performance flexible strain sensor with bio-inspired crack arrays, Nanoscale, 2018;10(32):15178-86.

[32] Jung H, Park C, Lee H, Hong S, Kim H, Cho SJ. Nano-cracked strain sensor with high sensitivity and linearity by controlling the crack arrangement, Sensors, 2019 Jan;19(12):2834.

[33] Tanner JL, Mousadakos D, Giannakopoulos K, Skotadis E, Tsoukalas D. High strain sensitivity controlled by the surface density of platinum nanoparticles, Nanotechnology, 2012 Jun 21;23(28):285501.

[34] Patsiouras L, Skotadis E, Gialama N, Drivas C, Kennou S, Giannakopoulos K, Tsoukalas D, Atomic layer deposited Al2O3 thin films as humidity barrier coatings for nanoparticle-based strain sensors, Nanotechnology, 2018 Sep 20;29(46):465706.

[35] Zheng M, Li W, Xu M, Xu N, Chen P, Han M, Xie B, Strain sensors based on chromium nanoparticle arrays, Nanoscale, 2014;6(8):3930-3.

[36] Xie B, Mao P, Chen M, Li Z, Liu C, Qin Y, Yang L, Wei M, Liu M, Wang X, Han D, A tunable palladium nanoparticle film-based strain sensor in a Mott variable-range hopping regime, Sensors and Actuators A: Physical, 2018 Apr 1;272:161-9.

[37] Lee GY, Kim MS, Min SH, Kim HS, Kim HJ, Keller R, Ihn JB, Ahn SH, Highly Sensitive Solvent-free Silver Nanoparticle Strain Sensors with Tunable Sensitivity Created Using an Aerodynamically Focused Nanoparticle Printer, ACS applied materials & interfaces, 2019 May 31;11(29):26421-32.

[38] Zhang P, Dai Y, Viktorova J, Offenhäusser A, Mayer D, Electronic Responses to Humidity in Monolayer and Multilayer AuNP Stripes Fabricated by Convective Self-Assembly, Physica status solidi (a), 2018 Aug;215(15):1700950.

[39] Ketelsen B, Yesilmen M, Schlicke H, Noei H, Su CH, Liao YC, Vossmeyer T, Fabrication of Strain Gauges via Contact Printing: A Simple Route to Healthcare Sensors Based on Cross-Linked Gold Nanoparticles, ACS applied materials & interfaces, 2018 Oct 3;10(43):37374-85.

[40] Digianantonio L, Gauvin M, Alnasser T, Babonneau D, Viallet B, Grisolia J, Viau G, Coati A, Garreau Y, Ressier L, Influence of the humidity on nanoparticle-based resistive strain gauges, The Journal of Physical Chemistry C, 2016 Mar 17;120(10):5848-54.

[41] Aslanidis E, Skotadis E, Moutoulas E, Tsoukalas D, Thin Film Protected Flexible Nanoparticle Strain Sensors: Experiments and Modeling, Sensors, 2020 Jan;20(9):2584.

[42] Jiang CW, Ni IC, Tzeng SD, Kuo W, Nearly isotropic piezoresistive response due to charge detour conduction in nanoparticle thin films, Scientific reports, 2015 Jul 15;5(1):1-9.

[43] Olichwer N, Leib EW, Halfar AH, Petrov A, Vossmeyer T, Cross-linked gold nanoparticles on polyethylene: resistive responses to tensile strain and vapors, ACS applied materials & interfaces, 2012 Nov 28;4(11):6151-61.

[44] Kano S, Kim K, Fujii M, Fast-response and flexible nanocrystal-based humidity sensor for monitoring human respiration and water evaporation on skin, ACS sensors, 2017 Jun 23;2(6):828-33.

[45] Nehm F, Klumbies H, Richter C, Singh A, Schroeder U, Mikolajick T, Mönch T, Hoßbach C, Albert M, Bartha JW, Leo K, Breakdown and protection of ALD moisture barrier thin films, ACS applied materials & interfaces, 2015 Oct 14;7(40):22121-7.

[46] Yin J, Hu P, Luo J, Wang L, Cohen MF, Zhong CJ, Molecularly mediated thin film assembly of nanoparticles on flexible devices: electrical conductivity versus device strains in different gas/vapor environment, ACS nano, 2011 Aug 23;5(8):6516-26.

Chapter 4: Monte Carlo Simulations

4.1. Introduction

As seen in the previous chapter, NPs have been proven a highly promising sensing material for sensor sensitivity enhancement [1-3]. Although different kind of sensors have taken advantage from the use of NP films [4-16] to demonstrate high sensitivity, strain sensors have gained interest years due to their application in a plethora of different application areas [17-24].

While trying to create more sensitive sensors arose the need of creating a simulation tool, capable of predicting the sensitivity of various NP films. We explained in the previous chapter how we developed strain sensors based on platinum NPs (Pt-NPs) on flexible substrates [5], resulting in GF of 26. The gas phase condensation technique was used for the manufacture of the NPs, which offers control over NP density as well as NP diameter[8] [25].

In order to increase the NP strain sensors' performance it is imperative to understand the underlying physical mechanisms that control their sensitivity. In this chapter we present a Monte Carlo simulation tool (implemented in Matlab) that was developed in order to calculate the sensitivity of NP strain sensors. The high advantage given by simulation is that, once benchmarked with experimental data, it makes it possible to perform a large number of low-cost and fast turnaround 'experiments' giving so a positive feedback to new real experiments. The Monte Carlo method is on the other hand a simple deterministic method [26], which has been used to simulate a variety of phenomena [27-30] and has been adopted herein to describe the random nature of the Pt-NPs deposition process.

The developed simulation tool inputs includes the nanoparticle diameter dimension and their surface coverage as well as the strain value, whereas the tool's output provides the resulting resistance value and the gauge factor. Although the followed methodology for the achievement of the calculation is being extensively presented in the 'Simulation Methods' section of this chapter (pp. 66), we can briefly mention that it is achieved through the calculation of all conductive paths and their resistance value. Xiaojuan N. et al. [31], at their 2018 study, have also reported an approach that calculates the resistance of an array of 1D and 2D conductive nanofillers within a polymer, using the Monte Carlo simulation tool, while at their study one year later, they extended to 3D networks [32]. Park et al [33] have also used Monte-Carlo simulations in order to compare with experimental data in a system with similar materials. In these studies, the array of nanofillers is transformed into a resistor network and the resistance is calculated by solving the Kirchhoff's current equations through Gaussian elimination. This study and for the

[8] It should be noted that the deposited NP layer is of 2D nature, having a diameter of Pt-NPs ranging from 2 - 5 nm depending on the deposition process parameters.

purpose of simulating our 2D experiments, the NP network is also being represented as a series of resistors.

This study differentiates from the above- mentioned in terms of the methodology being used, as the linear equations were not solved by Gaussian elimination. Instead a different methodology is being presented (pp.) that calculates the Laplacian Matrix from which we extract the effective resistance between two nodes by calculating the Moore – Penrose pseudoinverse matrix [34 - 37]. The advantage of this approach is the significant amount of computer processing time being saved and thus the ability of conducting an abundance of simulation experiments without loss of accuracy. This simulation tool has been used to compare its results with experimental data obtained with strain sensors developed using the gas condensation technique for the deposition of platinum NPs on flexible substrate. Following this benchmarking step, we then investigated the effect of substrate coverage and nanoparticle size on sensor sensitivity. The results reviled that the sensor sensitivity can be precisely tuned from the above parameters within the chosen experimental platform. It should be remark that although the main usage for the simulation was –for our team- the comparison of sensors developed on polymeric substrate. Nevertheless, the specific approach is applicable for any substrate material and can be extended to tackle a variety of other similar systems like nanocomposite materials filled with metallic NPs or nanowires for flexible and stretchable electronic applications.

4.2. Simulation Methodology

This simulation approach is based on a 2D (n x n) matrix which represents the simulation area. The matrix is consisted of unitary cells (n x n), where each unitary cell covers a surface of 1 nm^2. Assuming that the NPs are deposited uniformly, then the simulation area is only a fraction of the sensors' sensitive area and thus it represents only a fraction of the total resistance. Thus, a small part of the sensitive area is simulated, reducing the required simulation time and processing power. Then the total resistance can be calculated by extending the simulated area of the device, over the entire device-surface; this results in a network of resistors in series as well as in parallel, the total resistance of which can be easily calculated.

The first step of the simulation is to randomly place Pt-NPs - with a mean diameter (size) of 4 nm and standard deviation of 0.8 nm (Fig. 4.1(a)) - over the simulation area. This step is achieved with the Monte Carlo method where in each simulation cell there is a predetermined probability. A random number generated by the code is compared with the probability and if the probability is, then this cell will be the center of a spherical NP. The next step is to initiate a search process for the conductive paths between the edges of the simulated area (Fig. 4.1(c)). Conductive paths should have a length of no more than one empty unitary cell (in the case of vertical and parallel resistances), as can be seen in Fig. 4.2(a); diagonal conductive pathways, should also not exceed the length of the pathway represented by resistance R_{25} in Fig. 4.2(a).

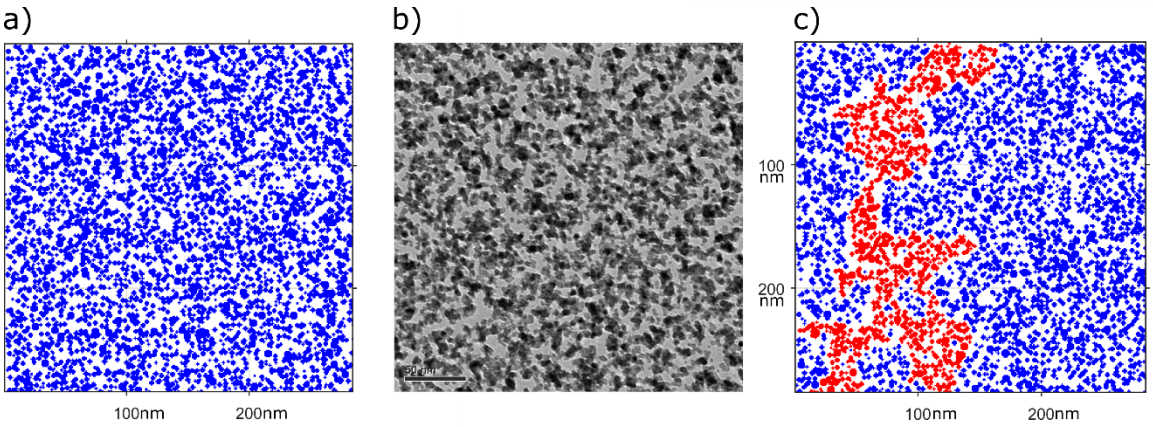

Figure 4.1: a) Simulation of the Pt-NP deposition, blue color represents the NPs and white the substrate, b) TEM image of Pt-NPs, c) Conductive path of Pt-NPs. Red colour represents the NPs that are contributing to the conductive path [38]

The conductive paths are calculated in three steps. The first step is to calculate the path from the bottom to top the electrode. The second is the exact opposite procedure i.e. top to bottom electrode and finally the overlap between the paths this produces the final conductive path as it is illustrated in Fig. 4.3(a) and 4.3(b). By reversing the first two steps we obtain the exact same result. Which is not unreasonable because the real sensors do not have polarity. After the conductive path calculation, the code calculates paths resistance. The path is then translated into an equivalent circuit by considering that the NPs and the NP- islands define the nodes and the inter-particle gaps define the resistances (Fig. 4.2).

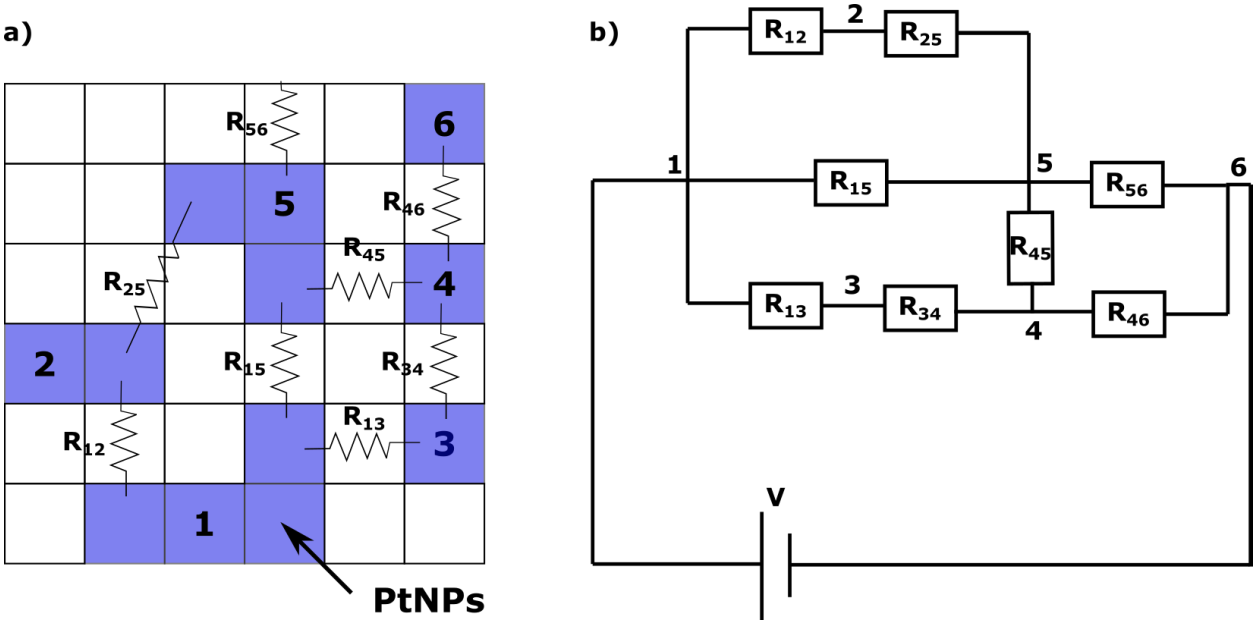

Figure 4.2: a) Schematic representation of the resistances between NPs and NP-islands, b) their equivalent circuit. [38]

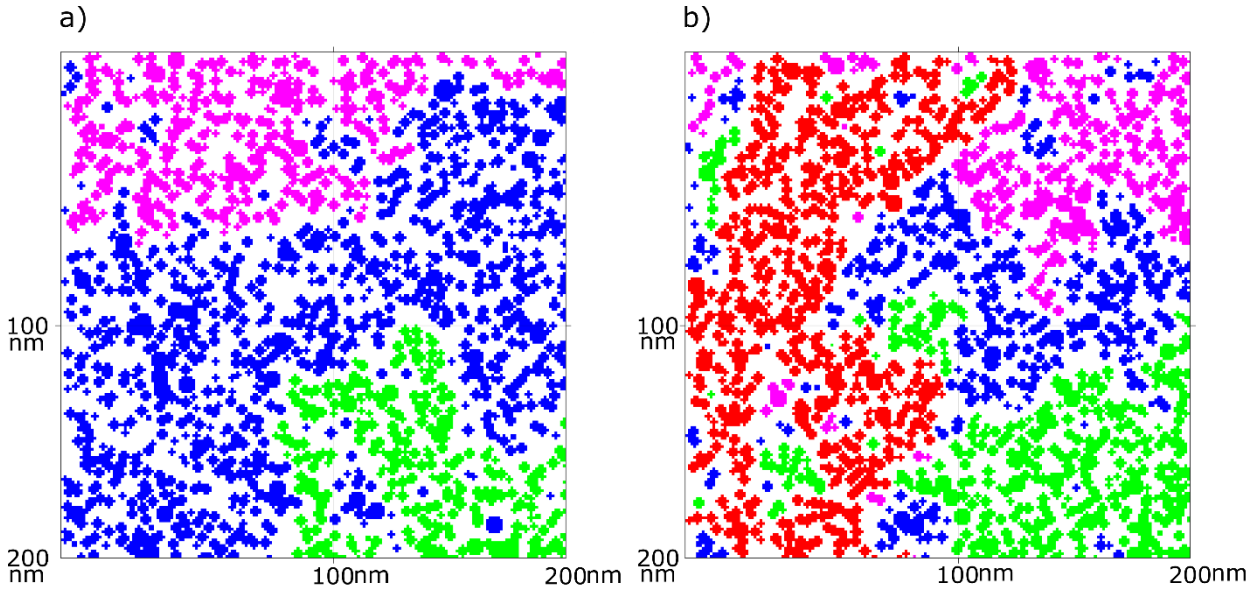

Figure 4.3: Calculation of the conductive path. a) Calculation of the path from the bottom electrode to the top (green) and from the top to the bottom (pink). In the first case the two paths do not overlap and there is no connection between the two electrodes. In the second case b) the two paths partially overlap, therefore producing the red path, which is conductive Blue represents the NPs that do not contribute to either paths [38]

Each resistance can be then calculated by the equation (3.6). In the following table are listed the physical constants values that were used in the simulations.

	Symbol	Value	Units
Poisson ratio of kapton	V	0.278	-
electron charge	E	$1.60217662*10^{-19}$	C
vacuum permittivity	ε_0	$8.854878128*10^{-12}$	$C^2/(Nm^2)$
relative permittivity of air	E	1.000589	-
Boltzmann constant	K_b	$8.617333262145*10^{-5}$	eV/K
Temperature	T	300	K
electron coupling term	β	28	1/nm
pre-exponential constant	R_0	$8.5*10^{-8}$	Ohm

Table 4.1: Table of constants [38]

Resistance's value is calculated based on its orientation. For example, resistances R_{12}, R_{15}, R_{46} etc. in the illustrating example of Fig. 4.3 are vertical to the electrodes; resistances R_{13}, R_{45} are parallel to the electrodes and finally resistance R_{25} has a diagonal orientation. The next step is the calculation of the effective resistance of the entire circuit. Because of the complexity of the circuits that are generated by the conductive paths, the effective resistance is calculated with the use of the Laplace (Kirchhoff) matrix. The most common method to calculate the resistance in complex circuits is to calculate the current that flows through the circuit via the Kirchhoff equations. Usually a large number of equations must be solved in that case and thus the computational time becomes exceedingly large.

The resistance is calculated with the use of the Laplacian Matrix L^w, which is defined by the following equation [34 - 37]:

$$L_{ij}^{w} = \begin{cases} c_{ii} = \sum_{i} c_{ij}, & if\ i = j \\ -c_{ij}, & if\ i \neq j \end{cases} \tag{4.1}$$

Where c_{ij} is the conductivity between the nodes *i* and *j*. The Laplace matrix could be also created by applying the Kirchhoff's Current Law (KCL) and the Kirchhoff's Voltage Law (KVL).

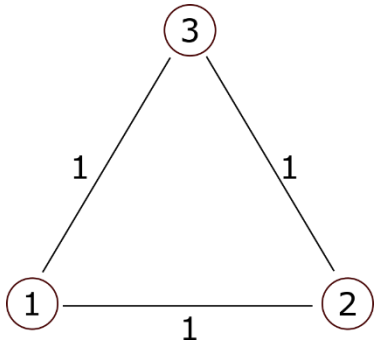

Figure 4.4: Example of three nodes connected each other with a resistance of 1 Ohm [38]

For example in Fig. 4.4 three nodes are represented (namely 1, 2 and 3), each one connected with the other with a resistance of 1 Ohm. If the current flow from node-1 to node-2 is denoted by *I*, then the effective resistance is calculated by the application of the KCL:

$$\begin{aligned} i_{12} + i_{13} &= I \\ i_{21} + i_{23} &= -I \\ i_{31} + i_{32} &= 0 \end{aligned} \tag{4.2}$$

Combing with Ohm's Law:

$$i_{12} = c_{12}(v_1 - v_2) \tag{4.3}$$

Where $c_{ij} = 1/r_{ij}$, which in this example is equal to 1 S. The above equations become:

$$\begin{aligned} 2v_1 - v_2 - v_3 &= I \\ -v_1 + 2v_2 - v_3 &= -I \end{aligned} \tag{4.4}$$

$$-v_1 - v_2 + 2v_3 = 0$$

This can be written in matrix form as follows:

$$\begin{bmatrix} 2 & -1 & -1 \\ -1 & 2 & -1 \\ -1 & -1 & 2 \end{bmatrix} \begin{bmatrix} v_1 \\ v_2 \\ v_3 \end{bmatrix} = \begin{bmatrix} I \\ -I \\ 0 \end{bmatrix} \tag{4.5}$$

$$CV = I \tag{4.6}$$

The matrix C is the weighted Laplacian matrix for the system, while it satisfies the Ohm's Law (4.3). The matrix L^w is symmetric and the sum of all rows and columns equals to zero. In order to calculate the effective resistance we must apply the KCL and the KVL. If a voltage source is being connected between the nodes a and b, then the KCL will be written as:

$$\sum_{i,j \in N(i)} I_{ij} = \begin{cases} I, & if\ i = a \\ -I, & if\ i = b \\ 0, & otherwise \end{cases} \tag{4.7}$$

Where *N(i)* is in the neighborhood of the values of node *i*. Equation (4.7) expresses that the current flow into a node equals the flow out of it. Combining (4.7) with $c_{ij} = 1/r_{ij}$

$$\sum_{i,j \in N(i)} (v_i - v_j)c_{ij} = v_i \sum_{j \in N(i)} c_{ij} - \sum_{j \in N(i)} v_i c_{ij} = \begin{cases} I, & if\ i = a \\ -I, & if\ i = b \\ 0, & otherwise \end{cases} \tag{4.8}$$

$$L^w v = I(e_a - e_b) \tag{4.9}$$

Where e_i is the base vector with value 1 in position *i* and zero everywhere else.

$$v = I(L^w)^+(e_a - e_b) \tag{4.10}$$

Where $(L^w)^+$ is the Moore-Penrose pseudoinverse Laplacian matrix. From Ohm's Law:

$$R_{ab} = \frac{v_a - v_b}{I} \tag{4.11}$$

$$R_{ab} = (e_a - e_b)^T \frac{v}{I} \tag{4.12}$$

Combining equations (4.10) and (4.12):

$$R_{ab} = (e_a - e_b)^T (L^w)^+ (e_a - e_b) \tag{4.13}$$

$$R_{ab} = (L^w)^+_{aa} - 2(L^w)^+_{ab} + (L^w)^+_{bb} \tag{4.14}$$

Where $(L^w)^+_{ij}$ is the *ij* element of the Moore-Penrose pseudo-inversed Laplacian matrix. Equation (4.14) gives the effective resistance between nodes a and b. This method is much faster than solving equation (4.6) and calculates all currents and voltages of the circuit. However, we note that the proposed method is useful if resistance is the only quantity of interest, the case herein, or in similar problems. If physical quantities such as currents and voltages must be also calculated, the equation (4.6) must be solved analytically.

From equation (4.14) the effective resistance between nodes a and b can be calculated. If we assume that nodes a and b are the electrodes, equation (4.14) calculates the resistance corresponding to the entire simulation area. After the calculation of the initial resistance, strain (γ) is applied to the entire simulation area. The unitary cells change their dimensions from 1 nm x 1nm to *(1 + ds)* nm x *(1 – ds')* nm where *ds* is the unit length change due to the application of strain and ds' its corresponding change due to Poisson ratio of the substrate. While the simulation area is under strain, the nanoparticles are considered pinned at their initial positions. After each step, the Laplacian matrix is updated and the resistance is recalculated.

The GF of the sensor is then calculated by the following equation:

$$GF = \frac{\Delta R}{R} / \gamma \tag{4.15}$$

Fig. 4.5 presents the flow chart of the simulation process. The entire simulation code is attached in appendix A.

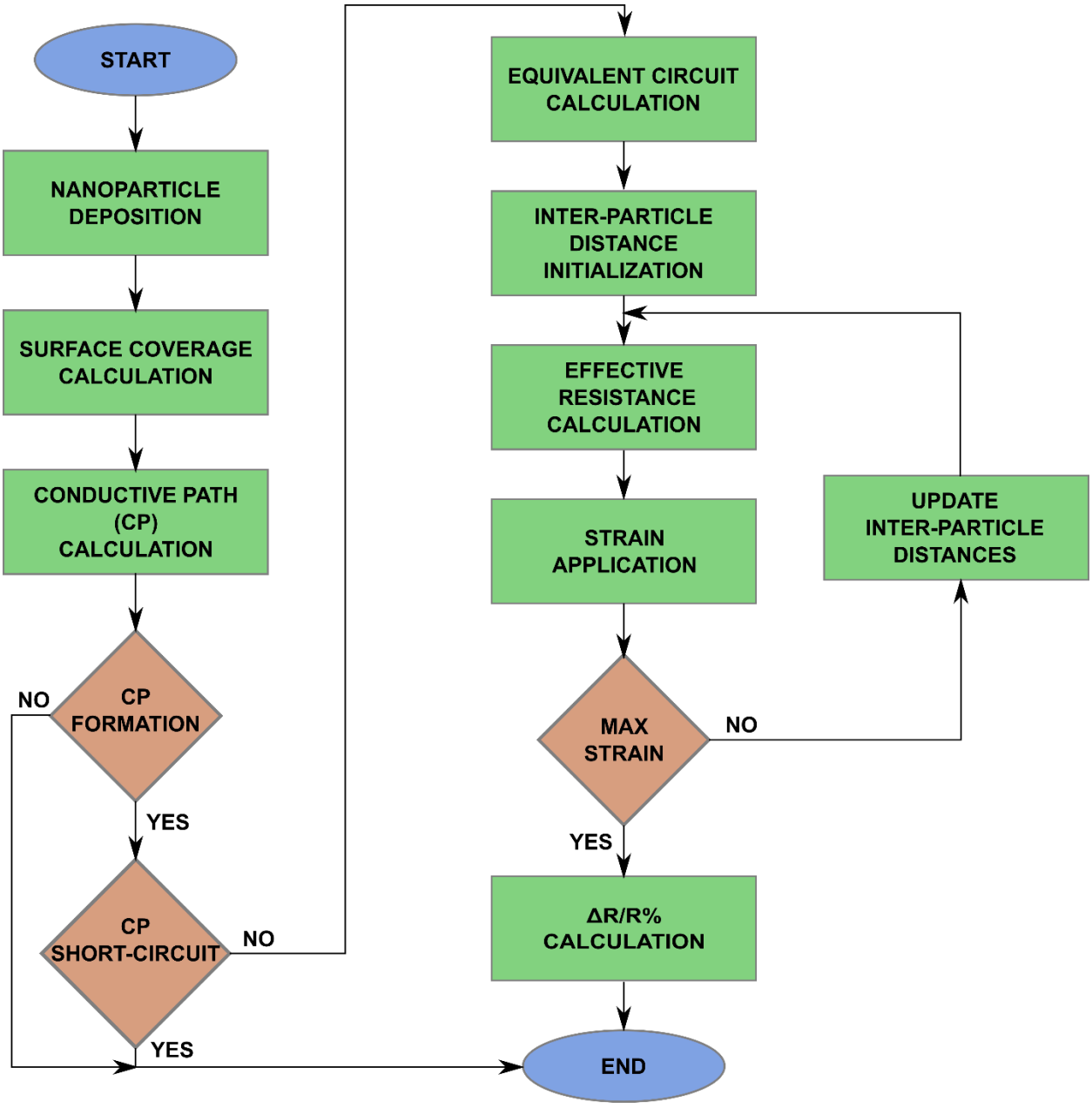

Figure 4.5: Flow chart of the simulation. [38]

4.3. Results

4.3.1. Comparison of simulation and experimental results

The simulations were compared with experimental data from chapter 3 on NPs between interdigitated electrodes strain sensors made on kapton substrates [5], in order to benchmark the simulation results. Along these lines, inter-finger spacing was set to 10 µm, electrode width

was 3 cm while NP mean diameter was 4 nm and the surface coverage was 50%. The relative resistance change, which determines the sensitivity, is given by the following equation:

$$\frac{\Delta R}{R} = \exp(\beta ds)\exp\left(\frac{e^2}{8\pi\varepsilon\varepsilon_0 K_b T}\right)\left(\frac{1}{r+s} - \frac{1}{r+s+ds}\right) - 1 \qquad (4.16)$$

Where *ds* is the additional length between the nanoparticles due to strain. Equation 4.16 shows that *ΔR/R* is highly dependent on *β* value. Fig. 4.6 shows a fitting of experimental data using a nanoparticle strain sensor with the simulation results from which the value of *β* is determined to be 28 nm^{-1}.

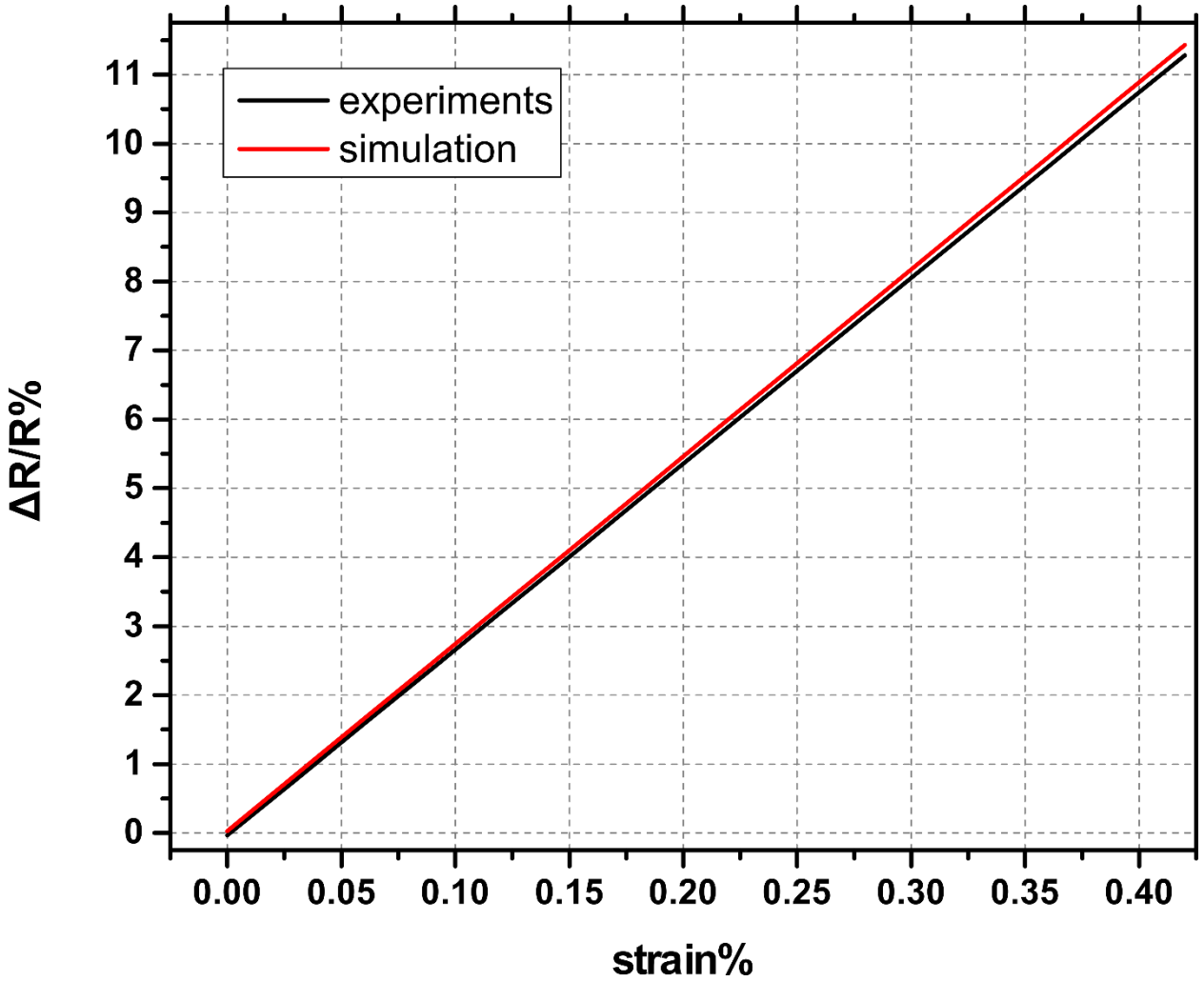

Figure 4.6: Comparison of the experimental data (red) and the simulation results (black). [38]

The simulation results and the experimental data have great agreement regarding the sensitivity. The initial resistance of the sensors is also in great agreement with a mean value of 500 kΩ for both experimental and simulation results.

4.3.2. Surface coverage calculation

Sensors based on nanoparticles exhibit their optimum performance in a specific surface coverage working window. In this working window the NPs must be dense enough to create a conductive path from one electrode to the other, but at the same time not to create short-circuit between the two electrodes. The working window was realized by calculating the probability to form a conductive path that does not create short-circuit between the two electrodes, after performing 100 simulations for NPs with mean diameter of 2, 4, 6, 8 and 10 nm and with varying surface coverage. The probabilities have been calculated with reference to the total number of simulation runs (i.e. 100). To calculate an accurate working window, an acceptable percentage of devices with a conductive path (and without a short circuit) must be chosen. In this case, the percentage is chosen to be above 50% for every surface coverage and NP mean diameter. The next step is to estimate the surface coverage working window in which the Gaussian distribution function value is greater or equal to 0.5 -probability greater than 50% (grey area in Fig. 4.7). We remark that the percentage of 100% was not chosen since in some cases, e.g. for the NPs with mean diameter of 6, 8 and 10 nm, this value cannot be reached; a probability equal or higher than 50% can be attained by all the NP mean diameters and is also large enough to ensure that the majority of the simulation-runs will return a useful result.

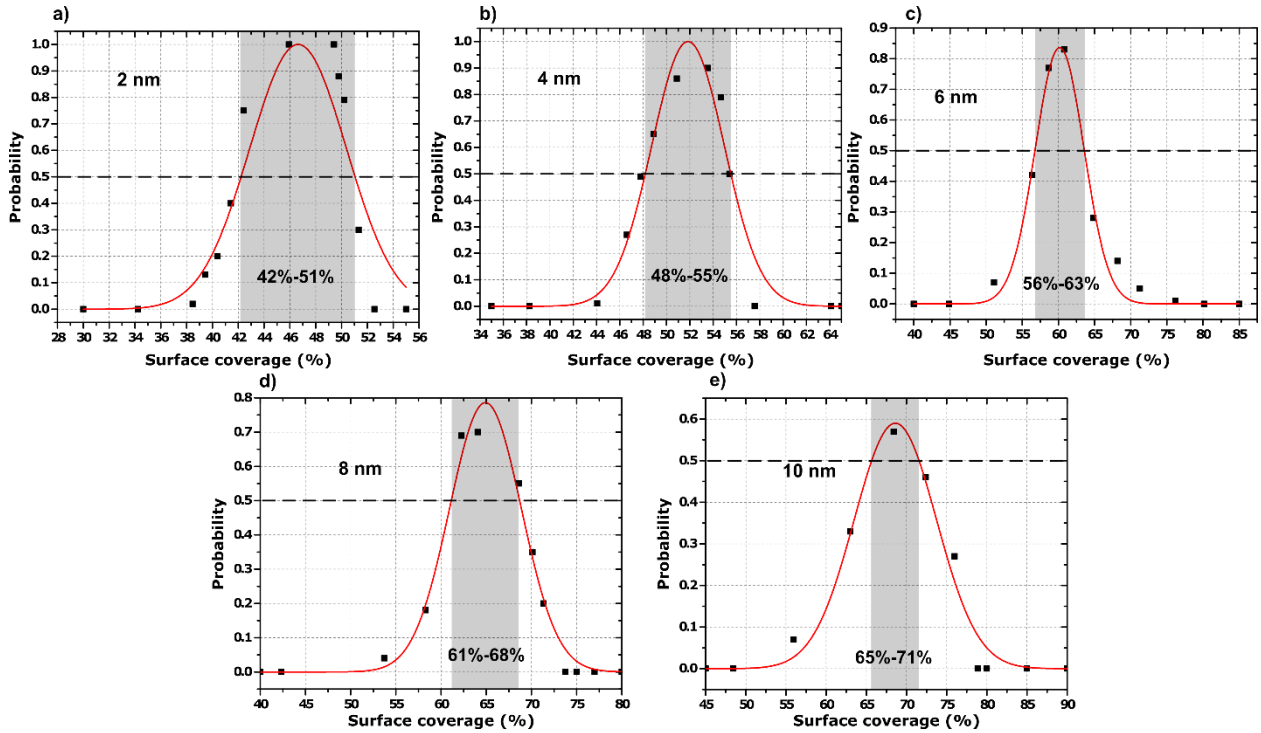

Figure 4.7: Gaussian distribution function of the probability for sensors with NPs mean diameter of a) 2 nm, b) 4 nm, c) 6 nm, d) 8 nm and e) 10 nm. The grey area indicates the working window for each NPs film. [38]

Diameter (nm)	Surface coverage %

2	42 - 51																														
4						48 - 55																									
6													56 – 63																	
8																	61 – 68													
10																						65 – 71								

Table 4.2: Results of the working window for each NP mean diameter. [38]

Table 4.2 shows the results of the working window for each NPs mean diameter. The width of the window is 9 %, 7 %, 7 %, 7 % and 6 % for NPs with mean diameter of 2 nm, 4 nm, 6 nm, 8 nm and 10 nm respectively. The gradual reduction of the working window is due to the increase of the mean surface of the individual NPs. As can be seen in Fig. 4.8, films with larger NPs resulted in larger surface coverage with fewer NPs, which is to be expected. In addition, for conductive devices with larger NPs (NP mean diameter ≥ 6 nm) any additional NPs lead to the creation of a short-circuit.

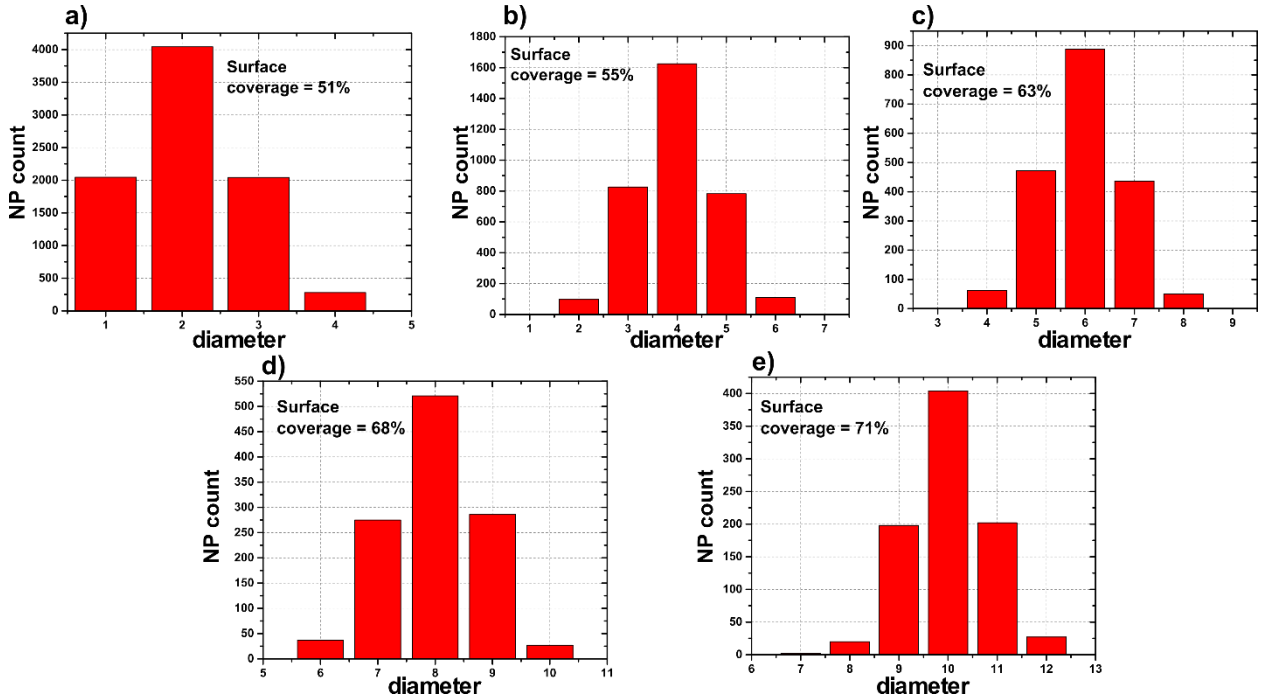

Figure 4.8: Number of NPs in films with mean diameter of a) 2 nm, b) 4 nm, c) 6 nm, d) 8 nm and e) 10 nm with surface coverage of 51%, 55%, 63%, 68% and 71% respectively. Each one of them have standard deviation of 0.8. [38]

4.3.3. Predicting sensor sensitivity through Simulation

Simulation tool can be used to explore the impact of a large number of parameters on device performance. That process that can be cumbersome or impossible if it is to be performed experimentally. The simulation tool presented herein has the capability to predict the sensitivities of NP based sensors with varying NP mean diameter and surface coverage. After the calculation of the working window for different NP mean diameter, the sensitivities of the

corresponding sensors have also been calculated. Fig. 4.9 shows the sensitivities of different sensors, within their corresponding surface coverage working-windows.

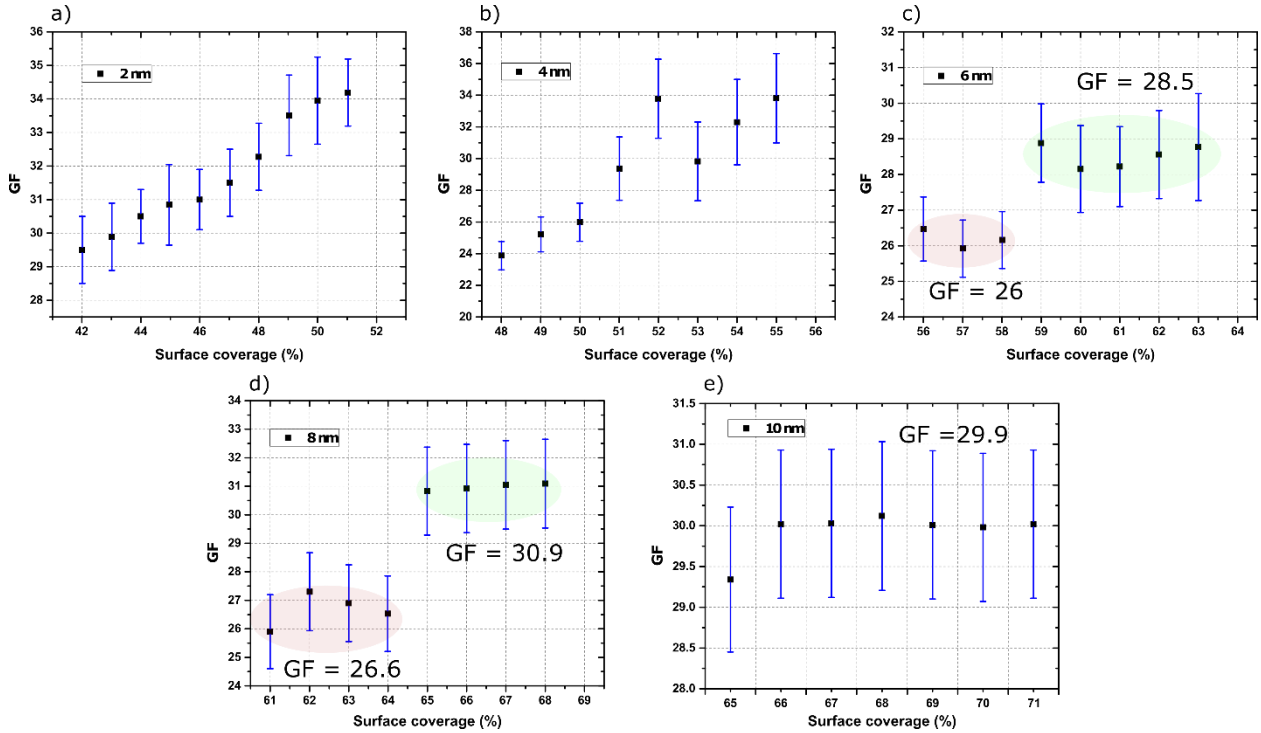

Figure 4.9: Sensitivities of sensors using NPs films with NPs mean diameter of a) 2 nm, b) 4 nm, c) 6 nm, d) 8 nm and e) 10 nm. [38]

The shape of the conductive paths (Fig. 4.10) as well as the number and distribution of inter-particle gaps in vertical/diagonal and parallel (Fig. 4.11 and 4.12), can explain the sensitivity variations as seen in Fig. 4.9. As the NP surface coverage increases more inter-particle distances are introduced (Fig. 4.10(a) and 4.10(b)), contributing to the formation of additional conductive paths. These new inter-particle distances can again be matched with vertical, parallel or diagonal resistances. Vertical and diagonal resistances increase in value with the application of strain while parallel resistances decrease, according to the Poisson ratio. Analytical calculations of the overall number of vertical/diagonal and parallel paths, for varying NP mean diameter and surface coverage can be seen in Fig. 4.11. As shown in Fig. 4.11(a) and 4.11(b) for NPs of 2 and 4 nm in size, the addition of new inter-particle distances with reinforcing effect to the sensitivity (vertical and diagonal resistances) is more likely than the addition of ones that decrease the sensitivity (parallel resistances); this holds true up to a certain surface coverage value that depends on NP mean diameter. Fig. 4.11(a) and 4.11(b) show that the rate of change for parallel resistances is lower than the one for vertical/diagonal resistances, for increasing surface coverage. Thus, as the surface coverage increases sensitivity will also increase, since vertical/diagonal resistances contribute constructively in device sensitivity. After a certain surface coverage, the overall number of resistances decreases and the sensitivity remains constant henceforth, since both resistances now show a similar rate of reduction. In the case of devices with NPS of 6 and 8 nm in size sensitivity can be seen to fluctuate around two distinctive mean values, while in the case

of 10 nm its value remains relatively constant (Fig. 4.9(d) and 4.9(e)). In the case of 10 nm NPs, device sensitivity can be seen to be more stable with less abrupt changes while it fluctuates around specific mean values of GFs (Fig. 4.9(d) and 4.9(e)). The latter goes hand in hand with the small fluctuation in the difference between vertical/diagonal and parallel paths (Fig. 4.11(e)) and the small fluctuation in the total number of resistances (Fig. 4.12(e)) as well as their small value. Increasing NP size leads to ever smaller number of required NPs for conductive pathway formation, as well as to smaller numbers of inter-particle resistances. In addition, the sensitivity jump that is observed for a surface coverage of 59% and 65% in the case of 6 and 8 nm NPs respectively, can be again attributed in the respective increase in the absolute number of vertical/diagonal resistances in relation to parallel resistances (Fig. 4.11(c), 4.11(d) and 4.12(c), 4.12(d)).

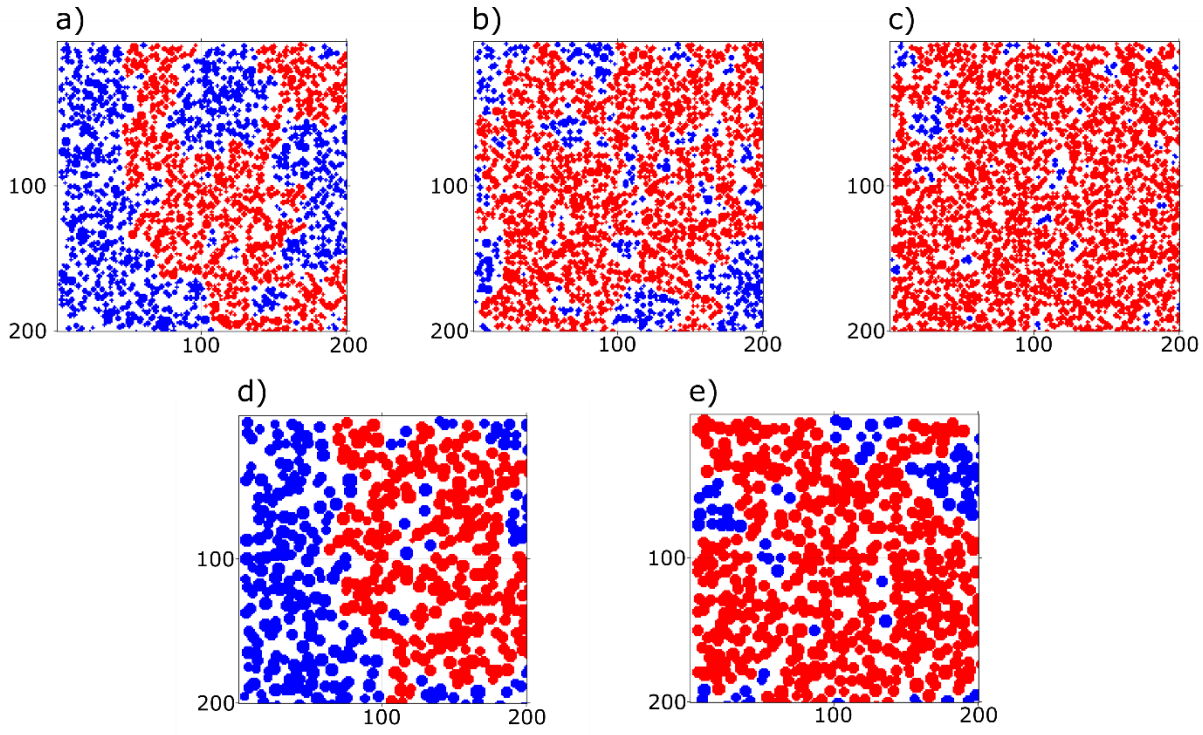

Figure 4.10: Conductive paths (red) for NPs mean diameter of 4 nm for surface coverage of a) 49%, b) 52% and c) 55%. Conductive paths for NPs with NPs mean diameter of 8 nm for surface coverage of d) 63% e) 66%. [38]

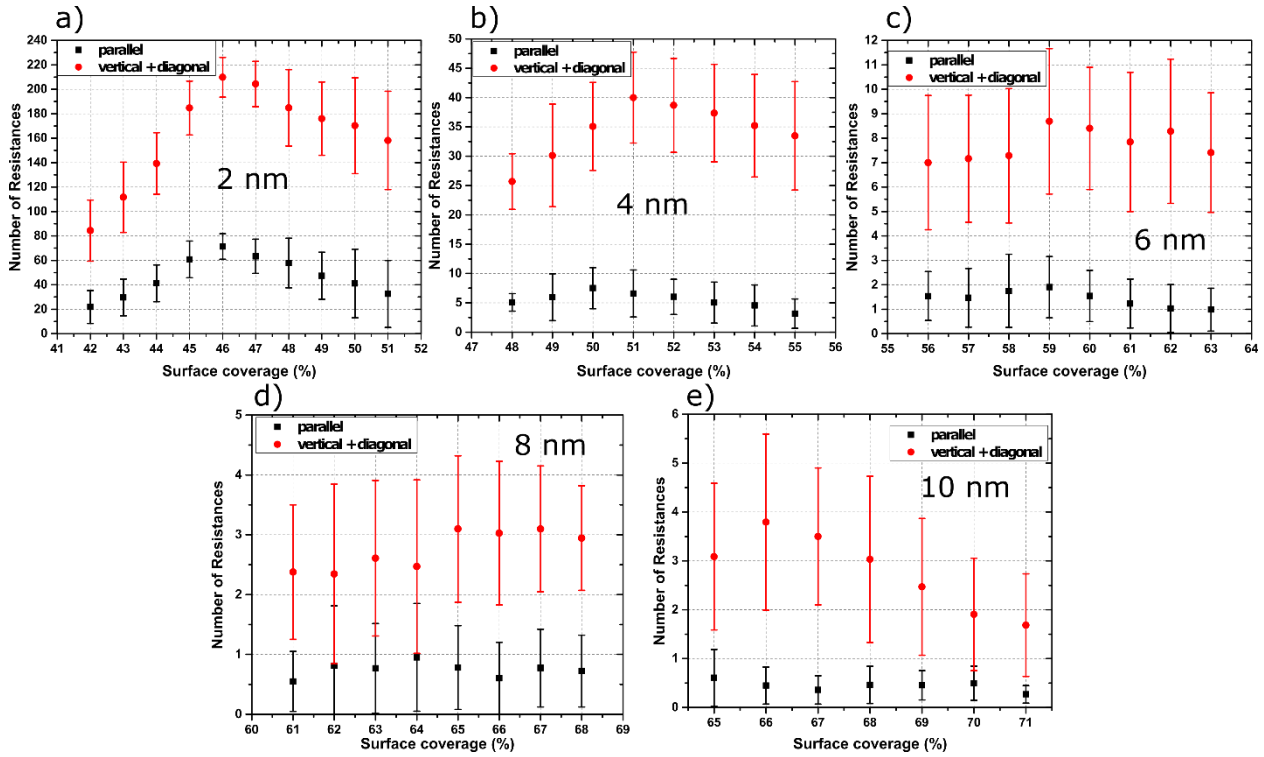

Figure 4.11: Comparison between the mean number of vertical and diagonal resistances (red) and parallel resistances (black), for varying surface coverage and for NP size of a) 2 nm, b) 4 nm, c) 6 nm, d) 8 nm and e) 10 nm. Error bars represent the standard deviation after 100 simulations. [A]

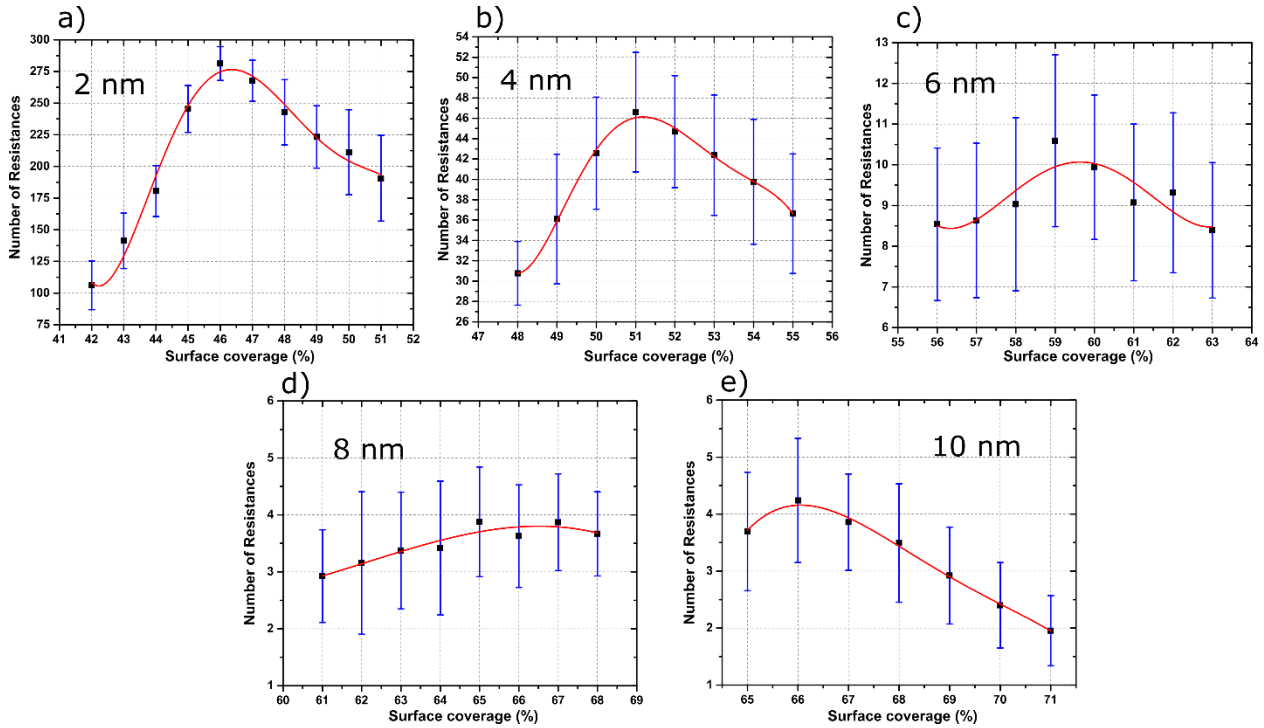

Figure 4.12: Mean number of inter-particle distances that contribute to the conductive path (resistances) for varying surface coverage and for NP mean diameter of a) 2 nm, b) 4 nm, c) 6 nm, d) 8 nm and e) 10 nm. Error bars represent the standard deviation after 100 simulations. [38]

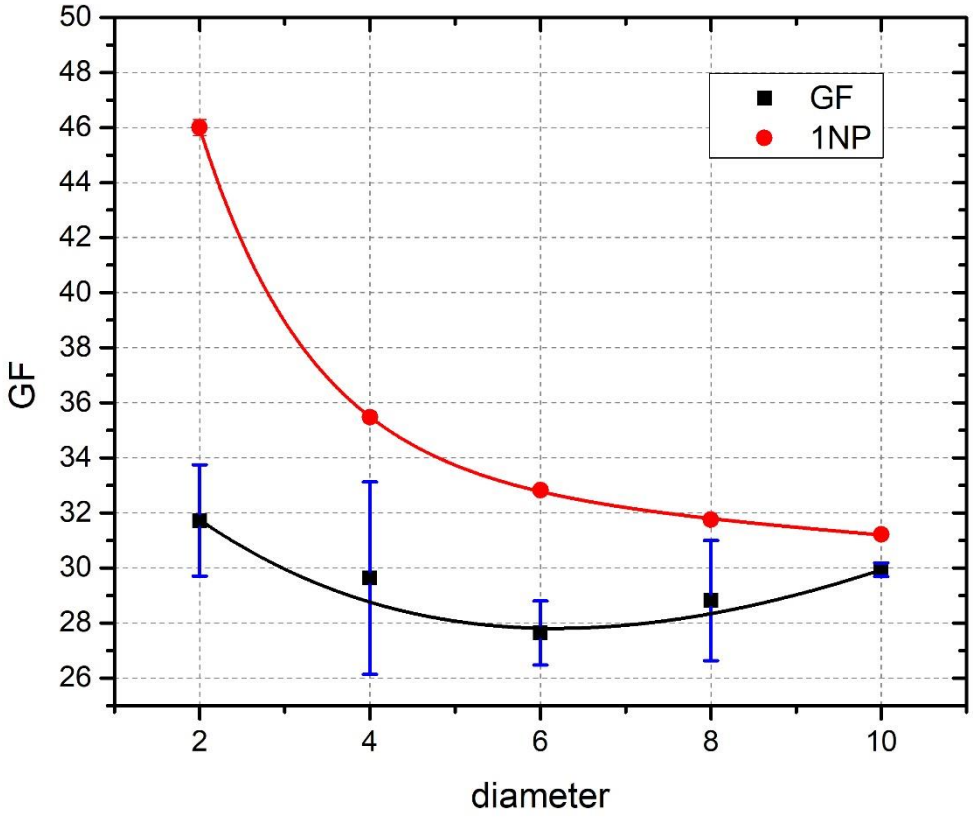

Figure 4.13: Sensitivity of one NP sensor (red), mean value of NP film sensor (black). [38]

The maximum *ΔR/R%* can be achieved if a single nanoparticle is placed between two electrodes and for a small tunneling-distance (0.5 nm); in this case the distances between particle and electrodes are defined as "vertical". Fig. 4.13 shows simulation results comparing the sensitivity of a single-NP sensor and sensors with NP-films, for varying NP mean diameter. The results for a single-NP sensor are obtained using equation (4.17), which depends from the values of *β* and *r*. The inter-particle distance *s* was kept constant for all NP mean diameter. As can be seen in Fig. 4.13, sensors with NP-films show a different trend from the single-NP sensors. Both sensitivities start with large values, because of the very small mean diameter of the NPs, and then gradually decrease. The sensitivity of the single-NP sensor approaches the value of 30 while the GF of the NP-film sensor first decreases and then slightly increases approaching the same value with the single-NP sensor. The initial sensitivity decrease of the NP-film sensor is due to the addition of parallel inter-particle gaps, which decrease the relative resistance change value. After the NP mean diameter becomes greater than 6 nm the sensitivity increase approaches the same value as the single-NP sensor. This increase is due to the saturation of the NP films, which causes the majority of the inter-particle gaps to be vertical rather than parallel. As the NPs' mean

diameter increases, more inter-particle distances disappear and both sensitivities approach the same value.

Sangeetha et al [39] and Hermann et al [40] found that as the NP diameter increases, the sensitivity should also increase. Their finding is based on the following argument: the NPs have surface coverage of 100%, making it possible to express the length of the sensor in relation to NP diameter as the next equation shows:

$$L = N(r + s) \tag{4.17}$$

Where *L* is the sensors' length and *N* the number of NPs. The GF then is given by the following equation:

$$GF = \beta(r + s) \tag{4.18}$$

Equation (4.17) holds true only if L can be expressed in proportion to the number of NPs. When the NPs do not cover the entirety of the surface and the electron transfer from one electrode to the other does not follow a straight path, equation (4.17) is not valid and neither is equation (4.18). As it is shown in Fig. 4.10(c) and 4.10(a) for small NP diameter and small surface coverage, the conductive path can rarely be a straight line. Consequently, it is not possible to express the length of the sensor using equation (4.17) and therefore the GF does not depend from the diameter of the NPs. However, as the NPs mean diameter increases and their working window shifts to larger surface coverage values (Fig. 4.10(d) and 4.10(e)), almost all NPs are contributing to the conductive path and equation (4.17) can describe the length of the sensor. However, the inter-particle distance l is not always the same and a mean value should be calculated. Fig. 4.13 shows that the GF of NP-film sensors begins to depend from NP diameter when this is larger than 6 nm. In this case, the NPs contributing to the conductive path can be described by equation (4.17) hence sensor sensitivity depends from the diameter of the NPs.

4.4. Conclusions

The Monte Carlo simulation tool was deemed necessary as to calculate and predict the sensitivity of NP strain sensors. Although this method has been used in the past in this chapter we presented a different methodology that allows faster computing processing and consequently more simulation experiments, without sacrificing accuracy.

During this study we used Platinum NPs as sensing material and kapton as the substrate, however the tool can be used with different materials and a large range of application from the calculation of the sensitivity to the calculation of percolation threshold.

The Monte Carlo simulation tool can be used to predict the optimum surface coverage so as to obtain the highest sensitivity when the size of the NPs is known. Apart from that it can be used as a mean of predicting the sensitivity of the sensor for various NP sizes, and define the optimum surface coverage for each one of them. All of the above could be very useful for optimizing the fabrication of NP strain sensors, given the variety of application areas and the ever-growing need of energy saving, cost reduction and increased needs of everyday life.

This work was published in the scientific journal Nanotechnology [38].

4.5. References

[1] Lee WS, Lee SW, Joh H, Seong M, Kim H, Kang MS, Cho KH, Sung YM, Oh SJ, Designing metallic and insulating nanocrystal heterostructures to fabricate highly sensitive and solution processed strain gauges for wearable sensors, Small, 2017 Dec;13(47):1702534.

[2] Lee WS, Kim D, Park B, Joh H, Woo HK, Hong YK, Kim TI, Ha DH, Oh SJ, Multiaxial and Transparent Strain Sensors Based on Synergetically Reinforced and Orthogonally Cracked Hetero-Nanocrystal Solids, Advanced Functional Materials, 2019 Jan;29(4):1806714.

[3] Zhang S, Cai L, Li W, Miao J, Wang T, Yeom J, Sepúlveda N, Wang C, Fully Printed Silver-Nanoparticle-Based Strain Gauges with Record High Sensitivity, Advanced Electronic Materials, 2017 Jul;3(7):1700067.

[4] Tanner JL, Mousadakos D, Giannakopoulos K, Skotadis E, Tsoukalas D, High strain sensitivity controlled by the surface density of platinum nanoparticles, Nanotechnology, 2012 Jun 21;23(28):285501.

[5] Aslanidis E, Skotadis E, Moutoulas E, Tsoukalas D, Thin Film Protected Flexible Nanoparticle Strain Sensors: Experiments and Modeling, Sensors, 2020 Jan;20(9):2584.

[6] Patsiouras L, Skotadis E, Gialama N, Drivas C, Kennou S, Giannakopoulos K, Tsoukalas D, Atomic layer deposited Al2O3 thin films as humidity barrier coatings for nanoparticle-based strain sensors, Nanotechnology, 2018 Sep 20;29(46):465706.

[7] Zheng M, Li W, Xu M, Xu N, Chen P, Han M, Xie B, Strain sensors based on chromium nanoparticle arrays, Nanoscale, 2014; 6(8):3930-3.

[8] Xie B, Mao P, Chen M, Li Z, Liu C, Qin Y, Yang L, Wei M, Liu M, Wang X, Han D, A tunable palladium nanoparticle film-based strain sensor in a Mott variable-range hopping regime, Sensors and Actuators A: Physical, 2018 Apr 1;272:161-9.

[9] Lee GY, Kim MS, Min SH, Kim HS, Kim HJ, Keller R, Ihn JB, Ahn SH, Highly Sensitive Solvent-free Silver Nanoparticle Strain Sensors with Tunable Sensitivity Created Using an Aerodynamically Focused Nanoparticle Printer, ACS applied materials & interfaces, 2019 May 31;11(29):26421-32.

[10] Aslanidis E, Skotadis E, Tsoukalas D, Resistive crack-based nanoparticle strain sensors with extreme sensitivity and adjustable gauge factor, made on flexible substrates, Nanoscale, 2021;13(5):3263-74.

[11] Chen M, Luo W, Xu Z, Zhang X, Xie B, Wang G, Han M, An ultrahigh resolution pressure sensor based on percolative metal nanoparticle arrays, Nature communications, 2019 Sep 6;10(1):1-9.

[12] Kano S, Kim K, Fujii M, Fast-response and flexible nanocrystal-based humidity sensor for monitoring human respiration and water evaporation on skin, ACS sensors, 2017 Jun 23;2(6):828-33.

[13] Willner MR, Vikesland PJ, Nanomaterial enabled sensors for environmental contaminants, Journal of nanobiotechnology, 2018 Dec;16(1):1-6.

[14] Skotadis E, Kanaris A, Aslanidis E, Michalis P, Kalatzis N, Chatzipapadopoulos F, Marianos N, Tsoukalas D, A sensing approach for automated and real-time pesticide detection in the scope of smart-farming, Computers and electronics in agriculture, 2020 Nov 1;178:105759.

[15] Madianos L, Tsekenis G, Skotadis E, Patsiouras L, Tsoukalas D, A highly sensitive impedimetric aptasensor for the selective detection of acetamiprid and atrazine based on microwires formed by platinum nanoparticles, Biosensors and Bioelectronics, 2018 Mar 15;101:268-74.

[16] Chang CC, Chen CP, Wu TH, Yang CH, Lin CW, Chen CY, Gold nanoparticle-based colorimetric strategies for chemical and biological sensing applications, Nanomaterials, 2019 Jun;9(6):861.

[17] Kang MS, Joh H, Kim H, Yun HW, Kim D, Woo HK, Lee WS, Hong SH, Oh SJ, Synergetic effects of ligand exchange and reduction process enhancing both electrical and optical properties of Ag nanocrystals for multifunctional transparent electrodes, Nanoscale, 2018;10(38):18415-22.

[18] Russo S, Ranzani T, Liu H, Nefti-Meziani S, Althoefer K, Menciassi A, Soft and stretchable sensor using biocompatible electrodes and liquid for medical applications, Soft robotics, 2015 Dec 1;2(4):146-54.

[19] Ha M, Lim S, Ko H, Wearable and flexible sensors for user-interactive health-monitoring devices, Journal of Materials Chemistry B, 2018;6(24):4043-64.

[20] Lee WS, Jeon S, Oh SJ, Wearable sensors based on colloidal nanocrystals, Nano convergence, 2019 Dec;6(1):10.

[21] Shengbo S, Lihua L, Aoqun J, Qianqian D, Jianlong J, Qiang Z, Wendong Z, Highly sensitive wearable strain sensor based on silver nanowires and nanoparticles, Nanotechnology, 2018 Apr 25;29(25):255202.

[22] Joh H, Lee SW, Seong M, Lee WS, Oh SJ, Engineering the Charge Transport of Ag Nanocrystals for Highly Accurate, Wearable Temperature Sensors through All-Solution Processes, Small, 2017 Jun;13(24):1700247.

[23] Yi Y, Wang B, Bermak A, A Low-Cost Strain Gauge Displacement Sensor Fabricated via Shadow Mask Printing, Sensors, 2019 Jan;19(21):4713.

[24] Zhang Y, Anderson N, Bland S, Nutt S, Jursich G, Joshi S, All-printed strain sensors: Building blocks of the aircraft structural health monitoring system, Sensors and Actuators A: Physical, 2017 Jan 1;253:165-72.

[25] Skotadis E, Aslanidis E, Kainourgiaki M, Tsoukalas D, Nanoparticles Synthesised in the Gas-Phase and Their Applications in Sensors: A Review, Applied Nano, 2020 Dec;1(1):70-86.

[26] Kroese DP, Brereton T, Taimre T, Botev ZI, Why the Monte Carlo method is so important today, Wiley Interdisciplinary Reviews: Computational Statistics, 2014 Nov;6(6):386-92.

[27] Mesta M, Carvelli M, De Vries RJ, Van Eersel H, Van Der Holst JJ, Schober M, Furno M, Lüssem B, Leo K, Loebl P, Coehoorn R, Molecular-scale simulation of electroluminescence in a multilayer white organic light-emitting diode, Nature materials, 2013 Jul;12(7):652-8.

[28] Forró C, Demkó L, Weydert S, Vörös J, Tybrandt K, Predictive model for the electrical transport within nanowire networks, ACS nano, 2018 Nov 6;12(11):11080-7.

[29] Stenzel O, Koster LJ, Thiedmann R, Oosterhout SD, Janssen RA, Schmidt V, A new approach to model-based simulation of disordered polymer blend solar cells, Advanced Functional Materials, 2012 Mar 21;22(6):1236-44.

[30] Thiedmann R, Stenzel O, Spettl A, Shearing PR, Harris SJ, Brandon NP, Schmidt V, Stochastic simulation model for the 3D morphology of composite materials in Li–ion batteries, Computational Materials Science, 2011 Dec 1;50(12):3365-76.

[31] Ni X, Hui C, Su N, Jiang W, Liu F, Monte Carlo simulations of electrical percolation in multicomponent thin films with nanofillers, Nanotechnology, 2018 Jan 11;29(7):075401.

[32] Ni X, Hui C, Su N, Cutler R, Liu F, A 3D percolation model for multicomponent nanocarbon composites: the critical role of nematic transition, Nanotechnology, 2019 Feb 20;30(18):185302.

[33] Park SH, Hwang J, Park GS, Ha JH, Zhang M, Kim D, Yun DJ, Lee S, Lee SH, Modeling the electrical resistivity of polymer composites with segregated structures, Nature communications, 2019 Jun 10;10(1):1-1.

[34] Ellens W, Spieksma FM, Van Mieghem P, Jamakovic A, Kooij RE, Effective graph resistance, Linear algebra and its applications, 2011 Nov 15;435(10):2491-506.

[35] Benda R, Cancès E, Lebental B, Effective resistance of random percolating networks of stick nanowires: Functional dependence on elementary physical parameters, Journal of Applied Physics, 2019 Jul 28;126(4):044306.

[36] Wu FY, Theory of resistor networks: the two-point resistance, Journal of Physics A: Mathematical and General, 2004 Jun 16;37(26):6653.

[37] Devriendt K, Effective resistance is more than distance: Laplacians, Simplices and the Schur complement, arXiv preprint arXiv:2010.04521, 2020 Oct 9.

[38] Aslanidis E, Skotadis E, Tsoukalas D, Simulation tool for predicting and optimizing the performance of nanoparticle based strain sensors, Nanotechnology, 2021 Mar 24.

[39] Sangeetha NM, Decorde N, Viallet B, Viau G, Ressier L, Nanoparticle-based strain gauges fabricated by convective self assembly: Strain sensitivity and hysteresis with respect to nanoparticle sizes, The Journal of Physical Chemistry C, 2013 Jan 31;117(4):1935-40.

[40] Herrmann J, Müller KH, Reda T, Baxter GR, Raguse BD, De Groot GJ, Chai R, Roberts M, Wieczorek L, Nanoparticle films as sensitive strain gauges, Applied Physics Letters, 2007 Oct 29;91(18):183105.

Chapter 5: Crack-based Strain Sensors

5.1. Introduction

As presents so far, flexible sensors are becoming more are more important in the number of application fields [1-7]. Especially, the high sensitivity of NP sensors to a plethora of different stimuli [8-21] -and particularly NP strain sensors, which are more sensitive than sensors made using continuous metal films- have enabled new applications, such as the detection of small human motions [22, 23]. Chemically grown [9, 24] and sputtered [25, 26] metal NPs have been used as sensing materials, taking advantage of the exponential dependence of their resistance on strain [9] and resulting in high sensitive piezo-resistive strain and pressure sensors[27].Up to now we have demonstrated the behavior of Pt NPs based sensors both based on a simulation model and experimentally. However, their sensitivity remains under 100. In chapter three we showed that when alumina was used as protective layer against RH, in some cases cracks are noticed to be developed. Hereafter we are going to demonstrate how we used this exact property of alumina (the development of cracks) to increase the sensitivity of our Pt NPs sensors.

Crack-based sensors [28-30] have been reported to exhibit very high GF which have intensified the need of further studies [31-34]. Most research groups studying the influence of cracked metal films on strain [29, 35-43], attribute the increased sensitivity on the gradual opening of the cracks which results in the break of the continuity of the metal film which greatly increases the resistivity of the strained film. However, metal film crack based sensors' technology does not exhibit increased sensitivity throughout a large sensor operating range. As sensitivity depends on the differential resistance change over the applied strain, , it is very high when the cracks are open, whereas for small deformations the continuity of the film is not particularly disturbed so sensitivity remains relatively low. Zou et al [36] managed to develop a crack-based strain sensor on a polydimethylsiloxane (PDMS) substrate with crack formation that could be predicted, which is capable to achieve GFs up to 2585 when strain is larger than 60%. In their study, Kang et al [28] first demonstrated a crack-based strain sensor on a polyurethane acrylate (PUA) substrate with a GF of 2000 for strains up to 2% and Li et al [39] developed a crack-based sensor on PDMS using a cracked Ag film as sensing material, achieving so GF of 44013 for a strain value of 0.88%. Han et al [29] also deposited Au on a PDMS substrate, achieving this way a GF up to 5885.59 for strain values between 1.5% and 2% and a GF up to 945.65 for strain values between 0% and 1.5%.

The first to report the use of NPs in a crack-based sensor was Schwebke et al [44] in 2018. They studied the behavior of Pt NPs embedded in boron nitride as well as in aluminum oxide films as strain sensors on polyimide substrates. They demonstrated how the presence of Pt NPs within the alumina film results in crack formation, which highly increases sensor resistance. Puyoo et al [45] have further explored the effect and developed a crack-based strain sensor with Pt NPs into an ALD alumina film on polyimide substrate, achieved a very high GF of up to 20000, at strain values of 0.3%. The disadvantage of their method was that the NPs were buried into the alumina-

film, having as a result a very high initial resistance (220 MΩ) and a very low working strain operating range (of just 1%).

In this chapter we are going to demonstrate how a flexible strain sensor based on the use of both NPs and cracks was developed by our team. To achieve this we deposited thin films of Al2O3 (alumina) on a polyimide substrate with various thicknesses (between 6 and 20 nm) and mechanically cracked by intentionally applying strain. Pt NPs were deposited on top of the cracked alumina film as to act as a sensitive/conductive material. We deposited two different surface coverages of Pt NPs, namely a sparse and a dense one. The sparse corresponds to a surface coverage of around 49% which is right below the 50% percolation threshold of the system. The dense one corresponds to a surface coverage of 73% which is exceeds the percolation threshold. The resistivity of the sparse NP films is determined by the inter-NP distance while their initial resistance was about 600 kΩ. After the application of strain the cracks begin to widen and therefore the distance between NPs is further increased, having as result an increase of the sensor's resistance. As far as the dense NP films is concerned, the NPs are in actual contact and their sensitivity is determined mainly by the crack opening itself and the strain applied to the sensor. Their initial resistance was about 20 Ω and by the application of 7.2% strain their final resistance reached values up to 700 MΩ. This gave as a colossal GF of 2.6 x 108, which is the highest ever to be reported. This GF is due to the small initial sensor's resistance and the fact that the cracks have disrupted the continuity of the NPs film, having as a result an enormous increase of the sensor's resistance.

In the case of sparse NP films, we managed to achieve a maximum GF of was 2795 for a strain value of 7.2% while GF values larger than 100 were achieved for small strain values down to 0.1%. For both in the case of sparse and dense NPs films, the sensitivity can be controlled by the thickness of the cracked alumina film. The thickest alumina films (20 nm) result in wider crack-openings, which gradually increases the sensor's resistance values and consequently its sensitivity.

In short, in this chapter we present the development of an extremely sensitive strain sensor through the combination of two thin film layers deposited on a flexible substrate, the bottom one being a cracked alumina layer and the top a 2-D metallic nanoparticle network. In contrary to other publications which employ NPs as the conductive layer of a crack-based sensor [45], this work does not use NPs embedded in the oxide layer rendering their density easily controlled. Sensor sensitivity can be tuned by the adjustment of alumina thickness and nanoparticle density, which offers a unique versatility to the proposed configuration for use to a large range of applications.

It's noteworthy that sensor that is being proposed could be used in applications were high sensitivity is necessary, particularly in a small strain regime, such as in biomechanical detection [46] or the detection of cells in a microfluidic channel [47]. Lastly, the employed techniques for device fabrication (ALD, sputtering) are compatible with batch-processing and are therefore suitable for manufacturing of low cost devices.

5.2. Sensors fabrication

All sensors have been fabricated using flexible polyimide (kapton) substrates, of 125 μm in thickness. Alumina thin films of various thicknesses of 6 nm, 10 nm and 20 nm, have been deposited using an RS-200 Picosun ALD system. The alumina thin films are fabricated by feeding the system with specific precursors, namely tetramethylaluminum (TMA) and deionized water (DI water), as discussed in chapter 2. During the deposition, the ALD reactor was under a 10 mbar pressure and under a constant flow of 300 sccm of 99.999% purity N_2. Each ALD cycle featured an exposure time of 0.1s (for both TMA and DI water), while the purge time was 10 s for TMA and 15 s for DI water. The deposition temperature was 80 °C, for all ALD cycles (60, 100 and 200). The overall thickness of the deposited film is determined by the number of cycles as well as the temperature, resulting thicknesses of 6 nm, 10 nm and 20 nm for 60, 100 and 200 cycles respectively. Furthermore, Pt NPs with a mean diameter of 4 nm and standard deviation of 0.8 were deposited on top of the alumina films, using a modified DC magnetron sputtering system (Chapter 2). Each alumina thickness and surface coverage of the Pt NPs, ten sensors were fabricated. The next step is the deposition of two gold electrodes on top of the NP film, using an electron-gun evaporator and a shadow mask. An adhesion layer of 4 nm thick Ti were deposited prior to the Au deposition (Fig. 5.1a). The electrodes were 40 nm thick, 4 mm wide and with a 150 μm inter-electrode gap (Fig. 5.1b). Prior to any strain-sensing experiments, the sensors were submitted in 200 strain cycles (strain between 0 and 7.2%) in order to create cracks in the entire thickness of the alumina film. When the cracks are eventually formed, the initial resistance increased slightly since even for zero deformation probably the cracks remain slightly open. Also, during the first application of strain the cracks are not formed in the entirety of the alumina film; this can be observed from the ever-increasing resistivity and sensitivity of the sensor during the following stress cycles. When the sensitivity stops to increase, which in this case is around 200 cycles of strain up to 7.2%, the cracks have been formed throughout the entire alumina film and the sensors are ready to be measured.

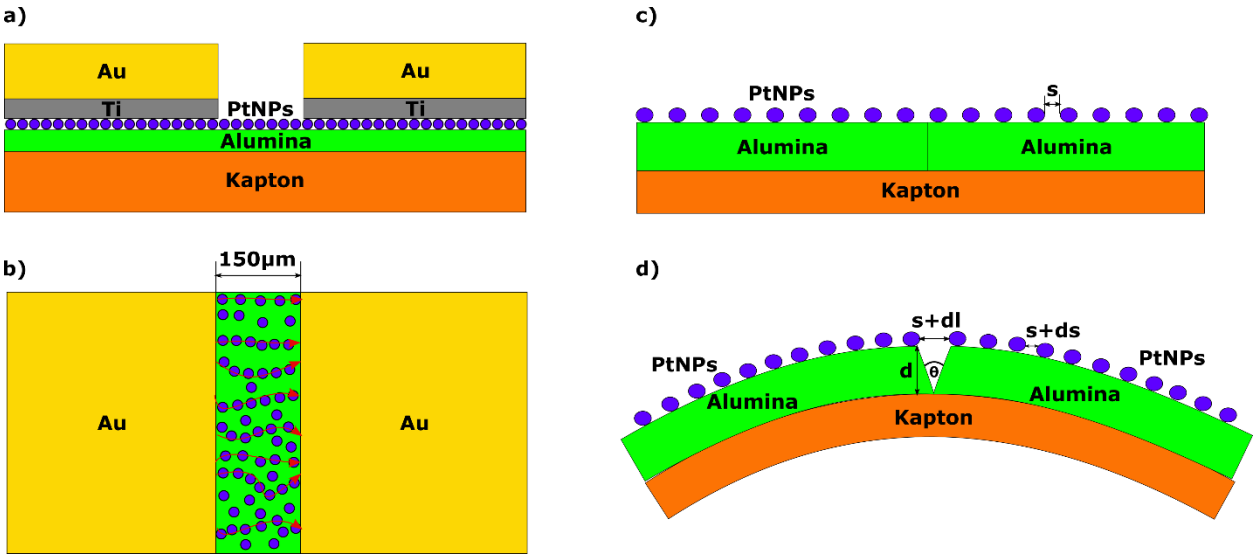

Figure 5.1: a) cross-section schematic of the sensor. b) Top-down schematic of the sensor. Red arrows represent the conductive paths on the Pt NPs film. c) Cross-section schematic of a flat sensor (no strain). d) cross-section schematic of a bended sensor and a crack opening. [48]

In addition to the above sensors, reference samples –without alumina layer- were also fabricated. The sensitivity of the sensors was calculated by monitoring their resistance under gradual application of strain. The resistance of the devices was measured with a Keithley 2400 multimeter by measuring the current under a DC voltage of 1 Volt. Strain was applied using a homemade stage capable of applying strains up to 1.17%. Ambient conditions like temperature and relative humidity that NP films are sensitive to [49, 50], are eliminated by conducting the experiments under constant relative humidity of 45% and at a temperature of 20° C. Strain sensing experiments were conducted by fixing the sensors on a PCB for more uniform strain application; the application of strain was made by using a micro-vernier and a stepper-motor that was controlled by Arduino Uno and a home-made software. The Resistance of a NP based device is given by the equation (3.6). If cracks are present in the alumina film, the bending of the device will result in an anisotropic opening of the cracks (Fig. 5.1c, d).

The “top” of the crack will feature a larger opening than the bottom (Fig. 5.1d). The NPs have been deposited only on top of the alumina film and not inside the cracks; as a consequence, when strain is applied the cracks will begin to emerge, imposing an increased inter-NP distance than what would be achieved if the NP layer layer has been deposited directly on top of the flexible polyimide substrate. The opening in the “top” area of the crack is determined by the thickness “*d*” of the cracked alumina film and the applied strain. The distance *s + dl* on the “top” opening (Fig. 5.1d) is much larger than the distance *s + ds*, where *ds* is the extra distance due to strain, resulting in strain sensors with great sensitivities. As far as the sensors with dense NPs are concerned, their behaviour is similar to the continuous metal foil films. Their initial resistance is around 20 Ω which is a major advantage in comparison to the sparse NPs sensors and feature an

extremely high sensitivity. Due to the fact that sensitivity is determined by equation 3.9, a low initial resistance combined with a very high final resistance (because of crack openings) will result in an extremely high ΔR/R%.

5.3. Results

5.3.1. Sparse NP sensor

Fig. 5.2 shows the sensitivity of the sensors with sparse NPs; each point in the graphs shows the mean value obtained after measuring 10 same sensors (with the same alumina thickness), while the error bars is the standard deviation of the measurements. In Fig. 5.2a the reference sensor (without alumina coating) can be seen while Fig. 5.2b to 5.2e show the crack-based sensors. Each of the crack-based sensors graph is divided in three areas with different sensor sensitivity. In the case of the reference sensor, the two measured sensitivities are attributed to the new inter-particle gaps that have been created due to strain [26] as discussed in chapter 3. On the other hand, the three areas that are observed in the crack-based sensors are due to the crack formation. As can be seen in Fig. 5.3, the cracks do not form a straight line but they have an asperity. However, the cracks are formed parallel to each other (and parallel to the electrodes) and vertical to the applied strain. When no strain is applied, there is a maximum number of conductive paths (Fig. 5.3a); as strain is gradually applied, cracks in the alumina film begin to emerge, resulting in the “collapse” of some of the conductive paths (Fig. 5.3b). As long as the crack opening “x” is smaller than the crack asperity height “h”, a finite number of conductive paths will remain active (areas marked in yellow, in Fig. 5.2 b-e). Any further application of strain will cause “x” to become larger than “h”, resulting in the discontinuation and ultimately the collapse of the majority of the conductive paths (Fig. 5.3c). However, some conductive paths will

remain, forming conductive charge-pathways via the tunneling effect; this corresponds to the pink color areas of Fig. 5.2.

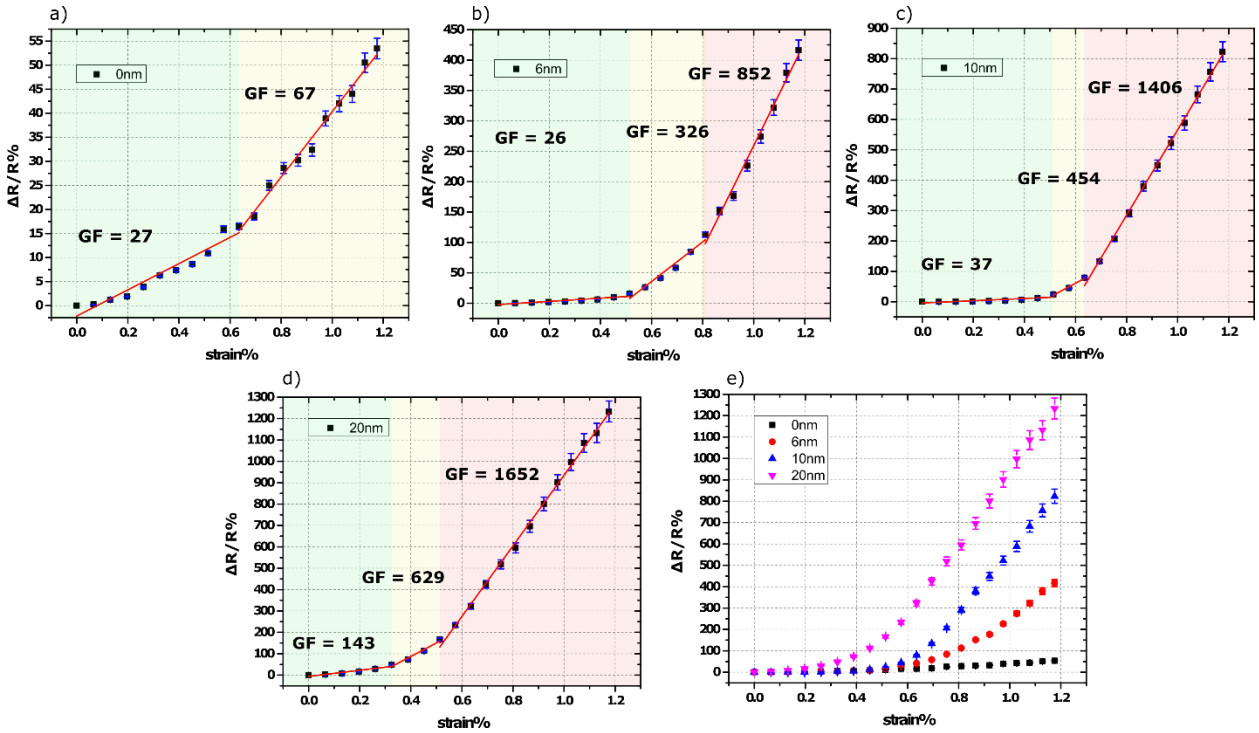

Figure 5.2: ΔR/R% over strain% graphs for Sparse NP sensors and strain values up to 1.2% a) reference sensors without any cracks, b) sensors with 6 nm thick, cracked alumina, c) sensors with 10 nm thick, cracked alumina, d) sensors with 20 nm thick, cracked alumina, e) comparison graph for all the above mentioned sensors. [48]

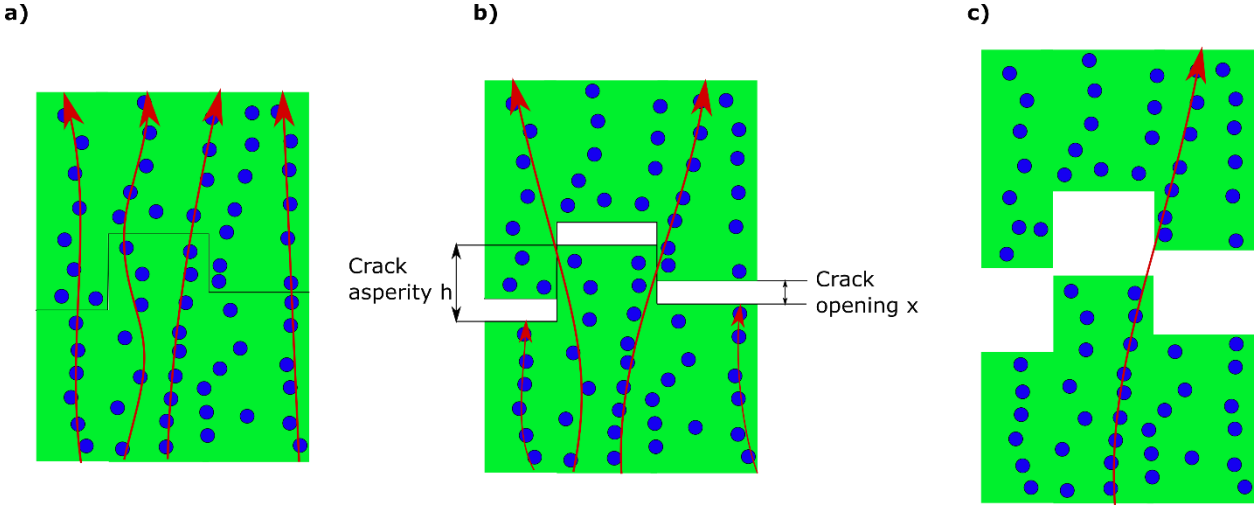

Figure 5.3: Schematic representation of conductive paths and crack asperity. a) Conductive paths when no strain is applied, b) Conductive path collapse when the crack opening is smaller than the crack asperity. c) Collapse of the majority of conductive paths when the crack opening is larger than the crack asperity. [48]

	strain %											
thickness	0.1	0.2	0.3	0.4	0.5	0.6	0.7	0.8	0.9	1	1.1	1.2
0 nm	27						67					
6 nm	26					326			852			
10 nm	37					454	1406					
20 nm	143			629		1652						

Table 5.1: Table with sensors' sensitivities (GF) across the strain range 0.1 – 1.2%. [48]

Table 5.1 shows sparse-NP sensor sensitivities across the strain-range of 0.1-1.2%. The results shows that sensors with thicker alumina films (10 nm and 20 nm) show increased sensitivity for smaller strain values than sensors with the thinner alumina film (6 nm). More specifically, sensors with 20 nm thick alumina film achieve GFs up to 1652 for strain values higher than 0.5% while sensors with a 10 nm thick alumina film achieve a GF of 1406 for strain values higher than 0.6%. Sensors with thinner alumina films achieve best sensitivity for increasingly larger strain values. In any case, the sensitivities of crack-based strain sensors remain larger than what can be achieved without cracks. It is then clear that by controlling the alumina thickness, sensors with high sensitivities in specific strain ranges can be developed so as to address the needs of the desired application.

Sensor sensitivity should be further increased if thicker alumina films are employed. However, since the NPs have been deposited only on top of the alumina film and not inside the cracks, the resistance of the device strongly depends on the crack opening "x" which in most cases represents an interparticle gap. The crack opening in the case of even thicker films becomes very large for increased strain values and terminate all the conductive paths, rendering the sensor useless and with a limited working range as it is illustrated in the following experiments.

5.3.2. Calculation of strain from the bending angle

Fig. 5.4 shows a graphic representation of a bended substrate. Tensile and compressive stresses will be applied to the substrate causing the upper surface to increase their distance from l_0 to l'. Uniform substrates remain unstrained at their medium (l_0 in Fig. 5.4).

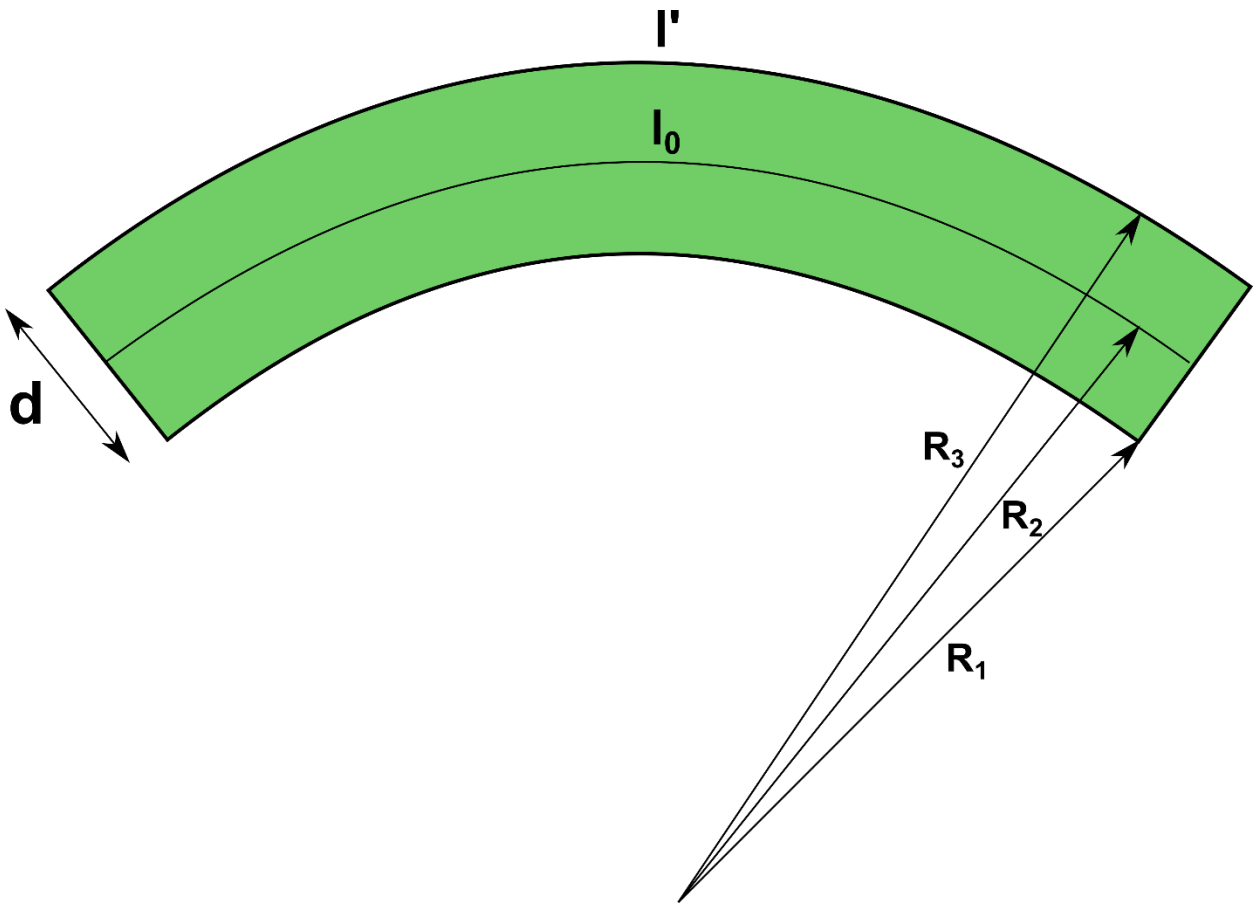

Figure 5.4: Schematic representation of a bended substrate with d thickness. [48]

The distance l_0 is given by the following equation:

$$l_0 = R_2\theta \tag{5.1}$$

Where ϑ is the angle corresponding angle of the arc length. The distance l' can be calculated by the equation:

$$l' = (R_2 + \frac{d}{2})\theta \tag{5.2}$$

Strain is defined by the following:

$$\varepsilon = \frac{l' - l_0}{l_0} \tag{5.3}$$

By applying (5.1) and (5.2) to (5.3):

$$\varepsilon = \frac{\left(R_2 + \frac{d}{2}\right)\theta - R_2\theta}{R_1\theta} = \frac{d}{2R_2} \tag{5.4}$$

Since radials R_1 R_2 R_3 are much larger than the thickness d it can be therefore assumed that they are all equal to R_2, if the sensor is bent according to what can be seen in Fig. 5.5.

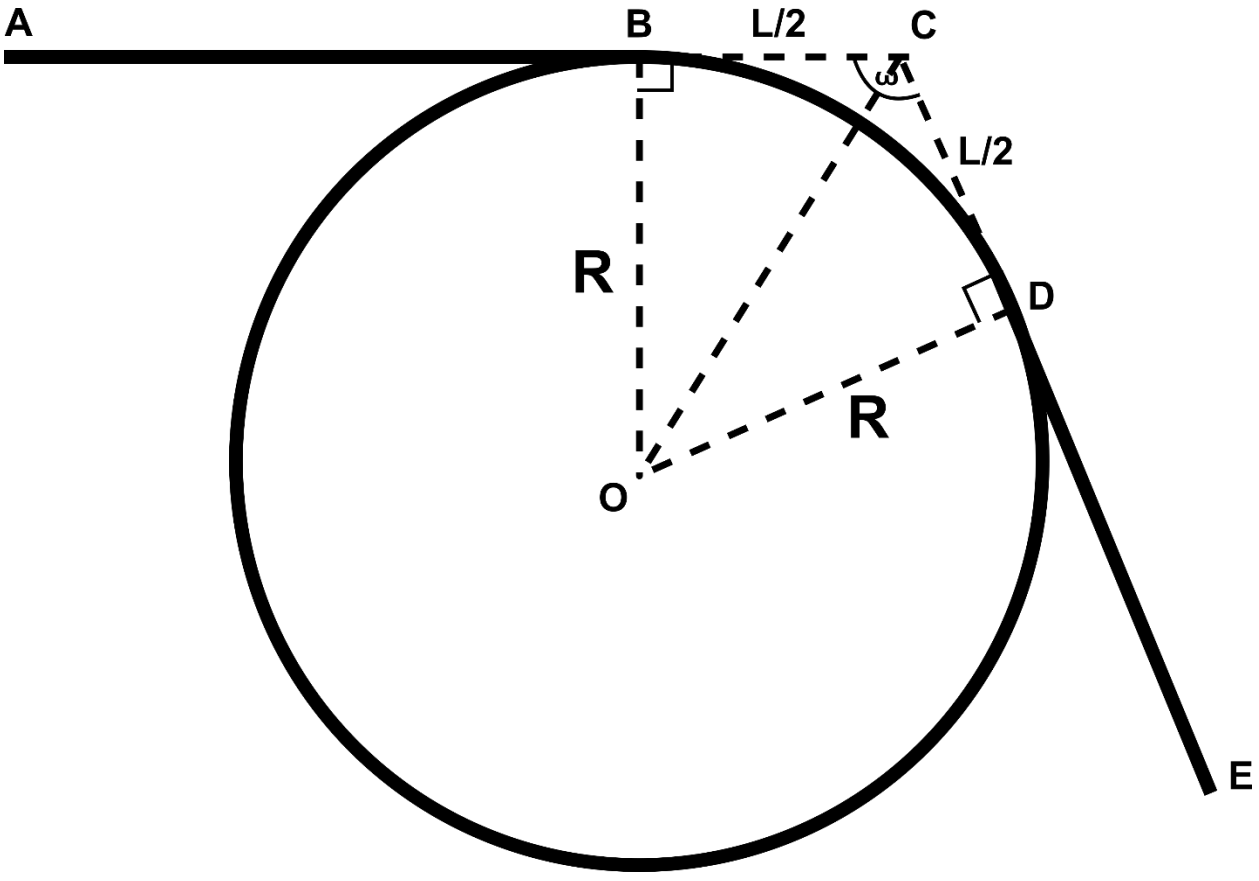

Figure 5.5: Schematic representation of the bended sensor and the circle with radius equal with the bended radius. The strain-sensor extends from point A to point B. and can be bent according to the bending angle ω. [48]

As can be seen in Fig. 5.5, the sensor can be deformed between two fixed points *B* and *D*. The distance between *B* and *D* when no bending occurs equals to *L*, which in our case is 3000 μm. Therefore, the overall distance of the two straight sections *BC* and *CD* is L. In addition, the straight section *OC* bisects the angle *ω* and the angle *BOD*. The schematic representation in Fig. 5.5 shows the circle with a radius equal to the bending radius *R*. The radius *R* can be calculated by the following equation:

$$R = \frac{L}{2\cot(\frac{\omega}{2})} \tag{5.5}$$

By applying the equation (5.5) to equation (5.4):

$$\varepsilon = \frac{dcot(\frac{\omega}{2})}{L} \tag{5.6}$$

The sensors' working range was investigated by bending them at 7 different angles 150^{o}, 135^{o}, 120^{o}, 105^{o}, 90^{o}, 75^{o} and 60^{o} (Fig. 5.6), which correspond to strain values of 1.12%, 1.73%, 2.4%, 3.2%, 4.17%, 5.43% and 7.2% respectively.

Measurements have been again conducted using a homemade stage capable of bending the sensor in strains larger than 1.2%. All the sensors have linear response to strain and exhibit GFs up to 80 for reference samples (without alumina film) while sensors with alumina films feature GFs of 775, 1571 and 2795 for 6 nm, 10 nm and 20 nm alumina thickness respectively. Sensors with 6 nm and 10 nm alumina thickness films show the same behavior for the smaller strain values, resulting in the same sensitivities. The 20 nm thick alumina films were by far the most sensitive ones, due to the limited conductive paths, but are operational for strains up to 4.17%. Their working range is limited since for large strain, the crack openings become too large for any charge-transport to take place. In addition, the ability of the sensor to be incorporated in e-skin applications has been validated by attaching it on a nitrile flexible glove and bending it in the 4

aforementioned “ω” angles (Fig. 5.7). The sensor performed with sensitivity similar to the one of the homemade stage characterization step.

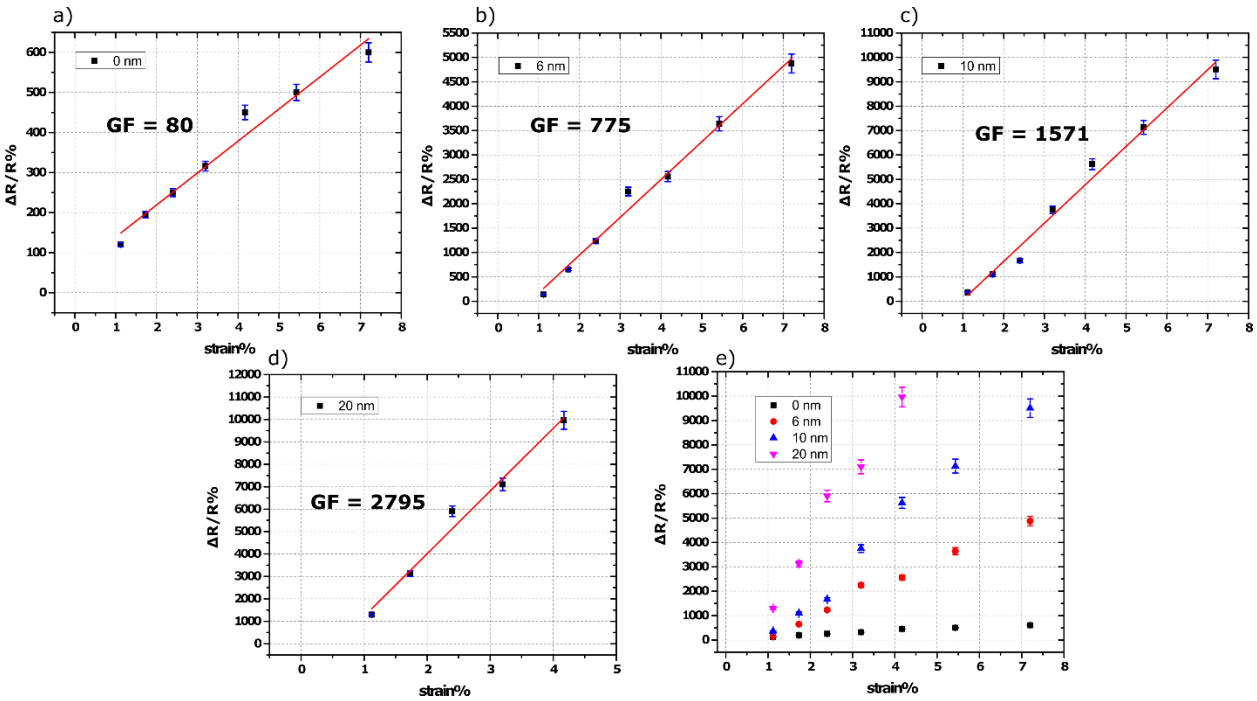

Figure 5.6: ΔR/R% over strain% graphs for Sparse NP sensors and strain values from 1.12% up to 7.2% a) reference sensors without cracked alumina b) sensors with 6 nm thick alumina film, c) sensors with 10 nm thick alumina film d) sensors with 20 nm thick alumina film and e) comparison of the different samples. [48]

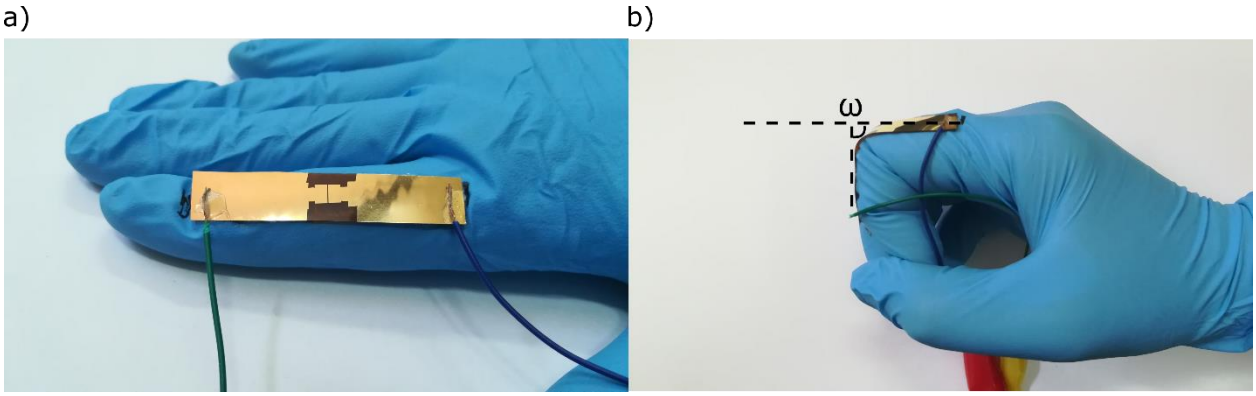

Figure 5.7: a) Demonstration of a sensor attached in the index finger of a glove b) Sensor-bending in different ω angles. [48]

Fig. 5.1d, portrays the effect of alumina thickness on crack opening. From this figure the crack opening can be calculated using the following equation:

$$x = 2dsin\frac{\theta}{2} \tag{5.7}$$

Where, d is the alumina thickness, θ the angle on the bottom of the crack and x the crack opening (s + dl in Fig. 5.1d). Thicker films will result in increased the crack openings “x” and thus higher sensitivities. However, since the crack opening “x” represents an interparticle gap only for large strains (Fig. 5.3c), for high “x” values the tunneling effect is suppressed and all conductive paths are cut-off. Therefore, thick alumina films will demonstrate increased sensitivities for small strain values and no sensitivity at all in large strain values (table 5.2). On the other hand, thin alumina films exhibiting high sensitivities in high strain values and medium sensitivity in low strain values. More specifically, thin alumina films have high sensitivity in a strain-range where thick alumina film sensors are ineffective due to the fact that crack openings become too large.

Finally, sensors’ ability to work reliably after a large number of stress cycles were tested. These fatigue tests were performed using the homemade stage where the sensors were bent for 1000 cycles of strain up to 1.17%. Fig. 5.8 shows the relative resistance change of the sensors throughout the 1000 strain-cycles. Their performance remains practically unchanged, which means that the cracks have been formed in the entirety of the alumina film thickness and remain unaffected by any further application of strain. The initial application of 200 cycles of strain, following their fabrication, is sufficient in order to form the cracks throughout the whole alumina film thickness.

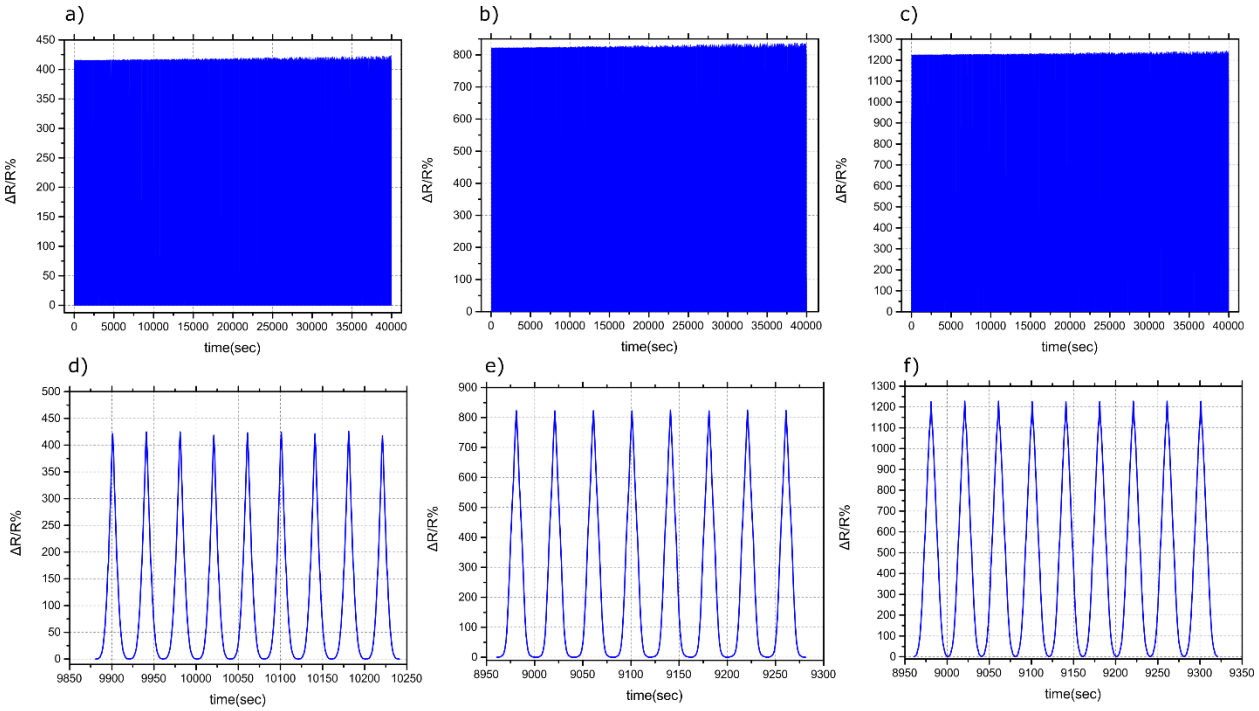

Figure 5.8: ΔR/R% over time graphs for Sparse NP sensors throughout the 1000 cycles of strain up to 1.17%: a) sensor with 6 nm thick alumina, b) sensor with 10 nm thick alumina and c) sensor with 20 nm thick alumina. Graphs d – f show a limited numbers of stress cycles: d) sensor with 6 nm thick alumina, e) sensor with 10 nm thick alumina and f) sensor with 20 nm thick alumina. The maximum shift in ΔR/R% (between first and last strain cycle) was 1.5%, 2.1% and 1.6% for sensors with 6, 10 and 20 nm alumina thickness respectively. [48]

5.3.3. Dense NP sensor

Strain sensor sensitivity is determined by equation (3.9) and thus by the relative resistance change. The relatively small sensitivity for sensors with sparse NPs can be attributed to their high initial resistance, which results in a limited relative resistance change. Most of the research groups that have demonstrated strain sensors with very large sensitivities are using continuous metal films as sensing materials that exhibit very low initial resistance. The cracks that are formed in these films break/disrupt their continuity resulting in the drastically increase of their resistance. Similarly, in order to decrease the initial resistance of the NP sensors, NPs with surface coverage of 73% were deposited on top of the alumina film, so as to create a film close to continuous film (Fig. 5.9). The initial resistance of the continuous-NP sensors was 20 Ω, which is much lower than the one for sensors with sparse NPs. Moreover continuous-NP sensors have much larger ‘’resistance-window’’.

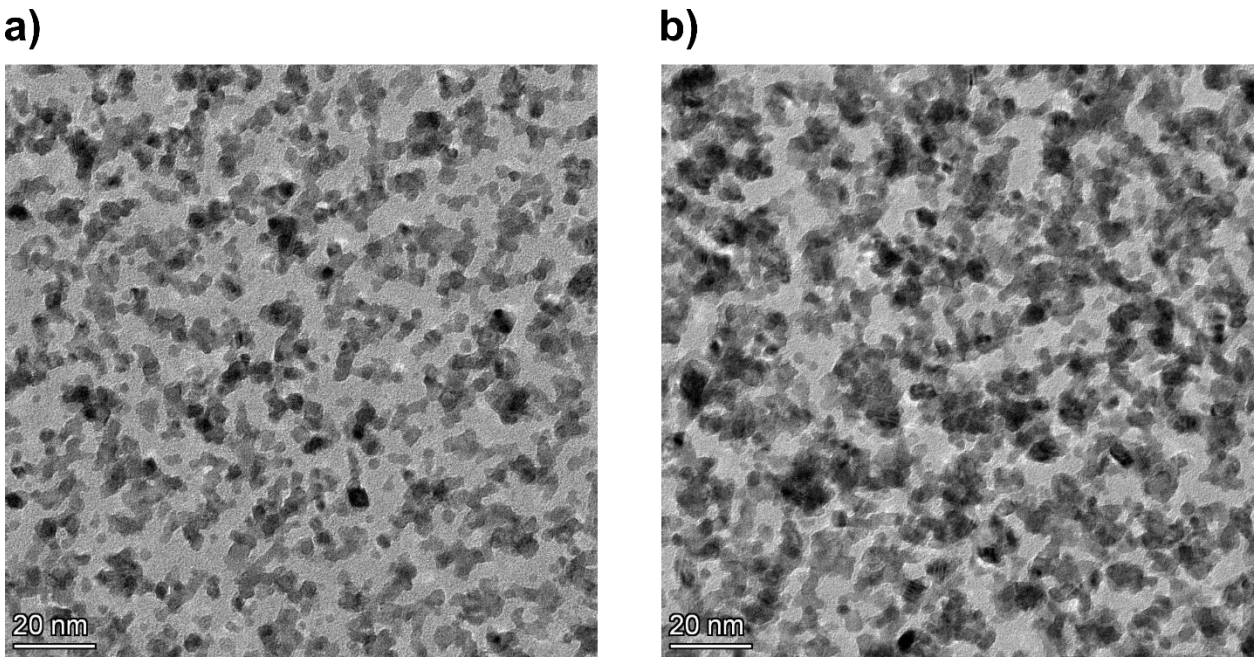

Figure 5.9: TEM, Pt NP images for: a) sparse NPs with surface coverage of 49% and with b) dense NPs with surface coverage of 73%. [48]

Fig. 5.10 shows the performance of sensors featuring 6, 10, and 20 nm thick alumina films, for small strain values. The graphs show the relative resistance change mean value after the measurement of 10 sensors for each alumina thickness, while the error bars represent the standard deviation of the measurements. Reference samples without any alumina are not shown because they did not exhibit any sensitivity. The same has been found for sensors with a 6 nm thick alumina film, but only for limited strain values up to 0.7%; above this value, sensors with 6 nm alumina thickness show a GF of 339. Sensors with a 10 and 20 nm thick alumina film exhibit better performance, resulting in sensitivities of 33 and 320 and 93, 238 and 863 respectively. Sensors with 20 nm thick alumina film seem to have much higher sensitivity for small strain values. This behavior is anticipated since, as discussed previously, the crack's opening is sensitive even to the smallest of deformations; at the same time, thin film sensors are expected to show low sensitivity at small strain values.

The overall performance of dense NP sensors for small strain values is inferior to that of sparse NPs sensors. This is because of the different conductivity mechanisms for each NP density. For sparse NPs films, the conductivity is greatly depends by the number of conductive paths as well as by the tunneling effect between inter-particle distances; thus it is very sensitive to even the smallest deformations. In the case of dense NPs films there is no tunneling effect and an extremely high number of "continuous" conductive paths are available for charge transport, resulting in limited sensitivity for small strain values. The role of the cracked alumina substrate is to limit the number of conductive paths for both cases. The thickness of the film also plays a very important role by affecting the crack opening. Thinner alumina films feature very small crack

openings for small strain values; this leaves the resistivity either completely unaffected (Fig. 5.10a) or with a very small effect (Fig. 5.10b). Thicker films have large crack openings, even for very small strain values and therefore the sensitivity of these sensors is increased (Fig. 5.10c). For strain values above 0.6% all of the different alumina thicknesses seem to affect the conductivity of the sensors, showing increased sensitivity by limiting the number of conductive paths. For larger strain values ($1.12\% < \varepsilon < 7.2\%$) the sensors show extremely high sensitivities. In particular sensors with a 20nm thick alumina film show a GF of 7998 for strains up to 4.17% and a colossal GF of 2.6×10^8 for strain up to 7.2% (Fig. 5.11c), which is the highest sensitivity that has ever been reported [48].

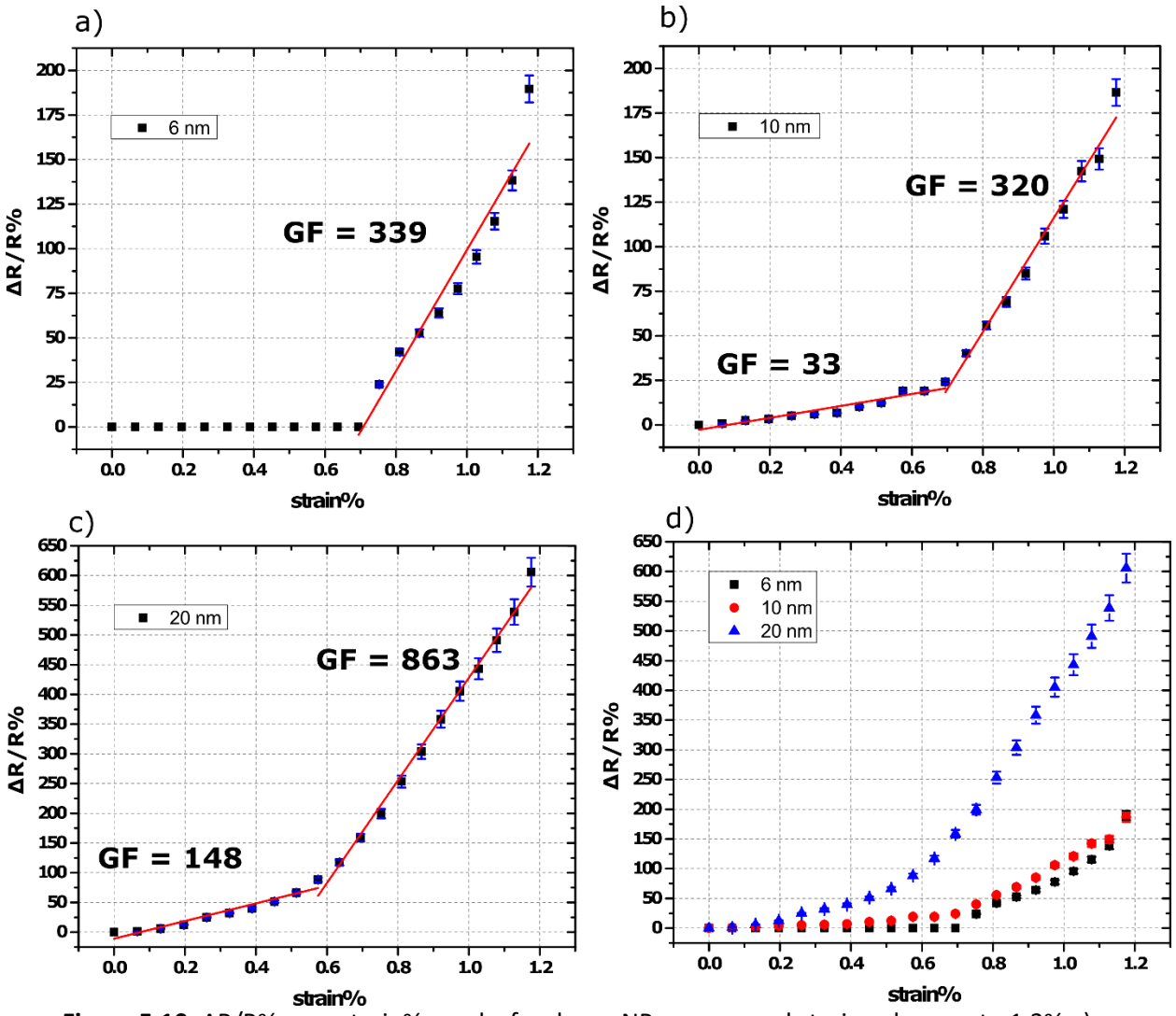

Figure 5.10: ΔR/R% over strain% graphs for dense NP sensors and strain values up to 1.2% a) sensors with 6 nm thick cracked alumina, b) sensors with 10 nm thick cracked alumina, c) sensors with 20 nm thick cracked alumina, d) comparison graph for all the above mention sensors. [48]

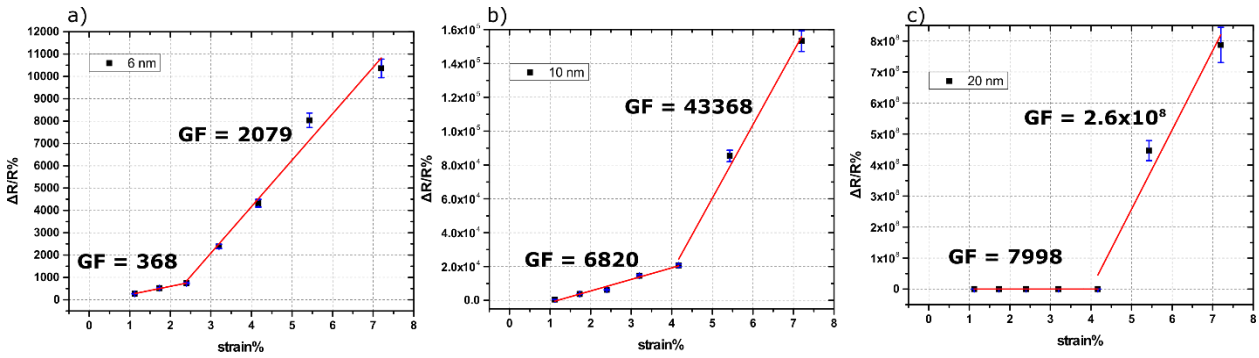

Figure 5.11: ΔR/R% over strain% graphs for Dense NP sensors and strain values up to 7.2% a) sensors with 6 nm thick alumina film, b) sensors with 10 nm thick alumina film c) sensors with 20 nm thick alumina film. [48]

The performance of the sensor can be better understood if the SEM images of Fig. 5.10 are taken into account. For a 6 nm thick alumina film, the opening of the cracks was adequate so as to segment the nanoparticle film but their asperity was comparable to the opening. This results in areas where the different nanoparticle segments are still connected (Fig. 5.12a). In the case of 10 nm alumina thickness, the crack opening was even wider than what has been observed for a 6 nm film but for small strain values the crack asperity limits sensor sensitivity. However, above 4.17% strain, crack opening was wide enough to completely segment the nanoparticle film into semi-isolated sub-areas and the GF was increased by 536% (Fig. 5.12b). Finally in the case of a 20 nm thick alumina film, crack asperity plays an important role only for strains up to 4.17% where the GF of the sensor is 7998. Above 4.17% strain values, the GF rapidly increased from 7998 to 2.6×10^8. This extremely high GF can be explained by the formation of a crack opening that is overly wide (Fig. 5.12c, d); in this case the charge-transport between the nanoparticle film sub-areas can only take place through tunneling. The final resistance of the sensor (after a strain application of 7.2%) with 20 nm alumina thickness was 700 MΩ which is a very high resistance that can still be safely measured; in the case of dense nanoparticle films, the entire film contributes to the conductivity and for wide enough cracks charge transport can still exist due to the crack asperity. Although the crack opening is very wide, crack asperity still exists and creates areas where the crack opening limits its length, and the tunneling effect is still possible. In the case of sparse nanoparticle films, the final resistance was over 1 GΩ and the sensor was not responding to any strain changes. This behavior can be explained by the fact that the initial conductive paths for sparse nanoparticle films were limited and are eliminated by the crack openings, hence resulting in no conductivity between the electrodes. Fig. 10 d to 10 f show the evolution of the crack opening under different strain values for a sensor with 20 nm thick alumina film. The strains that were applied were 5.4% (Fig. 5.12d), 0.9% (Fig. 5.12e) and 0.4% (Fig. 5.12f). The images support our arguments about varying sensor-sensitivity in the entire strain working-range. At high strain values the crack opening (Fig. 5.12d) is wide enough to disrupt the majority of conductive paths. At medium strain values (Fig. 5.12e) the crack opening can disrupt a limited number of conductive paths, but still a significant number remains operational due to the crack's

asperity. Finally at low strain values (Fig. 5.12f) the crack opening is not wide enough to significantly affect GF; however, GF is affected by disrupting a small number of conductive paths. Sensors with sparse nanoparticles are more sensitive even to the smallest crack openings because of the fact that the initial number of conductive paths is very limited, hence GF is increased for lower strain values.

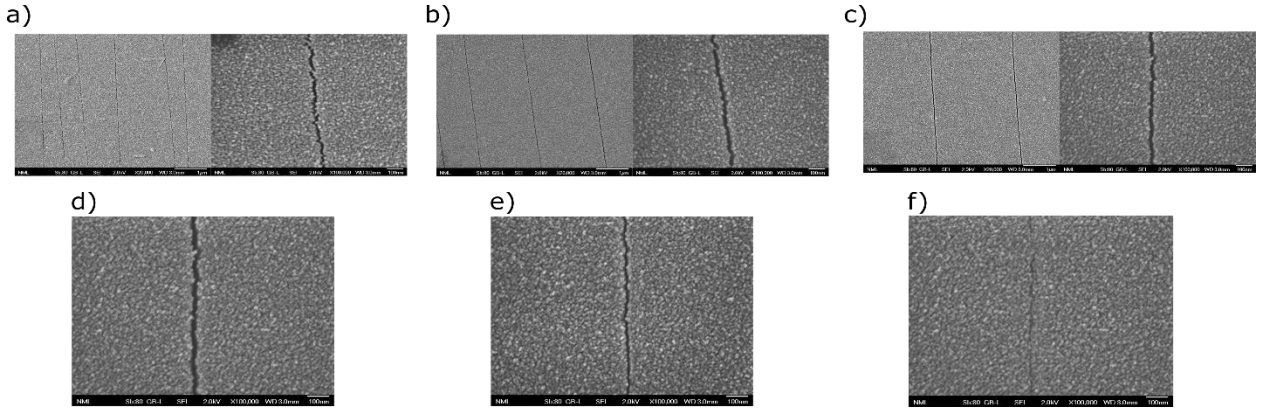

Figure 5.12: SEM images of dense Pt NP sensors, for a strain of 5.4% and for alumina film-thicknesses of) 6nm b) 10 nm and c) 20 nm. Crack-opening evolution, for a 20 nm thick alumina film at d) 5.4% strain e) 0.9% strain and f) 0.4% strain. [48]

Finally, 1000 cycles of strain up to 1.12% were submitted to the sensors as fatigue tests, as in the case of sparse nanoparticle sensors. The results shown in Fig. 5.13 validate that the sensors' performance remains the same.

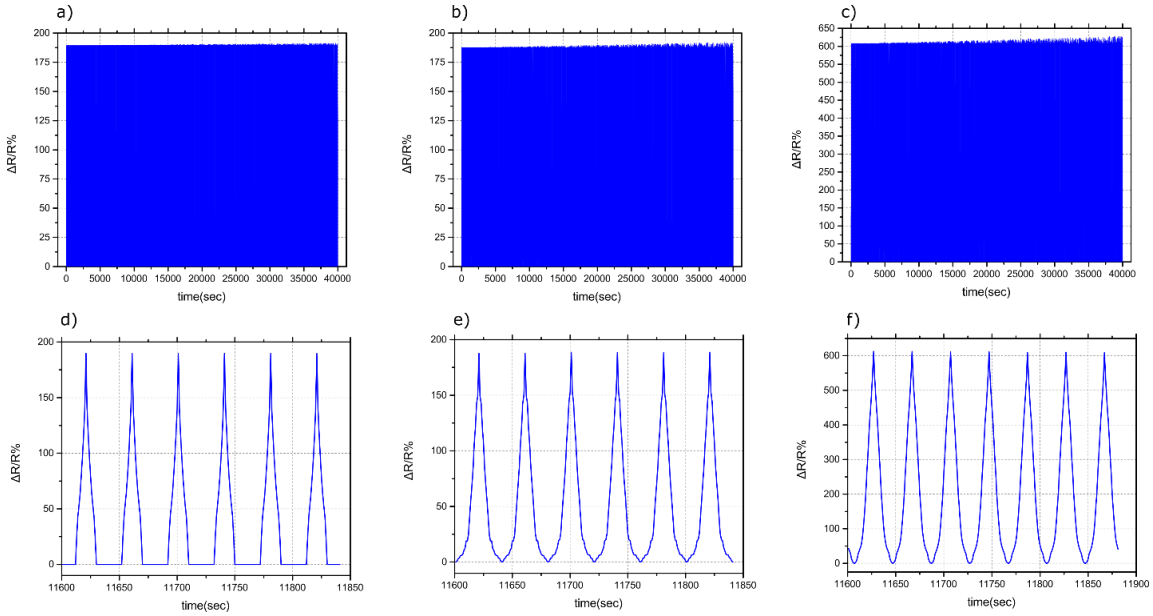

Figure 5.13: ΔR/R% over time graphs for dense NP sensors throughout the 1000 cycles of strain up to 1.17%: a) sensor with 6 nm thick alumina, b) sensor with 10 nm thick alumina and c) sensor with 20 nm thick alumina. Graphs d – f show a limited numbers of stress cycles: d) sensor with 6 nm thick alumina, e) sensor with 10 nm thick alumina and f) sensor with 20 nm thick alumina. The maximum shift in ΔR/R% (between first and last strain cycles) was 1%, 2.7% and 3.4% for sensors with 6, 10 and 20 nm alumina thickness respectively. [48]

Table 5.2 summarizes sensors' sensitivities for both sparse and dense nanoparticles and for all alumina thicknesses.

		strain %																	
	thickness	0.1	0.2	0.3	0.4	0.5	0.6	0.7	0.8	0.9	1	1.1	1.2	1.73	2.4	3.2	4.2	5.43	7.2
sparse NPs	6 nm	26					326			852				775					
	10 nm	37					454	1406						1571					
	20 nm	143			629		1652							2795				X	
dense NPs	6 nm	0							339					368		2079			
	10 nm	33							320					6820				43368	
	20 nm	93			238			863						7998				$2.6x10^8$	

Table 5.2: Sensitivities of the sensors through the whole working range from 0% to 7.2% strain. [48]

5.4. Conclusions

The manufacture of sensors with extremely high sensitivities by simply controlling the alumina thickness in tandem with NP surface coverage was represented extensively. The sensors were fabricated by utilizing two different Pt NP concentrations, namely one using sparse NPs right under the percolation threshold of the system (49% surface coverage) and the other using dense NPs (73% surface coverage) behaving like a continuous metal foil.

We can conclude that in the case of sparse NPs sensors with thicker alumina films, high sensitivities have been found for smaller strain values, especially if we compare them to sensors that use thinner alumina films. However, alumina thickness seems to be a limiting factor for the working-range of the sensors as they stop operating at large strain values (above 4.17%) while these with thinner alumina films remain functional even up to 7.2% strain.

When it comes to dense NP films, the sensors show relatively low sensitivity in the small strain regime but in cases of larger strain values the sensors feature extremely high sensitivities. In particular, sensors employing 20 nm thick alumina films show a record-high sensitivity of $2.6x10^8$, for strain up to 7.2%. We should note here that all sensors remain operational regardless of the strain value.

While sparse NPs film sensors are very sensitive to the small strain regime and with an adjustable sensitivity, sensors with dense NPs are extremely sensitive to strains larger than 1%. Additionally, although the sparse NPs sensors are less sensitive than their counterparts, they remain in a high sensitivity regime (GF above 1000).

In conclusion, Pt NPs strain based sensors have demonstrated high sensitivities when working in a range of 0.1% to 7.2%. The alumina film thickness enables tuning sensitivity for a specific strain value and creates extremely sensitive strain sensors for strain values above 4.17%. Sparse NPs show high sensitivities for small strain values while dense NPs record an unpresented high sensitivity for large strain values. This versatility paves the way for a wide range of applications extending from emerging new fields like the manufacture of e-skin and biomedical applications

to more traditional ones like structural health monitoring and pressure sensors. Last but not least, the devices are cost competitive since they are produced using processing steps like ALD and sputtering which are compatible with batch fabrication.

This work was published in the scientific journal Nanoscale [48].

5.5. References

[1] Kang MS, Joh H, Kim H, Yun HW, Kim D, Woo HK, Lee WS, Hong SH, Oh SJ, Synergetic effects of ligand exchange and reduction process enhancing both electrical and optical properties of Ag nanocrystals for multifunctional transparent electrodes, Nanoscale, 2018;10(38):18415-22.

[2] Ha M, Lim S, Ko H, Wearable and flexible sensors for user-interactive health-monitoring devices, Journal of Materials Chemistry B, 2018;6(24):4043-64.

[3] Shengbo S, Lihua L, Aoqun J, Qianqian D, Jianlong J, Qiang Z, Wendong Z, Highly sensitive wearable strain sensor based on silver nanowires and nanoparticles, Nanotechnology, 2018 Apr 25;29(25):255202.

[4] Joh H, Lee SW, Seong M, Lee WS, Oh SJ, Engineering the Charge Transport of Ag Nanocrystals for Highly Accurate, Wearable Temperature Sensors through All-Solution Processes, Small, 2017 Jun;13(24):1700247.

[5] Kim KK, Ha I, Kim M, Choi J, Won P, Jo S, Ko SH, A deep-learned skin sensor decoding the epicentral human motions, Nature communications, 2020 May 1;11(1):1-8.

[6] Tang N, Zhou C, Qu D, Fang Y, Zheng Y, Hu W, Jin K, Wu W, Duan X, Haick H, A Highly Aligned Nanowire-Based Strain Sensor for Ultrasensitive Monitoring of Subtle Human Motion, Small, 2020 Jun;16(24):2001363.

[7] Khatib M, Zohar O, Saliba W, Haick H, A Multifunctional Electronic Skin Empowered with Damage Mapping and Autonomic Acceleration of Self-Healing in Designated Locations, Advanced Materials, 2020 Apr;32(17):2000246.

[8] Tanner JL, Mousadakos D, Giannakopoulos K, Skotadis E, Tsoukalas D, High strain sensitivity controlled by the surface density of platinum nanoparticles, Nanotechnology, 2012 Jun 21;23(28):285501.

[9] Herrmann J, Müller KH, Reda T, Baxter GR, Raguse BD, De Groot GJ, Chai R, Roberts M, Wieczorek L, Nanoparticle films as sensitive strain gauges, Applied Physics Letters, 2007 Oct 29;91(18):183105.

[10] Zheng M, Li W, Xu M, Xu N, Chen P, Han M, Xie B, Strain sensors based on chromium nanoparticle arrays, Nanoscale, 2014;6(8):3930-3.

[11] Lee GY, Kim MS, Min SH, Kim HS, Kim HJ, Keller R, Ihn JB, Ahn SH, Highly Sensitive Solvent-free Silver Nanoparticle Strain Sensors with Tunable Sensitivity Created Using an Aerodynamically Focused Nanoparticle Printer, ACS applied materials & interfaces, 2019 May 31;11(29):26421-32.

[12] Lee WS, Lee SW, Joh H, Seong M, Kim H, Kang MS, Cho KH, Sung YM, Oh SJ, Designing metallic and insulating nanocrystal heterostructures to fabricate highly sensitive and solution processed strain gauges for wearable sensors, Small, 2017 Dec;13(47):1702534.

[13] Tian B, Yao W, Zeng P, Li X, Wang H, Liu L, Feng Y, Luo C, Wu W, All-printed, low-cost, tunable sensing range strain sensors based on Ag nanodendrite conductive inks for wearable electronics, Journal of Materials Chemistry C, 2019;7(4):809-18.

[14] Lee WS, Jeon S, Oh SJ, Wearable sensors based on colloidal nanocrystals, Nano convergence, 2019 Dec 1;6(1):10.

[15] Skotadis E, Aslanidis E, Kainourgiaki M, Tsoukalas D, Nanoparticles Synthesised in the Gas-Phase and Their Applications in Sensors: A Review, Applied Nano, 2020 Dec;1(1):70-86.

[16] Kano S, Kim K, Fujii M, Fast-response and flexible nanocrystal-based humidity sensor for monitoring human respiration and water evaporation on skin, ACS sensors, 2017 Jun 23;2(6):828-33.

[17] Willner MR, Vikesland PJ, Nanomaterial enabled sensors for environmental contaminants, Journal of nanobiotechnology, 2018 Dec;16(1):1-6.

[18] Madianos L, Tsekenis G, Skotadis E, Patsiouras L, Tsoukalas D, A highly sensitive impedimetric aptasensor for the selective detection of acetamiprid and atrazine based on microwires formed by platinum nanoparticles, Biosensors and Bioelectronics, 2018 Mar 15;101:268-74.

[19] Chang CC, Chen CP, Wu TH, Yang CH, Lin CW, Chen CY, Gold nanoparticle-based colorimetric strategies for chemical and biological sensing applications, Nanomaterials, 2019 Jun;9(6):861.

[20] Skotadis E, Tsekenis G, Chatzipetrou M, Patsiouras L, Madianos L, Bousoulas P, Zergioti I, Tsoukalas D, Heavy metal ion detection using DNAzyme-modified platinum nanoparticle networks, Sensors and Actuators B: Chemical, 2017 Feb 1;239:962-9.

[21] Liu G, Zhang R, Li L, Huang X, Li T, Lu M, Xu D, Wang J, Anti-agglomeration behavior and sensing assay of chlorsulfuron based on acetamiprid-gold nanoparticles, Nanomaterials, 2018 Jul;8(7):499.

[22] Souri H, Banerjee H, Jusufi A, Radacsi N, Stokes AA, Park I, Sitti M, Amjadi M, Wearable and stretchable strain sensors: materials, sensing mechanisms, and applications. Advanced Intelligent Systems, 2020 Aug;2(8):2000039.

[23] Cai Y, Shen J, Ge G, Zhang Y, Jin W, Huang W, Shao J, Yang J, Dong X, Stretchable Ti3C2T x MXene/carbon nanotube composite based strain sensor with ultrahigh sensitivity and tunable sensing range, ACS nano, 2018 Jan 23;12(1):56-62.

[24] Ketelsen B, Yesilmen M, Schlicke H, Noei H, Su CH, Liao YC, Vossmeyer T, Fabrication of Strain Gauges via Contact Printing: A Simple Route to Healthcare Sensors Based on Cross-Linked Gold Nanoparticles, ACS applied materials & interfaces, 2018 Oct 3;10(43):37374-85.

[25] Xie B, Mao P, Chen M, Li Z, Liu C, Qin Y, Yang L, Wei M, Liu M, Wang X, Han D, A tunable palladium nanoparticle film-based strain sensor in a Mott variable-range hopping regime, Sensors and Actuators A: Physical, 2018 Apr 1;272:161-9.

[26] Aslanidis E, Skotadis E, Moutoulas E, Tsoukalas D, Thin Film Protected Flexible Nanoparticle Strain Sensors: Experiments and Modeling, Sensors, 2020 Jan;20(9):2584.

[27] Chen M, Luo W, Xu Z, Zhang X, Xie B, Wang G, Han M, An ultrahigh resolution pressure sensor based on percolative metal nanoparticle arrays, Nature communications, 2019 Sep 6;10(1):1-9.

[28] Kang D, Pikhitsa PV, Choi YW, Lee C, Shin SS, Piao L, Park B, Suh KY, Kim TI, Choi M, Ultrasensitive mechanical crack-based sensor inspired by the spider sensory system, Nature, 2014 Dec;516(7530):222-6.

[29] Han Z, Liu L, Zhang J, Han Q, Wang K, Song H, Wang Z, Jiao Z, Niu S, Ren L, High-performance flexible strain sensor with bio-inspired crack arrays, Nanoscale, 2018;10(32):15178-86.

[30] Kim KH, Hong SK, Ha SH, Li L, Lee HW, Kim JM, Enhancement of linearity range of stretchable ultrasensitive metal crack strain sensor via superaligned carbon nanotube-based strain engineering, Materials Horizons, 2020;7(10):2662-72.

[31] Kim SJ, Mondal S, Min BK, Choi CG, Highly sensitive and flexible strain–pressure sensors with cracked paddy-shaped MoS2/graphene foam/Ecoflex hybrid nanostructures, ACS applied materials & interfaces, 2018 Sep 27;10(42):36377-84.

[32] Li Q, Wang K, Gao Y, Tan JP, Wu RY, Xuan FZ, Highly sensitive wearable strain sensor based on ultra-violet/ozone cracked carbon nanotube/elastomer, Applied Physics Letters, 2018 Jun 25;112(26):263501.

[33] Zhang W, Liu Q, Chen P, Flexible strain sensor based on carbon black/silver nanoparticles composite for human motion detection, Materials, 2018 Oct;11(10):1836.

[34] Wang S, Xiao P, Liang Y, Zhang J, Huang Y, Wu S, Kuo SW, Chen T, Network cracks-based wearable strain sensors for subtle and large strain detection of human motions, Journal of Materials Chemistry C, 2018;6(19):5140-7.

[35] Park B, Lee S, Choi H, Kim JU, Hong H, Jeong C, Kang D, Kim TI, A semi-permanent and durable nanoscale-crack-based sensor by on-demand healing, Nanoscale, 2018;10(9):4354-60.

[36] Zou Q, Zheng J, Su Q, Wang W, Gao W, Ma Z, A wave-inspired ultrastretchable strain sensor with predictable cracks, Sensors and Actuators A: Physical, 2019 Dec 1;300:111658.

[37] Lee E, Kim T, Suh H, Kim M, Pikhitsa PV, Han S, Koh JS, Kang D, Effect of metal thickness on the sensitivity of crack-based sensors, Sensors, 2018 Sep;18(9):2872.

[38] Kwon Y, Park C, Kim J, Kim H, Park C, Lee B, Jeong Y, Cho SJ, Effects of bending strain and crack direction on crack-based strain sensors, Smart Materials and Structures, 2020 Sep 22;29(11):115007.

[39] Li J, Bao R, Tao J, Dong M, Zhang Y, Fu S, Peng D, Pan C, Visually aided tactile enhancement system based on ultrathin highly sensitive crack-based strain sensors, Applied Physics Reviews, 2020 Mar 18;7(1):011404.

[40] WhanáChoi Y, MoonáKim S, Crack-based strain sensor with diverse metal films by inserting an inter-layer, RSC advances, 2017;7(55):34810-5.

[41] Park B, Lee S, Choi H, Kim JU, Hong H, Jeong C, Kang D, Kim TI, A semi-permanent and durable nanoscale-crack-based sensor by on-demand healing, Nanoscale, 2018;10(9):4354-60.

[42] Yang T, Li X, Jiang X, Lin S, Lao J, Shi J, Zhen Z, Li Z, Zhu H, Structural engineering of gold thin films with channel cracks for ultrasensitive strain sensing, Materials Horizons, 2016;3(3):248-55.

[43] Choi YW, Kang D, Pikhitsa PV, Lee T, Kim SM, Lee G, Tahk D, Choi M, Ultra-sensitive pressure sensor based on guided straight mechanical cracks, Scientific reports, 2017 Jan 6;7(1):1-8.

[44] Schwebke S, Winter S, Koch M, Schultes G, Piezoresistive granular metal thin films of platinum–boron nitride and platinum–alumina at higher strain levels, Journal of Applied Physics, 2018 Dec 21;124(23):235308.

[45] Rafael R, Puyoo E, Malhaire C, Piezo-tunneling strain sensors integrated on plastic by combining vacuum thin film coatings and 3D printing technologies, Microsystem Technologies, 2020 Dec;26(12):3623-8.

[46] Ramírez J, Polat B, Lipomi DJ, Metallic Nanoislands on Graphene for Biomechanical Sensing, ACS omega, 2020 Jun 23;5(26):15763-70.

[47] Dhong C, Edmunds SJ, Ramírez J, Kayser LV, Chen F, Jokerst JV, Lipomi DJ, Optics-free, non-contact measurements of fluids, bubbles, and particles in microchannels using metallic nano-islands on graphene, Nano letters, 2018 Jul 19;18(8):5306-11.

[48] Aslanidis E, Skotadis E, Tsoukalas D, Resistive crack-based nanoparticle strain sensors with extreme sensitivity and adjustable gauge factor, made on flexible substrates, Nanoscale, 2021;13(5):3263-74.

[49] Zhang P, Dai Y, Viktorova J, Offenhäusser A, Mayer D, Electronic Responses to Humidity in Monolayer and Multilayer AuNP Stripes Fabricated by Convective Self-Assembly, physica status solidi (a), 2018 Aug;215(15):1700950.

[50] Patsiouras L, Skotadis E, Gialama N, Drivas C, Kennou S, Giannakopoulos K, Tsoukalas D, Atomic layer deposited Al_2O_3 thin films as humidity barrier coatings for nanoparticle-based strain sensors, Nanotechnology, 2018 Sep 20;29(46):46.

Chapter 6: Strain Sensor Array on Flexible Substrates

In this chapter we present how the sensors that were developed and studied by our team were used to create a strain sensor array. The sensors were developed on kapton flexible substrate and placed on a rubber glove right upon the metacarpophalangeal joints of the hand, as demonstrated in Fig. 6.1. They are capable of detecting even the simplest everyday movements of the hand.

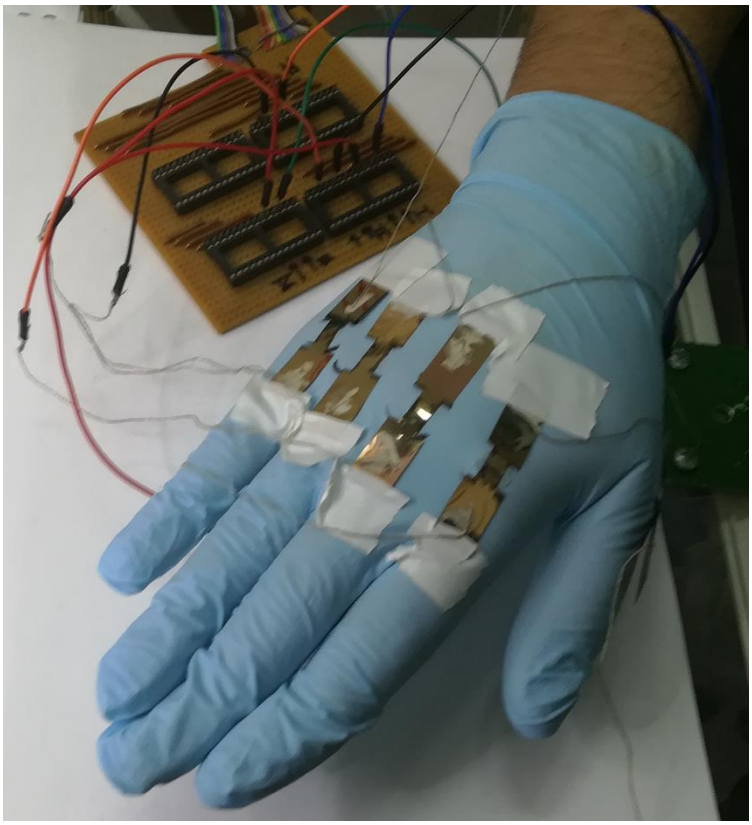

Figure 6.1: Flexible strain sensors on a rubber glove. The sensors are located above the metacarpophalangeal joints of the hand which are the more active joints in terms of hand movement.

The measurements of the sensors were taken using an electronic circuit designed for the simultaneous measurement of a sensor array as well as a Keithley 2400 unit.

6.1. Sensor array measurements

6.1.1. Strain sensors

We used two types of strain sensors for these measurements. The first one was Pt NPs based strain sensors on flexible substrate with NPs surface coverage of 49% deposited directly on top

of the substrate without using cracked alumina. These specific strain sensors have GF around 67. The second one was Pt NPs based strain sensors with cracked alumina of 20 nm thickness. The NPs surface coverage was of 79% which results in a very high GF of 8000 for strains from 1.2% to 4.2%. All sensors were glued on a rubber clove and their electrodes were connected with a conductive thread using silver paste (Fig. 6.1). Afterwards, the conductive thread was connected with commercial jumper wires which were connected to the measurement unit.

6.2. Circuit design and analysis

The circuit is a modification of the circuit that was originally designed in NCSR Demokritos [1, 2].Modifications and selections of components and operational amplifiers were made so that the system would responds optimally.

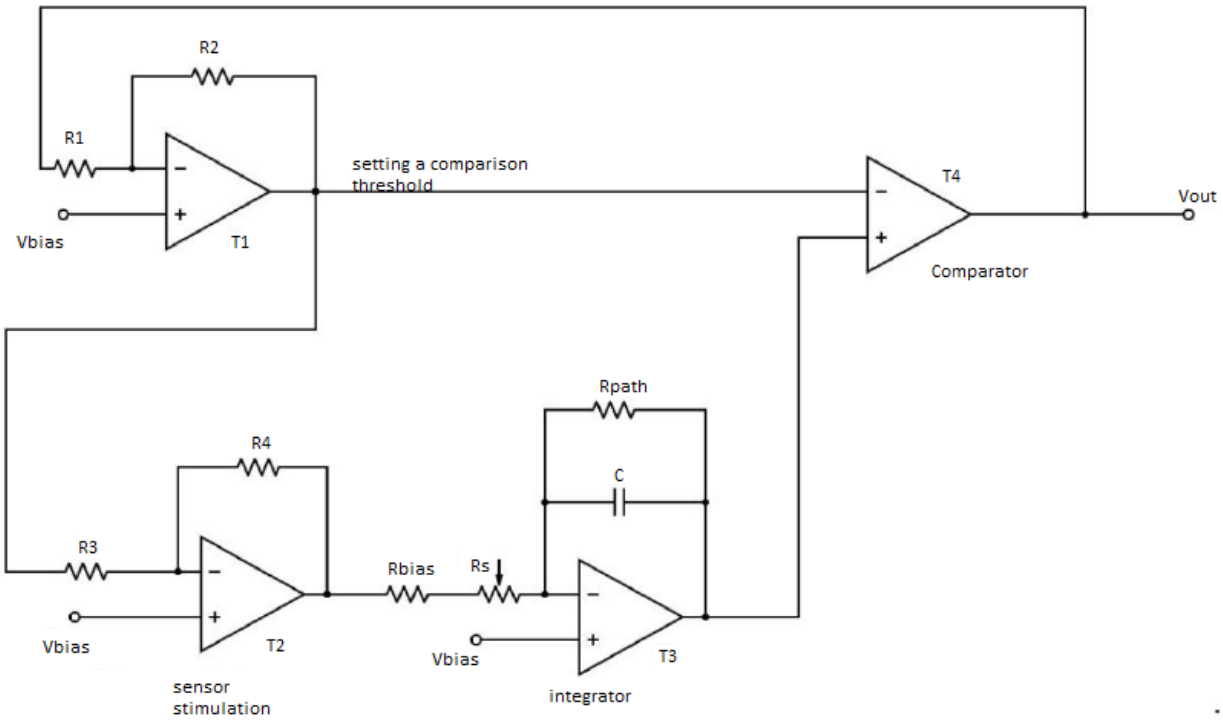

Figure 6.2: The analog circuit.

The advantage of the analog circuit (and the reason it prevailed over other options) is that it produces as an output a square waveform between the supply voltages of the operational amplifiers [3], with a period proportional to the sensors' resistance R_s. By properly selecting the power supply of the circuit, a digital pulse series is finally created which feeds the digital circuit (Arduino Mega) directly, without the use of an analog-to-digital converter and thus adding noise and errors to that stage. This option corresponds to $V_{DD} = 5\ V$ and $V_{SS} = 0\ V$, that is selecting single source operational amplifiers.

The operational amplifier T1 (Fig. 6.2) determines the comparison threshold based on which the output of the operational amplifier T4 will occur (digital pulse series between 0 and 5 V). Amplifier T2 appropriately modulates the width of the square pulse which feeds the sensor. Finally, amplifier T3. Finally, T3 produces a triangular pulse which is compared to the threshold voltage in order to generate the output pulse and determines -depending on the choice of passive elements- the output waveform period. It is important to note that the operational amplifiers T1, T2 and T3 operating in the linear region with negative feedback, create symmetrical waveforms with respect to the reference voltage at their positive input. If a single supply voltage is used, half of the supply voltage is selected as the reference voltage (virtual ground), $V_{bias} = V_{DD}/2 = 2.5\ V$. Therefore all waveforms generated during the transient operation of the circuit will be added to the reference voltage.

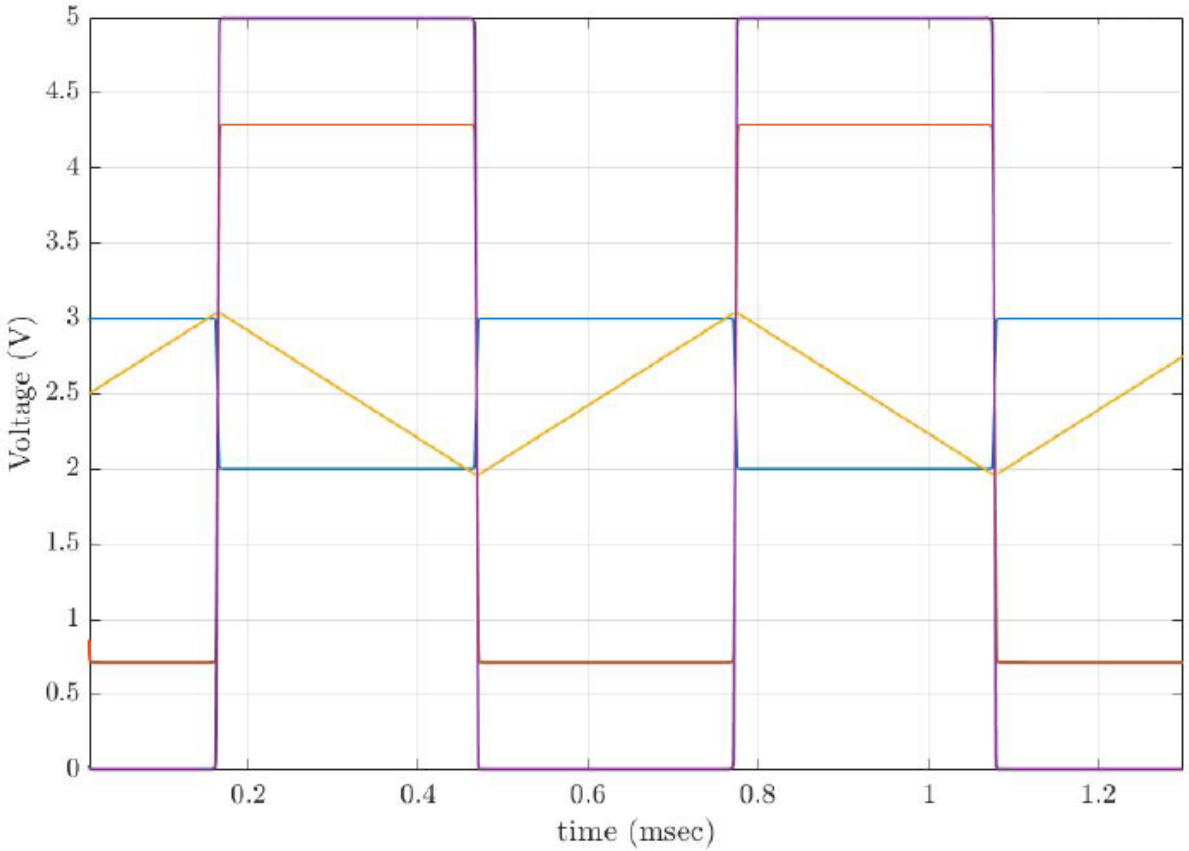

Figure 6.3: Indicative snapshot of analog circuit operation. Blue line represents the comparison threshold, red line represents the operator output, yellow line represents the integrator output and purple line represents the comparator output.

In the followings, we study the behavior of the circuit in the case of operation at high frequencies, which is its practical application. The circuit operates with reference voltage V_{bias}, producing symmetrical waveforms. It is initially considered important that the output voltage of an operational amplifier operating in the linear region with negative feedback, with feedback resistance Rf and input resistance R, is:

$$u_{out} = \left(\frac{R_f}{R} + 1\right) V_{bias} - \frac{R_f}{R} u_{in} \tag{6.1}$$

where u_{out} and u_{in} are the output and input voltages accordingly. The output voltages of the comparator in relation with time is:

$$u_{out} = \begin{cases} V_{DD}, & u_{T_{4+}} > u_{T_{4-}} \\ 0, & u_{T_{4+}} < u_{T_{4-}} \end{cases} \tag{6.2}$$

Where u_{T4+} and u_{T4-} are the input voltages of the T4 operation amplifier of the positive and negative inputs accordingly. From equation (6.1) we can predict the shape of the output signals at each stage of the circuit. Since this is a square pulse series, the output of T1 and T2 will also be a square pulse series, while the output of the T3 (integrator) will be a trigonal pulse series. Due to the fact that the circuit is an oscillator and since the operational amplifier T4 acts as a comparator, sometime after the connection to the power supply, due to noise the output of the comparator will go to one of the two possible states (0 or V_{DD}). This time is defined as t = 0. The output of the T1 is:

$$u_{T_{1.0}} = \left(1 + \frac{R_2}{R_1}\right) V_{bias} - \frac{R_2}{R_1} u_{out} \tag{6.3}$$

This voltage is the input voltage of the T2:

$$u_{T_{2.0}} = \left(1 + \frac{R_4}{R_3}\right) V_{bias} - \frac{R_4}{R_3} u_{T_{1.0}} \tag{6.4}$$

Applying the (6.3) to (6.4):

$$u_{T_{2.0}} = \left(1 - \frac{R_4 R_2}{R_3 R_1}\right) V_{bias} + \frac{R_4 R_2}{R_3 R_1} u_{out} \tag{6.5}$$

In the next stage the operational amplifier is an integrator (T3). At time t = 0 the initial value of the integrator will be $u_{T3.0}$ and the output is given by the following equation:

$$u_{T_{3.0}}(t) = u_{T_{3.0}}(0) + \frac{1}{(R_s + R_{bias})C}\int_0^t \frac{R_2R_4}{R_1R_3}(V_{bias} - u_{out})dt \quad (6.6)$$

The values of the comparison threshold and the processor remain constant until the output of the circuit (i.e. T4) changes value. Therefore as long as the output of the circuit has a constant value, the output voltage at the ends of the integrator can be calculated by integrating from 0 to t ($t < t_{high}$ or $t < t_{low}$ where the output is 5 V and 0 V accordingly).

$$u_{T_{3.0}}(t) = u_{T_{3.0}}(0) + \frac{1}{(R_s + R_{bias})C}\frac{R_2R_4}{R_1R_3}(V_{bias} - u_{out})t \quad (6.7)$$

A change in the output voltage of the comparator will occur at time t where the voltage at the positive and negative input terminals will be equal $u_{T4,+} = u_{T4,-}$.

$$V_{bias} + \frac{R_2}{R_1}(V_{bias} - u_{out}) = u_{T_{3.0}}(0) + \frac{1}{(R_s + R_{bias})C}\frac{R_2R_4}{R_1R_3}(V_{bias} - u_{out})t \quad (6.8)$$

The time variable in the equation corresponds to the slope of the triangular waveform produced by this stage and therefore determines the period of the pulse series which is created. From the equation (6.8) the initial condition of the equation (6.7) is obtained, i.e. the load of the integrator (which depends on the capacitor) at time t = 0.

$$u_{T_{3.0}}(0) = \left(1 + \frac{R_2}{R_1}\right)V_{bias} - \frac{R_2}{R_1}u_{out}(0^-) \quad (6.9)$$

where $u_{out}(0^-)$ is the output voltage of the comparator just before the time t = 0.

6.2.1. Period calculation of the square pulse series

The time interval t requires from the time t = 0 to the time when the equation (6.8) will be satisfied and the output voltage changes is given by the following equation:

$$t_1 = \frac{(R_s + R_{bias})R_1R_3C}{R_4R_2(V_{bias} - u_{out})}(V_{bias} + \frac{R_2}{R_1}(V_{bias} - u_{out}) - u_{T_{3.0}}(0)) \quad (6.10)$$

Initially we consider that the circuit when $u_{out} = V_{DD}$, ie for $t = t_{high}$.

$$t_{high} = \frac{V_{DD}}{V_{DD} - V_{bias}} \frac{(R_s + R_{bias})C}{|G_{T_2}|} \tag{6.11}$$

where $G_{T2} = -R_4/R_3$ is the gain of the T2. In the same manner, we can calculate the time interval when the voltage output is low, i.e. $u_{out} = 0$ and $t_1 = t_{low}$.

$$t_{low} = \frac{V_{DD}}{V_{bias}} \frac{(R_s + R_{bias})C}{|G_{T_2}|} \tag{6.12}$$

Adding the equations (6.11) and (6.12):

$$T = \frac{V_{DD}^2}{V_{bias}(V_{DD} - V_{bias})} \frac{(R_s + R_{bias})C}{|G_{T_2}|} \tag{6.13}$$

For $V_{bias} = V_{DD}/2$ we obtain:

$$T = \frac{4(R_s + R_{bias})C}{|G_{T_2}|} \tag{6.14}$$

The equation (6.14) is the most important of the circuit. The digital circuit calculates the period and decides on the measured resistance of the sensor. We suppose that the smallest resistance to be measured is R_{min} and the largest R_{max} with periods T_{min} and T_{max} respectively. The equation (6.14) becomes:

$$\frac{4(R_{min} + R_{bias})}{|G_{T_2}|} \leq \frac{T}{C} \leq \frac{4(R_{max} + R_{bias})}{|G_{T_2}|} \tag{6.15}$$

We can obtain the capacitance from the next equations:

$$C \geq \frac{|G_{T_2}|T_{min}}{4(R_{min} + R_{bias})} \tag{6.16}$$

$$C \leq \frac{|G_{T_2}|T_{max}}{4(R_{max} + R_{bias})} \tag{6.17}$$

At the equation (6.16) the period corresponding to the minimum measured resistance is selected. Contrary to the equation (6.17) the time required to measure a period by the digital system is determined. Hence the maximum response time of the analog system. From the equations it can be deduced that as R_s increases, so does the period of the waveform. It is also understood that the value of the capacitor determines the maximum and the minimum value of the measured resistance within a reasonable time. It is not possible to achieve a small amount of uncertainty and fast response time, so a compromise is necessary. The larger the capacitor value the lower the measurement uncertainty but it can be proven to be extremely slow. In contrary with smaller capacitor value, the measurement will be very fast but with very high uncertainty. For the above-mentioned reasons, the following electrical elements were selected so that the circuit can measure resistances 200 from kOhm to 1Mohm. For the implementation was used the OPA 4353 amplifier from Texas Instruments.

Components	Value
R_1	10 kOhm
R_2	2 kOhm
R_3	10 kOhm
R_4	35 kOhm
R_{bias}	100 kOhm
C	400 pF
R_{div1}	1 MOhm
R_{div2}	1 MOhm

6.2.2. Digital system analysis – Period measurements

To measure the period of the pulse series, it is enough to find the space between two positive edges. Accurate detection of positive edges is accomplished by managing them as interrupts. When the first positive pulse arrives, the interrupt service routine activates one of the microcontroller meters (Arduino Mega 2560), the value of which increases at a frequency determined by us. The value we have chosen is 16 Mhz, which is the maximum possible frequency. As soon as the second positive pulse arrives, the service routine stops the meter and stops receiving other interrupts.

If we know the value of the meter and the period of its increase we can find the time interval from the first to the second pulse. In order to get the meter value correctly we must take into account the overflow that can occur. The meter is 16bit which means that it counts from 0 to 2^{16} – 1. Whenever an overflow occurs (which is also treated as an interruption) a routine service is called which leads to the increase of another meter that maintains the number of overflows ($N_{overflows}$).

The value of the timer is given by:

$$N_{total} = N_{overflows}2^{16} + N_{timer} \quad (6.18)$$

The period of the square pulse series is given by:

$$T = N_{total}T_{timer} \quad (6.19)$$

For accuracy instead of measure the time difference between two edges, we measure k and obtain the mean value:

$$T = \frac{N_{total}T_{timer}}{k-1} \quad (6.20)$$

6.3. Sensor array

A basic requirement of the system is the ability to measure multiple resistors from a single sensor matrix. For reasons of simplicity during the development of the system, a 1x8 matrix was implemented.

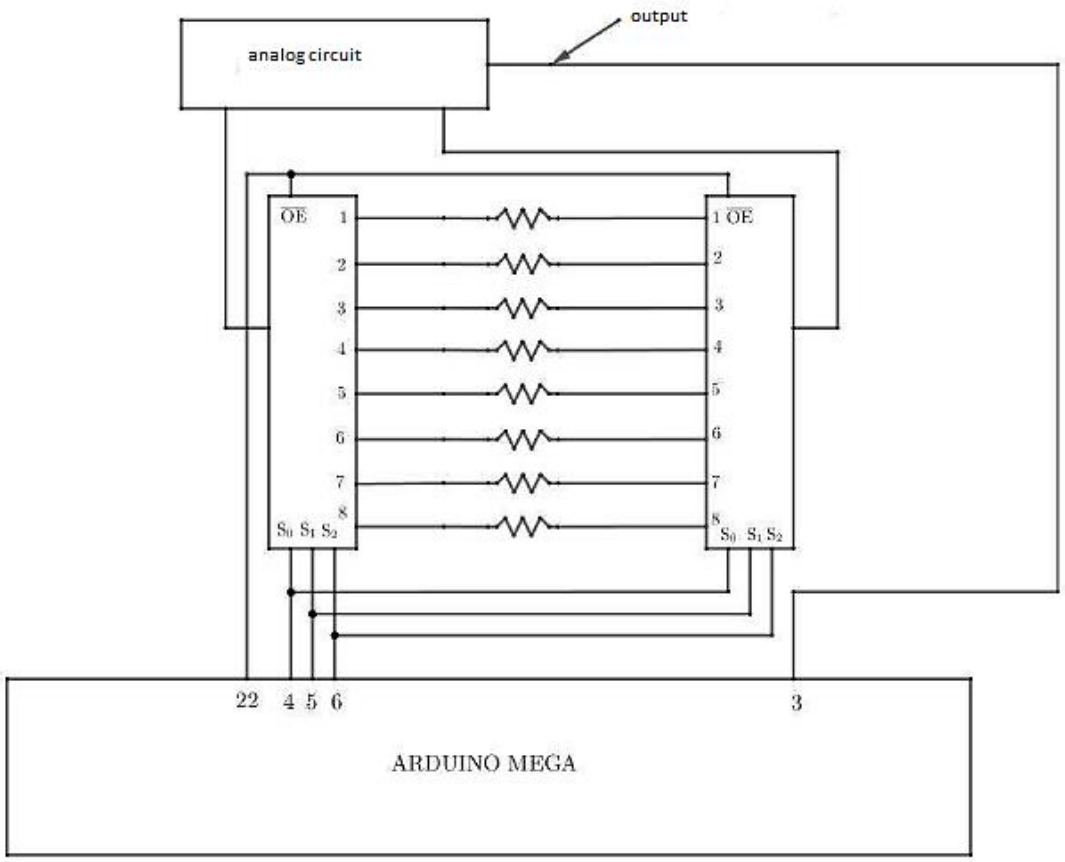

Figure 6.4: Schematic representation of the 1x8 sensor matrix. Each sensor is located between two multiplexers. The sensors are represented as resistors between the multiplexers OE.

Two 8-in-1 multiplexers with the possibility of bidirectional current flow were used. As shown in Fig. 6.4 each resistor / sensor R_i of the matrix was connected to the inputs i of the two multiplexes. The outputs of the multiplexers were connected to the analog circuit at the position of the resistor R_s. The microprocessor controls the multiplexers so that the desired resistance is selected each time and the rest are isolated.

sensor	s0	s1	s2
0	0	0	0
1	0	0	1
2	0	1	0
3	0	1	1
4	1	0	0
5	1	0	1
6	1	1	0
7	1	1	1

Table .The table above shows the selection signals, which should be common to the two multiplexers for the proper operation of the circuit.

6.4. Measurements

Sensors' resistance was measured while the clove was worn and was performing some everyday movements, such as making a fist or counting up to five etc.

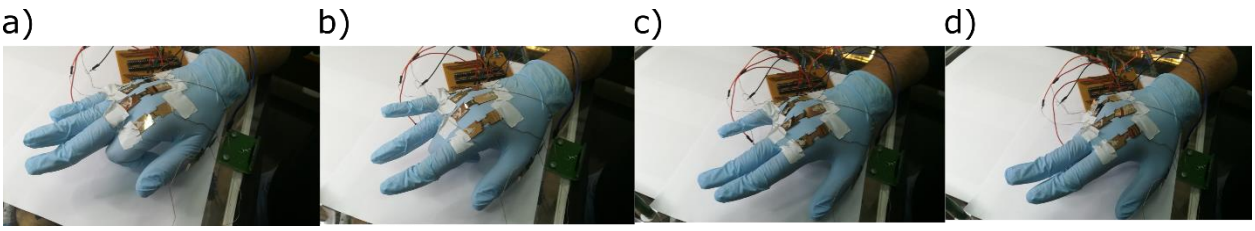

Figure 6.5: Finger movements a) index finger, b) Middle finger, c) Ring finger and d) Little finger with simultaneously slight movement of the ring finger

Below are demonstrated the results from four sensors, which were glued on a glove. The measurements were taken from the above-mentioned system.

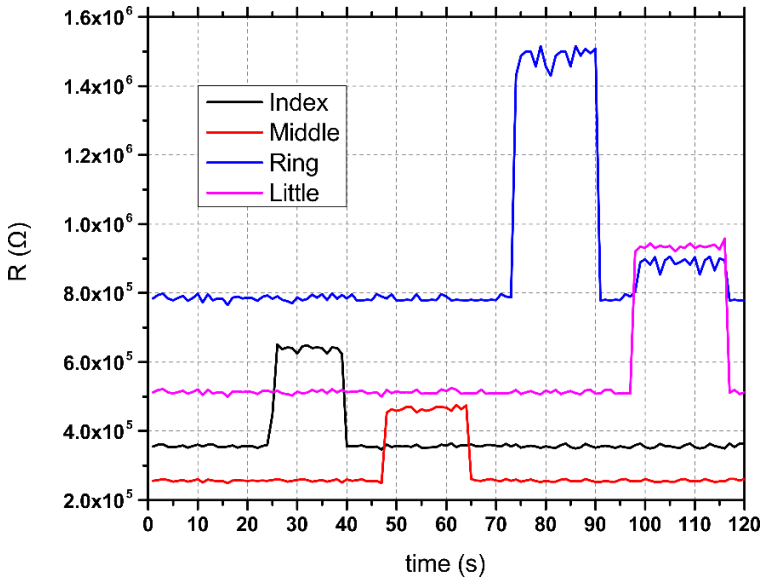

Figure 6.6: Resistance response of sensors array. Black line represents the sensor of the index finger, red line represents the sensor of the middle finger, blue line represents the sensor of the ring finger and pink line represents the sensor of the little finger.

The sensors react when there is movement in the corresponding finger. For example, the motion of the index finger (Fig. 6.5) makes the corresponding sensor react and increase its resistance. In the same manner, when any finger moves the sensors detect the movement and increase their resistance. Their initial resistance were around one hundreds of kOhm and their response varied depending the finger.

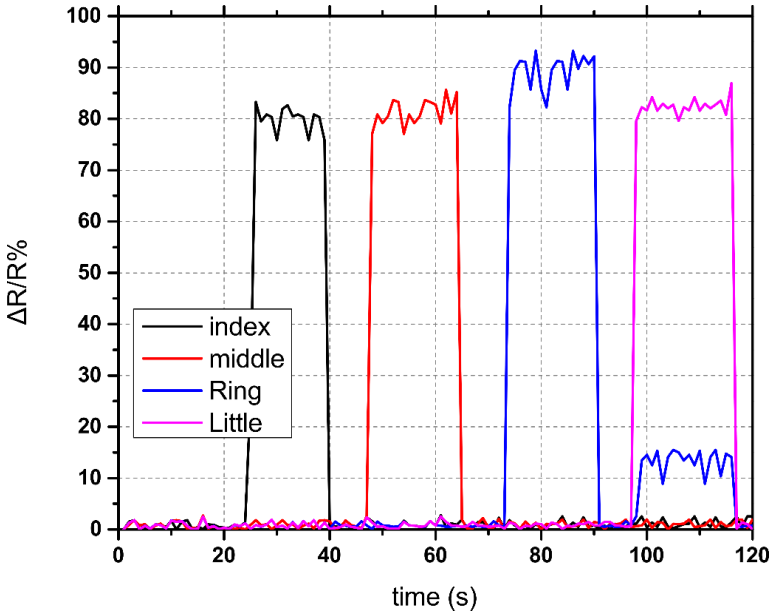

Figure 6.7: Relative resistance change of sensor array.

In this simple example, the change in resistance of all the sensors was measured as each finger performed a simple movement. We observe that when the little finger closes the

resistance of the ring finger also changes as it is impossible the individual movement of the little finger. The sensors on average have a relative change of resistances of 80%, which is increased but as we saw in the previous chapters we can build extremely sensitive sensors. Nevertheless, the very sensitive sensors have a large G factor and therefore the change in resistance will be very large, making it difficult to detect by the system we mentioned. In addition, the initial resistance of the sensors is of the order of a few ohms, which makes it even more difficult to detect with the system. So we used the Keithley 2400 for the next measurements.

6.5. Measurements by a Keithley unit

Below are demonstrated the measurements for the sensors of the previous paragraph so that a comparison of the results can be made directly between our system and a professional system.

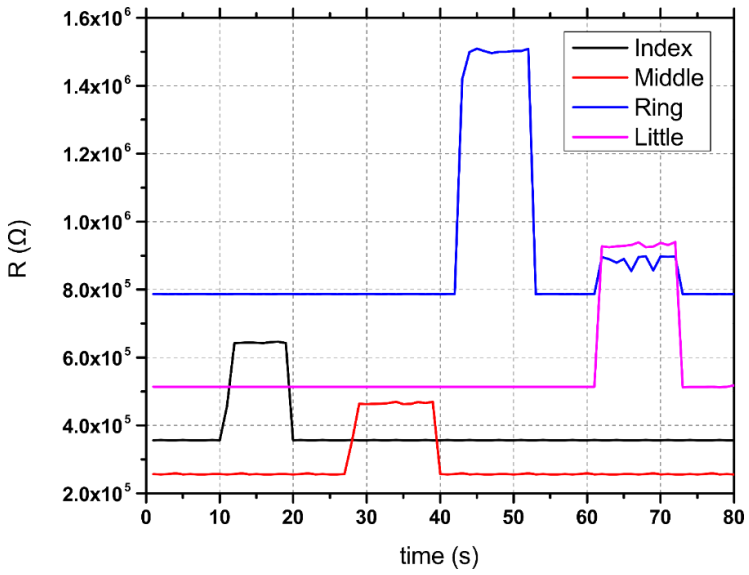

Figure 6.8: Resistance response of sensors array of sensors with low sensitivity

The results show that the noise is extremely low with Keithley compared to previous measurements. However, the values for the resistors as well as the values for the relative change in resistance remain the same for both systems. This is a proof that -in the window where the system is set to measure- it does so quite well.

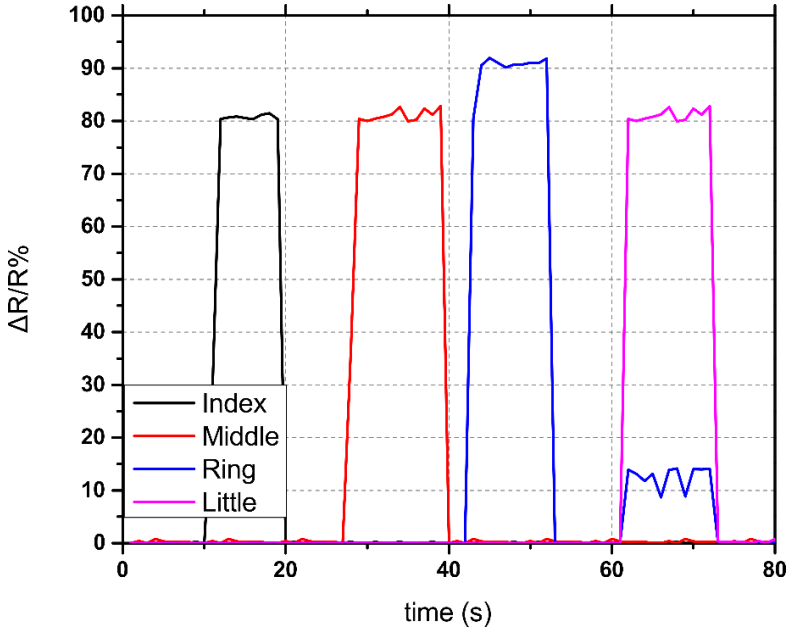

Figure 6.9: Relative resistance change of the sensor array with low sensitivity

In Fig. 6.9 is depicted the performance of the above-mentioned sensors. All sensors have relatively the same response; around 80%. Assuming that the sensors have the same sensitivity of 67, the applied strain is calculated to be 1.19%. Afterwards we measure the very sensitive sensors in corresponding experiments with the previous measurements.

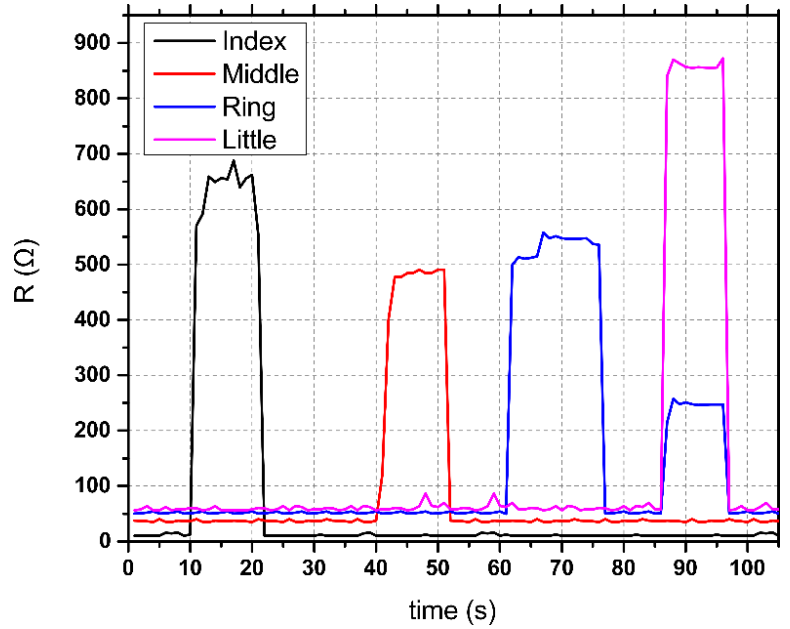

Figure 6.10: Resistance response of sensors array of sensors with high sensitivity.

In Fig. 6.10 is demonstrated the resistance response of the sensor array using sensors with high sensitivity. Initially, the initial resistance is very low from 10 Ohm for the sensor of the index finger to 55 Ohm for the sensors of Ring and Little fingers. Their performance is presented below.

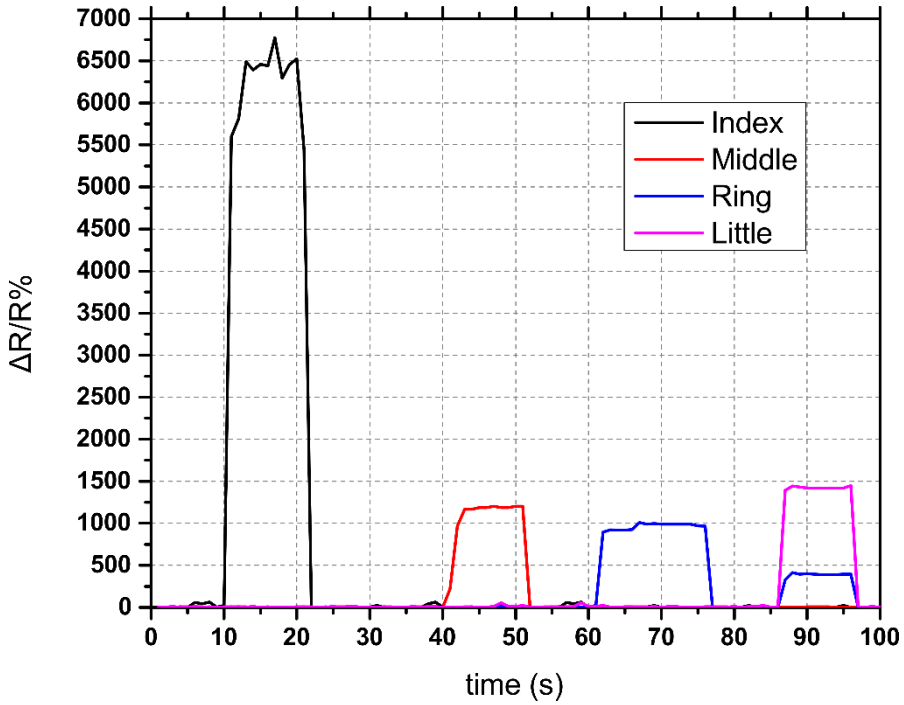

Figure 6.11: Relative resistance change of the sensor array with high sensitivity

The exceptional performance of the cracked based strain sensors is presented in Fig. 6.11. Their relative resistance change is increased to around 1000%, with the exception of the index finger sensor which has an extremely high response of 6500% but the majority of the sensors does not response the same. Assuming that the sensors with low sensitivity predict the correct applied strain (that of 1.19%), then the GF of the sensors with high sensitivity is calculated to be 840. This calculation is in agreement with Table 5.2.

6.6. Suggestions for improvement

It is worth noting that the original purpose of the system was to make a matrix of sensors as shown in the figure below.

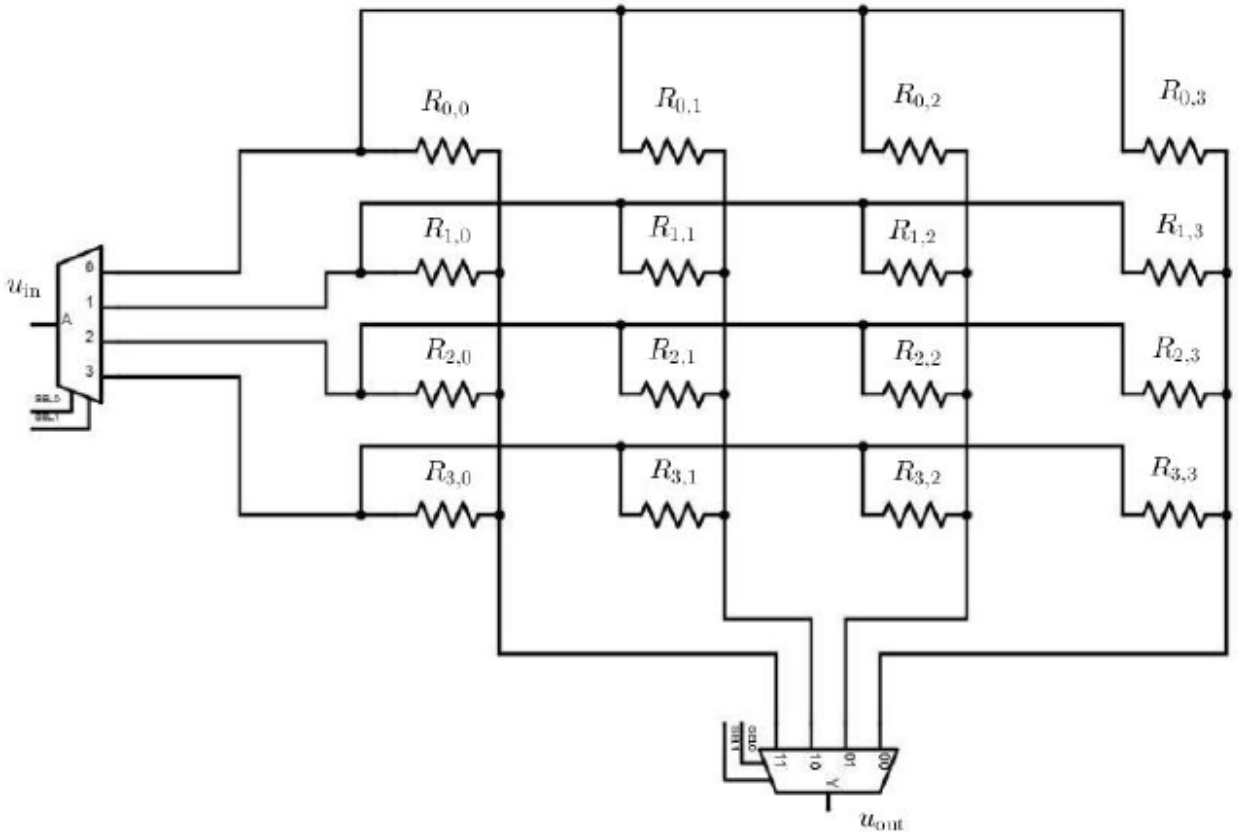

Figure 6.12: Schematic representation of a 4x4 matrix of resistances. Each resistance is represents a sensor

In this case n x 1 multiplexers were used with backflow current, creating a panel with n^2 sensors. When we want to measure the sensor located in position ij then one multiplexer integrates the line i and the another the column j. The problem with concrete design is that there are too many conductive paths between the unselected sensors and consequently the addition of significant errors. The larger the matrix size, the harder it is to predict and eliminate errors.

A common solution for such problems is to add a diode in series to each sensor. However, such an addition would prevent the measurement of the sensor as during its measurement there is not only one direction of current. The existence of the diode allowed only one direction of current. One solution is to add MOSFETs in series with each sensor, which will act as switches. But, in addition to the additional hardware, it also requires the management of n^2 control signals by the microprocessor.

6.7. References

[1] Chatzandroulis S, Tsoukalas D, Capacitance to frequency converter suitable for sensor applications using telemetry, Analog Integrated Circuits and Signal Processing, 2001 Apr;27(1):31-8.

[2] Chatzandroulis S, Tsoukalas D, Neukomm PA, A miniature pressure system with a capacitive sensor and a passive telemetry link for use in implantable applications, Journal of Microelectromechanical Systems, 2000 Mar;9(1):18-23.

[3] http://www.ti.com/lit/ds/symlink/opa353.pdf

Chapter 7: Conclusions and Perspectives

In this dissertation an extensive study of strain sensors on flexible substrates was performed. Specifically, sensors based on platinum nanoparticles on flexible Kapton substrates were studied. The techniques mentioned in the first chapter were used to fabricate the sensors as a two-terminal resistive device while in the second chapter we illustrate the physical principles of its operation.

The third chapter includes first the already accepted model in the literature that explains the sensitivity of NPs based strain sensors which applies well in the case of colloidal nanoparticles where an ordered NP array is formed after deposition. The main difference in our case is that for sputtered NPs during the application of strain, new gaps are created which are responsible for the gradually increased sensitivity. Apart from that in the same chapter we have presented a technical study that elaborates the influence on the device stability against R.H. of protective coatings. As protective coating against humidity we use an alumina film of various thicknesses deposited by the ALD technique. The alumina layers were evaluated as far as their protective properties against the effect of fatigue under varying relative humidity conditions for both unstrained and under applied strain devices.

In the fourth chapter, the sensitivity of nanoparticle-based strain sensors was further studied with the help of a Monte Carlo simulation tool we have developed. The code was written in Matlab and its main purpose was to provide sensitivity analysis of random nanoparticle networks. To achieve this, it calculates first the potential conductive paths formed by the nanoparticles and creates an equivalent circuit model from them. The circuit is calculated by assuming that each nanoparticle or nanoparticle island is a node in the circuit and each inter-particle gap is a resistor. The value of each resistor depends on the length of the gap. With the help of the Laplace matrix the total resistance and hence the sensitivity is calculated. The specific tool predicts sensitivities for nanoparticles of various sizes but also deposited under different surface coverage percentages.

In the fifth chapter, we analyze the case of extremely sensitive NP sensors based on cracks. To achieve this, alumina films were deposited first on the flexible substrate through ALD which create cracks when they undergo large deformations. Nanoparticles and electrodes were then deposited on the top of the alumina films as before. The effect of the alumina thickness and the surface coverage of the nanoparticles on the sensitivity of the sensors was studied. With this technique we were able to develop the most sensitive strain sensor ever reported at the time of writing.

In the sixth chapter we discuss the design of a circuit for measuring sensor arrays. The configuration including the circuit and individual highly sensitive NP sensors although still in very prototype form, has very good accuracy with relatively little error in the measurements. However, it has a very small working window regarding the sensor resistance in which it can be efficient. Efforts to develop further the system by integrating the sensors on the

same piece of flexible substrate will continue towards the demonstration of a more compact sensing system towards the artificial skin concept.

As future ideas, regarding the sensors of the third chapter, the study of different coatings for protection from moisture is proposed. While alumina film manages to adequately protect against moisture, as shown in chapter five, it tends to crack when large strain value is applied. Cracks allows moisture to enter in to the nanoparticle film and add a large error in measuring the strain. Coatings -not as rigid as alumina- should be considered, as it is not easy to create cracks by mechanical deformation and at the same time block moisture molecules. Such coatings could be polymeric films, which are extremely flexible, such as DPMS or even a combination of polymeric films with alumina. Thus, the alumina (that we know that does not allow the passage of moisture molecules) could be deposited on a flexible polymer (or between different polymers) and the combination of those films will protect the nanoparticles. Another study of great interest would be the characterization of nanoparticle devices in AC voltage and the measurement of their impedance. With such a study, we could enrich our understanding of the electrical behavior of sensors. Their characterization for different temperature values and how the correlation with temperature could be eliminated, as the nanoparticle sensors are also sensitive to its changes would be also very important. Of course, other materials could also be studied for the substrate, such as DPMS, which is stretchable while kapton is not. In addition, different materials for nanoparticles could be studied, such as non-noble metals that are cheaper.

As far as the simulation is concerned, the code which is given in Appendix A, could easily be enriched in order to be able to simulate structures other than spherical nanoparticles. For example, it could simulate films from nanotubes and structures that are more complex. In addition, it would be useful to be modified so that it could also predict the impedance of a system for different frequencies. Of course, the above is probably quite difficult as it is written to solve only linear systems of equations and the transition to the differentials (which may be needed to find the impedance) could be very complicated.

Further, the sensors' technique with the cracks may be able to be introduced in other fields. For example, they could be used as chemical sensors to detect moisture, pesticides or other substances. This could be achieved by depositing some polymers on them, which would swell when in a wet environment. They essentially absorb moisture and increase their size while supporting the nanoparticles below them. If this technique is combined with a crack sensor it could result in a chemical sensor with extremely high sensitivity. In this case is also very important the characterization of the sensors based on the temperature as it is the study of their impedance.

Other materials could also be studied for the role of the cracked substrate. Possibly other deposition techniques, such as ionizing. At the same time it would be very interesting to study in depth the physical mechanism that creates the cracks and how one could control their density,

direction, periodicity (if any) and other quantities. By checking the periodicity and direction, for example, a cracked film could be used as a lithography mask.

Finally, in terms of the sensor array counting system, it could be developed as a portable device for measuring the sensor array without the need to connect to a computer. Thus measurements could be made, for example, of a pesticide directly in the field (field, greenhouse, etc.) for long periods of time without the presence of a human being there. Firstly, one would need to design and build a suitable case that could be printed with a 3D printer. The circuit must then be properly designed to be powered by a battery. Appropriate software can also be designed, which may be controlled by a mobile phone, with which it can download the measurements and control the operation of the system. To do this, the appropriate antennas must be inserted into the system. Finally, it should be studied whether it is possible to measure the sensors as elements of a matrix and how the electrically measured elements will be electrically isolated.

Publications List

Journal Papers

1. **Aslanidis E,** Skotadis E, Tsoukalas D, Simulation tool for predicting and optimizing the performance of nanoparticle based strain sensors, Nanotechnology, 2021 Mar 24.
2. **Aslanidis E,** Skotadis E, Tsoukalas D, Resistive crack-based nanoparticle strain sensors with extreme sensitivity and adjustable gauge factor, made on flexible substrates, Nanoscale, 2021;13(5):3263-74.
3. **Aslanidis E**, Skotadis E, Moutoulas E, Tsoukalas D, Thin Film Protected Flexible Nanoparticle Strain Sensors: Experiments and Modeling, Sensors, 2020 Jan;20(9):2584.
4. Skotadis E, **Aslanidis E**, Kainourgiaki M, Tsoukalas D, Nanoparticles Synthesised in the Gas-Phase and Their Applications in Sensors: A Review, Applied Nano, 2020 Dec;1(1):70-86.
5. Skotadis E, Kanaris A, **Aslanidis E**, Michalis P, Kalatzis N, Chatzipapadopoulos F, Marianos N, Tsoukalas D, A sensing approach for automated and real-time pesticide detection in the scope of smart-farming, Computers and electronics in agriculture, 2020 Nov 1;178:105759.
6. Tsigkourakos M, Bousoulas P, **Aslanidis V**, Skotadis E, Tsoukalas D, Ultra-Low Power Multilevel Switching with Enhanced Uniformity in Forming Free TiO2− x-Based RRAM with Embedded Pt Nanocrystals, physica status solidi (a), 2017 Dec;214(12):1700570.
7. Bousoulas P, Karageorgiou I, **Aslanidis V**, Giannakopoulos K, Tsoukalas D, Tuning Resistive, Capacitive, and Synaptic Properties of Forming Free TiO2-x-Based RRAM Devices by Embedded Pt and Ta Nanocrystals, physica status solidi (a), 2018 Feb;215(3):1700440.

Conferences

1. **Aslanidis E**, Patsiouras L, Moutoulas E, Skotadis E, Kennou S, Tsoukalas D, Humidity Protected Platinum nanoparticles strain sensor using alumina coating, (Micro and Nano 2018 Conference)
2. **Aslanidis E**, Patsiouras L, Skotadis E, Giannakopoulos K, Tsoukalas D, The effect of cracked alumina substrate on high sensitive Pt nanoparticles strain sensor, (45th international conference on MNE 2019)
3. Patsiouras L, Moutoulas E, Gialama N, **Aslanidis E**, Skotadis E, Tsoukalas D, Kennou S, Humidity barrier coatings for Pt nanoparticle – based strain sensors deposited by atomic layer deposition, (MNE 2018, Micro & Nano Engineering Conference, Copenhagen)
4. Patsiouras L, **Aslanidis E**, Skotadis E, Moutoulas E, Gialama N, Kennou S, Giannakopoulos K, Tsoukalas D, Protection of Pt nanoparticles strain sensors against humidity by atomic layer deposition, (33rd Panhellenic conference on Solid State Physics and Materials Science)

5. Skotadis E, Patsiouras L, Kousoulas-Vargkas E, **Aslanidis E**, Tsoukalas D, Nanomaterial based Flow-sensor, for facile microfluidic chip integration, (45th international conference on MNE 2019)

APPENDIX A

Monte Carlo code

```
sa = 216; % y dimension in nm
sb = 216; % x dimension in nm
sar = 100000; % electrode distance in nm of the real sensor
sbr = 4000000; % electrode width in nm of the real senor
SA = sar/(sa - 16); % real over simulation length ratio
SB = sbr/(sb - 16); % real over simulation length ratio
EF = SA/SB; % multiplier factor for correction in the final resistance
E = rand(sa, sb) < 0.02; % random filling E matrix with aces with probability
less than x%
A = zeros(sa, sb); % pre-allocation of A matrix
X = zeros(sa, sb); % pre-allocation of X matrix
Pathfinder = zeros(sa, sb); % pre-allocation of the Pathfinder matrix
Pathfinder1 = zeros(sa, sb); % pre-allocation of the Pathfinder1 matrix
Pathfinder2 = zeros(sa, sb); % pre-allocation of the Pathfinder2 matrix
D = zeros(sa, sb); % pre-allocation of D matrix
K = zeros(sa, sb); % pre-allocation of K matrix
v = 0.278; % Poisson ratio
step = 0.0003; % strain step
dy = v*step; % length change due to Poisson ratio
xf = 1.0042; % final length
r = 5.4*10^-6; % pre-exponetial constant in Ohms
b = 28; % electron coupling term in nm^-1
e = 1.60217662*10^-19; % electron charge in C
e0 = 8.8541878128*10^-12; % Vacuum permittivity in C^2/N*m^2
eair = 1.000589; % relative permittivity of air
meandiameter = 8; % nanoparticles mean diameter
radius = meandiameter/2; % nanoparticles radius
standardeviation = 0.8; % mean diameter standard deviation
Ec = (e^2/(8*pi*e0*eair)); % mean activation energy in N*m
Ecsi = Ec*6.24150913*10^18; % mean activation energy in eV
Kb = 8.617333262145*10^-5; % Boltzmann constant in eV*K^-1
T = 300; % Temperature in K
Ecfinal = Ecsi/(Kb*T);
for i = 1 : sa
    for j = 1 : sb
        if E(i, j) == 1
            A(i, j) = round(normrnd(meandiameter, standardeviation));
        end
    end
end

% counting how many 1, 2, 3 etc. existing in A matrix
c0 = 0;
c1 = 0;
c2 = 0;
c3 = 0;
c4 = 0;
c5 = 0;
c6 = 0;
c7 = 0;
c8 = 0;
c9 = 0;
```

```
c10 = 0;
c11 = 0;
c12 = 0;
c13 = 0;
for i = 1:sa
    for j = 1:sb
        if A(i, j) == 1
            c1 = c1 + 1;
        elseif A(i, j) == 2
            c2 = c2 + 1;
        elseif A(i, j) == 3
            c3 = c3 + 1;
        elseif A(i, j) == 4
            c4 = c4 + 1;
        elseif A(i, j) == 5
            c5 = c5 + 1;
        elseif A(i, j) == 6
            c6 = c6 + 1;
        elseif A(i, j) == 7
            c7 = c7 + 1;
        elseif A(i, j) == 8
            c8 = c8 + 1;
        elseif A(i, j) == 9
            c9 = c9 + 1;
        elseif A(i, j) == 10
            c10 = c10 + 1;
        elseif A(i, j) == 11
            c11 = c11 + 1;
        elseif A(i, j) == 12
            c12 = c12 + 1;
        elseif A(i, j) == 13
            c13 = c13 + 1;
        end
    end
end

% nanoparticles formation
if c13 ~= 0
    for i = 7 :sa - 7
        for j = 7 :  sa - 7
            if A(i, j) == 13
                for ii = i - 6 : i + 6
                    for jj = j - 4 : j + 4
                        if X(ii, jj) == 0
                            X(ii, jj) = 13;
                            A(ii, jj) = 0;
                        end
                    end
                end
                for ii = i - 4 : i + 4
                    for jj = j - 6 : j + 6
                        if X(ii, jj) == 0
                            X(ii, jj) = 13;
                            A(ii, jj) = 0;
                        end
                    end
                end
```

```
                for ii = i - 5 : 10 : i + 5
                    for jj = j - 5 : 10 : j + 5
                        if X(ii, jj) == 0
                            X(ii, jj) = 13;
                            A(ii, jj) = 0;
                        end
                    end
                end
            end
        end
    end
end

if c12 ~= 0
    for i = 7 : sa - 7
        for j = 7 : sb - 7
            if A(i, j) == 12
                for ii = i - 6 : i + 5
                    for jj = j - 3 : j + 4
                        if X(ii, jj) == 0
                            X(ii, jj) = 12;
                            A(ii, jj) = 0;
                        end
                    end
                end
                for ii = i - 4 : i + 3
                    for jj = j - 5 : j + 6
                        if X(ii, jj) == 0
                            X(ii, jj) = 12;
                            A(ii, jj) = 0;
                        end
                    end
                end
                for ii = i - 5 : 9 : i + 4
                    for jj = j - 4 : 9 : j + 5
                        if X(ii, jj) == 0
                            X(ii, jj) = 12;
                            A(ii, jj) = 0;
                        end
                    end
                end
            end
        end
    end
end

if c11 ~= 0
    for i = 6 : sa - 6
        for j = 6 : sb - 6
            if A(i, j) == 11
                for ii = i - 5 : i + 5
                    for jj = j - 3 : j + 3
                        if X(ii, jj) == 0
                            X(ii, jj) = 11;
                            A(ii, jj) = 0;
                        end
```

```
                    end
                end
                for ii = i - 3 : i + 3
                    for jj = j - 5 : j + 5
                        if X(ii, jj) == 0
                            X(ii, jj) = 11;
                            A(ii, jj) = 0;
                        end
                    end
                end
                for ii = i - 4 : 8 : i + 4
                    for jj = j - 4 : 8 : j + 4
                        if X(ii, jj) == 0
                            X(ii, jj) = 11;
                            A(ii, jj) = 0;
                        end
                    end
                end
            end
        end
    end
end

if c10 ~= 0
    for i = 6 : sa - 6
        for j = 6 : sb - 6
            if A(i, j) == 10
                for ii = i - 5 : i + 4
                    for jj = j - 2 : j + 3
                        if X(ii, jj) == 0
                            X(ii, jj) = 10;
                            A(ii, jj) = 0;
                        end
                    end
                end
                for ii = i - 3 : i + 2
                    for jj = j - 4 : j + 5
                        if X(ii, jj) == 0
                            X(ii, jj) = 10;
                            A(ii, jj) = 0;
                        end
                    end
                end
                for ii = i - 4 : 7 : i + 3
                    for jj = j - 3 : 7 : j + 4
                        if X(ii, jj) == 0
                            X(ii, jj) = 10;
                            A(ii, jj) = 0;
                        end
                    end
                end
            end
        end
    end
end
```

```
if c9 ~= 0
    for i = 5 : sa - 5
        for j = 6 : sa - 5
            if A(i, j) == 9
                for ii = i - 4 : i + 4
                    for jj = j - 2 : j + 2
                        if X(ii, jj) == 0
                            X(ii, jj) = 9;
                            A(ii, jj) = 0;
                        end
                    end
                end
                for ii = i - 2 : i + 2
                    for jj = j - 4 : j + 4
                        if X(ii, jj) == 0
                            X(ii, jj) = 9;
                            A(ii, jj) = 0;
                        end
                    end
                end
                for ii = i - 3 : 6 : i + 3
                    for jj = j - 3 : 6 : j + 3
                        if X(ii, jj) == 0
                            X(ii, jj) = 9;
                            A(ii, jj) = 0;
                        end
                    end
                end
            end
        end
    end
end

if c8 ~= 0
    for i = 5 : sa - 5
        for j = 5 : sb - 5
            if A(i, j) == 8
                for ii = i - 4 : i + 3
                    for jj = j - 1 : j + 2
                        if X(ii, jj) == 0
                            X(ii, jj) = 8;
                            A(ii, jj) = 0;
                        end
                    end
                end
                for ii = i - 2 : i + 1
                    for jj = j - 3 : j + 4
                        if X(ii, jj) == 0
                            X(ii, jj) = 8;
                            A(ii, jj) = 0;
                        end
                    end
                end
                for ii = i - 3 : 5 : i + 2
                    for jj = j - 2 : 5 : j + 3
                        if X(ii, jj) == 0
                            X(ii, jj) = 8;
```

```
                            A(ii, jj) = 0;
                        end
                    end
                end
            end
        end
    end
end

if c7 ~= 0
    for i = 4 : sa - 4
        for j = 4 : sb - 4
            if A(i, j) == 7
                for ii = i - 1 : i + 1
                    for jj = j - 3 : j + 3
                        if X(ii, jj) == 0
                            X(ii, jj) = 7;
                            A(ii, jj) = 0;
                        end
                    end
                end
                for ii = i - 3 : i + 3
                    for jj = j - 1 : j + 1
                        if X(ii, jj) == 0
                            X(ii, jj) = 7;
                            A(ii, jj) = 0;
                        end
                    end
                end
                for ii = i - 2 : 4 : i + 2
                    for jj = j - 2 : 4 : j + 2
                        if X(ii, jj) == 0
                            X(ii, jj) = 7;
                            A(ii, jj) = 0;
                        end
                    end
                end
            end
        end
    end
end

if c6 ~= 0
    for i = 4 : sa - 4
        for j = 4 : sb - 4
            if A(i, j) == 6
                for ii = i - 2 : i + 1
                    for jj = j - 2 : j + 3
                        if X(ii, jj) == 0
                            X(ii, jj) = 6;
                            A(ii, jj) = 0;
                        end
                    end
                end
                for ii = i - 3 : 5 : i + 2
                    for jj = j - 1 : j + 2
```

```
                        if X(ii, jj) == 0
                            X(ii, jj) = 6;
                            A(ii, jj) = 0;
                        end
                    end
                end
            end
        end
    end

if c5 ~= 0
    for i = 3 : sa - 3
        for j = 3 : sb - 3
            if A(i, j) == 5
                for ii = i - 2 : i + 2
                    if X(ii, j) == 0
                        X(ii, j) = 5;
                        A(ii, j) = 0;
                    end
                end
                for jj = j - 2 : j + 2
                    if X(i, jj) == 0
                        X(i, jj) = 5;
                        A(i, jj) = 0;
                    end
                end
                for ii = i - 1 : 2 : i + 1
                    for jj = j - 1 : 2 : j + 1
                        if X(ii, jj) == 0;
                            X(ii, jj) = 5;
                            A(ii, jj) = 0;
                        end
                    end
                end
            end
        end
    end
end

if c4 ~= 0
   for i = 3 : sa - 3
       for j = 3 : sb - 3
            if A(i, j) == 4
                for ii = i - 1 : i
                    for jj = j - 1 : j + 2
                        if X(ii, jj) == 0
                            X(ii, jj) = 4;
                            A(ii, jj) = 0;
                        end
                    end
                end
                for ii = i - 2 : 3 : i + 1
                    for jj = j : j + 1
                        if X(ii, jj) == 0
                            X(ii, jj) = 4;
```

```
                            A(ii, jj) = 0;
                        end
                    end
                end
            end
        end
    end

if c3 ~= 0
    for i = 2 : sa - 2
        for j = 2 :sb - 2
            if A(i, j) == 3
                for ii = i - 1 : i + 1
                    if X(ii, j) == 0
                        X(ii, j) = 3;
                        A(ii, j) = 0;
                    end
                end
                for jj = j - 1 : 2 : j + 1
                    if X(i , jj) == 0
                        X(i, jj) = 3;
                        A(i, jj) = 0;
                    end
                end
            end
        end
    end
end

if c2 ~= 0
    for i = 1 : sa - 1
        for j = 1 : sb - 1
            if A(i, j) == 2
                for ii = i : i + 1
                    for jj = j : j + 1
                        if X(ii, jj) == 0
                            X(ii, jj) = 2;
                            A(ii, jj) = 0;
                        end
                    end
                end
            end
        end
    end
end

if c1 ~= 0
    for i = 1 : sa
        for j = 1 : sb
            if A(i, j) == 1
                if X(i, j) == 0
                    X(i, j) = 1;
                    A(i, j) = 0;
                end
            end
```

```
        end
    end
end

% counting the absence of nanoparticles
 for i = 8 : sa - 8
     for j = 8 : sb - 8
         if X(i, j) == 0;
             c0 = c0 + 1;
         end
     end
 end

cover = (1 - c0/((sa - 8)*(sb - 8)))*100;
% finding the conductive path from the bottom to the top

% creating the Pathfinder matrix which sees as conductive path every %
nanoparticle that have interparticle distance less than 1 nm
for j = 1 : sb
    if X(sa - 2, j) ~= 0
        Pathfinder1 (sa - 2, j) = 1;
    end
end

stop = 0;
while stop == 0
    cp = 0;
    for i = sa - 2 : -1 : 2
        for j = 4 : sb - 4
            if X(i, j) ~= 0
                for jj = j - 1 : j + 1
                    if Pathfinder1 (i + 2, jj) == 1
                        if Pathfinder1 (i, j) ~= 1
                            Pathfinder1 (i, j) = 1;
                            cp = cp + 1;
                        end
                    end
                end
            end
        end
    end
    for i = 2 : sa - 1
        for j = 2 : sb - 1
            if Pathfinder1 (i, j) == 1
                for ii = i - 1 : i + 1
                    for jj = j - 1 : j + 1
                        if X(ii, jj) ~= 0
                            if Pathfinder1 (ii, jj) ~= 1
                                Pathfinder1 (ii, jj) = 1;
                                cp = cp + 1;
                            end
                        end
                    end
                end
            end
        end
```

```
    end
    if cp == 0
        stop = 1;
    end
end

% finding the conductive path from the top to the bottom
for j = 1 : sb
    if X(2, j) ~= 0
        Pathfinder2 (2, j) = 1;
    end
end

stop = 0;
while stop == 0
    cp = 0;
    for i = 3 : sa - 3
        for j = 2 : sb - 2
            if X(i, j) ~= 0
                for jj = j - 1 : j + 1
                    if Pathfinder2 (i - 2, jj) == 1
                        if Pathfinder2 (i, j) ~= 1
                            Pathfinder2 (i, j) = 1;
                            cp = cp + 1;
                        end
                    end
                end
            end
        end
    end
    for i = 2 : sa - 1
        for j = 2 : sb - 1
            if Pathfinder2 (i, j) == 1
                for ii = i - 1 : i + 1
                    for jj = j - 1 : j + 1
                        if X(ii, jj) ~= 0
                            if Pathfinder2 (ii, jj) ~= 1
                                Pathfinder2 (ii, jj) = 1;
                                cp = cp + 1;
                            end
                        end
                    end
                end
            end
        end
    end
    if cp == 0
        stop = 1;
    end
end
 % the conductive path is the overlap of pathfinder1 and Pathfinder2
for i = 1 : sa
    for j = 1 : sb
        if Pathfinder1 (i, j) == 1
            if Pathfinder2 (i, j) == 1
                Pathfinder (i, j) = 1;
```

```
            end
        end
    end
end

% Painting the nanoparticles that contribute to the path with red color
for i = 1 : sa
    for j = 1 : sb
        if X(i, j) ~= 0
            D(i, j) = 2;
            if Pathfinder (i, j) ~= 0
               if Pathfinder2 (i, j) ~= 0
                   D(i, j) = 1;
               end
            end
        end
    end
end

% creating the nodes matrix
for j = 1 : sb
    if D (sa - 13, j) == 1
        K (sa - 13, j) = 1;
    end
end

stop = 0;
while stop == 0;
    cp = 0;
    for i = sa - 1 : -1 : 2
        for j = 2 : sb - 1
            if D (i, j) == 1
                for ii = i - 1 : i + 1
                    for jj = j - 1 : j + 1
                        if D (ii, jj) == 1 && K (i, j) == 1
                            if K (ii, jj) ~= 1
                                K (ii, jj) = 1;
                                cp = cp + 1;
                            end
                        end
                    end
                end
            end
        end
    end
    if cp == 0
        stop = 1;
    end
end

% nanoparticles that have number 1 and 2 are the two electrodes
for j = 1 : sb
    if D (2, j) == 1
        K (2  , j) = 2;
    end
end
```

```
stop = 0;
while stop == 0;
    cp = 0;
    for i = 2 : sa - 1
        for j = 2 : sb - 1
            if D (i, j) == 1
                for ii = i - 1 : i + 1
                    for jj = j - 1 : j + 1
                        if D (ii, jj) == 1 && K (i, j) == 2
                            if K (ii, jj) ~= 2
                                K (ii, jj) = 2;
                                cp = cp + 1;
                            end
                        end
                    end
                end
            end
        end
    end
    if cp == 0
        stop = 1;
    end
end

%creating the matrix that names the contributing nanoparticles with numbers
except 1 and 2
n = 2;
for i = 2 : sa - 1
    for j = 2 : sb - 1
        if D(i, j) == 1
            if K(i, j) == 0 && K(i - 1, j - 1) == 0 && K(i, j - 1) == 0 &&
K(i + 1, j - 1) == 0 && K(i - 1, j) == 0 && K(i + 1, j) == 0 && K(i - 1, j +
1) == 0 && K(i, j + 1) == 0 && K(i + 1, j + 1) == 0
                n = n + 1;
                K(i, j) = n;
                if D(i, j + 1) == 1
                    K(i, j + 1) = n;
                end
                if D(i + 1, j - 1) == 1
                    K(i + 1, j - 1) = n;
                end
                if D(i + 1, j) == 1
                    K(i + 1, j) = n;
                end
                if D(i + 1, j + 1) == 1
                    K(i + 1, j + 1) = n;
                end
                if D(i - 1, j + 1) == 1
                    K(i - 1, j + 1) = n;
                end
                if D(i - 1, j) == 1
                    K(i - 1, j) = n;
                end
                if D(i - 1, j - 1) == 1
                    K(i - 1, j - 1) = n;
```

```
                end
                if D(i, j - 1) == 1
                    K(i, j - 1) = n;
                end
            end
        end
    end
end

stop = 0;
while stop == 0
    cp = 0;
    for i = 2 : sa - 1
        for j = 2 : sb - 1
            if K(i, j) > 2
                B = zeros(9, 1);
                B(1, 1) = K(i - 1, j - 1);
                B(2, 1) = K(i, j - 1);
                B(3, 1) = K(i + 1, j - 1);
                B(4, 1) = K(i - 1, j);
                B(5, 1) = K(i + 1, j);
                B(6, 1) = K(i - 1, j + 1);
                B(7, 1) = K(i, j + 1);
                B(8, 1) = K(i + 1, j + 1);
                B(9, 1) = K(i, j);
                o = min(B(B > 2));
                if o < K(i, j)
                    K(i, j) = o;
                    cp = cp + 1;
                end
            end
        end
    end
    if cp == 0
        stop = 1;
    end
end

% correcting matrix K
stop = 0;
while stop == 0;
    cp = 0;
    for i = 2 :  sa - 1
        for j = 2 : sb - 1
            if K (i, j) ~= 0
                n = K(i, j);
                for ii = i - 1 : i + 1
                    for jj = j - 1 : j + 1
                        if D (ii, jj) == 1 && K (ii, jj) == 0
                            K (ii, jj) = n;
                            cp = cp + 1;
                        end
                    end
                end
            end
        end
```

```
    end
    if cp == 0
        stop = 1; % \m/
    end
end

stop = 0;
while stop == 0
    cp = 0;
    for i = 2 : sa - 1
        for j = 2 : sb - 1
            if K(i, j) > 2
                B = zeros(9, 1);
                B(1, 1) = K(i - 1, j - 1);
                B(2, 1) = K(i, j - 1);
                B(3, 1) = K(i + 1, j - 1);
                B(4, 1) = K(i - 1, j);
                B(5, 1) = K(i + 1, j);
                B(6, 1) = K(i - 1, j + 1);
                B(7, 1) = K(i, j + 1);
                B(8, 1) = K(i + 1, j + 1);
                B(9, 1) = K(i, j);
                o = min(B(B > 2));
                if o < K(i, j)
                    K(i, j) = o;
                    cp = cp + 1;
                end
            end
        end
    end
    if cp == 0
        stop = 1;
    end
end

% correcting matrix K and the edges
for j = 1: sb
    if K(1, j) ~= 0 && K(1, j) ~= 2
        K(1, j) = 2;
    end
    if K(sa, j) ~= 0 && K(sa, j) ~= 1
        K(sa, j) = 1;
    end
end

for i = 1 : sa
    if K(i, 1) ~= 0
        for ii = i - 1 : i + 1
            if K(ii, 2) ~= 0
                n = K(ii, 2);
            end
        end
        if K(i, 1) ~= n
            K(i, 1) = n;
        end
    end
```

```
    if K(i, sb) ~= 0
        for ii = i - 1 : i + 1
            if K(ii, sb - 1) ~= 0
                n = K(ii, sb - 1);
            end
        end
        if K(i, sb) ~= n
            K(i, sb) = n;
        end
    end
end

% counting the different numbers of K
BA = unique(K);
[cnodes, dim] = size(BA);

% subtracting the zeros and the result is the number of nodes in the
equivalent circuit
nodes = cnodes - 1;

p = 3;
for i = 1 : cnodes
    d = BA(i, 1);
    if d > 2
        for ii = 1 : sa
            for j = 1 : sb
                if K(ii, j) == d
                    K(ii, j) = p;
                end
            end
        end
        p = p + 1;
    end
end

option = 2; % checking if the conductive path connects directly the two
electrodes
for j = 1 : sb
    if K(2, j) == 1 || K(sa - 1, j) == 2
        option = 1;
    end
end
f = 0;
drf = int16((xf - 1)/step + 1);
Rs = zeros(drf, 1);
Rf = zeros(drf, 1);
strain = zeros(drf, 1);
dRF = zeros(drf, 1);
GF = zeros(drf, 1);
R1 = zeros(nodes, nodes);
R2 = zeros(nodes, nodes);
R3 = zeros(nodes, nodes);
R = zeros(nodes, nodes);
for i = 3 : sa - 3
    for j = 3  : sb - 3
        if K(i, j) >= 1
```

```
            if K(i - 1, j - 1) == 0 || K(i, j - 1) == 0 || K(i + 1, j - 1) ==
0 || K(i - 1, j) == 0 || K(i + 1, j) == 0 || K(i - 1, j + 1) == 0 || K(i, j +
1) == 0 || K(i + 1, j + 1) == 0
                q = K(i, j);
                if K(i - 2, j) ~= 0 && K(i - 2, j) ~= q
                    w1 = K(i - 2, j);
                    R1(q, w1) = R1(q, w1) + 1;
                end
                if K(i, j - 2) ~= 0 && K(i, j - 2) ~= q
                    w2 = K(i, j - 2);
                    R2(q, w2) = R2(q, w2) + 1;
                end
                if K(i + 2, j) ~= 0 && K(i + 2, j) ~= q
                    w3 = K(i + 2, j);
                    R1(q, w3) = R1(q, w3) + 1;
                end
                if K(i, j + 2) ~= 0 && K(i, j + 2) ~= q
                    w4 = K(i, j + 2);
                    R2(q, w4) = R2(q, w4) + 1;
                end
                if K(i - 2, j - 1) ~= 0 && K(i - 2, j - 1) ~= q
                    w5 = K(i - 2, j - 1);
                    R3(q, w5) = R3(q, w5) + 1;
                end
                if K(i - 2, j + 1) ~= 0 && K(i - 2, j + 1) ~= q
                    w6 = K(i - 2, j + 1);
                    R3(q, w6) = R3(q, w6) + 1;
                end
                if K(i - 1, j - 2) ~= 0 && K(i - 1, j - 2) ~= q
                    w7 = K(i - 1, j - 2);
                    R3(q, w7) = R3(q, w7) + 1;
                end
                if K(i - 1, j + 2) ~= 0 && K(i - 1, j + 2) ~= q
                    w8 = K(i - 1, j + 2);
                    R3(q, w8) = R3(q, w8) + 1;
                end
                if K(i + 1, j - 2) ~= 0 && K(i + 1, j - 2) ~= q
                    w9 = K(i + 1, j - 2);
                    R3(q, w9) = R3(q, w9) + 1;
                end
                if K(i + 1, j + 2) ~= 0 && K(i + 1, j + 2) ~= q
                    w10 = K(i + 1, j + 2);
                    R3(q, w10) = R3(q, w10) + 1;
                end
                if K(i + 2, j - 1) ~= 0 && K(i + 2, j - 1) ~= q
                    w11 = K(i + 2, j - 1);
                    R3(q, w11) = R3(q, w11) + 1;
                end
                if K(i + 2, j + 1) ~= 0 && K(i + 2, j + 1) ~= q
                    w12 = K(i + 2, j + 1);
                    R3(q, w12) = R3(q, w12) + 1;
                end
            end
        end
    end
end
dist1 = rand(nodes);
```

```
dist2 = rand(nodes);
dist3 = zeros(nodes, nodes);
for i = 1 : nodes
    for j = 1 : nodes
        dist3(i, j) = sqrt((dist1(i, j))^2 + (dist2(i, j))^2);
        if R1(i, j) > 0
            R1(i, j) = r*exp(b*dist1(i, j))*exp(Ecfinal*(1/(radius*10^-9) -
1/((radius + dist1(i, j))*10^-9)));
        end
        if R2(i, j) > 0
            R2(i, j) = r*exp(b*dist2(i, j))*exp(Ecfinal*(1/(radius*10^-9) -
1/((radius + dist2(i, j))*10^-9)));
        end
        if R3(i, j) > 0
            R3(i, j) = r*exp(b*dist3(i, j))*exp(Ecfinal*(1/(radius*10^-9) -
1/((radius + dist3(i, j))*10^-9)));
        end
    end
end
for i = 1 : nodes
    for j = 1 : nodes
        if R1(i, j) > 0 && R2(i, j) == 0 && R3(i, j) == 0
            R(i, j) = R1(i, j);
        elseif R1(i, j) == 0 && R2(i, j) > 0 && R3(i, j) == 0
            R(i, j) = R2(i, j);
        elseif R1(i, j) == 0 && R2(i, j) == 0 && R3(i, j) > 0
            R(i, j) = R3(i, j);
        elseif R1(i, j) > 0 && R2(i, j) > 0 && R3(i, j) == 0
            if R1(i, j) <= R2(i, j)
                R(i, j) = R1(i, j);
            else
                  R(i, j) = R2(i, j);
            end
        elseif R1(i, j) > 0 && R2(i, j) == 0 && R3(i, j) > 0
            if R1(i, j) <= R3(i, j)
                R(i, j) = R1(i, j);
            else
                R(i, j) = R3(i, j);
            end
        elseif R1(i, j) == 0 && R2(i, j) > 0 && R3(i, j) > 0
             if R2(i, j) <= R3(i, j)
                R(i, j) = R2(i, j);
             else
                R(i, j) = R3(i, j);
             end
        elseif R1(i, j) > 0 && R2(i, j) > 0 && R3(i, j) > 0
             if R1(i, j) <= R2(i, j) && R1(i, j) <= R3(i, j)
                R(i, j) = R1(i, j);
             elseif R2(i, j) <= R1(i, j) && R2(i, j) <= R3(i, j)
                R(i, j) = R2(i, j);
             elseif R3(i, j) <= R1(i, j) && R3(i, j) <= R2(i, j)
                R(i, j) = R3(i, j);
             end
        end
    end
end
for i = 1 : nodes
```

```
    for j = 1 : nodes
        if R(i, j) ~= R(j, i);
            R(i, j) = R(j, i);
        end
    end
end

for x = 1 : step : xf  %vertical distance
    for i = 1 : nodes
        for j = 1 : nodes
            dist1(i, j) = dist1(i, j) + step;
            dist2(i, j) = dist2(i, j) - dy;
            dist3(i, j) = sqrt((dist1(i, j))^2 + (dist2(i, j))^2);
            if R1(i, j) > 0
                R1(i, j) = r*exp(b*dist1(i, j))*exp(Ecfinal*(1/(radius*10^-9)
- 1/((radius + dist1(i, j))*10^-9)));
            end
            if R2(i, j) > 0
                R2(i, j) = r*exp(b*dist2(i, j))*exp(Ecfinal*(1/(radius*10^-9)
- 1/((radius + dist2(i, j))*10^-9)));
            end
            if R3(i, j) > 0
                R3(i, j) = r*exp(b*dist3(i, j))*exp(Ecfinal*(1/(radius*10^-9)
- 1/((radius + dist3(i, j))*10^-9)));
            end
        end
    end
    for i = 1 : nodes
        for j = 1 : nodes
            if R1(i, j) > 0 && R2(i, j) == 0 && R3(i, j) == 0
                R(i, j) = R1(i, j);
            elseif R1(i, j) == 0 && R2(i, j) > 0 && R3(i, j) == 0
                R(i, j) = R2(i, j);
            elseif R1(i, j) == 0 && R2(i, j) == 0 && R3(i, j) > 0
                R(i, j) = R3(i, j);
            elseif R1(i, j) > 0 && R2(i, j) > 0 && R3(i, j) == 0
                if R1(i, j) <= R2(i, j)
                    R(i, j) = R1(i, j);
                else
                    R(i, j) = R2(i, j);
                end
            elseif R1(i, j) > 0 && R2(i, j) == 0 && R3(i, j) > 0
                if R1(i, j) <= R3(i, j)
                    R(i, j) = R1(i, j);
                else
                    R(i, j) = R3(i, j);
                end
            elseif R1(i, j) == 0 && R2(i, j) > 0 && R3(i, j) > 0
                if R2(i, j) <= R3(i, j)
                    R(i, j) = R2(i, j);
                else
                    R(i, j) = R3(i, j);
                end
            elseif R1(i, j) > 0 && R2(i, j) > 0 && R3(i, j) > 0
                if R1(i, j) <= R2(i, j) && R1(i, j) <= R3(i, j)
                    R(i, j) = R1(i, j);
                elseif R2(i, j) <= R1(i, j) && R2(i, j) <= R3(i, j)
```

```
                    R(i, j) = R2(i, j);
                elseif R3(i, j) <= R1(i, j) && R3(i, j) <= R2(i, j)
                    R(i, j) = R3(i, j);
                end
            end
        end
    end
    for i = 1 : nodes
        for j = 1 : nodes
            if R(i, j) ~= R(j, i);
                R(i, j) = R(j, i);
            end
        end
    end
    C = zeros(nodes, nodes);
    for i = 1 : nodes
        for j = 1 : nodes
            if R(i, j) ~= 0
                C(i, j) = 1/(R(i, j));
            end
            C(i, j) = - C(i, j);
        end
    end
    S = sum(C, 2);
    for i = 1 : nodes
        C(i, i) = - S(i, 1);
    end
    if nodes ~= 0
        f = f + 1;
        L = pinv(C); % pseudoinverce laplace matrix
        Rs(f, 1) = L(1, 1) - 2*L(1, 2) + L(2, 2);
        Rf(f, 1) = Rs(f, 1)*EF;
        strain(f, 1) = ((x - 1)/1)*100;
        dRF(f, 1) = ((Rf(f, 1) - Rf(1, 1))/Rf(1, 1))*100;
        GF(f, 1) = dRF(f, 1)/strain(f, 1);
    end
end

coverD = 0;
for i = 8 : sa - 8
    for j = 8 : sb - 8
        if D (i, j) == 1
            coverD = coverD + 1;
        end
    end
end
coverDpercent = (coverD*100)/((sa - 8)*(sb - 8));

clear('Y'); % Clear the name Y
Y = zeros(sb - 16, sa - 16, 3); % Pre-allocate space for the color array
% Filling the color array
for idxx = 1 : sb - 16
    for idxy = 1 : sa - 16
        if (D(idxx, idxy) == 0) %white
            Y(idxx, idxy, 1) = 1;
            Y(idxx, idxy, 2) = 1;
```

```
            Y(idxx, idxy, 3) = 1;
        end
        if (D(idxx, idxy) == 2) % blue
            Y(idxx, idxy, 1) = 0;
            Y(idxx, idxy, 2) = 0;
            Y(idxx, idxy, 3) = 1;
        end
        if (D(idxx, idxy) == 1) % red
            Y(idxx, idxy, 1) = 1;
            Y(idxx, idxy, 2) = 0;
            Y(idxx, idxy, 3) = 0;
        end
    end
end

imshow(Y, 'InitialMagnification', 1000)
grid on;
axis on;
set(gca, 'xtick', (0:100:sa - 16));
set(gca, 'ytick', (0:100:sb - 16)); % Plot the results with a grid.3
```